CONTROL OF
SWITCHED RELUCTANCE MACHINES

A THESIS FOR THE DEGREE OF DOCTOR OF PHILOSOPHY

Presented to

Dublin City University (DCU)

by

Eoin Kennedy, B. Eng.

School of Electronic Engineering
Dublin City University

Research Supervisor
Dr. Marissa Condon

August 2005

Declaration

I hereby certify that this material, which I now submit for assessment on the programme of study leading to the award of PhD in Electronic Engineering, is entirely my own work and has not been taken from the work of others save and to the extent that such work has been cited and acknowledged within the text of my work.

Signed: Eóin Kennedy

ID No.: 96083492

Date: 9/9/2005

Abstract

This thesis is concerned with the control of switched reluctance machines for both motoring and generating applications. There are different control objectives in each case. For motoring operation, there are two possible control objectives. If the SRM is being employed in a servo-type application, the desire is for a constant output torque. However, for low performance applications where some amount of torque ripple is acceptable, the aim is to achieve efficient and accurate speed regulation. When the SRM is employed for generating purposes, the goal is to maintain the dc bus voltage at the required value while achieving maximum efficiency.

Preliminary investigative work on switched reluctance machine control in both motoring and generating modes is performed. This includes the implementation and testing through simulation of two control strategies described in the literature. In addition, an experimental system is built for the development and testing of new control strategies.

The inherent nonlinearity of the switched reluctance machine results in ripple in the torque profile. This adversely affects motoring performance for servo-type applications. Hence, three neuro-fuzzy control strategies for torque ripple minimisation in switched reluctance motors are developed. For all three control strategies, the training of a neuro-fuzzy compensator and the incorporation of the trained compensator into the overall switched reluctance drive are described. The performance of the control strategies in reducing the torque ripple is examined with simulations and through experimental testing.

While the torque ripple is troublesome for servo-type applications, there are some applications where a certain amount of torque ripple is acceptable. Therefore, four simple motor control strategies for torque ripple-tolerant applications are described and tested experimentally. Three of the control strategies are for low speed motoring operation while the fourth is aimed at high speed motoring operation.

Finally, three closed-loop generator control strategies aimed at high speed operation in single pulse mode are developed. The three control strategies are examined by testing on the experimental system. A comparison of the performance of the control strategies in terms of efficiency and peak current produced by each is presented.

Acknowledgements

I wish to express my sincere gratitude to my supervisor, Dr. Marissa Condon, for all her guidance, advice and support throughout the duration of this project.

Many thanks to Jim Dowling for his help and support during my time in DCU.

I would like to thank PEI Technologies and DCU for financial support and assistance during the course of this research.

I am very grateful to the staff in PEI technologies, Liam Sweeney, Ciaran Waters and Claus Agersbaek, as well as my fellow postgrads for their help, support and suggestions.

Sincere thanks to Anthony Murphy for his invaluable assistance in the construction of the experimental rig.

Finally, I wish to thank my parents, family, girlfriend and friends for all their encouragement over the last few years.

Contents

Abstract I

Acknowledgements II

Contents III

1 Introduction 1

1.0 Motivation and overview 1

1.1 Historical review 4

1.2 Outline of thesis 11

2 Operating principles and characteristics of SRMs 13

2.0 Introduction 13

2.1 The switched reluctance machine 13

2.2 Mathematical description of the SRM 19

2.2.1 Torque calculation using co-energy 22

2.3 Torque/speed characteristic 26

2.4 Power converter 27

2.5 Dynamic operation of the SRM 29

2.5.1 Low speed motoring 30

2.5.2 High speed motoring 35

2.6 Fundamentals of SR generation 37

2.7 Summary of the advantages/disadvantages of SRMs 43

3 Initial investigative work 46

3.0 Introduction 46

3.1 MATLAB/Simulink 46

3.1.1 MATLAB 46

3.1.2 Simulink 47

3.2 Simple SRM model employed in the simulation work 48

3.3 Torque estimation using a self-tuning SRM model 55

3.4 Self-tuning torque ripple minimisation controller 61

3.5 SR generator control using an inverse model approach 67

4 Torque ripple minimisation **75**

4.0 Introduction..... 75

4.1 Fuzzy Logic..... 75

4.2 Fuzzy Inference System..... 80

4.3 ANFIS..... 82

4.4 Basics of the proposed torque ripple minimisation approach..... 85

4.5 Neuro-fuzzy control strategy no. 1..... 86

4.6 Simulation results for control strategy no. 1..... 88

4.6.1 6/4 three-phase SRM results for control strategy no. 1..... 89

4.6.2 12/8 three-phase SRM results for control strategy no. 1..... 94

4.7 Neuro-fuzzy control strategy no. 2..... 95

4.8 Simulation results for control strategy no. 2..... 99

4.8.1 6/4 three-phase SRM results for control strategy no. 2..... 99

4.8.1.1 Initial tests – constant current reference..... 100

4.8.1.2 PI speed control tests..... 103

4.8.2 12/8 three-phase SRM results for control strategy no. 2..... 107

4.8.2.1 Initial tests – constant current reference..... 108

4.8.2.2 PI speed control tests..... 111

4.9 Neuro-fuzzy control strategy no. 3..... 116

4.10 Simulation results for control strategy no. 3..... 119

4.10.1 6/4 three-phase SRM results for control strategy no. 3..... 119

4.10.1.1 Initial tests – constant current reference..... 119

4.10.1.2 PI speed control tests..... 121

4.10.2 12/8 three-phase SRM results for control strategy no. 3... 124

4.10.2.1 Initial tests – constant current reference..... 125

4.10.2.2 PI speed control tests..... 127

4.11 Torque estimation..... 129

4.12 Summary and conclusions..... 131

5 Experimental set-up **134**

5.0 Introduction..... 134

5.1 The SRM..... 134

5.2 Power electronic converter..... 136

5.2.1 Converter topologies..... 137

5.2.2 Power converter circuit employed..... 141
5.3 DSP controller..... 144
5.4 Current measurement..... 146
5.5 Voltage measurement..... 150
5.6 Position sensor and speed estimation..... 152
5.6.1 Simple slotted optical disk encoder..... 152
5.6.2 Incremental encoder..... 154
5.6.3 Speed estimation..... 156
5.6.3.1 Speed estimation using a general-purpose timer... 156
5.6.3.2 Speed estimation using the EET..... 157
5.7 Experimental SRM development set-up..... 158

6 Experimental motor control **160**
6.0 Introduction..... 160
6.1 SRM start-up algorithm..... 160
6.2 Motor speed control for torque ripple-tolerant applications..... 162
6.2.1 Low speed motoring – current regulation..... 162
6.2.1.1 Simple control strategy..... 162
6.2.1.2 Automatic turn-off angle control strategy..... 166
6.2.1.3 Extended automatic turn-off angle control strategy.. 171
6.2.1.4 Optimal efficiency control strategy..... 179
6.2.2 High speed motoring – single pulse mode control..... 186
6.3 Torque estimation..... 189
6.3.1 Saturated flux-linkage determination..... 191
6.3.2 Flux-linkage estimation..... 193
6.3.3 Parameter identification..... 195
6.3.4 Flux-linkage comparison and nonlinear model verification.. 197
6.3.5 Calculation of phase torque..... 199
6.4 Neuro-fuzzy control strategy no. 3..... 201
6.4.1 Experimental results for neuro-fuzzy control strategy no. 3 203
6.4.1.1 Initial tests – constant current reference..... 204
6.4.1.2 PI speed control tests..... 209
6.5 Summary and conclusions..... 214

7 Experimental generator control **217**

7.0 Introduction 217

7.1 Generating characteristics of the experimental 12/8 three-phase SRM 217

7.2 Simple control strategy 224

7.3 Inverse model control strategy 227

7.4 Optimal control strategy 232

7.5 Efficiency comparison 240

7.6 Peak current comparison 245

7.7 Summary and conclusions 246

8 Summary and conclusions **248**

Bibliography **256**

Appendix A: Experimental system **265**

A1 Schematics 265

A2 Photos of the experimental system 269

Appendix B: ADSP-21992 EZ-KIT Lite evaluation board **275**

B1 Overview of the Analog-to-Digital Conversion unit 276

B2 Overview of the Encoder Interface Unit 278

B3 Overview of the general-purpose timer unit 280

B4 Overview of the Flag I/O peripheral unit 281

B5 Writing C-callable assembly functions and creating libraries 281

B6 DSP clock frequency 282

Appendix C: DSP C and assembly code **283**

C1 Writing C-callable assembly language functions 283

C2 Increasing the DSP core clock frequency 284

C3 C functions employed in current and voltage measurement 285

C4 Flux-linkage estimation 286

C5 Position derivation information 286

Appendix D: Publications **289**

Chapter One – Introduction

1.0 Motivation and overview

The aim of the work detailed in this thesis is the development and testing of several control strategies for the Switched Reluctance Machine (SRM) for operation both as a motor and as a generator. An SRM may operate as a motor or as a generator by simply changing the placement of the current pulses with respect to rotor position. However, there are important differences in the control objectives and in the implementation of the control strategies for the two operating modes.

In motoring mode, the inherent nonlinearity of the SRM results in periodic pulsations or ripple in the torque profile. The magnitude and periodicity of the torque ripple is machine-dependent while the level of torque ripple deemed acceptable is very much application-dependent. There are some low performance applications where a significant amount of torque ripple is permissible. However, for servo-type applications, the torque ripple is troublesome and is one of the primary reasons why the SRM has seen little penetration in industry. For example, the target torque ripple in electric power-steering systems is a maximum of 2% (Husain 2002). To this end, various approaches have been proposed for torque ripple reduction. Improvements in the magnetic design of the motor itself can lead to reduced torque ripple [(Byrne 1985), (Tormey 1991) and (Lee 2004)]. Furthermore, control strategy design for torque ripple reduction has been one of the major research areas in relation to SRMs over the last number of years.

Numerous control approaches for torque ripple reduction have been investigated and described in the literature including: knowledge of the magnetic characteristics of the machine [(Moreira 1992) and (Schramm 1992)], use of mathematical models of the SRM [(Rochford 1993), (Kjaer 1997), (Inanc 1997), (Russa 1998) and (Bizkevelci 2004)] and on-line adaptive control techniques using complex algorithms [(Russa 1998) and (Russa 2000)]. Because of the SRM's strong nonlinear magnetic characteristics, artificial intelligence based methods such as Fuzzy Logic [(Bolognani 1996) and (Mir 1999)], Neural Networks [(Reay 1993) and (O' Donovan 1994)] and neuro-fuzzy compensation [(Henriques 2000), (Henriques 2001) and (Henriques 2001a)] are particularly suited to SRM control. With the advent of new powerful

Digital Signal Processors (DSPs) at reduced prices, more advanced control algorithms can be implemented in a cost-effective manner. This thesis introduces three torque ripple minimisation control schemes that fully utilise the powerful DSP technology currently available and which are aimed at low speed servo-type applications.

Three neuro-fuzzy control strategies for torque ripple minimisation in Switched Reluctance (SR) motors are developed. As with any torque ripple reduction control scheme, the essential problem is choosing the appropriate current waveforms to ensure low ripple. The three neuro-fuzzy control schemes achieve this by adding a compensating signal to the output of a PI controller in a current-regulated speed control loop. The parameters employed in the training of the compensating current signal profile and the manner in which the training is conducted differ for the three control strategies. In the particular implementations described in this thesis, all three neuro-fuzzy compensators are trained off-line. However, there is no obstacle to on-line training. A torque estimator is employed in the training of the compensators and, in the case of two of the control strategies, also in the subsequent operation of the SR drive. Simulated results confirm a significant reduction in the torque ripple for the three control strategies. In addition, the performance of one of the control strategies is verified by experimental implementation and testing. The three control schemes have the advantage that a pre-existing model of the SRM, for example a model in the form of torque-current-position characteristics, is not required and only a few easily measurable parameters are needed.

For certain motoring applications, some degree of torque ripple may be acceptable. In this thesis, four simple SR motor speed control schemes for torque ripple-tolerant applications are described and experimental results are presented. Three of these control schemes are for low speed motoring operation while the fourth is aimed at high speed motoring operation.

While there has been a considerable body of work produced in the area of SR motor control, there is arguably a dearth of material on the control of SR generators. In fact, according to one source (Fleadh Electronics 2004), of the 4515 papers published on SRMs, only 318 relate to the subject of SR generators. This thesis intends to make a contribution to the area of SR generator control.

While the control objective when motoring is to achieve smooth torque production, the objective when generating is to maintain the dc link voltage at the required value while achieving maximum efficiency. High efficiency is important in that, in addition to leading to lower energy consumption (supplying the same electrical output power for a lower mechanical input power), it enables a smaller and lighter SRM to be used. This thesis describes three possible generator closed-loop voltage control schemes with their performance evaluated experimentally. All of the control strategies assume that the SR generator is operating at a sufficiently high speed to enable operation in single pulse mode. In single pulse mode operation, no current regulation is employed and the power switches are left turned on throughout the entire conduction cycle producing a single pulse of current. The first control scheme is quite simplistic and involves the selection of a fixed turn-off angle (the rotor position where a phase current is switched off) and the subsequent adjustment of the turn-on angle (the rotor position where a phase current is switched on) to regulate the dc link voltage. The second control scheme employs an inverse machine model that relates the firing angles to the average dc link current, the dc link voltage and the generator speed. Although both the simple and inverse model control strategies succeed in regulating the dc link voltage as required, neither strategy enables operation at the preferred optimum efficiency level. Thus, the final control scheme is aimed at achieving operation of the SR generator at optimal efficiency. Experimental measurements enable characterisation of the machine (this could also be done through simulation if an accurate model of the machine is available). This enables a mathematical relationship to be determined between the optimal efficiency turn-off angle and a given dc link current and rotational speed for a particular dc link voltage (in many applications, SR generators deliver energy to a dc link of fixed voltage). While the turn-off angle is varied in pursuit of the optimum efficiency point, the turn-on angle is used to ensure regulation of the dc link voltage (as for the first simplistic control strategy).

In summary, this thesis contributes to the significant body of research conducted on SR motor control over the years through the development of three torque ripple reduction control strategies for the SRM in motoring mode. In addition, the efficacy of four SR motor speed control schemes for torque ripple-tolerant applications is examined. This thesis also describes the findings of a comprehensive experimental

investigation into the control of an SR generator, a research area that has had a notably smaller impact in the literature to date.

1.1 Historical review

SR motors were amongst the first electric machines to be developed (1830s – 1850s) and, at that time, they were known as 'electromagnetic engines'. A comprehensive history of the development of the SRM detailing the advances made since those first machines is included in (Miller 2001). The following historical review draws considerable information from that particular publication as well as from many additional sources.

According to (Miller 2001), the principle behind early 'electromagnetic engines' was an attempt at converting the once-only attraction for an iron armature into continuous motion and they were based on the horseshoe electromagnet of William Sturgeon (1824) (Sturgeon 1825) and the improved version of Joseph Henry. In essence, these 'electromagnetic engines' used the pull of sequentially excited dc electromagnets to achieve continuous torque and were self-synchronised.

Pioneers in the area of 'electromagnetic engine' design included Callan (an Irishman whose early reluctance motors can still be seen at Maynooth College), Davidson (The Penny Mechanic and Chemist 1843) and Taylor (Mechanic's Magazine 1840) who all built 'electromagnetic engines' independently between 1837 and 1840. These machines had a number of problems associated with them, including poor electromechanical energy conversion efficiency. The large iron volumes used without lamination led to excessive iron losses. In addition, at the end of each switching cycle the stored inductive energy in the electromagnet had to be dissipated. While modern SR motors have the means of feeding the stored energy back to the supply during the demagnetisation process, the early 'electromagnetic engines' dissipated energy wastefully in the form of arcing and sparking at the commutation switches. The other major issue was the structural problems caused by the pulsating radial out-of-balance magnetic forces.

The ring wound armature dc machine was invented by the Italian Pacinotti (1865) and improved upon by Gramme (1869). This machine was far superior in performance to

the SR motor as it then existed and interest in the latter quickly declined. However, the arrival of silicon power switches in the 1960s led to a renewed interest in various dc and variable speed drive configurations including what is now termed the 'switched reluctance motor'. Important work was conducted at Queen's College Dundee in the early 1960s that, according to (Miller 2001), contained 'many of the key features of modern reluctance machines and their drives'. Research in the area of SR motors began to gather momentum with several developments key to the rapid rise of interest in this field. The development of the power transistor was crucial in the quest for efficient and reliable control of the machine. Similarly, the development of microprocessors (and more recently DSPs) enabled complex control algorithms to be implemented while the introduction of high-speed computers enabled improved design and analysis of the highly nonlinear SRM. Furthermore, a greater understanding of the magnetics involved in the SRM greatly improved the energy conversion efficiency. Finally, the general expansion in the use of variable speed drives in industry, automotive and residential applications drove research in that area as a whole.

In the early 1970s, Professor Byrne and his colleagues at University College Dublin published important work detailing the improvement in energy conversion efficiency through exploitation of magnetic saturation [(Byrne 1973) and (Byrne 1976)]. Since then, the positive influence of magnetic saturation on energy conversion efficiency has been verified [(Miller 1985) and (Stephenson 1989)]. Byrne also did valuable work on machines with low phase numbers (Byrne 1973). At around the same time, Lawrenson and Stephenson at the University of Leeds began research on SRMs. This work eventually led to the formation of SR Drives Ltd. (absorbed by Emerson in 1994, SR Drives Ltd. has produced about half of the commercial applications of SRMs since the early 1980s (Miller 2001)). In 1980, Lawrenson et al. produced a landmark paper (Lawrenson 1980) that examined SRMs in general and which awakened worldwide interest in the subject. This paper addressed many design issues such as the choice of the number of phases etc. as well as describing the favorable performance of a four-quadrant variable speed SR motor in comparison with an induction motor of the same size. This paper marked the beginning of the massive resurgence in interest in the SRM. Indeed, the huge increase in the numbers of papers,

dissertations and patents post-1980 is clearly visible from Figure 1.1 and Figure 1.2 (Fleadh Electronics 2004).

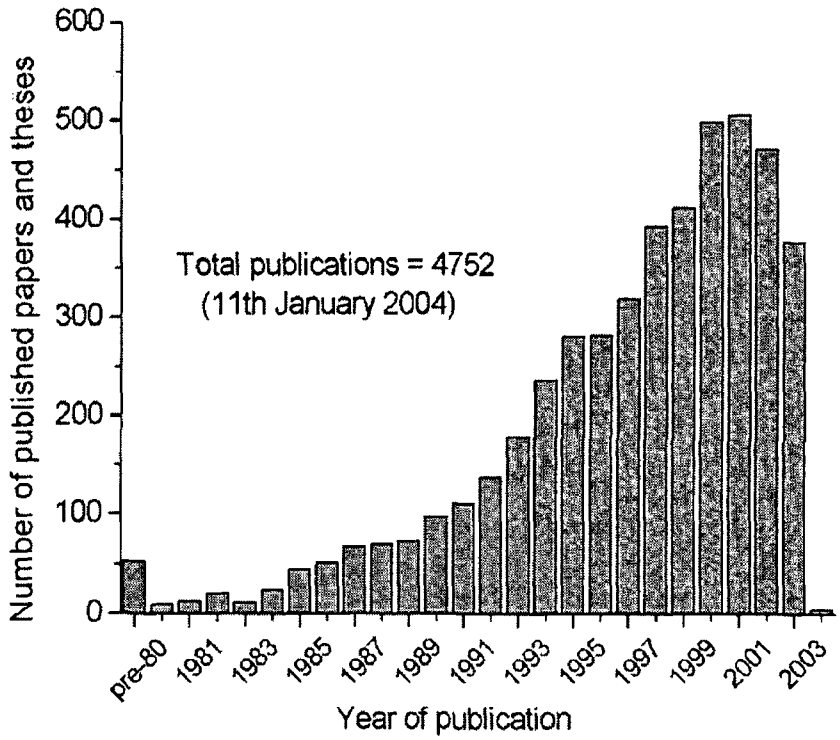

Figure 1.1: Number of published papers and theses over the years.

As can be seen, the numbers of patents published worldwide before 1980 was 275 compared to 6206 since 1980. The same source estimates the total number of papers and dissertations published before 1980 to be 54 with 4698 published post-1980. These numbers don't do justice to the quality and significance of the work conducted pre-1980 since the early work is more likely to contain higher levels of innovation. However, the apparent dearth of material pre-1980 is also due to the fact that much of the research was published in unusual places and has had considerable time to become 'lost' or 'forgotten' (Miller 2001). Despite this, the numbers are reflective of the huge growth in interest in the SRM over the last 30 years.

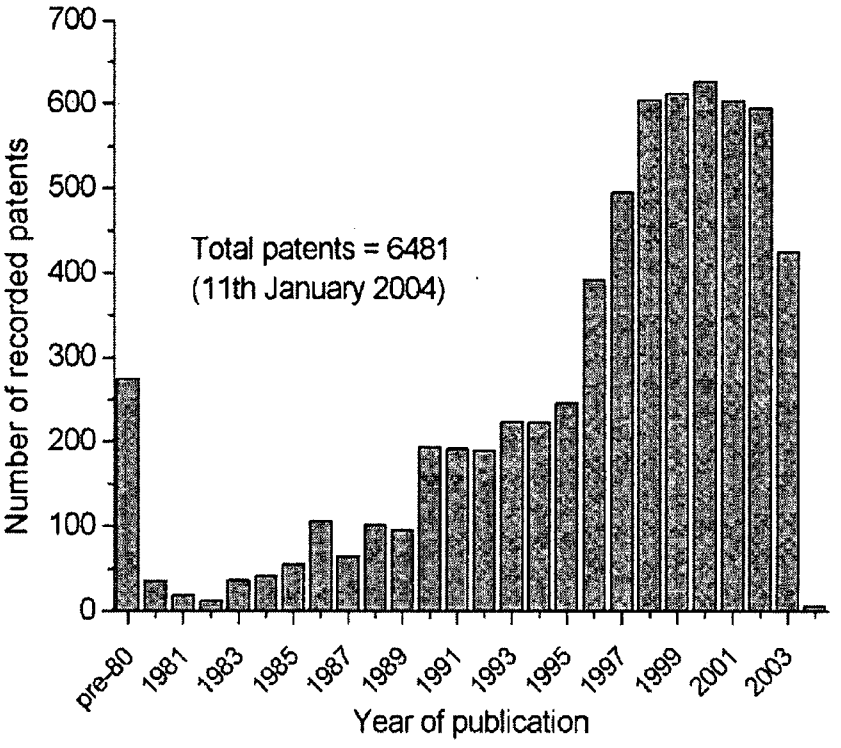

Figure 1.2: Number of recorded patents over the years.

As for the name 'switched reluctance motor' itself, according to (Miller 2001), the first use of that term was in a paper published by S.A Nasar in 1969 (Nasar 1969) and its use became increasingly widespread after publication of the seminal paper by Lawrenson et al. in 1980 (Lawrenson 1980). The term 'switched reluctance motor' could be deemed to be somewhat misleading as the reluctance itself isn't switched. Rather, the name refers to the switching of the phase currents, a necessary aspect of operation. In the USA, the term 'variable reluctance motor' is often employed while the precise term 'electronically commutated reluctance motor' has been used on occasion (Hancock 1990).

As previously stated, one of the key factors in the reemergence of the SRM has been the considerable improvement in the design and analysis of the SRM made possible with the availability of high-speed digital computers. Magnetic optimisation of the motor can be performed using finite element analysis while computer simulation packages enable the dynamic operation and control of the integrated SR drive system to be explored and analysed. For instance, Miller et al. developed a detailed CAD computer program, PC-SRD, that has been widely used over the last number of years

for the design and analysis of SRMs [(Miller 1990) and (Miller 1999)]. With this program, SRMs and basic drive components can be sized and analysed in detail.

Considerable research effort over the years has also been invested in the design of the power electronic converter for the SRM. Miller considered the effect of saturation on the volt-ampere (VA) requirement of the drive and a comparison between the VA rating of an SRM and an induction drive inverter was performed (Miller 1985). In addition, his team at the University of Glasgow introduced an inverter with only one switching device per phase and with a total switch count of N+1 where N is the number of phases (Miller 1988). This reduced switch count inverter was preceded by the single switch per phase inverter assembled by Unnewehr and Koch (Unnewehr 1974). Meanwhile, Ray and Davis looked at the component cost for the power inverter [(Ray 1979) and (Davis 1981)]. Various novel inverters have been designed since with N, N+1, 1.5N and 2N switches [(Krishnan 1990), (Le-Huy 1990), (Pollock 1990), (Krishnan 1993), (Mir 1997), (Dessouky 1998), (De Oliveira 1999) and (Deshpande 2000)]. However, despite the apparent cost saving in using only one switch per phase, according to Miller very few (if any) of the circuit configurations with one switch per phase are used in commercial products because they require auxiliary components, decrease efficiency and limit the control capability (Miller 2002). Both Vukosavic and Barnes have performed useful comparative evaluations of many of the different SRM inverter topologies developed over the years [(Vukosavic 1990) and (Barnes 1998)].

The development of microprocessors and related digital circuitry enabled the implementation of complex algorithms and has paved the way for improved control of the SRM (Bose 1986). Many attempts have been made to reduce the torque ripple inherent in SR motor operation. While one way of reducing the torque ripple is to improve the magnetic design of the motor itself [(Byrne 1985), (Tormey 1991) and (Lee 2004)], another is to employ sophisticated control techniques. Husain recently published a comprehensive paper reviewing the different control approaches to torque ripple reduction (Husain 2002). In addition, recent years have seen significant research into the operation of the SRM without a position sensor. These 'sensorless' schemes are aimed at reducing the overall cost of the drive and making the SRM more competitive with other variable speed drives. Removal of the position sensor also

improves reliability enabling operation in harsh environments. Important early contributions in this area include the chopping current detection technique (Acarnley 1985), open-loop control (Bass 1986) and flux/current methods [(Hedlund 1991) and (Lyons 1991)]. Many different methods of indirectly estimating the rotor position have been proposed but they all make use of the inductance variation in one way or another. A comprehensive review of the various 'sensorless' approaches is included in both (Husain 1996) and (Ehsani 2002).

While the vast majority of the literature focuses on the SRM operating as a motor, there is still a considerable body of work investigating the development and control of the SRM as a generator. Radun published an important paper in 1994 that discussed the instability of the SR generator system for open-loop operation with fixed turn-on and turn-off angles (Radun 1994). As a result, Radun emphasised the need for closed-loop control of the SR generator. In addition, Radun et al. investigated multiple-channel generating systems (Radun 1998). Nedic et al. performed interesting work on the self-excitation of the SR generator at start-up via the placement of permanent magnets in various positions on the stator. The SR generator has also been and is currently under investigation for many variable speed applications. In particular, a SRM based automotive starter/alternator is the subject of a large body of research [(Kokernak 1999), (Besbes 2000), (Mese 2000), (De Vries 2001) and (Fahimi 2001)]. There is also considerable interest in wind energy [(Torrey 1993), (Cardenas 1995) and (Cardenas 2004)] and aerospace applications [(MacMinn 1989), (Radun 1994), (Ferreira 1995), (Radun 1997) and (Cossar 2004)]. A good overview of the advancements made in SR generator control can be found in (Torrey 2002) and (Miller 2001).

Although there have been huge advancements in SRM technology over the last 40 years and a large body of published research, the SRM has yet to see widespread acceptance for application in industry. Table 1.1 lists a few examples of where the SRM has penetrated the market [(Miller 2002) and (Krishnan 2001)]. This is a very short list compared to the one that could be drawn up for induction motors or brushless permanent magnet motors (Miller 2002).

Products	Company
Mining drives	British Jeffrey Diamond
Plotter drive	Hewlett-Packard
Air-handler	A.O Smith
Fork lift/pallet truck drive	Radio Energie
Centrifuge	Beckman Instruments
EV drives	Aisin Seiki
Megatorque direct-drive	NSK Ltd
Several	Mavrik Motors
Automotive cruise control	DANA Corp.
Washer drive	Emerson/SRDL
Pumps,HVAC motion control	Emotron A/b
Floorcare	Ametek Lamb Electric
High-speed motors and controllers	AMC NEC/Densei
250kW low-speed drive	Elektro Magnetix Ltd
General purpose industrial drives	Oulton, Task Drives
Electric doors	Besam A/b
Compressors	Compare Broomwade
Industrial drives	Sicmemotori
Train air conditioning	Normalair Garrett
Weaving machine servos	Picanol

Table 1.1: Switched reluctance products.

There are several reasons why the SRM has yet to have a serious impact in industry. Firstly, other technologies are firmly entrenched in the marketplace and have had huge levels of investment in tooling and infrastructure. Moreover, while there have been great advances in knowledge and development of the SRM over the last 40 years, competing technologies have also made enormous strides. Furthermore, while the drive complexity for a SRM drive is comparable to that of the induction drive, the theory and architecture of SRM controllers are not nearly as widely known and according to Miller 'only a handful of engineers understand the art of designing these controllers at an adequate level to make commercially viable products' (Miller 2002). Despite this, the examples in Table 1.1 show that there are applications where the SRM can be cost-effective and provide good performance. Finally, the conclusion reached by Miller in (Miller 2002) is that, in the future, successful applications are likely to follow the pattern of those in Table 1.1, i.e. 'a highly engineered drive whose development cost must be borne by the application and whose unique features render it the most suitable choice'.

1.2 Outline of thesis

The objective of the work detailed in this thesis is the development and testing of control strategies for the SRM for operation both as a motor and as a generator. Initially, some preliminary investigative work was performed on SRM control along with the construction of an experimental rig. Having completed this, control strategies for the SRM in motoring and generating modes were developed and tested through simulation and/or experimental implementation.

The thesis introduces the basic operating principles and electromagnetic characteristics of the SRM in Chapter Two. The mechanics of torque production and the fundamental control of the machine are discussed. The dynamic operation of the machine in motoring mode is then described. Some background information on the control of SR generators is also provided before finally, a summary of the advantages and disadvantages of the SRM is presented.

Chapter Three describes the initial investigative work into SRM control in both motoring and generating modes. A nonlinear self-tuning model of the SRM that can serve as a torque observer is described and its performance verified through simulation. Two control strategies, one for motoring and one for generating, described in the literature are implemented and tested through simulation.

Chapter Four introduces Fuzzy Logic and explains the operation of the Adaptive Neuro-Fuzzy Inference System (ANFIS). Three torque ripple reduction control strategies are developed and their efficacy is tested through simulation with a full set of results provided.

Chapter Five describes the set-up used for experimental implementation and testing of the control strategies. The properties of the SRM that is employed are described and the key features of the DSP development board are outlined. A number of power electronic converters suitable for SRMs are reviewed and a description of the final power converter selected is given. In addition, the method of current sensing and voltage measurement is examined while the manner in which rotor position and rotational speed information are obtained is illustrated. Finally, the integration of the

SRM rig, power and measurement electronics, DSP, electronic load etc. into the overall experimental set-up is described.

Chapter Six describes the experimental implementation of several SR motor control strategies. The simple starting algorithm employed for 'start-up' of the experimental SR motor is described. Four simple speed control schemes covering low and high speed operation and which are suitable for applications that can tolerate a certain amount of torque ripple are outlined and experimental results are presented. A torque observer, described and tested through simulation in Chapter Three, is experimentally implemented. This torque observer is used in the experimental implementation and testing of one of the torque ripple minimisation control strategies that was previously tested through simulation in Chapter Four.

Chapter Seven addresses the subject of SR generator control. Firstly, the generating characteristics of the particular SRM employed in the experimental set-up are examined. The development and experimental testing of three control strategies is then described. In addition, a comparison of the performance of the three strategies is included.

Finally, Chapter Eight presents a summary of the thesis, conclusions and suggestions for possible further research.

Chapter Two – Operating principles of the SRM

2.0 Introduction

In this chapter, the principles of operation of the switched reluctance machine are introduced and the basic electromagnetic characteristics of the machine are described. A mathematical description of the machine is presented to aid in the understanding of the mechanism of torque production. The basic power converter circuit is introduced and the fundamental control mechanism of the machine is described in terms of the various switching strategies. This is followed by a description of the dynamic operation of the machine in motoring mode. The fundamentals of switched reluctance generation are then introduced. Finally, a summary of the advantages and disadvantages of the switched reluctance machine is presented.

2.1 The switched reluctance machine

The SRM is an extremely simple machine from a construction viewpoint. The rotor has neither magnets nor windings and consists solely of magnetically soft, low loss steel laminations stacked on a shaft. The stator (built from the same material as the rotor) has windings on each pole and one phase of the motor consists of the series connection of the stator windings on diametrically opposite poles. Both the stator and rotor have salient poles, hence the machine is referred to as being doubly salient. The cross-section of a simple regular 6/4 three-phase machine (6/4 implies six stator poles and four rotor poles) is shown in Figure 2.1, which also clearly illustrates the coil winding for a single phase.

When current is passed through one of the phases a magnetic flux path is generated around the stator, the rotor and in the air-gap between the stator and the rotor. The reluctance, $\mathcal{R}$, of any magnetic circuit is given by:

$$\Re = \frac{F}{\phi} = \frac{Hl}{BA} = \frac{l}{\mu A} \tag{2.1}$$

where F is the magnetomotive force, ϕ is the flux, H is the magnetic field strength, l is the length of the magnetic field path, B is the flux density, A is the cross-sectional area of the magnetic path and μ is the permeability of the magnetic material.

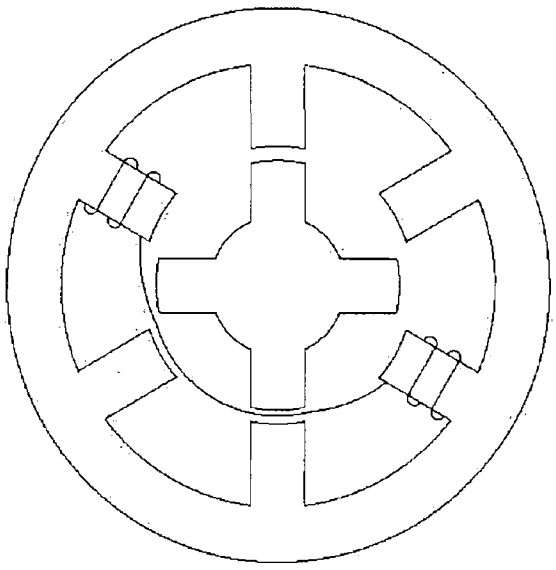

Figure 2.1: Cross-section of a 6/4 three-phase SRM.

The torque in an SRM is produced by the tendency of the moveable part, i.e. the rotor, to move to a position where the reluctance of the magnetic path is minimised (thereby maximising the stator flux-linkage and phase inductance). The permeability of the core material is much greater than the permeability of the air-gap between the rotor and stator. Consequently, the rotor pole-pair adjacent to the energised stator pole-pair seeks alignment since the aligned position is the position of minimum reluctance. The direction of torque generated is a function of the rotor position with respect to the energised phase and is independent of the direction of current flow through the phase winding. When two rotor poles are aligned to a particular set of stator poles, another set of rotor poles is out of alignment with respect to a different set of stator poles. This set of stator poles can then be excited to bring the second pair of rotor poles into alignment. Thus, by energising consecutive phases in succession, it is possible to develop continuous torque in either direction of rotation. Clearly, the term 'switched reluctance machine' does not mean that the reluctance itself is switched but rather it refers to the sequential switching of current from phase to phase as the rotor moves.

Although the machine is termed a switched *reluctance* machine, it may be more intuitive to describe the operation of the machine and the mathematical equations in terms of *inductance*. The inductance, L, is related to the reluctance by:

$$L = \frac{\psi}{i} = \frac{N\phi}{i} = \frac{NBA}{i} = \frac{N\mu HA}{i} = \frac{N\mu HA}{Hl/N} = \frac{N^2}{l/\mu A} = \frac{N^2}{\Re} \tag{2.2}$$

where ψ is the flux-linkage and N is the number of turns on the phase winding. For torque production, the SRM is designed such that the reluctance/inductance varies with rotor position with the regions of increasing and decreasing phase inductance corresponding to the variation in the level of overlap between the rotor and stator poles. Consider the simple 2/2 single-phase machine shown in Figure 2.2. The machine is shown in the aligned and unaligned positions. The phase inductance varies with rotor position in the manner shown in Figure 2.3. The phase inductance is its minimum value in the unaligned position and is at its largest in the aligned position.

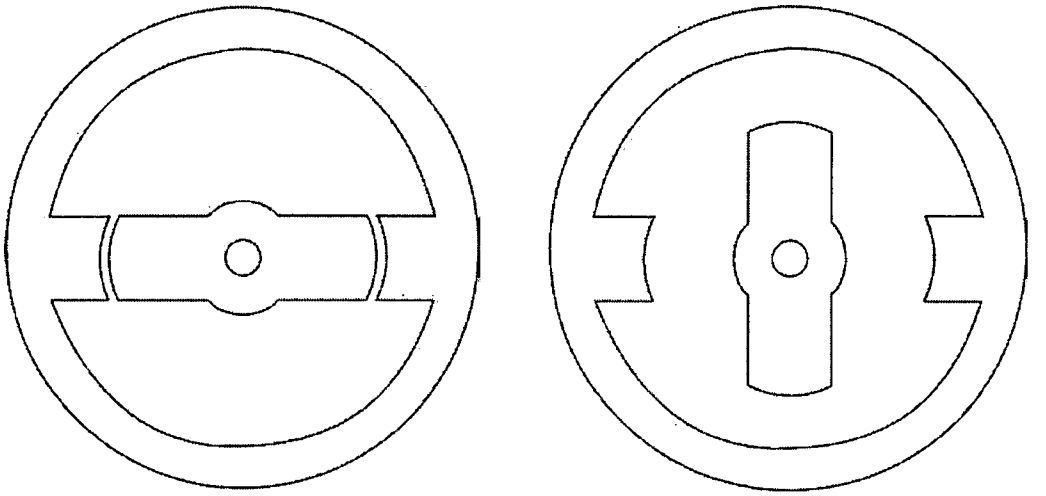

Figure 2.2: A single-phase 2/2 SRM showing the rotor in the aligned and unaligned positions.

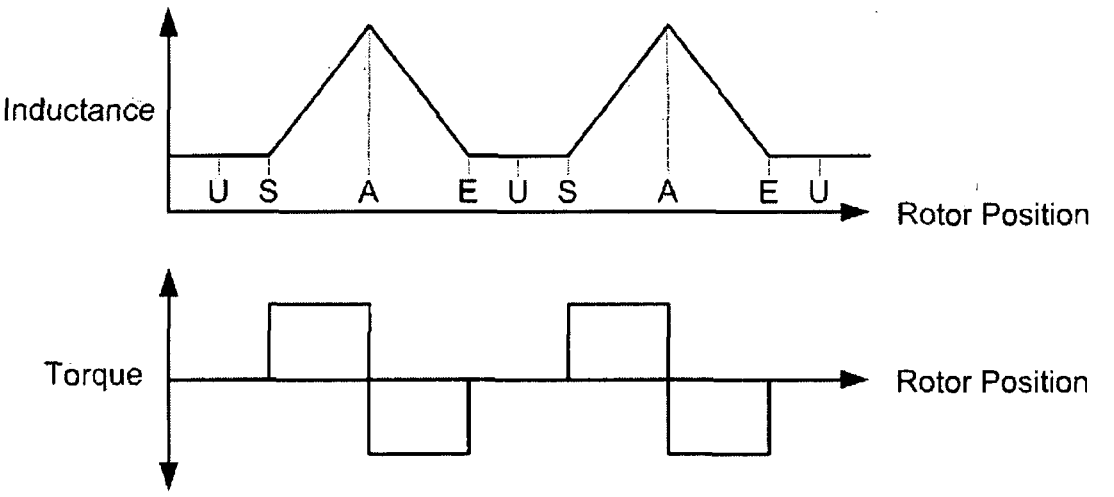

Figure 2.3: The variation of idealised inductance and torque with rotor position for a constant phase current.

An SRM can operate either as a motor or as a generator by simply changing the timing/placement of the current pulses. For motoring operation, the firing angles are chosen so that current flows when the phase inductance is increasing which occurs as the rotor and stator poles approach alignment. For generating operation, the firing angles are chosen so that current flows when the phase inductance is decreasing which occurs immediately after the rotor and stator poles have passed alignment. When motoring, the rotor experiences torque in the direction of rotation whereas when generating, the rotor experiences torque opposing rotation. It is clear that in order to ensure smooth control of the SRM either in motoring or generating mode of operation, it is essential to have accurate rotor position information. This may necessitate the use of a position sensor but it is possible to avoid this by using a sensorless position estimation technique.

Figure 2.3 shows the variation of idealised inductance and torque with rotor position for a constant phase current. Between positions S and A where the inductance is increasing, positive motoring torque is produced. Physically, position S corresponds to the start of overlap where the leading edge of the rotor pole is aligned with the first edge of the stator pole. Position A corresponds to full alignment while position E indicates the end of pole overlap. At alignment, the inductance starts to decrease. If the rotor is forced to continue past A, there is an attractive force between the rotor and stator that produces a braking effect and consequently, a change in torque direction.

Effectively, the mechanical energy expended by the prime mover in pulling the rotor pole away from the excited stator pole is converted to electrical energy i.e. generating operation.

If motoring operation is desired, it is clear that these negative torque impulses must be eliminated. Hence, the phase current must be reduced to zero before the A-E interval when the poles are separating. Therefore, the ideal motoring current waveform should be a series of pulses. The position of the pulses coincides with the rising inductance interval. Thus, an ideal motoring torque waveform has the shape shown in Figure 2.4. Figure 2.4 also shows the idealised sawtooth waveform of the flux-linkage, $\psi=Li$. This is not a practical waveform as an infinite negative voltage would be required to reduce the current and consequently, the flux-linkage to zero at position A.

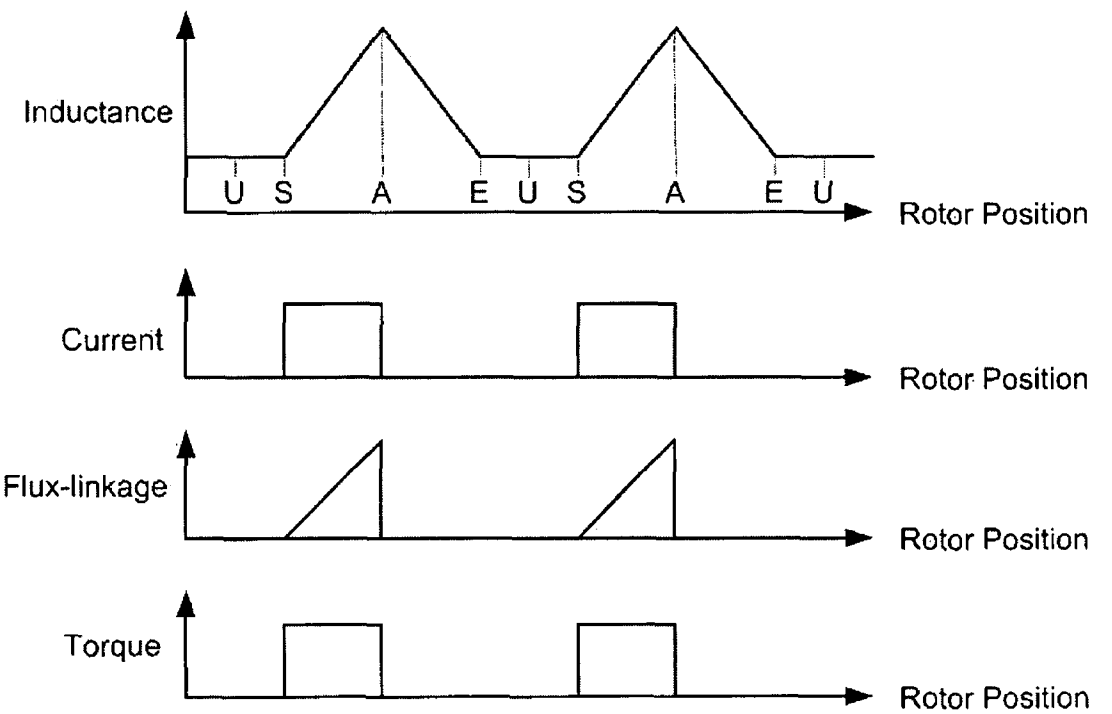

Figure 2.4: The idealised inductance, current, flux-linkage and torque for motoring operation.

In practice, the inductance at S is non-zero but very small. Consequently, although the current may not be established in an infinite manner, it may be established very quickly. The rectangular current waveform can then be approximated by chopping the current along S-A. To avoid the production of negative torque the current must be

reduced to zero before alignment and this can be achieved by placing a negative supply voltage across the phase just before alignment. The simple machine of Figure 2.2 can produce a non-zero average torque during rotation. However, the torque is discontinuous and continuous rotation relies on either the momentum of the machine when motoring or on the prime mover when generating. Similarly, the machine cannot self-start from every rotor position. It is shown in Section 2.2 that torque can only be produced in regions of increasing and decreasing inductance. Hence, no torque is produced in the 'dead-zone' between E and S and the torque at the aligned position A is also zero. To produce positive motoring torque from all rotor positions and to ensure self-starting capability from all rotor positions, the full 360 degrees of rotation must be 'covered' by areas of increasing inductance so that appropriately placed current pulses will produce continuous torque output. Figure 2.5 shows the idealised inductance, current and torque waveforms for the three-phase 6/4 SRM of Figure 2.1. A stroke is the cycle of torque production associated with each current pulse. The number of strokes per revolution, S, is related to the number of rotor poles, N_R, and the number of phases, P, by $S=N_RP$. Hence, for the 6/4 three-phase machine of Figure 2.1 $S = 4(3) = 12$.

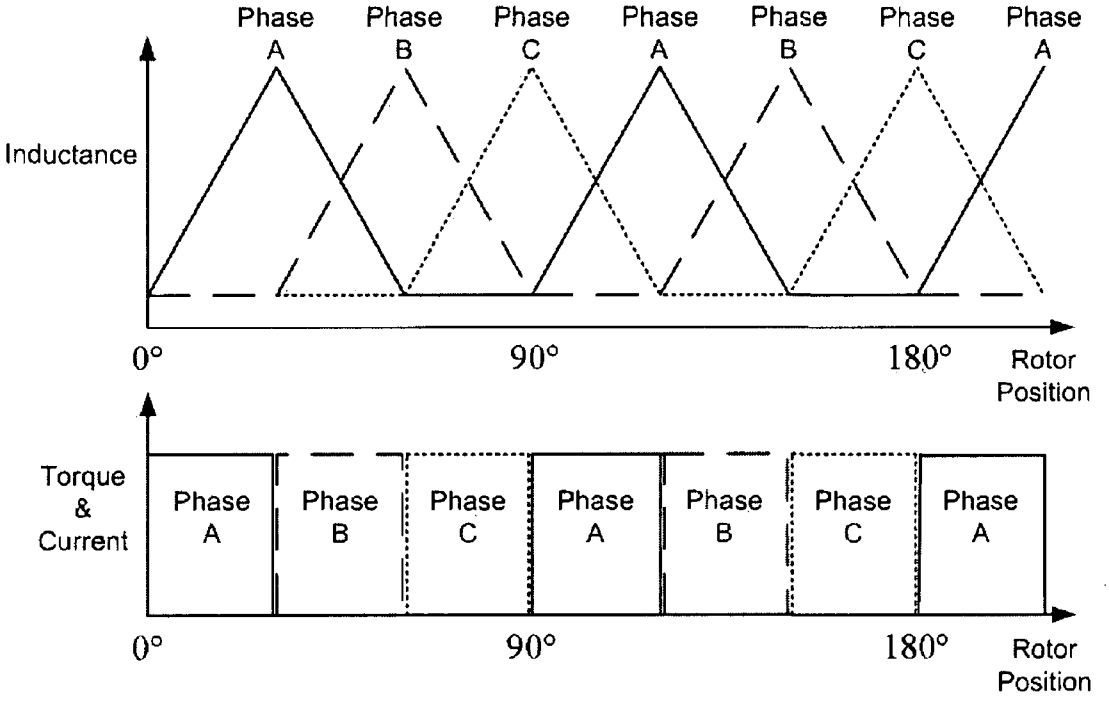

Figure 2.5: The idealised inductance, current and torque waveforms for a three-phase 6/4 SRM.

2.2 Mathematical description of the SRM

The terminal voltage and torque equations form the basis of the mathematical description of the SRM. A single phase is considered for simplicity and the results may be extended for multiple phases. A number of assumptions are made, specifically that:

(1) the phases are magnetically independent; mutual coupling between phases is normally zero or very small and so can be ignored.

(2) skin effect in the windings is negligible.

(3) hysteresis is negligible.

The instantaneous voltage across the terminals of a single phase of an SRM winding is related to the flux linked in the winding by Faraday's law:

$$v = iR + \frac{d\psi}{dt} \tag{2.3}$$

where, v is the terminal voltage, i is the phase current, R is the phase resistance and ψ is the flux-linkage. Magnetic saturation coupled with the effect of fringing flux around the pole corners results in the flux-linkage in an SRM phase varying as a function of rotor position, θ, and the phase current, i.

$$\psi = \psi(\theta, i) \tag{2.4}$$

Thus, equation (2.3) can be expanded as:

$$v = iR + \frac{\partial\psi(\theta,i)}{\partial i}\frac{di}{dt} + \frac{\partial\psi(\theta,i)}{\partial\theta}\frac{d\theta}{dt} \tag{2.5}$$

where $\partial\psi(\theta, i)/\partial i$ is defined as the instantaneous inductance, $L(\theta, i)$, and $d\theta/dt$ is the angular velocity, ω, in rad/s. However, if it is assumed that the inductance is unaffected by the current i.e. there is no magnetic saturation, then $L(\theta) = \psi/i$. Thus, linear analysis enables equation (2.5) to be further expanded as:

$$v = iR + L(\theta)\frac{di}{dt} + i\omega\frac{\partial L(\theta)}{\partial \theta} \tag{2.6}$$

In this equation, the three terms on the right-hand side represent the resistive voltage drop, the inductive voltage drop and the induced emf or 'back-emf', respectively. The back-emf, e, is equivalent to:

$$e = i\omega\frac{\partial L(\theta)}{\partial \theta} = i\omega K_B \text{ where } K_B = \frac{\partial L(\theta)}{\partial \theta} \tag{2.7}$$

K_B may be considered to be equivalent to the back-emf constant associated with the series-excited dc machine except that, in the case of the SRM, the term 'back-emf coefficient' (as opposed to 'constant') may be preferable to fully emphasise the variation of K_B with position and current. K_B is dependent on the operating point and is obtained with constant current at that point. The instantaneous electrical power, vi, is then:

$$vi = i^2R + L(\theta)i\frac{di}{dt} + i^2\omega\frac{\partial L(\theta)}{\partial \theta} \tag{2.8}$$

The rate of change of magnetic stored energy at any instant is given by:

$$\frac{d}{dt}\left(\frac{1}{2}L(\theta)i^2\right) = \frac{1}{2}i^2\frac{dL(\theta)}{dt} + L(\theta)i\frac{di}{dt} = \frac{1}{2}i^2\omega\frac{dL(\theta)}{d\theta} + L(\theta)i\frac{di}{dt} \tag{2.9}$$

From the law of conservation of energy, the mechanical power is equal to the electrical input power after subtraction of both the resistive power loss, i^2R, and the rate of change of magnetic stored energy. Thus, the instantaneous mechanical power, which is equivalent to ωT where T is the instantaneous electromagnetic torque, can be written as:

$$\omega T = \frac{1}{2}i^2\omega\frac{dL(\theta)}{d\theta} \tag{2.10}$$

which results in the following expression for electromagnetic torque:

$$T = \frac{1}{2} i^2 \frac{dL(\theta)}{d\theta} \tag{2.11}$$

The torque waveform for the idealised inductance profile at constant current shown in Figure 2.3 clearly follows the mathematical relationship of equation (2.11). Moreover, equation (2.11) indicates that the torque is independent of the sign of the phase current and is instead determined by the sign of $dL/d\theta$. The absolute value of $dL/d\theta$ contributes to the amount of torque produced. For this reason, SRMs are generally designed to have a large L_{MAX}/L_{MIN} ratio resulting in a large absolute value of $dL/d\theta$ and thus enabling high torque levels to be attained.

It is the dependence of the torque on both position and current that results in the SRM necessitating complex control. To produce a smooth torque output with minimum ripple requires control schemes that carefully profile the phase currents of the individual phases so that the torques produced by each of these phases sum to produce the desired total torque.

Furthermore, equation (2.6) appears to indicate that from the terminals, each phase of the SRM appears to have an equivalent circuit as shown in Figure 2.6 comprising a resistance, an incremental inductance and a back-emf that is proportional to speed. However, with L and e varying with both rotor position and current, the equivalent circuit cannot be interpreted in the same manner as that of a dc machine for instance.

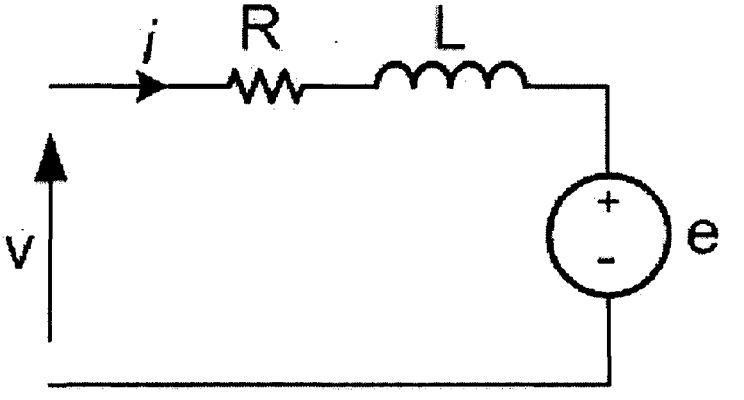

Figure 2.6: Equivalent circuit for a single phase of the SRM.

In short, the torque cannot be calculated from simple equivalent circuit considerations and simulation of SRM drives requires the direct solution of equations (2.3) and (2.11). An alternative analysis that also takes into account magnetic saturation enables the torque to be described in terms of the co-energy and is described in the next section.

2.2.1 Torque calculation using co-energy

The analysis presented here takes saturation of the magnetic circuit into account and is based on the use of magnetisation curves. A magnetisation curve is a graph of flux-linkage versus current for a fixed rotor position. Before starting, it is necessary to define the stored field energy, W_F, as well as introducing the concept of co-energy, W_C. Co-energy has no physical significance but it is often used to derive expressions for torque in electromagnetic systems. The energy stored in the magnetic field may be expressed as:

$$W_F = \int_0^{\psi} i(\psi,\theta)d\psi \tag{2.12}$$

It may be interpreted graphically as the area between the magnetisation curve and the flux-linkage axis as shown in Figure 2.7. The magnetic field co-energy is then the area between the curve and the current axis and can be expressed as:

$$W_C = \int_0^{i} \psi(i,\theta)di \tag{2.13}$$

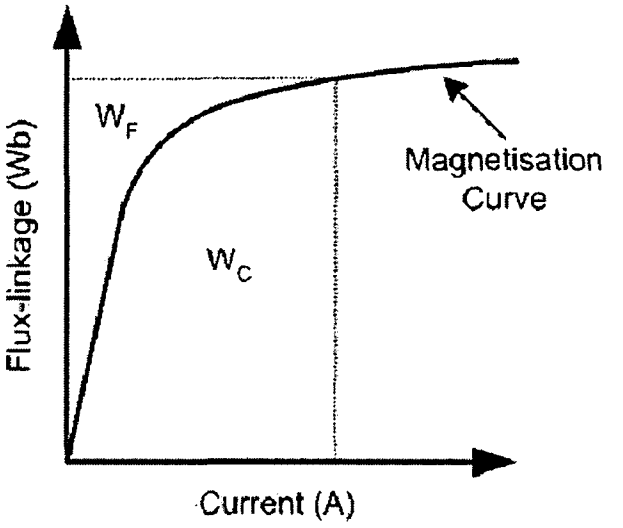

Figure 2.7: The flux-linkage current plane showing the magnetic field stored energy and the magnetic field co-energy.

Therefore, from Figure 2.7 the area defining the field energy and co-energy can be described by the relation:

$$W_C + W_F = i\psi \tag{2.14}$$

Now, consider a rotor movement from its original position, A, to a new position, B (through an angular displacement $\Delta\theta$). The magnetisation curves for both positions are shown in Figure 2.8.

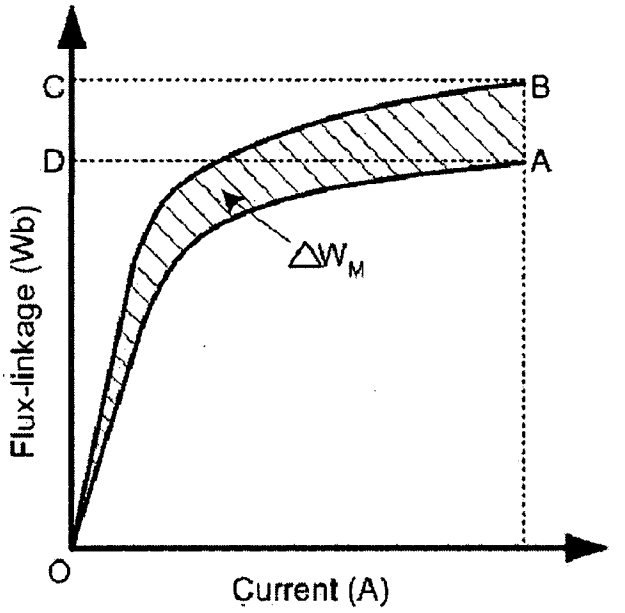

Figure 2.8: Flux-linkage current plane showing the effect of the rotor moving from position A to position B.

Assuming that the current remains constant during the motion, the electrical energy, W_E, exchanged with the supply is:

$$\Delta W_E = \int vidt = \int i\frac{d\psi}{dt}dt = \int id\psi = ABCD \tag{2.15}$$

The change in stored field energy is:

$$\Delta W_F = OBC - OAD \tag{2.16}$$

The mechanical work done, ΔW_M, is represented by the shaded area in Figure 2.8, which, in fact, is equal to the change in electrical energy minus the change in the magnetic field energy. Thus,

$$\Delta W_M = \Delta W_E - \Delta W_F \tag{2.17}$$

$$\Delta W_M = ABCD - (OBC - OAD)$$

$$\Delta W_M = OABCD - OBC$$

$$\Delta W_M = OAB \tag{2.18}$$

This value corresponds to the increase in the magnetic field co-energy i.e. $\Delta W_M = \Delta W_C$. Also, the mechanical work done during the displacement $\Delta\theta$, from A to B, can be expressed as:

$$\Delta W_M = T\Delta\theta = \Delta W_C \tag{2.19}$$

Therefore, in the limit when the angular displacement, $\Delta\theta$, is very small $\Rightarrow \Delta\theta \rightarrow 0$,

$$T = \left[\frac{\partial W_C}{\partial\theta}\right]_{i=CONSTANT} \tag{2.20}$$

If a motor with no saturation is considered then all the magnetisation curves would be straight lines and the stored magnetic field energy will equal the magnetic field co-energy at all times. Thus, at any rotor position the following would be true:

$$W_F = W_C = \frac{1}{2}L(\theta)i^2 \tag{2.21}$$

This expression for W_C implies that the expression for electromagnetic torque in equation (2.20) reduces to:

$$T = \frac{1}{2}i^2\frac{dL(\theta)}{d\theta} \tag{2.22}$$

which is identical to equation (2.11). The inductance only depends on position and is independent of current.

The above analysis is carried out for a single phase of the SRM. For multi-phase SRMs, the instantaneous torque equation becomes a summation of the form:

$$T = \sum_{j=1}^{m} T_j \tag{2.23}$$

where T_j is the torque produced by the jth phase and m is the total number of phases.

2.3 Torque/speed characteristic

Like other motors, the torque produced by the SRM is limited by the maximum allowed current and the rotational speed is limited by the available voltage supply. The torque/speed characteristic of the SRM for motoring operation in one direction is shown in Figure 2.9.

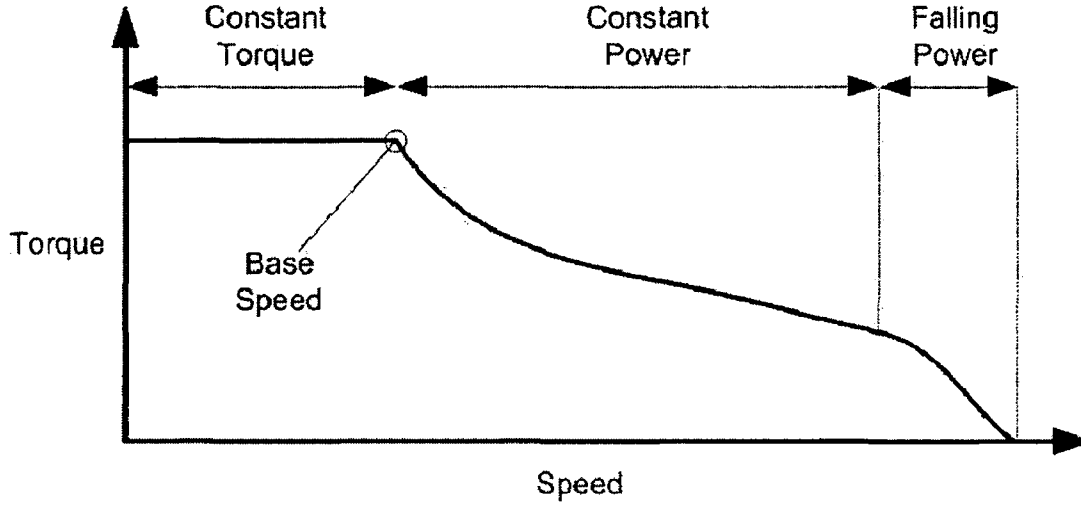

Figure 2.9: Torque/speed characteristic of the SRM.

At low speed, the torque is controlled by regulating the current and rated torque can be achieved up to a point known as the base speed. Because the back-emf of the SRM increases with rotational speed, there comes a point where the limited supply voltage can no longer force the current to the required level to achieve rated torque. Essentially then, the base speed is the maximum speed at which maximum current and rated torque can be achieved at the rated voltage. As the speed increases beyond base speed and the back-emf increases still further, the conduction angle can be increased to maintain constant power operation. Eventually however, the conduction angle can no longer be increased, and the torque falls off more rapidly with a consequent fall-off in the power. It is worth noting however that the SRM can still operate at very high speeds under a small load. Although Figure 2.9 only shows the torque/speed characteristic for motoring in a single given direction, the corresponding curve for generating with the same direction of shaft rotation can be obtained by reflection in the speed axis. Similarly, the characteristic for motoring and generating operation in the opposite direction of rotation can be obtained by reflection in the torque axis. Thus, four-quadrant operation of the SRM can be achieved.

2.4 Power converter

There are many different power converter circuits that can be used to excite the SRM, each with its own particular advantages and disadvantages and a large body of research exists documenting various design attempts for the SRM drive circuit [(Vukosovic 1990) and (Barnes 1998)]. The different designs have a number of similarities based on certain imposed conditions necessary for satisfactory SRM operation. Since torque is independent of current direction, the converter needs only to carry unidirectional current. However, since the flux-linkage must be returned to zero at the end of each stroke, a negative voltage must be placed across the phase to ensure that $d\psi/dt < 0$. It is important to ensure a high di/dt at the phase turn-off to prevent the production of negative torque, which would lower the total average torque. Since the phase inductance is high when the rotor is approaching the aligned position, the application of a high demagnetising voltage is the most effective means of increasing the turn-off di/dt. The most popular converter that accomplishes this requirement is the 'asymmetric half-bridge' converter, which is also termed the 'classic' converter. A single phaseleg of the 'classic' converter is shown in Figure 2.10. Each phase is connected to an asymmetric half-bridge consisting of two switches and two diodes (giving a total of 2N switches for an N phase machine) with each phaseleg usually operating from the same voltage supply.

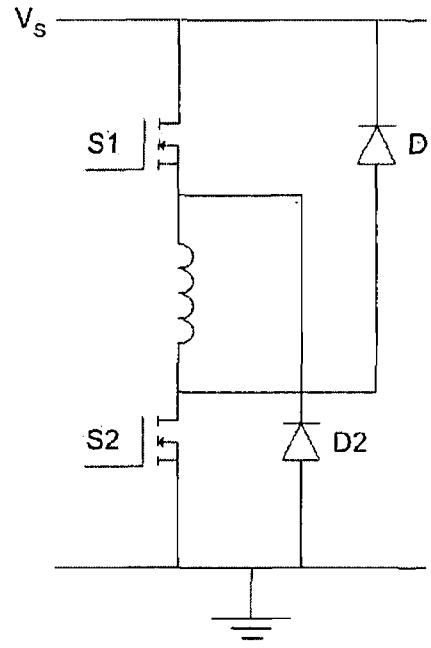

Figure 2.10: A single phaseleg of the 'classic' converter.

There are three possible states of operation for the 'classic' converter:

State (1): *Magnetisation.* Both S1 and S2 are on, the voltage across the phase winding is $v = V_S$ (V_S is the supply voltage) and current flows through the phase winding.

State (2): *Freewheeling.* Either S1 is off and D2 on or S2 is off and D1 on allowing the phase winding current to circulate in a continuous path. The rate of demagnetisation is low as the voltage across the phase winding is $v = 0$.

State (3): *Forced Demagnetisation.* This occurs when both S1 and S2 are turned off. D1 and D2 are forward biased and turned-on to allow current to flow through the phase winding and back to the supply. The rate of demagnetisation is high as the voltage across the winding is $v = -V_S$.

The equivalent circuits for magnetisation, freewheeling and forced demagnetisation are shown in Figure 2.11.

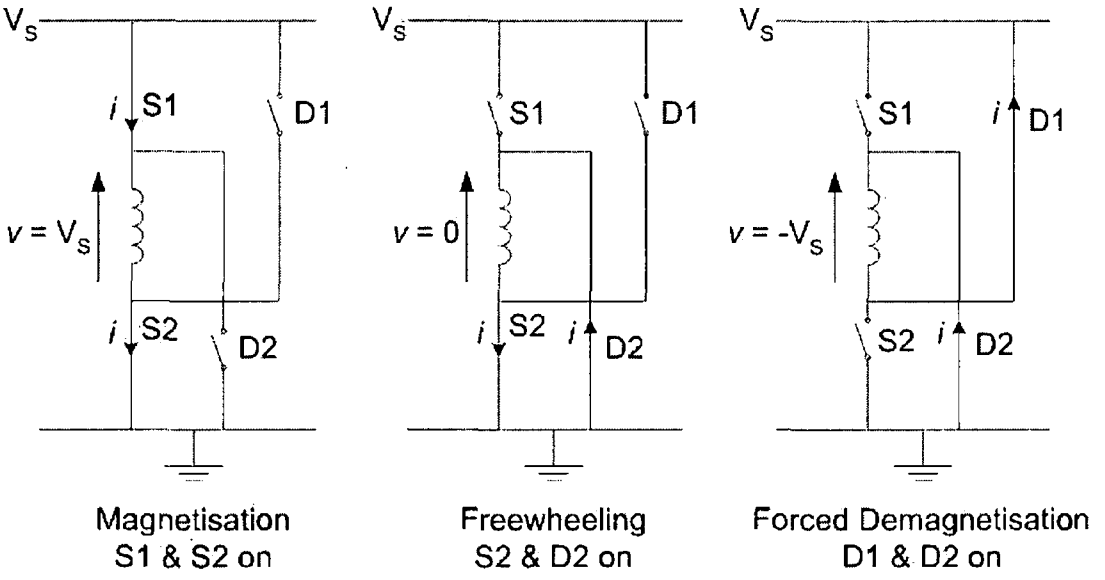

Figure 2.11: A single phaseleg of the 'classic' converter showing switch states, phase voltage and phase current for the magnetisation, freewheeling and demagnetisation states of operation.

The 'classic' converter has the advantage of providing independent control of phase currents in motors having current overlap. Current can be supplied to one phase while simultaneously demagnetising another phase allowing operation with any degree of phase current overlap. Another advantage, which is common to all SRM converter topologies and not just the 'classic' converter, is the fact that the switches are always in series with the phase winding so at no time can a shoot-through fault occur. There are many other converter topologies including N, (N+1), 1.5N and 2N switch topologies (where N is the number of phases) as well as converters that employ alternative approaches for producing the demagnetising voltage towards the end of each stroke. A more in-depth examination of SRM converters, including the 'classic' converter as well as some of the other topologies, is performed in Chapter Five. However, for the analysis of the dynamic operation of the SRM in Section 2.5, it will be assumed that the 'classic' converter is employed.

2.5 Dynamic operation of the SRM

Control of the SRM requires switching of current pulses from phase to phase as the shaft rotates. The type of current control employed at any given time depends on the operating point with respect to the torque/speed diagram shown in Figure 2.9. Prior to looking at controlling the current waveform, a few basic definitions need to be introduced.

Turn-on angle, θ_{ON} : The rotor position where a phase current is switched on.

Turn-off angle or *commutation angle,* θ_{OFF} : The rotor position where the phase current is switched off.

Conduction angle or *dwell angle,* θ_D: The angular difference between the turn-on and turn-off angles i.e. $\theta_D = \theta_{OFF} - \theta_{ON}$

Extinction angle, θ_{EXT}: The rotor position where the phase current reaches zero.

For the following analysis, it is assumed that the 'classic' converter is employed and hence the drive can apply three voltage levels to the phase winding, V_S, 0 or $-V_S$ (neglecting the voltage drops in the switches, diodes etc.). Only motoring operation will be examined but the same principles apply to generating operation.

2.5.1 Low speed motoring

For low speed operation, the back-emf is too small compared to the supply voltage, V_S, to limit the current and hence the current must be regulated by chopping of the current waveform. Chopping means that the power switches are turned on/off, usually at a much higher frequency than the fundamental frequency of the current waveform. This has the effect of reducing the average voltage applied to the winding thereby limiting the phase current. There are three possible states of operation of the converter (as outlined in Section 2.4) and hence there are two possible modes of chopping operation, known as hard chopping and soft chopping.

Soft chopping

The soft chopping strategy involves the chopping of a single power switch only. One switch is turned-on and left on until θ_{OFF} is reached while the other switch is turned on/off according to some pulsed signal from the controller. Hence the voltage across the phase winding switches between V_S and 0. During the zero-volt period, the rate of change of flux-linkage is low (equal to $-Ri$) and hence di/dt is relatively small.

Hard chopping

The hard chopping strategy involves driving both power switches with the same pulsed control signal such that the pair of switches are turned on/off in unison. Hence, the voltage across the phase winding switches between V_S and $-V_S$.

According to Miller, soft chopping is generally preferred as it reduces the current ripple and also produces less acoustic and electrical noise and less EMI (Miller 2001).

There are many methods of current regulation for low speed operation, all of which employ current chopping. Popular methods of current control include voltage Pulse Width Modulation (voltage PWM), current hysteresis and delta modulation.

Figure 2.12 and Figure 2.13 show the implementation of current control for a single phase using soft chopping and hard chopping respectively. Each figure shows the idealised inductance profile, the current reference or current command, I_{REF}, produced by the controller, the chopped current waveform, the resultant torque waveform, the

power switch states and the voltage across the phase winding. In each case, the current regulation method employed is hysteresis control. For this type of control, at least one of the two power switches is turned off when the current exceeds $I_{REF} + \Delta i/2$ where Δi is called the hysteresis band. Similarly, when the current drops below $I_{REF} - \Delta i/2$ the switch is turned back on again.

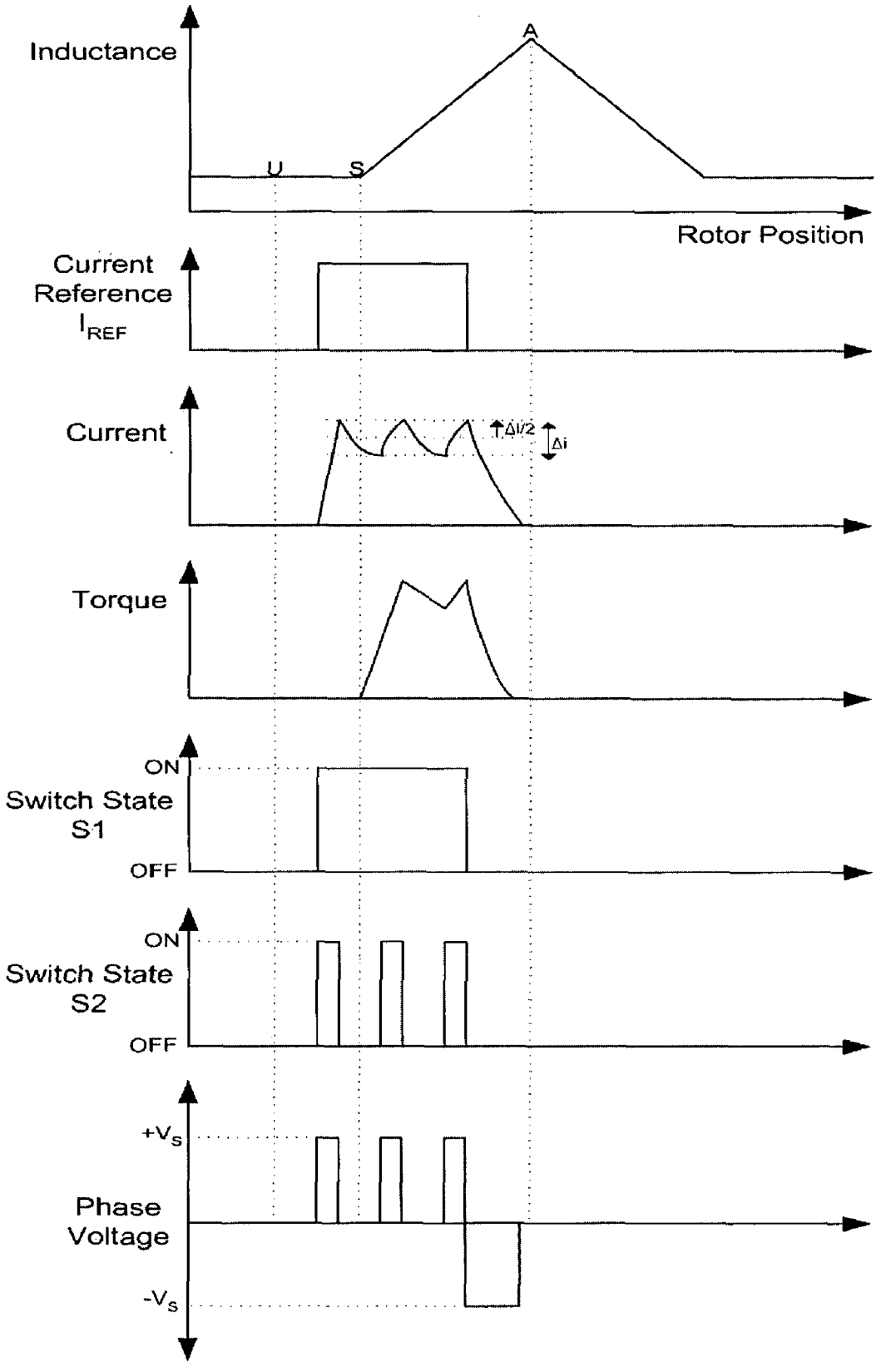

Figure 2.12: Hysteresis current control for a single phase using soft chopping.

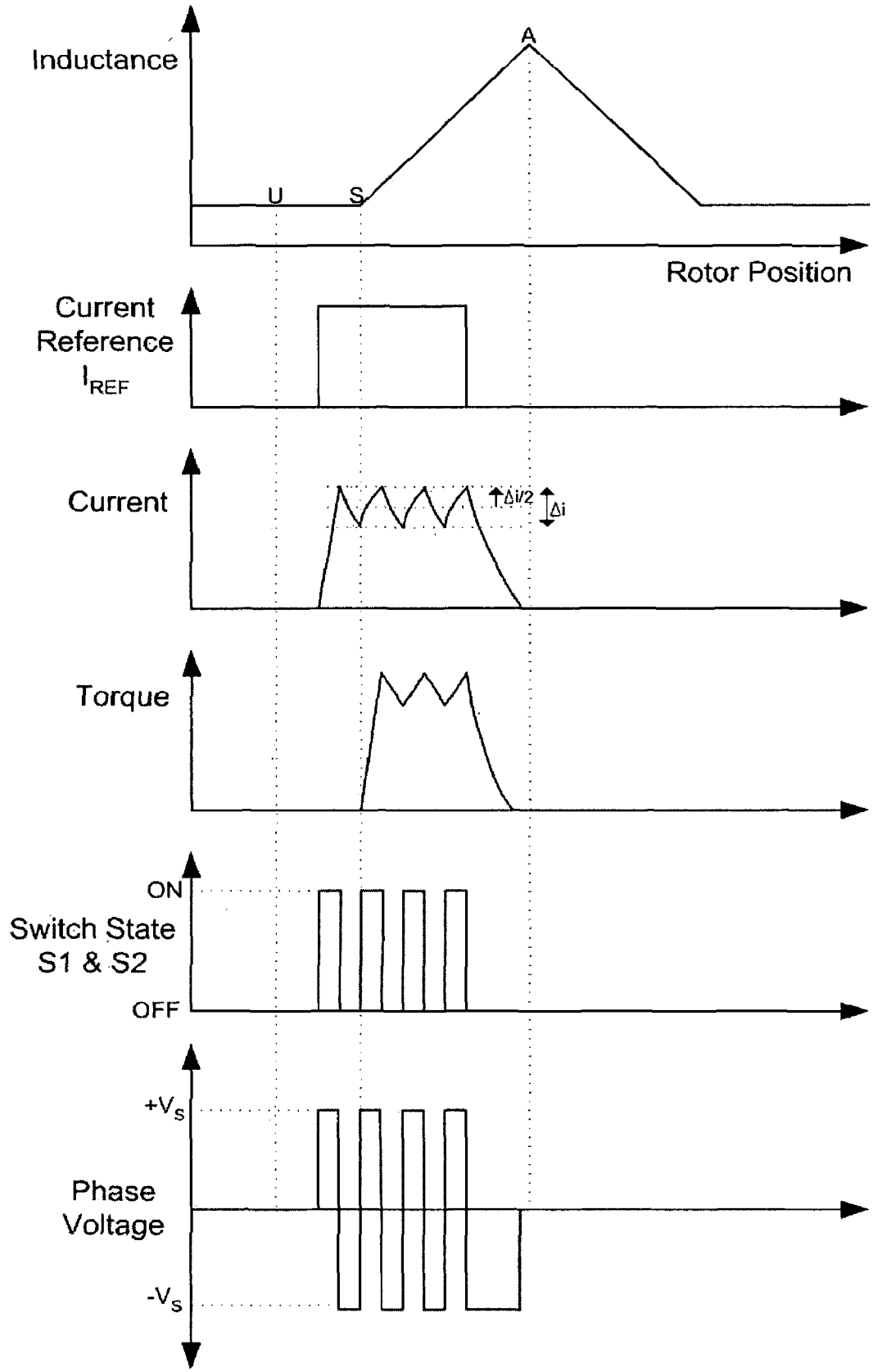

Figure 2.13: Hysteresis current control for a single phase using hard chopping.

In both Figures 2.12 and 2.13 the current starts to flow at the turn-on angle, shortly after the unaligned position is reached. Once the current rises to the required level, it is controlled via hysteresis control and the switch states and voltage across the winding are shown clearly. It can be seen that the current falls faster within the hysteresis band using hard chopping as opposed to soft chopping. Hence, soft chopping enables the chopping frequency and dc link capacitor current to be reduced for a given hysteresis band when compared to hard chopping. Notice also that no torque is produced initially as the inductance is low and constant. As the rotor and stator poles move closer together the inductance starts to increase, torque is produced and is subsequently controlled by the phase current. The turn-off angle is a few degrees before alignment and with both switches turned off, the current commutates into the diodes and the reverse supply voltage is placed across the winding. The current falls rapidly to zero with the extinction angle just before alignment to ensure that no negative torque is produced. The flux-linkage current plane for chopped current regulation is shown in Figure 2.14 with the loop being traversed in the anti-clockwise direction.

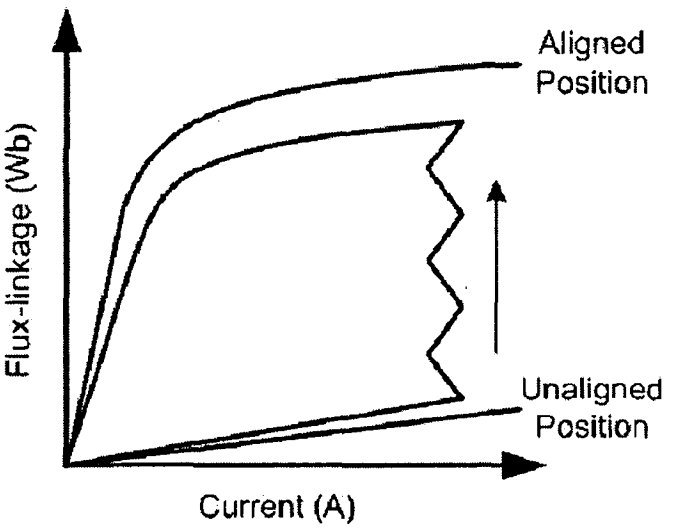

Figure 2.14: Flux-linkage current plane for a single phase for chopping operation at low speed.

2.5.2 High speed motoring

As the speed increases beyond the base speed, the back-emf is large enough to limit the current and hence, no current regulation is required. The power switches are left turned on throughout the entire conduction cycle producing a single pulse of current and hence this mode of operation is referred to as *single pulse mode*. At the turn-off angle, both switches are turned off and the current is suppressed to zero by the negative supply voltage across the winding. In the single pulse mode, the torque produced by the motor can only be controlled by varying θ_{ON} and θ_{OFF} or alternatively, by varying the supply voltage V_S. Figure 2.15 shows the idealised inductance as well as waveforms for the applied voltage, the phase current and the torque produced during single pulse mode operation. The switches are closed shortly after passing the unaligned position and the current rises rapidly due to the small inductance and small back-emf. Initially, no torque is produced by the motor. As the inductance starts to increase however, torque is produced. At the start of pole overlap, the back-emf rises rapidly and soon exceeds the supply voltage. This results in a negative *di/dt* and a fall in the current. The higher the speed of rotation the faster the current will fall. This results in a corresponding fall in the torque produced. During the conduction period, the flux-linkage rises linearly due to the constant supply voltage across the phase winding. At the turn-off angle, both switches are opened and the current commutates into the diodes and reduces to zero. The flux-linkage falls linearly to zero because of the constant negative voltage across the winding. In high speed operation, commutation must take place earlier than for low speed operation (reducing the dwell angle) because of the reduced time for current suppression and the desire to avoid large negative torque production. The trajectory in the flux-linkage current plane corresponding to the single pulse mode operation of Figure 2.15 is shown in Figure 2.16 where the loop is traversed in the anti-clockwise direction.

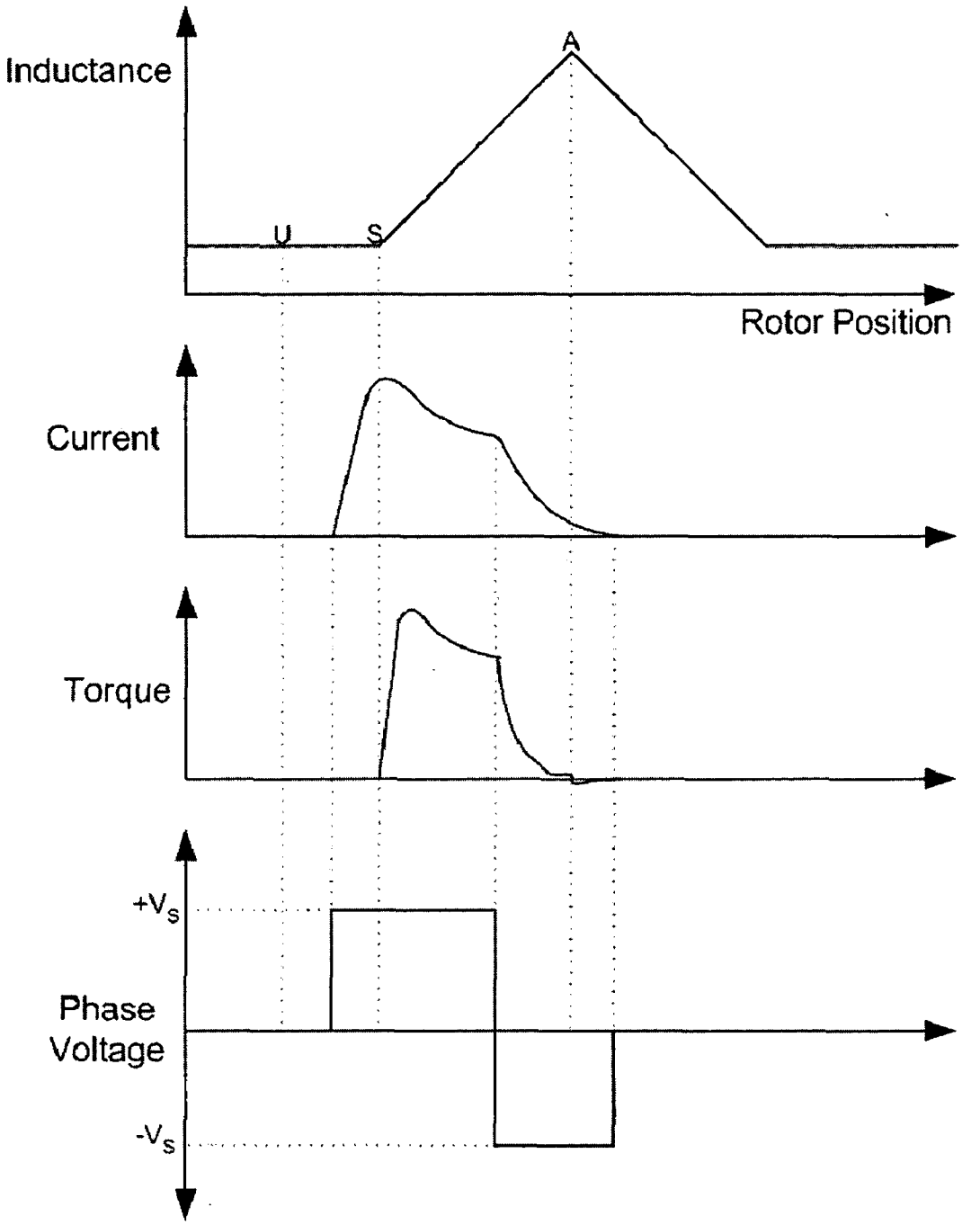

Figure 2.15: Single pulse mode control for a single phase for high speed motoring operation.

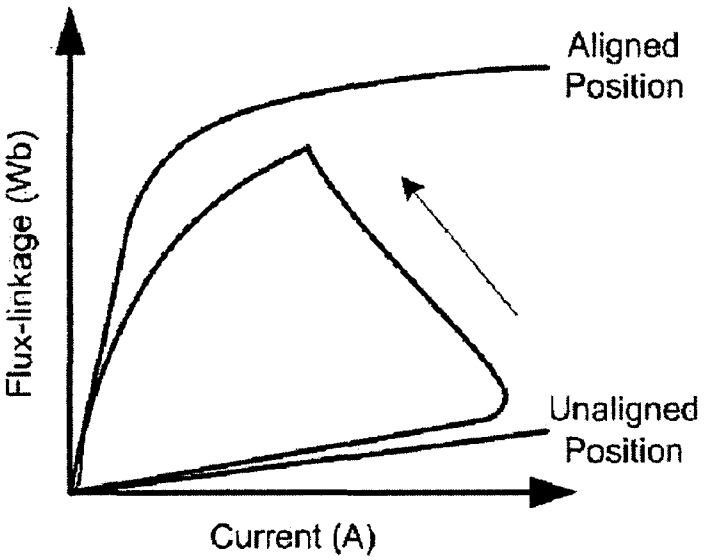

Figure 2.16: Flux-linkage current plane for a single phase for single pulse mode motoring control at high speed.

The various switching strategies outlined in this section are utilised in the complex control schemes usually required for smooth control of the SRM. In Chapters Three, Four, Six and Seven, control of the SRM for both the motoring and generating modes is examined in detail and a number of control schemes are developed which incorporate the basic switching strategies that have been outlined in this section.

2.6 Fundamentals of SR generation

Torque is produced in the SRM by the tendency of the nearest rotor poles to align themselves with the excited stator pole pair. Continuous torque development is then possible via energisation of consecutive stator phases in succession. The following expression for electromagnetic torque was derived in Section 2.2:

$$T = \frac{1}{2} i^2 \frac{dL(\theta)}{d\theta} \tag{2.24}$$

Equation (2.24) indicates that the torque does not depend on the direction of current flow but rather on the relative positioning of phase current with respect to the inductance profile. For generating operation, the firing angles are chosen so that current flows when the phase inductance is decreasing which occurs immediately after the rotor and stator poles have passed alignment. When generating, the rotor

experiences torque opposing the rotation of the prime mover. During normal generator operation, a phase is excited before the rotor has aligned with the corresponding stator pole pair. Typically, the excited phase draws its excitation energy (through the electronic power converter to the machine) from the same dc link that it will subsequently generate power back to (although this is not necessarily the case). At some point after the rotor has passed alignment, the excitation source is removed (the power electronic switches are turned off) and the phase generates into the dc link via a pair of freewheeling diodes until the current returns to zero. In essence, the work done by the prime mover in pulling the rotor poles away from the excited stator poles is returned as electrical energy to the dc link. The energy returned to the dc link includes the excitation energy plus additional generated energy. A good generator control strategy synchronises the phase current with rotor position precisely to ensure operation at the most efficient level and to minimise stress on the power converter.

Figure 2.17 shows a single phaseleg of the 'classic' converter often employed in SR generation along with the dc link capacitor, *C*, and the load. The various currents marked in Figure 2.17 are defined in the forthcoming paragraphs.

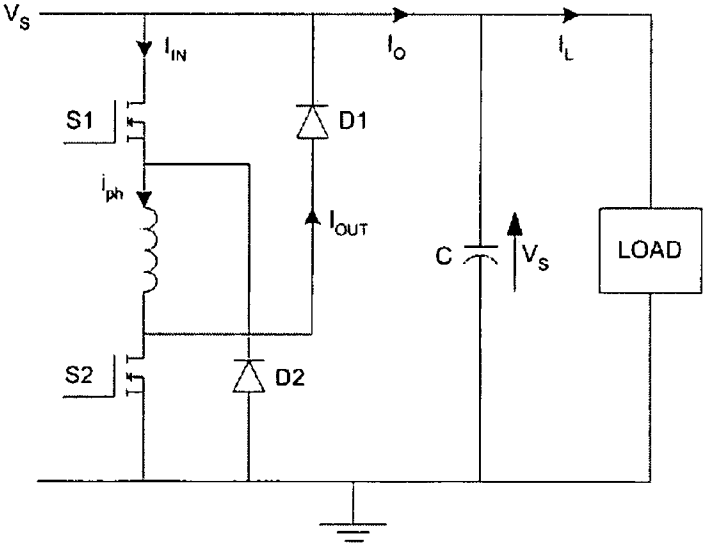

Figure 2.17: Phaseleg of the 'classic' converter circuit often employed in SR generation.

The average load current is defined as I_L while i_{ph} is the instantaneous current flowing in the phase winding. The integral of the excitation current, I_{IN}, over a single stroke is determined as follows:

$$I_{IN} = \int_{\theta_{ON}}^{\theta_{OFF}} i_{ph}\, d\theta \tag{2.25}$$

The integral of the generated current, I_{OUT}, over a single stroke is determined as follows:

$$I_{OUT} = \int_{\theta_{OFF}}^{\theta_{EXT}} i_{ph}\, d\theta \tag{2.26}$$

Thus, the net generated current over a single stroke, I_O, can be expressed as:

$$I_O = I_{OUT} - I_{IN} \tag{2.27}$$

The ratio between the excitation power supplied from the dc link, $P_{IN,ELEC}$, and the generated power returned to the dc link, $P_{OUT,ELEC}$, is called the excitation penalty, ε (Kjaer 1994) and it can be expressed as:

$$\varepsilon = \frac{P_{IN,ELEC}}{P_{OUT,ELEC}} = \frac{I_{IN}}{I_{OUT}} = \frac{I_{IN}}{I_O + I_{IN}} \tag{2.28}$$

It is clear that a small excitation penalty is desirable since it reduces losses. Three possible current waveforms often observed during SR generation in single pulse mode are shown in Figure 2.18 along with the idealised inductance profile. θ_A and θ_E refer to the aligned position and the end of pole overlap position, respectively whilst θ_{ON}, θ_{OFF} and θ_{EXT} have the same meaning as before.

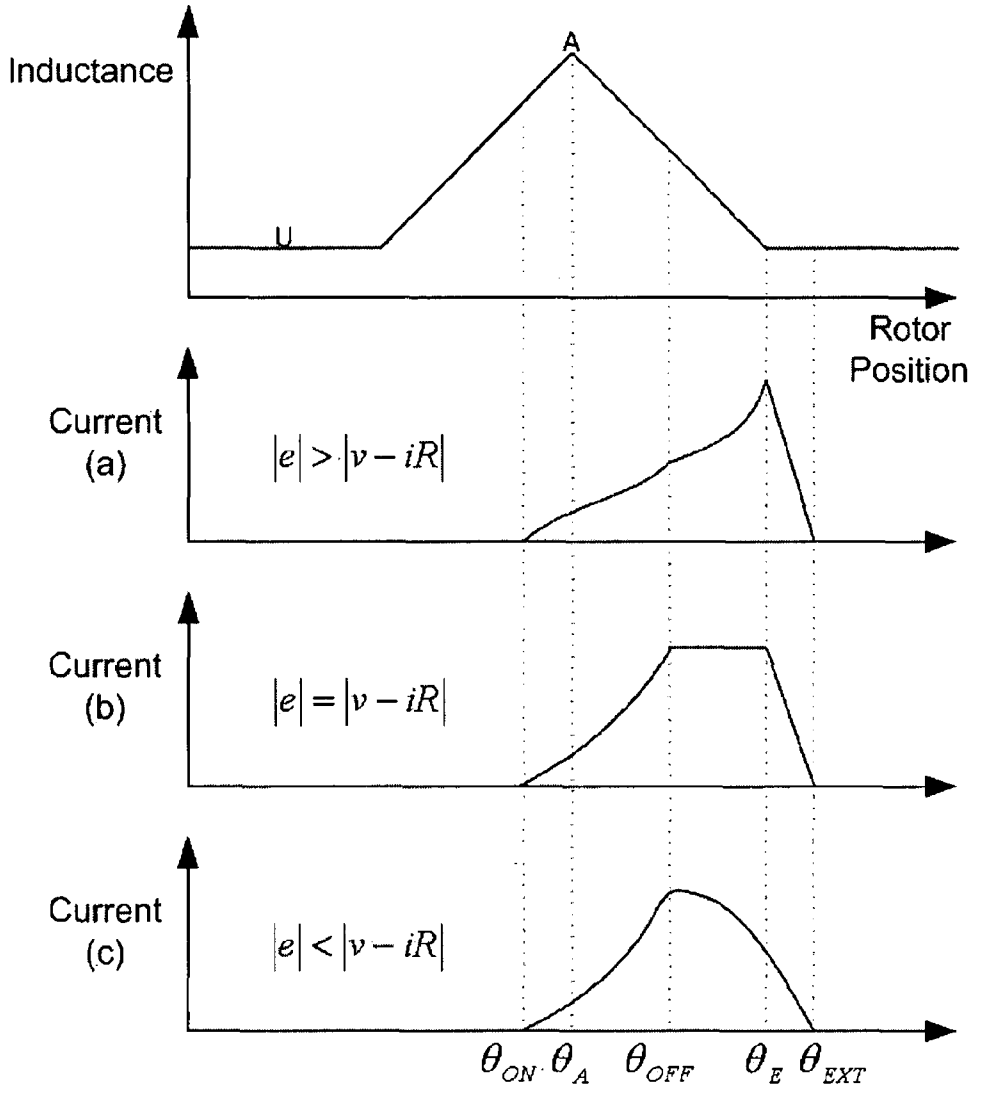

Figure 2.18: Three possible current waveforms often observed during SR generation in single pulse mode.

The shape of these current waveforms can be explained with the help of the following expression for the electrical dynamics of an SRM phase that was derived in Section 2.2:

$$v = iR + L(\theta)\frac{di}{dt} + i\omega\frac{\partial L(\theta)}{\partial \theta} \tag{2.29}$$

In this equation, the three terms on the right-hand side represent the resistive voltage drop, the inductive voltage drop and the back-emf presented by the phase winding, respectively. The back-emf, e, is equivalent to:

$$e = i\omega \frac{\partial L(\theta)}{\partial \theta} = i\omega K_B \text{ where } K_B = \frac{\partial L(\theta)}{\partial \theta} \tag{2.30}$$

where K_B is the back-emf coefficient. Clearly, the back-emf coefficient is the slope of the inductance profile (the partial derivative is taken with the current held constant). Thus, the back-emf coefficent is positive during the region of increasing inductance and negative during the region of decreasing inductance. In addition, the magnitude of the back-emf varies with rotational speed and current magnitude. The different current waveforms shown in Figure 2.18 are as a result of differences in the relative sign and magnitude of the back-emf compared to the applied dc link voltage. During excitation prior to the aligned position, the phase current builds up in the face of the back-emf which reduces the effectiveness of the supplied voltage. For this reason, the turn-on angle is often chosen well in advance of the aligned position (especially for high-speed operation) to enable the phase current to reach an adequate level before turn-off. The behaviour of the SR generator system during demagnetisation can be assessed by comparing the relative magnitude of the back-emf and the dc link source voltage. Rearranging equation (2.29) yields:

$$L(\theta)\frac{di}{dt} = v - iR - i\omega \frac{\partial L(\theta)}{\partial \theta} \tag{2.31}$$

During demagnetisation, $v = -V_S$ and $i\omega \frac{\partial L(\theta)}{\partial \theta} < 0$ (region of decreasing inductance). Therefore, $-i\omega \frac{\partial L(\theta)}{\partial \theta} > 0$. In Figure 2.18(a) the current increases after the switches are turned off at θ_{OFF}. This occurs when the back-emf in the phase winding has a larger magnitude than the combined magnitude of the dc link voltage plus the resistive voltage drop resulting in $\frac{di}{dt} > 0$. For the SR generator, the base speed is the speed at which phase currents are nominally constant without the need for current regulation (Torrey 2002). Figure 2.18(b) shows the case at base speed when the back-emf and the sum of the dc link voltage plus the resistive voltage drop have the same magnitude. In this case, $\frac{di}{dt} = 0$ and hence, the current remains constant until the pole

overlap ends at θ_E, at which point the current starts to decrease. Finally, below the base speed, the phase current will decrease after the switches are turned off at θ_{OFF} as shown in Figure 2.18(c). Figure 2.18(c) shows the phase current when the sum of the dc link voltage and the resistive voltage drop has a larger magnitude than the back-emf as is often the case at low speeds (since the back-emf is proportional to rotational speed). As can be seen, in this scenario the phase current starts to decrease immediately at θ_{OFF} since $\frac{di}{dt} < 0$. SR generation below the base speed necessitates multiple periods of excitation i.e. chopping of the current waveform. It is usual to use hard chopping for phase current regulation. When hard chopping is employed, energy is returned to the dc link every switching cycle. With soft chopping however, the voltage across the phase winding switches between V_S and 0. During the zero-volt period (freewheeling stage) there is no energy returned to the dc link. Essentially, soft chopping results in the SR generator generating into its phase windings, which is of no benefit.

According to (Miller 2001), the current waveform of Figure 2.18(a) has the smallest ε while (c) has the largest. Therefore, if the net generated current is equal for all three cases, the current waveform of (a) is preferable due to its smaller losses.

During steady-state SR generator operation, the excitation current is supplied by the dc link capacitor. However, during generator start-up (with no voltage on the dc link capacitor), the SRM requires a source of excitation such as a dc source (or a battery in automotive applications), since it is inherently passive and has no self-excitation capability. Once the dc link capacitor has been charged to an appropriate voltage level however, the dc source can then be disconnected. To eliminate the initial requirement for a dc source, research has been carried out into self-excitation during the starting of the SRM by the placement of permanent magnets in various positions on the stator (Nedic 2000). Work has also been conducted on multiple channel generating systems whereby a single SRM can supply power to two or more independent and separately loaded buses (Radun 1998).

Control of the SRM above base speed is more complicated for single pulse mode generating operation than for single pulse mode motoring operation. For SR motoring

operation, the peak phase current can be directly controlled using the turn-on angle. This enables separation of the duties of the turn-on angle and the conduction angle (Sozer 2003). However, for SR generation above base speed, the peak phase current will always occur around the point where the phase inductance decreases to its minimum inductance value (Torrey 2002). There are many combinations of turn-on angle and conduction angle that produce the same output power. Therefore, in SR generator control, the issue is the determination of the best choice of the turn-on angle and conduction angle.

(Radun 1994) discusses the instability of the SR generator system for open-loop operation with fixed turn-on and turn-off angles. In essence, an increase in the dc link voltage tends to increase the excitation current which in turn leads to an increase in the generated current. The increase in generated current tends to increase the dc link voltage still further providing the potential for instability. In addition, fixed firing-angle generator operation with a large load can result in the dc link voltage decaying to zero. For these reasons, closed-loop control of the SR generator must be employed.

2.7 Summary of the advantages/disadvantages of SRMs

A summary of the advantages and disadvantages of the SRM is presented below.

Advantages of the SRM

(1) The lack of windings and magnets on the rotor allows for a simple construction and enables a small machine. This implies a low moment of inertia, resulting in a large acceleration rate for the motor. Similarly, the simplicity of the rotor means that it is robust and suitable for high speed operation. Like ac machines, the SRM is brushless and is thus easier to maintain than a dc machine. The robustness of the SRM is further underlined by the electrical independence of the phases, i.e. if one phase fails during operation, the other phases aren't affected. Furthermore, with the SRM, the danger of generating into a shorted winding can be averted by simply removing the excitation. The induced emf is a function of the phase current and thus cutting off the current ensures that there is no emf induced in the phase. This is not the case for induction or permanent magnet synchronous and brushless dc machines.

(2) The main sources of heat are on the stator. This allows for greater ease of cooling as the stator is easier to access than the rotor.

(3) According to (Krishnan 2001), the SRM's power density is comparable to and even slightly higher than induction machines but lower than permanent magnet synchronous and brushless dc machines for speeds below 20,000rpm. At higher speeds, the SRM improves to yield an equivalent or a higher power density than these other machines.

(4) The phase inductance of the SRM is uniquely dependent on the rotor position and the phase current. Thus, a number of sensorless position estimation schemes have been developed (Husain 1996). All of these methods use the instantaneous phase inductance variation information in some way to detect the rotor position indirectly.

(5) The independence of torque with respect to current direction means that the converter needs only to carry unidirectional current. For this reason, many converter topologies with less than two switches per phase can be used to operate the SRM leading to a reduction in cost. Also, shoot-through faults cannot occur as the switches are always in series with the phase winding.

Disadvantages of the SRM

(1) The SRM's strong non-linear magnetic characteristics can result in significant torque ripple. Elimination of torque ripple is achievable but only at the expense of considerable control complexity.

(2) The SRM has higher acoustic noise levels than other motors. The origins of acoustic noise in SRMs are the radial magnetic forces that act on the stator structure as the SRM shaft rotates. Acoustic noise may be reduced through careful design of the SRM itself and by the choice of the control method.

(3) The SRM can not be run directly from a dc bus or an ac line. It must always be electronically commutated. In addition, the electronic converter requires a separate freewheeling diode for each switch increasing the overall cost of the drive.

(4) Accurate rotor position information is required in order to implement effective control, as it is necessary to synchronise the excitation of the phase windings with rotor position. The manner in which this position feedback is derived is

of enormous importance not only to the performance of the SRM drive but also to the cost of the SRM drive.

Chapter Three – Initial investigative work

3.0 Introduction

In this chapter, the initial investigative work performed into SRM control in both motoring and generating modes is described. The simulation package employed, MATLAB/Simulink, is introduced. This is followed by a description of the simple SRM model employed throughout the simulation work. Another SRM model, a nonlinear self-tuning model of the SRM that can serve as a torque observer, is then presented and its performance verified through simulation. The simulated results arising from the implementation and testing of some SR control strategies described in the literature are then presented. A self-tuning torque ripple minimisation controller for the SRM in motoring mode is comprehensively tested. Finally, an SR generator control strategy using an inverse model approach is described and simulated results are presented.

3.1 MATLAB/Simulink

MATLAB/Simulink was the computer package used for simulation of the SRM and its controller in motoring and generating modes. Brief descriptions of both MATLAB and Simulink are presented in Sections 3.1.1 and 3.1.2 respectively.

3.1.1 MATLAB (Using MATLAB 1999)

MATLAB is a high-performance high-level language for technical computing with the name MATLAB standing for 'matrix laboratory'. It enables problems and solutions to be expressed in familiar mathematical notation while integrating computation, visualisation, and programming in an easy-to-use environment. MATLAB (in conjunction with Simulink) enables the rapid modeling, simulation and prototyping of an SRM and its associated control system.

The basic data element in MATLAB is an array that does not require dimensioning. This enables the solution of many problems, especially those with matrix and vector formulations, in a fraction of the time it would take to write a comparable program in a scalar language such as C.

The MATLAB program incorporates a group of application-specific solutions called toolboxes. These toolboxes are extensive collections of MATLAB functions (M-files) that enable the application of specialised computational algorithms. They extend the MATLAB environment to help in the solution of various categories of problems. Areas in which toolboxes have been developed include digital signal processing, control systems, power systems, communications, neural networks, fuzzy logic and many others. These toolboxes are one of the primary reasons why MATLAB is very popular with both university researchers and in industry.

3.1.2 Simulink (Using Simulink 1999)

The Simulink software package enables the modeling, simulation and analysis of dynamic systems. It provides a Graphical User Interface (GUI) for constructing models in block diagram form, in a manner similar to that in which most textbooks depict them. Simulink includes a comprehensive block library of sinks, sources, linear and nonlinear components and connectors in addition to application-specific blocks provided by special toolboxes. It is also possible to create and customise new blocks. Simulink supports linear and nonlinear systems, modeled in continuous time, sampled time, or a hybrid of the two.

The Simulink model structure is hierarchical, enabling models to be built using both top-down and bottom-up approaches. A model can be viewed at a high level, while increased model detail can be attained by double-clicking on blocks to move down through the levels. After a model is built, it can be simulated, using a choice of integration methods. Since MATLAB and Simulink are integrated, the model can be simulated using the Simulink menus or alternatively, by entering commands in the MATLAB command window. Using display blocks, the simulation results can be viewed while the simulation is running. In addition, parameters can be changed 'on the fly' and the effect on the system behaviour can be seen immmediately. The simulation results can be saved in the MATLAB workspace for post-processing, analysis and plotting.

3.2 Simple SRM model employed in the simulation work

Two SRM models were employed throughout the simulation work. One model is derived using the SRM parameters and produces torque that is representative of the SRM being modeled. The other model employed is a nonlinear self-tuning model that involves fitting a general Fourier-type function to the torque produced by the SRM. Hence, the second model can be employed as a torque estimator.

The first model employed is that described in (Roux 2000) and (Roux 2002). In these papers, a simple model is derived from the nonlinear magnetisation characteristics of an SRM. The ability of this simple model to accurately estimate the instantaneous torque produced by the SRM is confirmed in both (Roux 2000) and (Roux 2002).

The model is formed from approximations of the magnetisation curves for the unaligned and aligned positions. One curve is sufficient to approximate the magnetisation curve for the unaligned position while two curves are required to approximate the magnetisation curve for the aligned position. One is for the linear part and one is for the nonlinear saturated part. Figure 3.1 shows the different curves chosen to approximate the flux-linkage current curves at the aligned and unaligned positions.

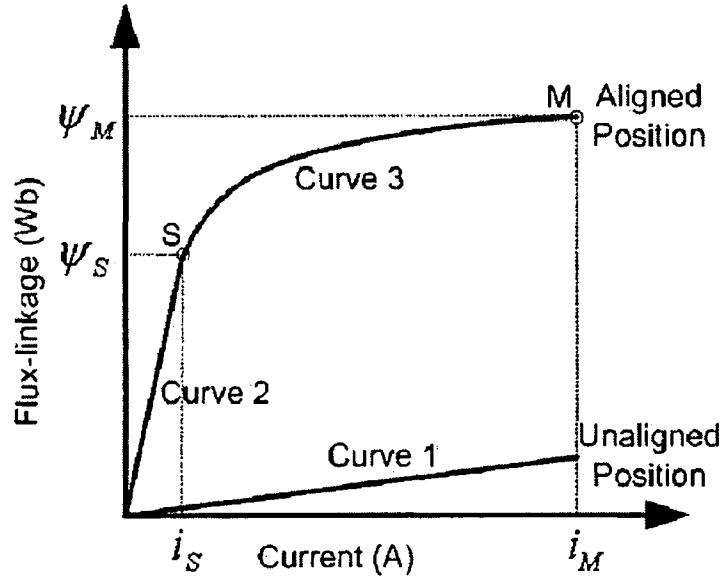

Figure 3.1: Approximated flux-linkage current curves for the aligned and unaligned positions.

The curve representing the unaligned position (curve 1) is approximated by a straight line such that, for any value of current, the flux-linkage, $\psi_U(i)$, is described by:

$$\psi_U(i) = L_U i \tag{3.1}$$

where L_U represents the equivalent inductance at the unaligned position and is a constant.

Two curves are required to represent the flux-linkage current relationship at the aligned position. The first curve (curve 2) describes the linear region where the flux-linkage is proportional to the current and hence, the inductance, L_A, is approximated as a constant value. Thus, for $i < i_S$, the flux-linkage is described by:

$$\psi_A(i) = L_A i \tag{3.2}$$

In the nonlinear saturated region, $i > i_S$, the flux-linkage current relationship is described by a horizontal parabola (curve 3) with the equation:

$$\psi_A(i) = \psi_{So} + \sqrt{4a(i - i_{So})} \tag{3.3}$$

where a, ψ_{So} and i_{So} are constants that may be determined as follows:

The curves 2 and 3 in Figure 3.1 must have the same gradient at the point S. Differentiating equations (3.2) and (3.3) and setting them equal at the point S yields:

$$i_{So} = i_S - \frac{a}{L_A^2} \tag{3.4}$$

$$\psi_{So} = \psi_S - \frac{2a}{L_A} \tag{3.5}$$

where ψ_S and i_S are the values of the flux-linkage and current at the point S. A value for the constant a may be determined from a second point, M, on the curve where M is chosen to be in the region of the nominal current. The value of a is thus:

$$a = \frac{\psi_{MS}^2}{4\left(i_{MS} - \frac{\psi_{MS}}{L_A}\right)} \tag{3.6}$$

where $\psi_{MS} = \psi_M - \psi_S$ and $i_{MS} = i_M - i_S$ and ψ_M and i_M are the values of the flux-linkage and current at the point M.

The variation of flux-linkage with position is approximated by a simple sinewave oscillating between its maximum value, $\psi_A(i)$, and its minimum value, $\psi_U(i)$. Thus, the final equation for the flux-linkage is:

$$\psi(\theta,i) = \frac{1}{2}\left(\psi_A(i) - \psi_U(i)\right)\left(\cos(2p\theta)+1\right) + \psi_U(i) \tag{3.7}$$

where p is a constant equal to half the number of rotor poles. The expression for the flux-linkage also assumes that $\theta = 0 \pm k\pi/p$ is defined as the aligned position and $\theta = \pi/2p \pm k\pi/p$ as the unaligned position where k is an integer.

The instantaneous phase torque can be calculated in terms of the flux-linkage from the following equation:

$$T(\theta,i) = \int_0^i \frac{\partial\psi(i,\theta)}{\partial\theta}\,di \tag{3.8}$$

Substituting the equation for flux-linkage of (3.7) into (3.8) gives:

$$T(\theta,i) = -p(\sin 2p\theta)\int_0^i \left(\psi_A(i) - \psi_U(i)\right)di \tag{3.9}$$

with $\psi_A(i)$ and $\psi_U(i)$ as in equations (3.1), (3.2) and (3.3).

For $0 < i < i_S$,
$$T(\theta,i) = -p(\sin 2p\theta)\frac{1}{2}(L_A - L_U)i^2 \tag{3.10}$$

For $i > i_S$,
$$T(\theta,i) = -p(\sin 2p\theta)\left[\begin{array}{c}\psi_{So}(i-i_{So}) + \frac{4\sqrt{a}}{3}\left((i-i_{So})^{\frac{3}{2}} - (i_S - i_{So})^{\frac{3}{2}}\right) \\ -\frac{1}{2}L_U(i-i_S)^2 + \frac{1}{2}(L_A - L_U)i_S^2\end{array}\right] \tag{3.11}$$

This simple SRM model was implemented in Simulink for a single phase of a 12/8 three-phase SRM. The parameter values for this SRM were as follows: $p = 4$ (half the number of rotor poles), $L_U =$ 0.21mH, $L_A =$ 1.93mH, $\psi_S =$ 0.0388Wb, $i_S =$ 20A, $\psi_M =$ 0.07Wb and $i_M =$ 50A. A MATLAB function was written to automatically calculate the values of a, ψ_{So} and i_{So} enabling the machine parameters (such as aligned and unaligned inductances) to be easily modified if so desired. A supply voltage of 120V was employed for magnetisation and demagnetisation of the phase winding. The current, torque and flux-linkage waveforms for motor operation at 1000rpm are shown in Figures 3.2, 3.3 and 3.4. The turn-on angle (θ_{ON}) was 22.5 degrees before alignment and the turn-off angle (θ_{OFF}) was 8 degrees before alignment. The current, torque and flux-linkage waveforms for generator operation at 1000rpm are shown in Figures 3.5, 3.6 and 3.7. The turn-on angle was 5 degrees before alignment and the turn-off angle was 10 degrees after alignment.

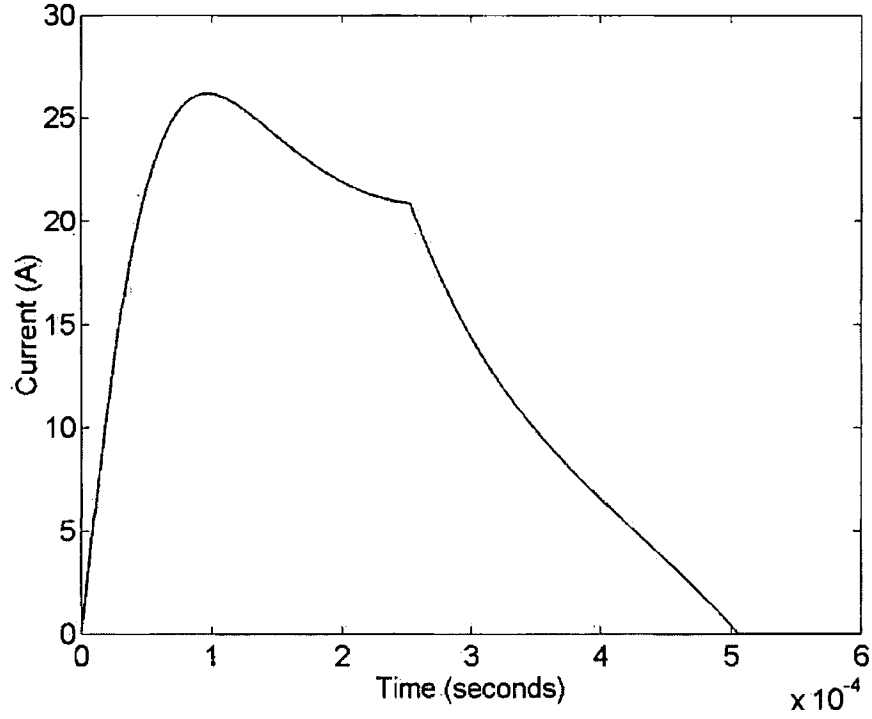

Figure 3.2: Phase current waveform for motor operation at 1000rpm with θ_{ON} = 22.5 degrees before alignment and θ_{OFF} = 8 degrees before alignment.

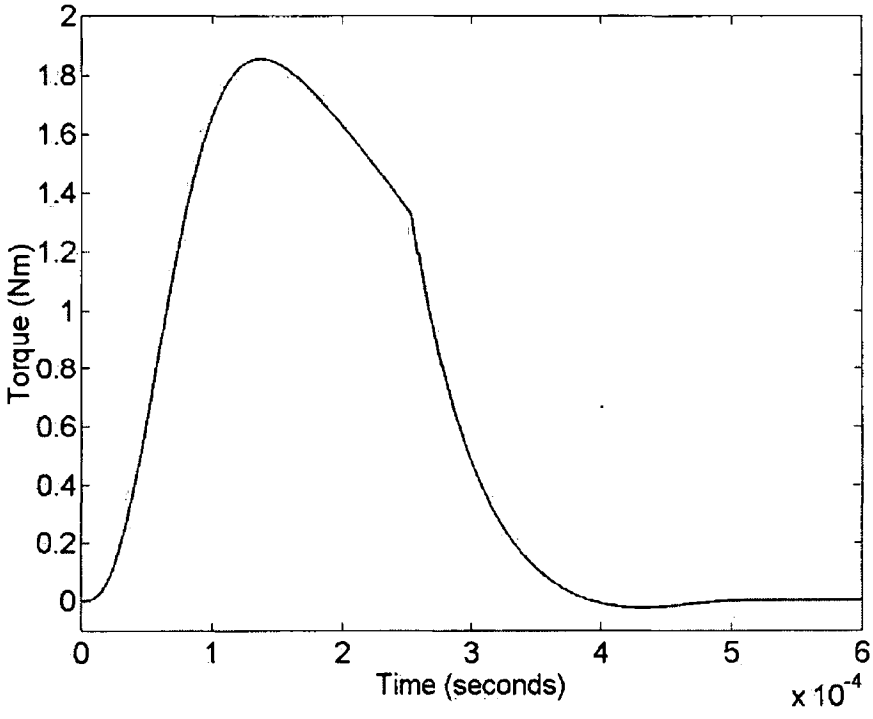

Figure 3.3: Phase torque waveform for motor operation at 1000rpm with θ_{ON} = 22.5 degrees before alignment and θ_{OFF} = 8 degrees before alignment.

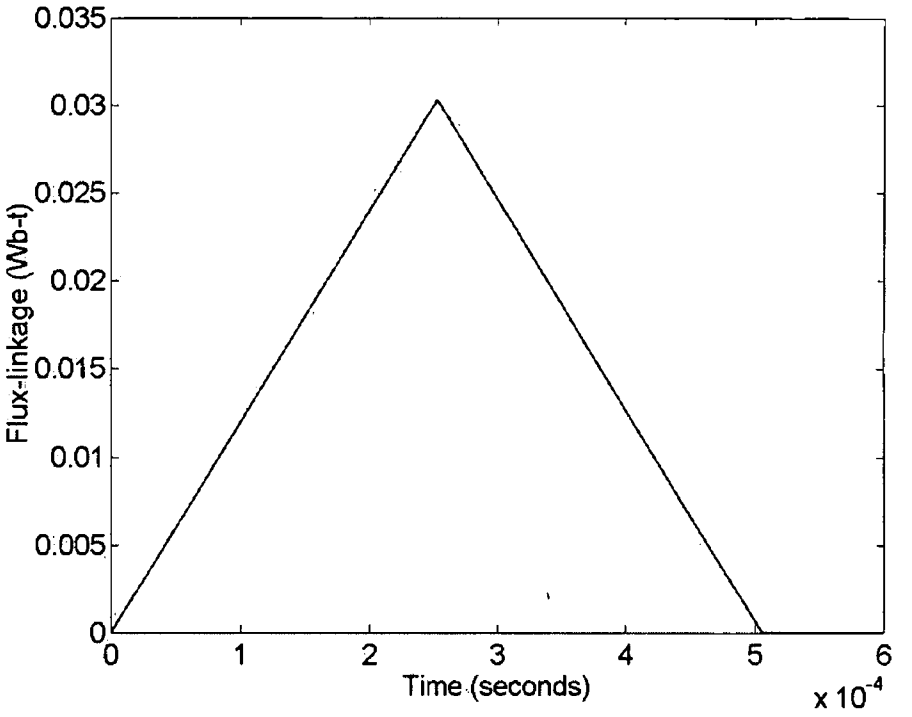

Figure 3.4: Phase flux-linkage waveform for motor operation at 1000rpm with θ_{ON} = 22.5 degrees before alignment and θ_{OFF} = 8 degrees before alignment.

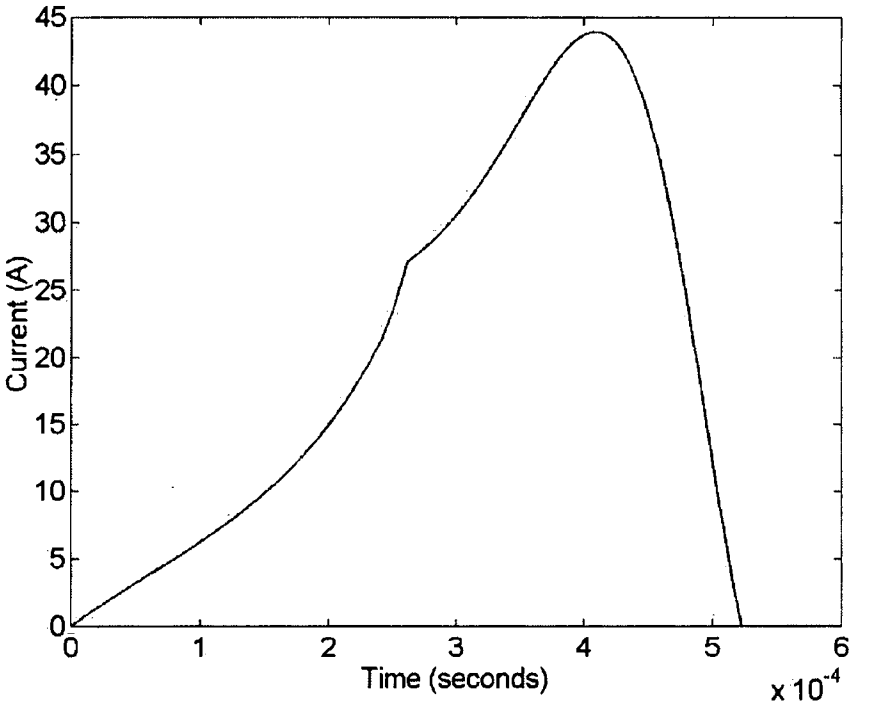

Figure 3.5: Phase current waveform for generator operation at 1000rpm with θ_{ON} = 5 degrees before alignment and θ_{OFF} = 10 degrees after alignment.

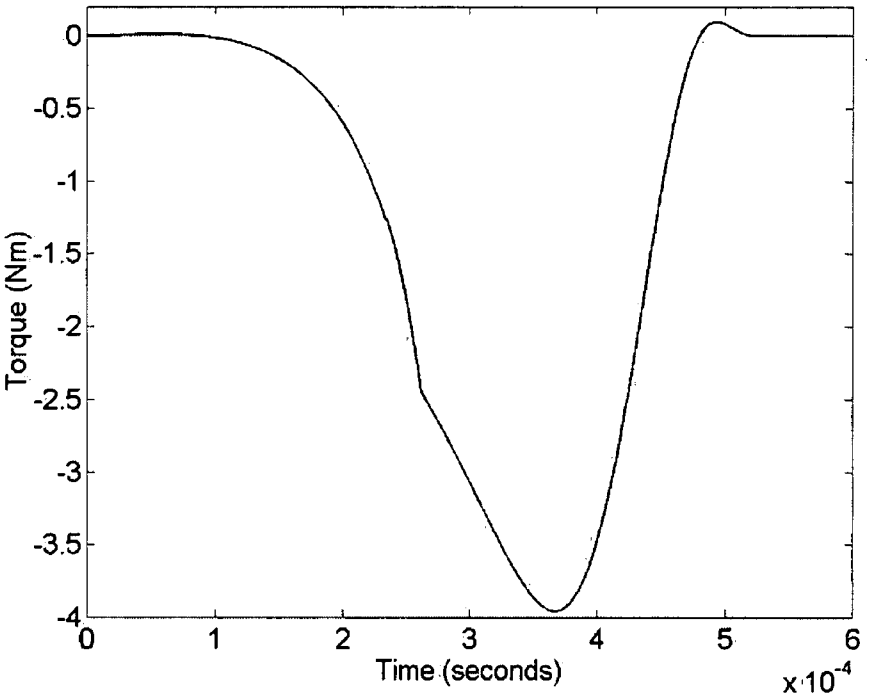

Figure 3.6: Phase torque waveform for generator operation at 1000rpm with $\theta_{ON} = 5$ degrees before alignment and $\theta_{OFF} = 10$ degrees after alignment.

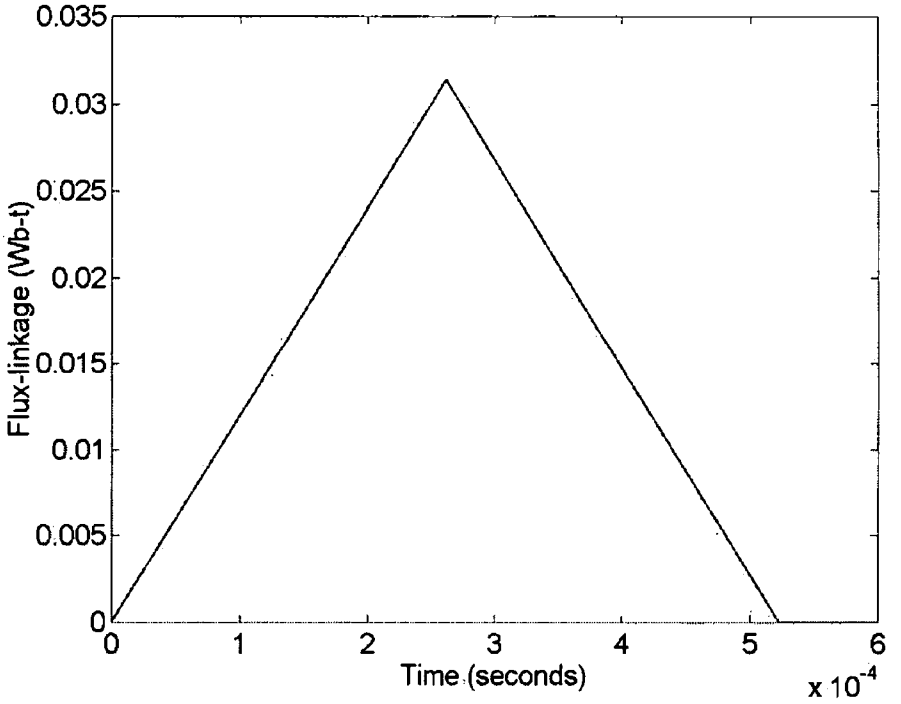

Figure 3.7: Phase flux-linkage waveform for generator operation at 1000rpm with $\theta_{ON} = 5$ degrees before alignment and $\theta_{OFF} = 10$ degrees after alignment.

The torque-position-current characteristic for a single phase of the 12/8 three-phase SRM model was determined and is shown below in Figure 3.8. As expected, positive torque is produced between the angle of 22.5 degrees before alignment and the angle of 0 degrees corresponding to the aligned position (motoring mode). At the aligned position, the torque is zero. From the aligned position to 22.5 degrees after alignment, negative torque is produced (generating mode).

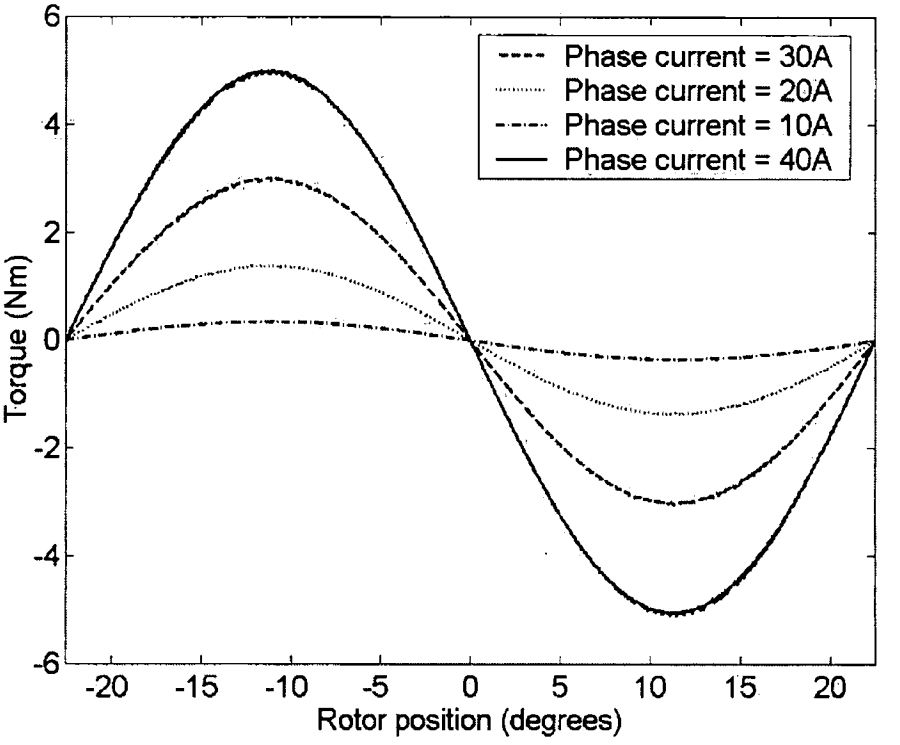

Figure 3.8: Torque-position-current characteristic for a single phase of the simple 12/8 three-phase SRM model.

3.3 Torque estimation using a self-tuning SRM model

For smooth control of the SRM during motoring operation, an accurate model of the machine that describes the torque characteristics is essential. A common approach is to use a model of the SRM based on stored current, position and torque profiles. However, these models employ data that is usually collected under static conditions and hence, any subsequent changes in the characteristics of the machine may affect the accuracy of the results. In addition, such models are highly dependent on accurate rotor position information.

The second model employed is that described in (Mir 1998) and which requires very little *a priori* knowledge of the machine. This paper presents a nonlinear model with on-line parameter estimation using recursive identification and it enables self-tuning of an SRM without any additional instrumentation. The model can serve as a torque observer and is unaffected by changes in the parameters of the machine or inaccuracies in the rotor position.

The flux-linkage is a periodic function of rotor position, θ, with a period of $2\pi/N$ where N is the number of rotor poles. Therefore, the flux-linkage in each phase of the machine can be represented by the following continuous function as:

$$\psi(\theta,i) = \psi_S\left(1 - e^{-i f(\theta)}\right) \tag{3.12}$$

where ψ_S is a constant whose magnitude is equal to or greater than the saturation flux-linkage of the SRM and $f(\theta)$ is a Fourier series function that is used to model the position-dependent nonlinearities in the machine characteristics. The $f(\theta)$ function can be represented by:

$$f(\theta) = a + b\cos N\theta + c\cos 2N\theta + d\sin N\theta + e\sin 2N\theta \tag{3.13}$$

where N is the number of rotor poles and the parameters a,b,c,d and e are variables that are determined on-line.

The instantaneous torque in each phase is given by:

$$T = \left[\frac{\partial W_C}{\partial \theta}\right]_{i=CONSTANT} \tag{3.14}$$

where W_C is the co-energy of each phase and is equivalent to:

$$W_C = \int_0^i \psi(\theta,i)di \tag{3.15}$$

The expression for flux-linkage can be substituted into the torque equation to give:

$$T = \frac{\psi_S \dfrac{df(\theta)}{d\theta}}{f(\theta)^2}\left[1-\left(1+if(\theta)\right)e^{-if(\theta)}\right] \tag{3.16}$$

All the variables in the torque equation are known or can be measured/calculated except for the Fourier coefficients a,b,c,d and e. A system identification technique is used to determine these parameters while the motor is running. The flux-linkage model of equation (3.12) needs to be rearranged to use the least squares identification method. Thus, equation (3.12) becomes:

$$i f(\theta) = \ln\left(\frac{\psi_S}{\psi_S - \psi}\right) \tag{3.17}$$

Replacing $f(\theta)$ with its Fourier representation as in equation (3.13) yields:

$$\begin{bmatrix} i & i\cos N\theta & i\cos 2N\theta & i\sin N\theta & i\sin 2N\theta \end{bmatrix}\begin{bmatrix} a \\ b \\ c \\ d \\ e \end{bmatrix} = \ln\left(\frac{\psi_S}{\psi_S - \psi}\right) \tag{3.18}$$

The flux-linkage, ψ, is required to calculate the log function on the right-hand side of equation (3.18) and this can be determined through numerical integration of the terminal measurements of voltage and current as follows:

$$\psi = \int (v - iR)dt \tag{3.19}$$

Equation (3.18) can be written in simplified notation as:

$$\phi\,\Delta = Y \tag{3.20}$$

where

$$\phi = \begin{bmatrix} i & i\cos N\theta & i\cos 2N\theta & i\sin N\theta & i\sin 2N\theta \end{bmatrix}$$

$$\Delta^T = \begin{bmatrix} a & b & c & d & e \end{bmatrix}$$

$$Y = \ln\left(\frac{\psi_S}{\psi_S - \psi}\right) \tag{3.21}$$

Equation (3.20) is the basic model for the parameter identification and is linear with respect to the parameter matrix, Δ, allowing its use in recursive least squares identification. Recursive least squares identification employs a covariance matrix, P, defined as:

$$P_t = \frac{1}{\alpha}\left[P_{t-1} - \frac{P_{t-1}\phi_t\phi_t^T P_{t-1}}{\alpha + \phi_t^T P_{t-1}\phi_t}\right] \tag{3.22}$$

This is used to update the parameter matrix, Δ, according to:

$$\Delta_t = \Delta_{t-1} + P_t\phi_t\left[Y_t - \phi_t^T\Delta_{t-1}\right] \tag{3.23}$$

The initial values in the covariance matrix P must be chosen to be greater than zero. α is called the learning rate and can be chosen in the range $0.95 < \alpha < 1$.

A block diagram of the torque estimation method is shown in Figure 3.9.

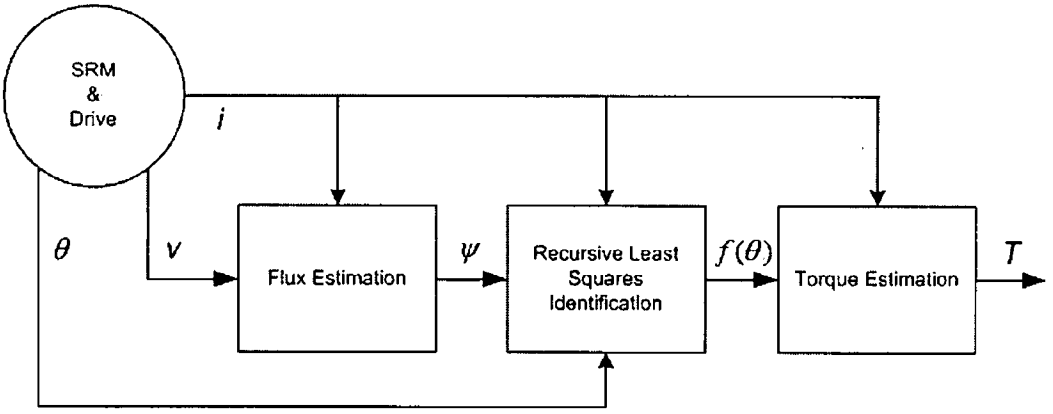

Figure 3.9: Block diagram of the torque estimation method.

An alternative expression to equation (3.16) for the torque can be derived using the magnetic circuit magnetomotive force decomposition as described in (Filicori 1993) and the results of this derivation are also included in (Russa 2000) and (Russa 1998). The phase torque is derived using the D'Alambert principle, which results in the following expression:

$$T = \frac{1}{2} \frac{\psi^2 \frac{df(\theta)}{d\theta}}{\psi_S f^2(\theta)} \tag{3.24}$$

where ψ is calculated from equation (3.12) using the measured phase current and the updated parameter values *a, b, c, d* and *e*.

The nonlinear SRM model with on-line parameter identification was tested in Simulink. In order to test the self-tuning abilities of this nonlinear model, it was necessary to have a separate SRM model that would represent the behaviour of a 'real' motor. The first simple SRM model described in Section 3.2 was used for this purpose. Figure 3.10 shows the simulated results for the torque produced by the simple SRM model representing a 'real' motor and the torque produced by the self-tuning nonlinear model. As can be seen, the two torque profiles match after the first electrical cycle. Thus, the nonlinear model is suitable for deployment as a torque estimator. This model is in fact employed as a torque estimator in the torque ripple minimisation schemes described in Chapters Four and Six.

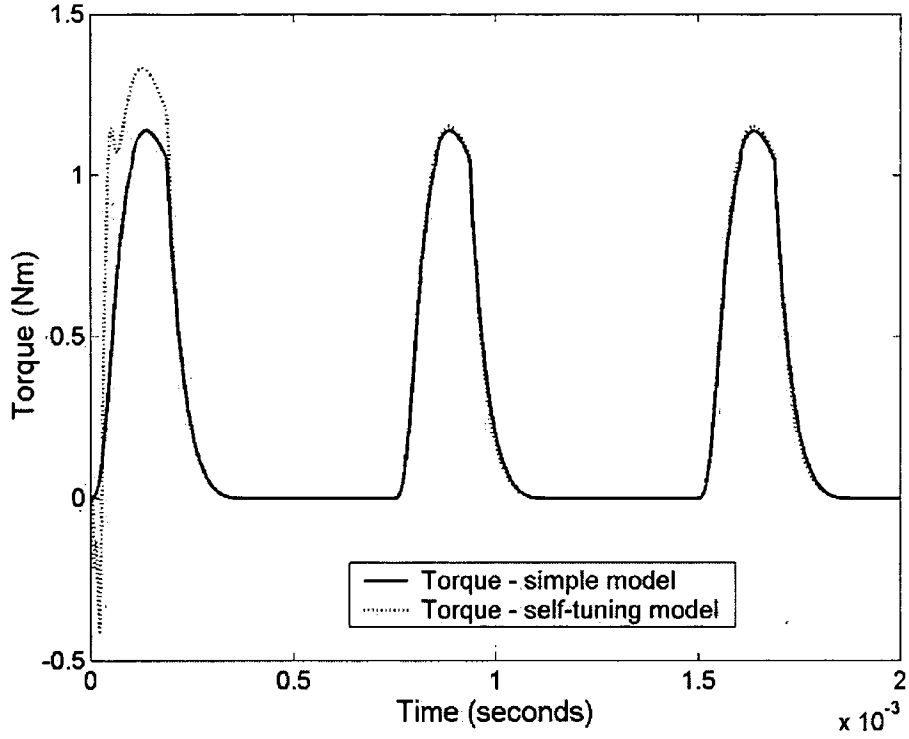

Figure 3.10: Torque profiles for a single phase of the simple SRM model representing the 'real' motor and the nonlinear SRM model with parameter identification.

During the parameter identification process, the parameters a,b,c,d and e assume values that account for the electromagnetic characteristics of the particular SRM being modeled. Figure 3.11 shows the values of these parameters during steady-state motoring operation for a single phase of the SRM. As can be seen, the parameters are continuously updated. This ensures that the torque produced by the self-tuning nonlinear model matches that of the simple SRM model representing the 'real' motor. When the torque produced by the phase of the 'real' motor undergoing parameter identification is zero, there is no change in the parameter values. However, when phase torque is being produced, the parameters are updated as can clearly be seen in Figure 3.11.

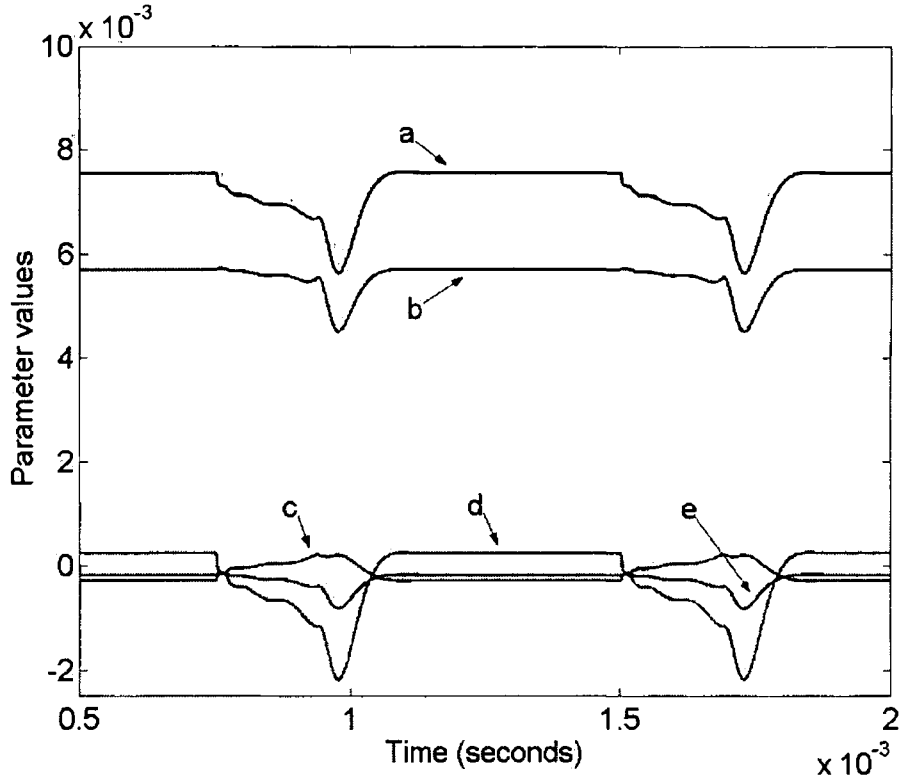

Figure 3.11: Parameters *a,b,c,d* and *e* during steady-state motoring operation.

3.4 Self-tuning torque ripple minimisation controller

The self-tuning nonlinear model of the SRM described in Section 3.3 was employed in the torque ripple minimisation motor control scheme described in (Russa 2000). In this paper, the model serves as a torque observer/estimator while a simple commutation strategy is used to minimise the torque ripple. It was decided to implement this control strategy to further verify the torque estimation capability of the self-tuning nonlinear model. This control scheme is adaptive to a wide range of speed operation. It is designed for SRMs in which at least two phases can develop positive torque at commutation. A block diagram of the controller is shown in Figure 3.12.

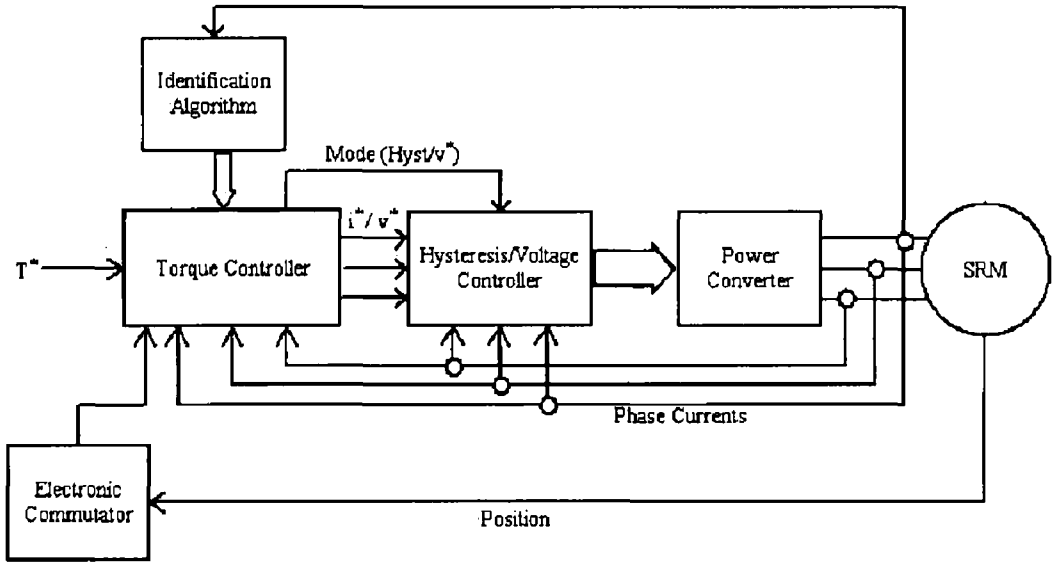

Figure 3.12: Block diagram of the SRM torque ripple minimisation motor control structure.

The torque reference signal, T^*, is used to generate the desired torque for a chosen phase or phases. The electronic commutator selects the most appropriate phases for developing torque while maximising regions where more than one phase is used for positive torque production. The torque controller estimates the phase torques using equation (3.24) (with the updated parameter values *a,b,c,d* and *e* being employed). The desired torque, T_k^*, for a particular phase k is obtained by subtracting the estimated torque values produced by the other $(N-1)$ phases from the total torque reference as follows:

$$T_k^* = T^* - \sum_{j=1, j\neq k}^{N} T_j \tag{3.25}$$

There are two modes of control involved in the production of the gate signals for the power converter, hysteresis current control and voltage control. Essentially, each phase conduction interval can be divided into three regions. During the torque production interval, the current is regulated by a hysteresis controller. However, during the commutation stage (of which there are two intervals), voltage control of the phase is employed. During the first commutation interval, the controller forces a zero-

voltage to be applied to the phase. This enables torque to build up in the next phase (resulting in a smooth transition of torque from one phase to the next). During the second commutation interval, a negative voltage is applied to the phase. This rapidly reduces the current to zero thereby avoiding the production of negative torque.

An important aspect of the torque controller is the production of the phase current command, i^*_k. In (Russa 2000), a mathematical expression relating the current command to the desired phase torque, T^*_k, is derived resulting in the following:

$$i_k^* = -\frac{1}{f(\theta)} \ln\left(1 - \sqrt{\frac{2T_k^* f^2(\theta)}{\psi_S f'(\theta)}}\right) \tag{3.26}$$

where $f(\theta)$ is the expression given in equation (3.13) and ψ_S is as defined in Section 3.3. This current command is used by the hysteresis current controller during the torque production interval. Figure 3.13 shows a block diagram of the torque controller (Russa 2000).

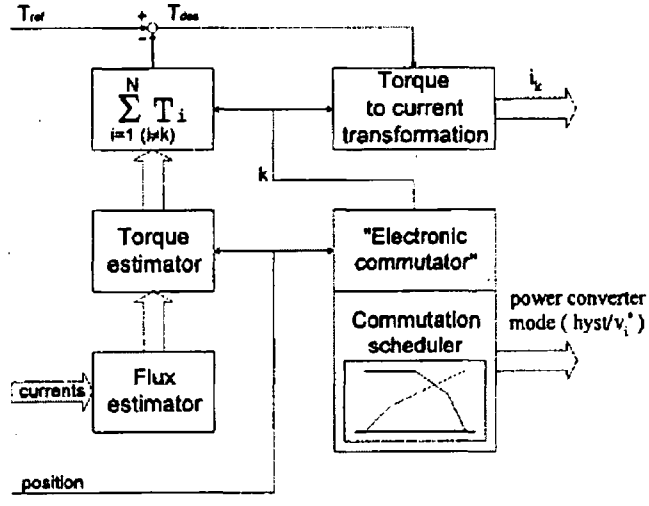

Figure 3.13: Block diagram of the torque controller.

Control systems based on the strategy just described were implemented in MATLAB/Simulink for both a 6/4 three-phase SRM and a 12/8 three-phase SRM.

Once again, the motor model used to act as a 'real' SRM was the simple model described in Section 3.2.

For both the 6/4 and 12/8 SRMs, the parameter identification routine was performed for all three phases of the machine. However, when the identification routine was performed for a single phase only and the results utilised for all the phases, there was no degradation in the performance of the control strategy. For the 6/4 SRM, the torque production interval during which the current is controlled using a hysteresis controller was set from 45 degrees before alignment to 15 degrees before alignment. The zero-voltage commutation interval was set from 15 degrees before alignment to 2.5 degrees before alignment. At 2.5 degrees before alignment, the negative supply voltage was applied to the phase until the current reduced to zero. Figure 3.14 shows the total torque produced by the 6/4 SRM at a speed of 60rpm under a 0.5Nm load. Figure 3.15 shows the individual phase torque profiles for all three phases. Figure 3.16 shows the current in a single phase of the SRM and the corresponding torque produced by that phase. As can be seen, the current waveform isn't flat-topped. It is instead profiled to reduce the torque ripple.

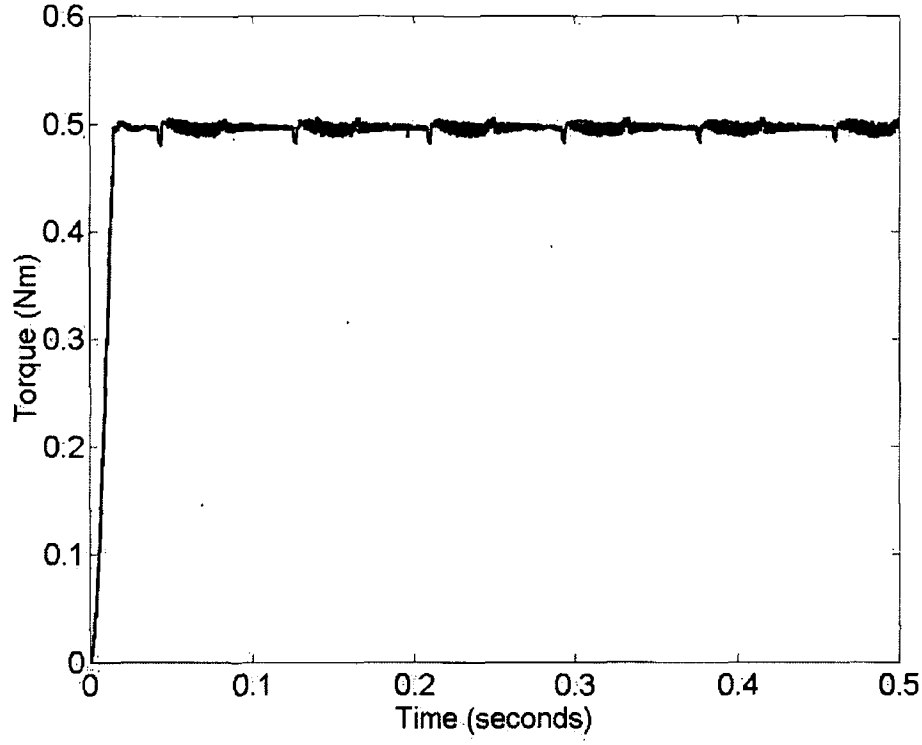

Figure 3.14: Total torque produced by the 6/4 three-phase SRM model at a speed of 60rpm under a 0.5Nm load.

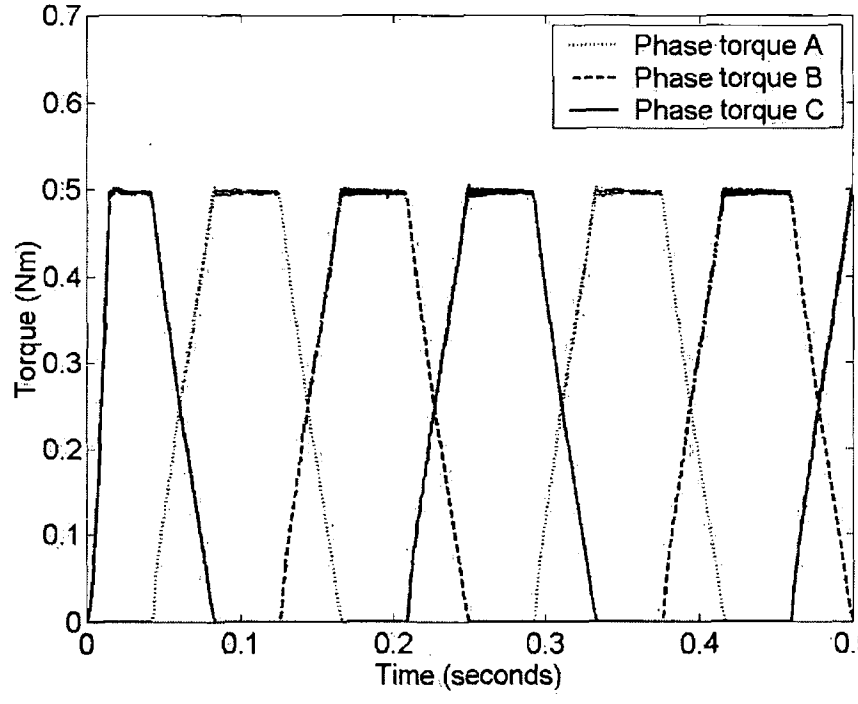

Figure 3.15: The individual phase torque profiles for all three phases produced by the 6/4 SRM model operating at a speed of 60rpm and under a 0.5Nm load.

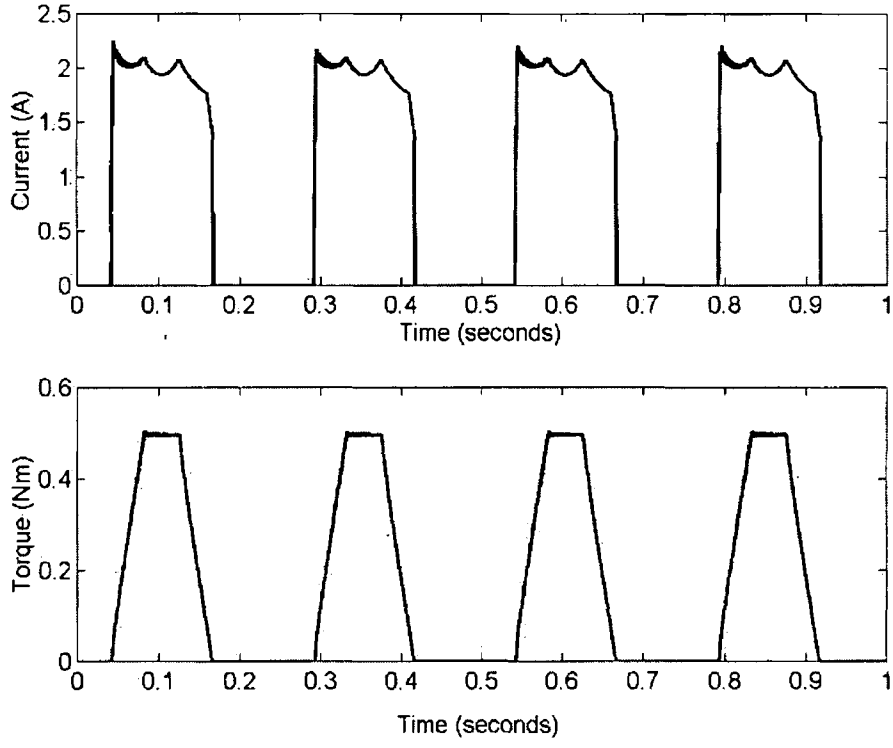

Figure 3.16: The current in a single phase of the 6/4 three-phase SRM model and the corresponding torque produced by that phase.

The control strategy was also implemented for a 12/8 three-phase SRM model. The hysteresis current control region was from 22.5 degrees before alignment to 7.5 degrees before alignment. The zero-voltage commutation interval was set from 7.5 degrees before alignment to 1.5 degrees before alignment at which point the negative supply voltage was applied. Figure 3.17 shows the total torque and the individual phase torque profiles for operation at a speed of 60rpm and with a 0.8Nm load. A 6/4 three-phase SRM demands 12 current pulses per rotor turn. A 12/8 three-phase SRM demands 24 current pulses per rotor turn. Therefore, for 6/4 and 12/8 three-phase machines operating at the same speed, the torque pulsations in the 12/8 machine will occur twice as often as in the 6/4 machine as can clearly be seen by comparing Figures 3.14 and 3.17.

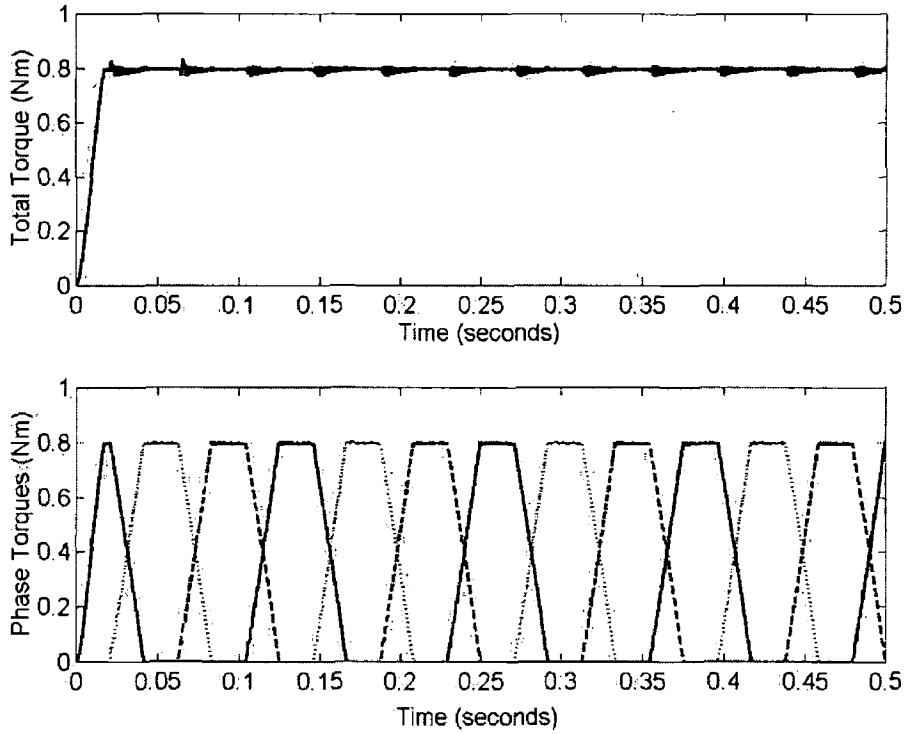

Figure 3.17: The total torque and the individual phase torque profiles produced by the 12/8 three-phase SRM model for operation at a speed of 60rpm and with a 0.8Nm load.

3.5 SR generator control using an inverse model approach

The SR generator requires an excitation source to enable the generation of electrical energy with the excitation current supplied via the machine's associated power converter. After an initial burst of energy has been supplied from the external excitation source however, the external power source may be disconnected and the SR generator may subsequently be self-excited. It is inherent in the operation of the SR generator that current flows to the active phase from the dc link during excitation whilst during generation, current flows from the active phase back to the dc link thereby charging the dc link capacitor. The net generated current, I_O, is the difference between the integral of the excitation current supplied and the integral of the current returned to the dc link.

In (Kjaer 1994), an inverse model of the SR generator that relates the firing angles, θ_{ON} and θ_{OFF}, for single pulse mode operation, to the average net generated current,

I_O, the dc link voltage, V_{dc}, and the rotational speed, ω, is derived. In the closed-loop generator controller described in (Kjaer 1994), a voltage controller outputs the required average net generated current to account for the voltage mismatch and the inverse model is then used to select the correct firing angles to produce the necessary current. A limitation of the described approach, however, is that the inverse model is obtained on the basis of a linear inductance profile. Under this assumption, it is shown in (Kjaer 1994) that there is a quadratic relationship between the turn-on angle, θ_{ON}, and the average net generated current, I_O, as follows:

$$I_O = \frac{V_{dc}}{\omega}\left(A\theta_{ON}^2 + B\theta_{ON} + C\right) \tag{3.27}$$

where the coefficents A, B and C are mathematical expressions that are given in (Kjaer 1994). Thus, it is possible to analytically deduce the turn-on angle using the required average net generated current from equation (3.27).

Rather than follow this approach exactly, the assumption of a linear inductance profile wasn't made and the relationship between θ_{ON} and I_O for a nonlinear model of a SRM inclusive of saturation was obtained by means of simulation. The nonlinear model employed in the simulation was that described in Section 3.2. While the use of a nonlinear model is an obvious advantage, the method described in (Kjaer 1994) has the advantage that no measurements are required and only geometry and unsaturated unaligned and aligned phase inductances need to be known.

Results were obtained for an 8/8-pole single phase SR generator whose parameters (0.8kW machine with phase resistance of 0.016Ω and unaligned/aligned inductances of 0.21/1.94mH) were chosen according to a prototype design described in (Miller 2001). Figure 3.18 shows the relationship between the turn-on angle and the average net generated current for different turn-off angles at 100V. The solid line represents the exact values obtained from simulations. The quadratic approximation is the dashed line superimposed on the exact result. Two sets of curves are provided to confirm the validity of the result for different turn-off angles (which are taken to be fixed). Figure 3.19 shows similar results at 270V. These graphs indicate that the

relationship between average net generated current and turn-on angle for a nonlinear model can still be adequately approximated using a quadratic.

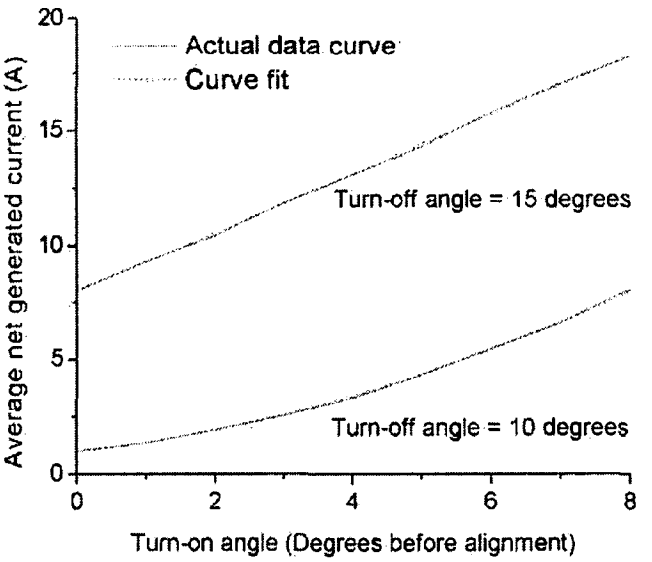

Figure 3.18: Relationship between the turn-on angle and average net generated current for $V_{dc} = 100$V.

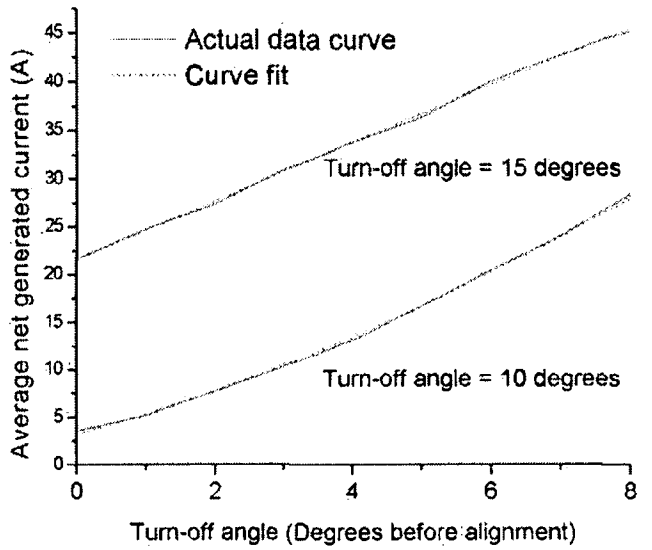

Figure 3.19: Relationship between the turn-on angle and average net generated current for $V_{dc} = 270$V.

Having established the essentially quadratic nature of the relationship between average net generated current and turn-on angle for a fixed turn-off angle, the control

system shown in block diagram form in Figure 3.20 is applicable. $F(\theta)$ is the quadratic approximation to the exact relationship between the turn-on angle and the average net generated current.

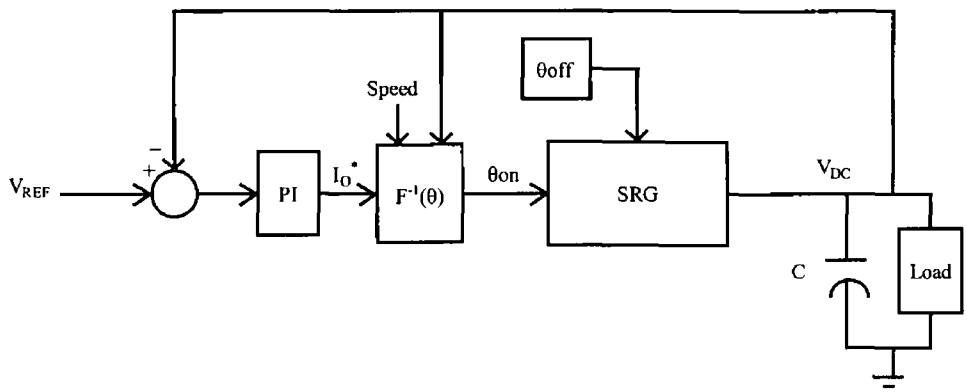

Figure 3.20: Block diagram of the generator controller structure.

The closed-loop voltage control strategy employs a PI controller that outputs the required net generated current, I_O^*, needed to bring the dc link voltage, V_{dc}, to the desired level. The inverse machine model, $F^{-1}(\theta)$, then selects the appropriate turn-on angle that will produce the necessary current.

The control strategy was implemented and tested in Simulink for the 8/8 single-phase SR generator. The dc link capacitor value was chosen to be 3500μF. The PI controller was implemented with anti-windup and a saturation block was employed to limit the maximum required net generated current to 8A. The turn-off angle was fixed at 10 degrees after alignment. Figure 3.21 shows the dc link voltage for a reference voltage of 100V. The generator rotational speed is 1000rpm and a 100Ω resistive load is connected across the dc link capacitor. The ripple on the dc link voltage results from the same dc link being used for excitation and generation i.e. the dc link voltage dips when current is drawn for excitation and rises again during the generation period.

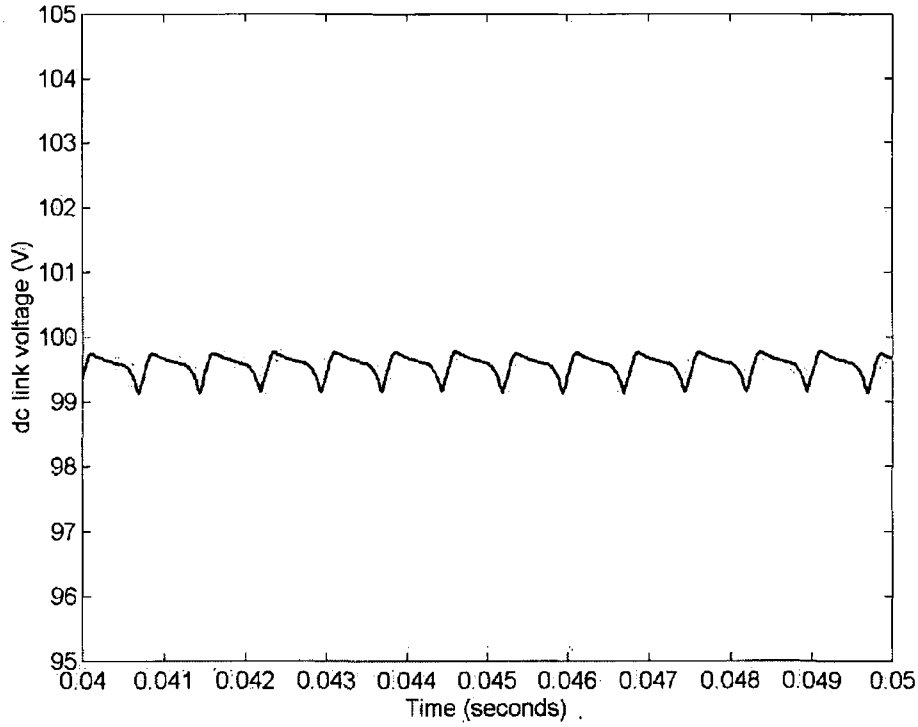

Figure 3.21: Dc link voltage for a 100V reference with operation at 1000rpm and with a 100Ω resistive load.

Figure 3.22 shows the steady-state phase current for operation with a reference voltage of 100V, at a rotational speed of 1000rpm and with a 100Ω resistive load connected across the dc link capacitor. The excitation turn-on and turn-off positions are clearly shown.

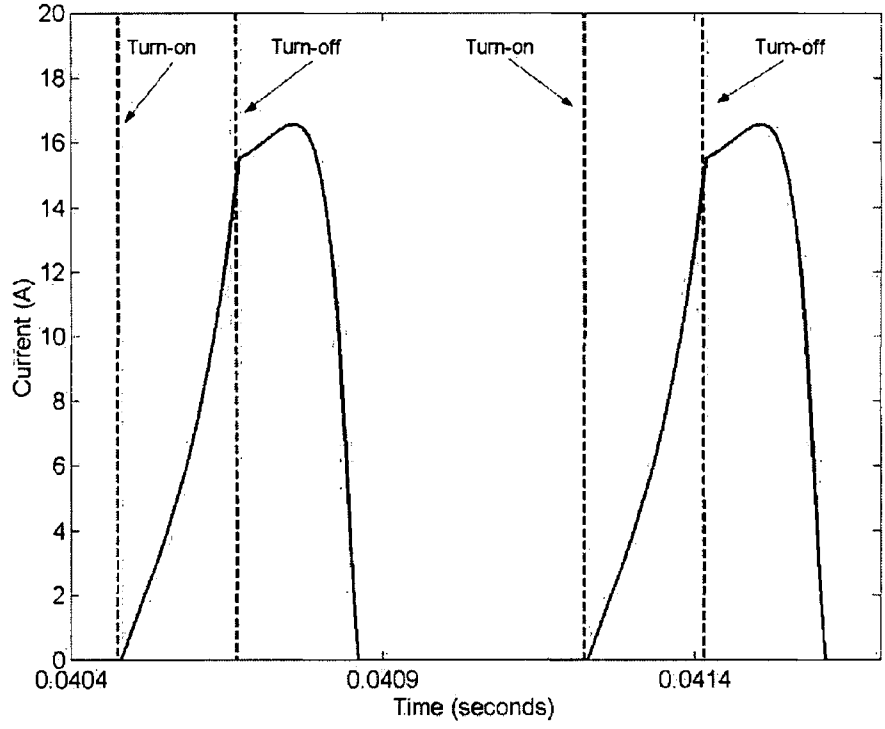

Figure 3.22: Phase current for operation with 100V reference at a speed of 1000rpm and with a 100Ω resistive load.

A critical test of the generator control system is its transient response to a change in the load. Figure 3.23 shows the response of the generator control system to a step in the load (from 100Ω to 50Ω) after 0.05 seconds for operation with a 100V reference and at a speed of 1000rpm. As can be seen, the dc link voltage recovers quickly. During this recovery period, there is a significant increase in the phase current. This increases the net generated current and therefore brings the dc link voltage back to the commanded level as quickly as possible. When the dc link voltage has recovered to 100V steady-state, the phase current has a higher peak value than prior to the reduction in the load impedance. This is as a consequence of needing to supply more generated current.

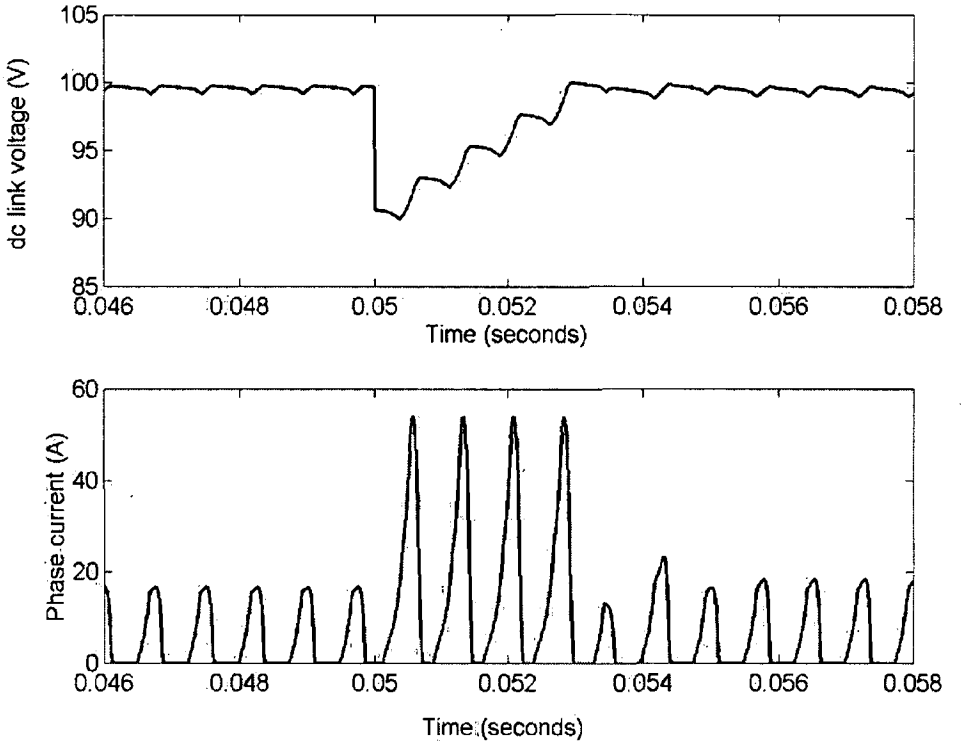

Figure 3.23: Response of the generator control system to a step in the load (from 100Ω to 50Ω) after 0.05 seconds for operation with a 100V reference and at a speed of 1000rpm.

In many SR generator applications, energy is delivered to a dc link of fixed voltage. However, there are also situations where SR generator systems are required to deliver energy to a dc link of variable voltage. Figure 3.24 shows the response of the generator control system to a step in the reference voltage from 100V to 110V at a speed of 1000rpm and with a 100Ω resistive load.

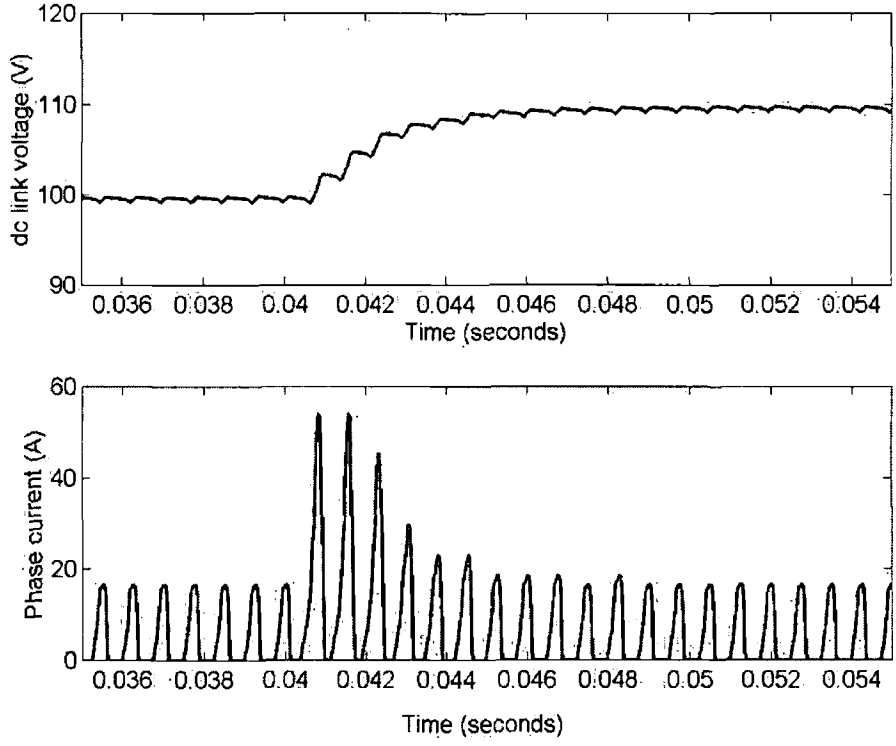

Figure 3.24: Response of the generator control system to a step in the reference voltage from 100V to 110V at a speed of 1000rpm and with a 100Ω resistive load.

Chapter Four – Torque ripple minimisation

4.0 Introduction

In this chapter, the implementation of three neuro-fuzzy control strategies for torque ripple minimisation in SR motors is described. Firstly, Fuzzy Logic and the operation of the Adaptive Neuro-Fuzzy Inference System (ANFIS) are explained. For each control strategy, the training of a suitable neuro-fuzzy compensator for torque ripple reduction and the incorporation of the trained compensator into the overall SR drive are then described. The performance of the three torque ripple minimisation control schemes is examined with simulations and the results are presented. Their efficacy is tested under current-regulated speed control operation implemented using a PI controller.

4.1 Fuzzy Logic

Conventional mathematical tools are often ill-suited to the modeling of poorly defined and/or uncertain systems (Jang 1993). An alternative approach to solving control problems associated with such systems involves Fuzzy Logic, a problem-solving control methodology that incorporates a simple rule based '*If x is A and y is B then z is C*' approach.

The concept of Fuzzy Logic was first introduced by Lofti Zadeh (Zadeh 1965) who presented a way of processing data by allowing partial set membership rather than crisp set membership. A classical crisp set, A, is defined as a collection of individual elements of a superset, X, which satisfy certain conditions governing A (Vas 1999). A crisp set can be characterised by the characteristic function, $\mu_C(x)$, such that

$$\mu_C(x) = \begin{cases} 1 & when\, x \in A\,(x\, belongs\, to\, set\, A) \\ 0 & when\, x \notin A\,(x\, does\, not\, belong\, to\, set\, A) \end{cases} \tag{4.1}$$

Thus, a crisp set, A, either totally includes or totally excludes any given element. As such, the characteristic function of a crisp set corresponds to binary or bivalued logic. An example of a classical crisp set is:

$$A = \{x \mid 4 < x < 10\} \tag{4.2}$$

In (Zadeh 1965), the idea of a fuzzy set was conceived by extending the notion of a binary characteristic function to a multivalued membership function such that a fuzzy set can contain elements with only a partial degree of membership. This corresponds to any given element having a degree of membership on the continuous interval [0, 1] where the endpoint of 0 means no membership, the endpoint of 1 corresponds to full membership and there is an infinite number of membership values between 0 and 1. Thus, a membership function, $\mu(x)$, is a curve which defines how each input point or element is mapped to a membership value (or degree of membership) between 0 and 1. A fuzzy set is a set of ordered pairs $(x, \mu(x))$ with the membership function mapping each element of the domain, X, to a membership value between 0 and 1. Thus, a fuzzy set can be expressed as:

$$B = \{(x, \mu(x)) \mid x \in X\} \tag{4.3}$$

For example, if x_1 is an element of the fuzzy set B and x_1 has a membership value of 0.5 then the element x_1 belongs to the fuzzy set B by a degree of truth equal to 0.5. The characteristic function of the crisp set A and the membership function of the fuzzy set B are shown in Figure 4.1.

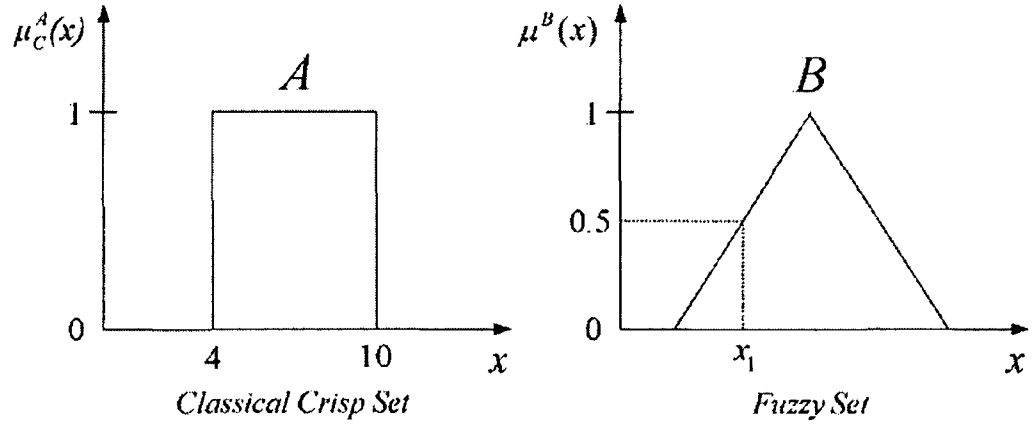

Figure 4.1: The characteristic function of the crisp set A and the membership function of the fuzzy set B.

There are many different types of membership functions since the only condition that must be satisfied is that it must vary between 0 and 1. There are smooth membership functions (bell-shaped, sigmoid, Gaussian etc.) and non-smooth membership functions (triangular, trapezoidal etc.). Two of the simplest membership function shapes are triangular and trapezoidal and these are shown in Figure 4.2.

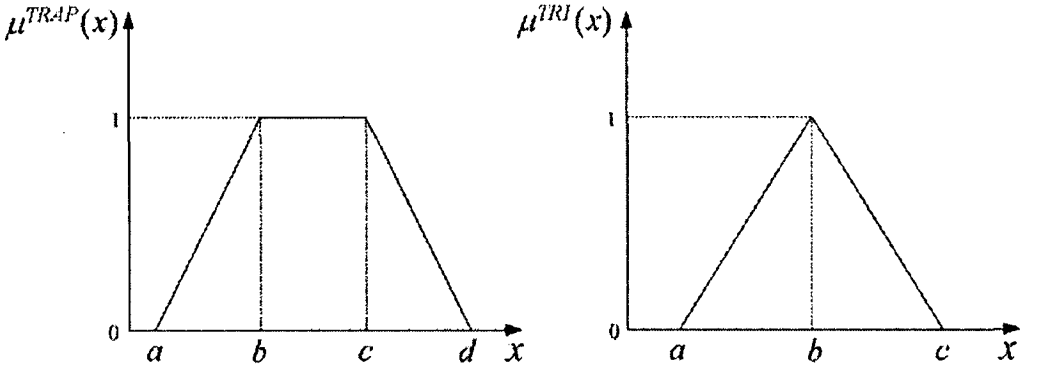

Figure 4.2: Trapezoidal and triangular membership functions.

As can be seen, the triangular membership function can be described using just three parameters, a, b and c and it can be represented mathematically as follows:

$$\mu_{TRI}(x) = \begin{cases} 0 & x < a \\ (x-a)/(b-a) & a \le x \le b \\ (c-x)/(c-b) & b \le x \le c \\ 0 & x > c \end{cases} \tag{4.4}$$

Similarly, the trapezoidal membership function can be described using just four parameters, a, b, c and d and it can be represented mathematically as follows:

$$\mu_{TRAP}(x) = \begin{cases} 0 & x < a \\ (x-a)/(b-a) & a \le x \le b \\ 1 & b \le x \le c \\ (d-x)/(d-c) & c \le x \le d \\ 0 & x > d \end{cases} \tag{4.5}$$

As already stated, Fuzzy Logic is a rule-based approach where the rules take the form of 'if-then' statements such as:

$$\begin{aligned} &\textit{If } x \textit{ is } A \textit{ and } y \textit{ is } B \textit{ then } z \textit{ is } C \\ &\textit{If } x \textit{ is } D \textit{ or } y \textit{ is } E \textit{ then } z \textit{ is } F \end{aligned} \tag{4.6}$$

The 'if-part' of each rule (eg. '*if x is A and y is B*') is called the antecedent or premise while the 'then-part' of each rule (eg. '*then z is C*') is referred to as the consequent. The interpretation of each rule involves a number of steps. Firstly, the antecedent must be evaluated, a process which involves the fuzzification of the inputs. Fuzzification essentially takes crisp input values and proceeds to resolve all the statements in the antecedent to a degree of membership between 0 and 1. Figure 4.3 shows the membership functions of two fuzzy sets, *A* and *B*. Consider, for example, that x_1 and y_1 are crisp input values to the fuzzy sets *A* and *B* respectively. It is clear from Figure 4.3 that x_1 and y_1 can be resolved to the following fuzzy values:

$$\mu^A(x_1) = 0.25 \quad \textit{and} \quad \mu^B(y_1) = 0.75 \tag{4.7}$$

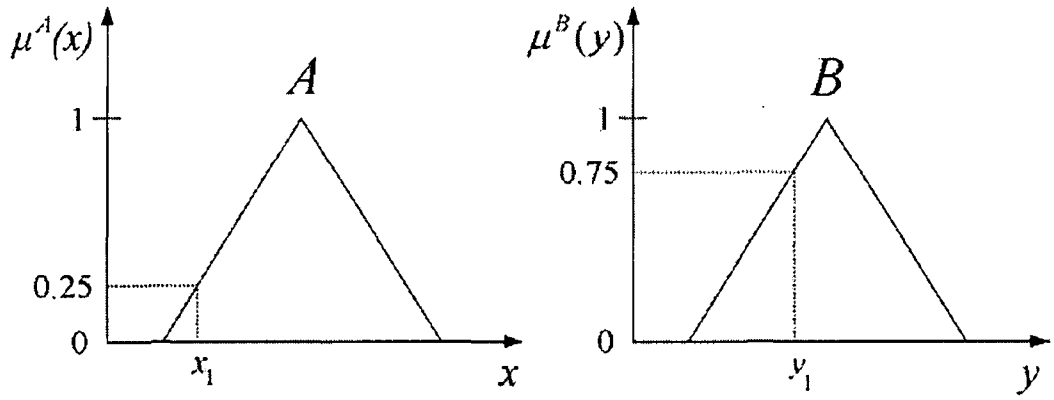

Figure 4.3: The membership functions of two fuzzy sets, *A* and *B*.

If there is only a single statement in the antecedent (eg. '*if x is A*'), then this is the support for the rule (also called the firing strength of the rule). However, if there is more than one statement (eg. '*if x is A and y is B*') then Fuzzy Logic operators are required to resolve the antecedent to a single number between 0 and 1. These operators are the fuzzy equivalent of *AND, OR* and *NOT* operators in standard boolean logic. Thus, it is possible to resolve the statement '*A AND B*', where *A* and *B* are fuzzy values limited to the range [0, 1], by using the function *min(A, B)*. Similarly, the operation '*A OR B*' can be replaced by *max(A, B)* while the operation '*NOT A*' can

be replaced by *1-A*. Fuzzy Logic is a superset of standard boolean logic. If the fuzzy values are kept at their extremes of 0 and 1, then the fuzzy operators return the same values as the standard equivalent boolean operators. Table 4.1 verifies this by showing the truth-tables for the standard *AND*, *OR* and *NOT* boolean operations and their equivalent fuzzy operations when the fuzzy values, *A* and *B*, are kept at the limits of 0 and 1. Of course in practice, the Fuzzy Logic operators are applied to fuzzy inputs in the range [0, 1]. Figure 4.4 illustrates the effect of the *min* operator when applied to inputs *A* and *B* (*A* and *B* are fuzzy values varying between 0 and 1) i.e. *min(A, B)*. If the *min* operator was applied to the fuzzy values in equation (4.7) then the result would be as follows:

$$min\left(\mu^{A}(x_1), \mu^{B}(y_1)\right) = min(0.25, 0.75) = 0.25 \tag{4.8}$$

A	B	A AND B	min(A,B)	A OR B	max(A,B)	NOT A	1 - A
0	0	0	0	0	0	1	1
0	1	0	0	1	1	1	1
1	0	0	0	1	1	0	0
1	1	1	1	1	1	0	0

Table 4.1: Truth-tables for the standard *AND*, *OR* and *NOT* boolean operations and their equivalent fuzzy operations.

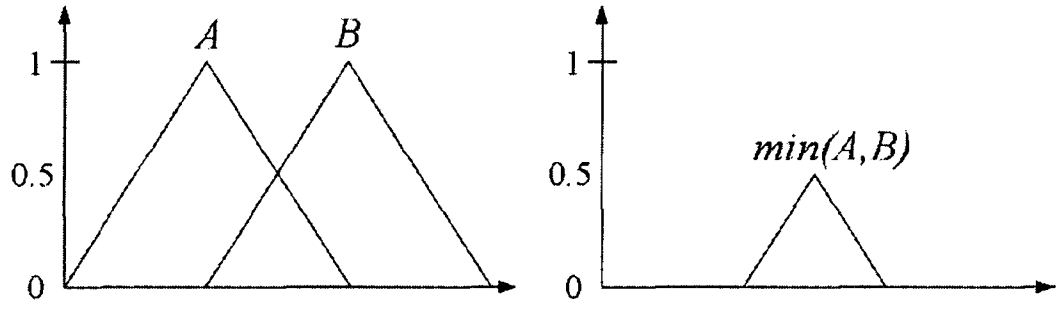

Figure 4.4: Result of the *min* operation on inputs *A* and *B* i.e. *min(A, B)*.

When the firing strength of each rule is known, the consequent of each fuzzy rule can be found and a final crisp output obtained through aggregation of the consequents. However, there are a number of different ways in which the consequent of each rule

can be inferred from the antecedent depending on the type of fuzzy reasoning employed including (Jang 1993):

- Type 1: The consequent of each fuzzy rule assigns an entire fuzzy set to the output (found by applying the *min* operation to the firing strength and the output membership function of each rule). The overall fuzzy output is derived by applying the *max* operation to the qualified fuzzy outputs of all the rules. Several schemes have been proposed to choose the final crisp output based on the overall fuzzy output with perhaps the most popular being the centroid of the area.

- Type 2: In a Sugeno-type system (Sugeno 1985), the output of each rule is a linear combination of input variables plus a constant term. The final output is the weighted average of each rule's output. Thus, in this type of system, fuzzy sets are only involved in the antecedent part of the 'if-then' rules.

4.2 Fuzzy Inference System

The block diagram of Figure 4.5 (Jang 1993) is representative of the first type of fuzzy inference (Type 1) described in Section 4.1. It is also known as Mamdani's fuzzy inference method (Mamdani 1975). Essentially, the term 'fuzzy inference' refers to the process of formulating the mapping from a given crisp input to a crisp output using Fuzzy Logic (Fuzzy Logic Toolbox Users Guide 2000).

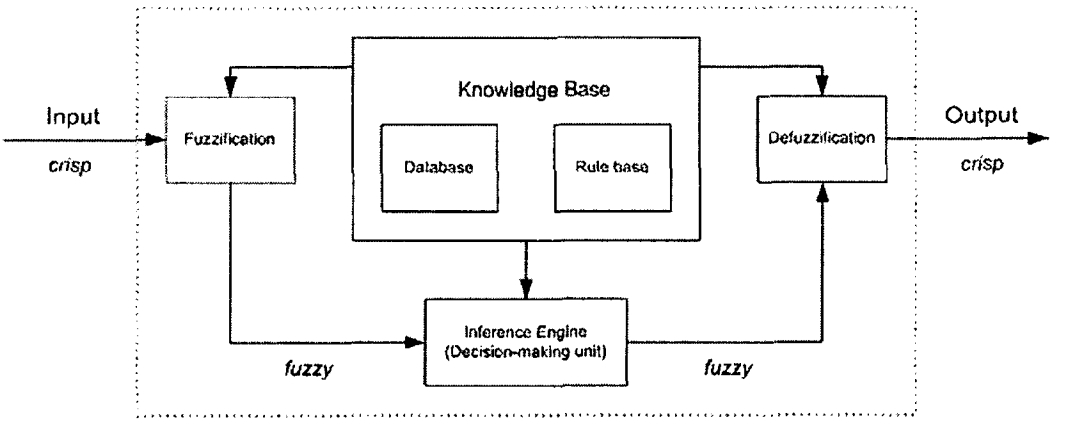

Figure 4.5: Block diagram of a Fuzzy Inference System.

The Fuzzy Inference System (FIS) comprises five main functional blocks (Jang 1993). These are the following:

- Rule base: The rule base contains a set of fuzzy 'if-then' rules that are developed using the experience and knowledge of an 'expert'.

- Database: The database contains the information that defines the membership functions of the fuzzy sets used in the fuzzy rules.

- Fuzzification: The fuzzification block takes input signals (crisp quantities with numerical values) and transforms them into fuzzy quantities. Essentially, this block determines the degree to which each input belongs to each of the appropriate fuzzy sets using the antecedent membership functions.

- Inference engine: This is the decision-making kernel of the FIS. The inference engine evaluates the set of 'if-then' rules with each rule producing a fuzzy quantity.

- Defuzzification: This block transforms the fuzzy results from the inference engine into a nonfuzzy crisp output using the consequent membership functions.

The Mamdani fuzzy inference process represented by the block diagram of Figure 4.5 is the most commonly employed fuzzy inference method (Fuzzy Logic Toolbox User's Guide 2000). However, another popular method of fuzzy inference is that introduced by Sugeno (Sugeno 1985). The Sugeno-type of fuzzy inference (Type 2 as described in Section 4.1) is similar to the Mamdani-type in many respects with the fuzzification of inputs and application of the fuzzy operators identical for both systems. However, the output membership functions for a Sugeno-type FIS are linear or constant. A first order Sugeno-type FIS has rules of the form:

$$if\ x\ is\ A\ and\ y\ is\ B\ then\ z = p*x + q*y + r \tag{4.9}$$

where A and B are fuzzy sets in the antecedent while p, q and r are all constants resulting in a consequent part that is described by a nonfuzzy equation of the input variables x and y. The Sugeno-type system is computationally more efficient than a Mamdani-type system and so the Sugeno-type system is better suited to the use of adaptive techniques for constructing fuzzy models. These adaptive techniques can be used to tune the membership functions to best model a set of input-output data. Such an adaptive technique is the Adaptive Neuro-Fuzzy Inference System (ANFIS), developed by Jang (Jang 1993), that is described in Section 4.3.

4.3 ANFIS

Consider an input-output data set obtained from a system whose behaviour it is desired to model using a FIS. Since any membership function is defined by its associated parameters, the accuracy of the modeling attempt for a given data set relies on the particular membership function shapes chosen (triangular, trapezoidal, bell-shaped etc.) as well as their individual associated parameters. Rather than choosing the parameters associated with a given membership function arbitrarily, adaptive neuro-fuzzy techniques enable the computation of membership function parameters that best allow the FIS to model/track the input-output data.

One such neuro-fuzzy technique that enables system modeling is ANFIS. ANFIS is similar to many other system identification techniques. Firstly, a parameterised model structure is defined. In the case of ANFIS, this involves choosing initial membership functions, defining the 'if-then' rules etc. The next step involves collecting a set of input-output training data from the system to be modeled. Finally, ANFIS is employed to train the FIS to emulate the training data by modifying the membership function parameters until the desired minimum modeling error has been achieved (Fuzzy Logic Toolbox Users Guide 2000). A block diagram of the ANFIS architecture for a two-input, two-rule first-order Sugeno model is shown in Figure 4.6 (Hynes 1997). To reflect different adaptive capabilities, both square and circular nodes are used in the block diagram of the ANFIS architecture. A square node has parameters associated with it (which can be updated during the training procedure) while a circular node has no parameters associated with it.

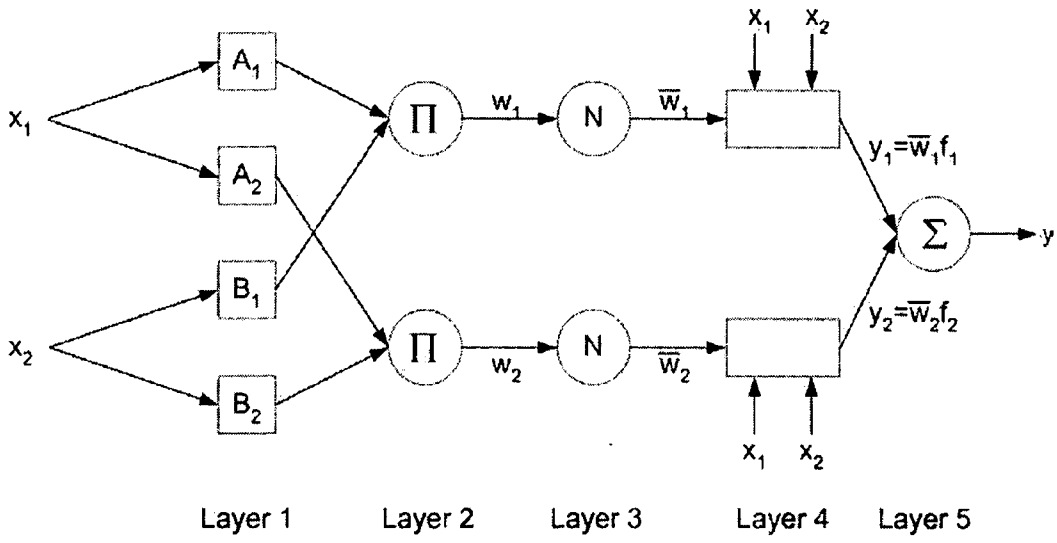

Figure 4.6: ANFIS architecture for a two-input, two-rule first-order Sugeno model.

As can be seen, the FIS shown in Figure 4.6 has two inputs, x_1 and x_2, and one output, y. The rule base contains two Sugeno-type fuzzy 'if-then' rules whose outputs sum to produce the overall output:

$$\begin{aligned} &\textit{Rule } 1: \quad \textit{if } x_1 \textit{ is } A_1 \textit{ and } x_2 \textit{ is } B_1 \textit{ then } y_1 = \overline{w}_1(p_1 * x_1 + q_1 * x_2 + r_1) \\ &\textit{Rule } 2: \quad \textit{if } x_1 \textit{ is } A_2 \textit{ and } x_2 \textit{ is } B_2 \textit{ then } y_2 = \overline{w}_2(p_2 * x_1 + q_2 * x_2 + r_2) \end{aligned} \tag{4.10}$$

Thus, the ANFIS architecture consists of two parameter sets that may be trained:

1) The antecedent membership function parameters [eg. $\{a, b, c\}$ for a triangular membership function]
2) The consequent parameters [$\{p, q, r\}$]

The ANFIS training procedure employs a gradient descent algorithm to optimise the antecedent parameters and a least squares algorithm to tune the consequent parameters. Since two different algorithms are employed in the system modeling, the training rule is often called a hybrid training rule. The consequent parameters are updated first using a least-mean-squared error type algorithm and the antecedent parameters are then updated by backpropagating the errors that still remain (Hynes 1997).

The ANFIS architecture consists of five layers (clearly labelled in Figure 4.6) with the output of the nodes in each respective layer represented by O_i^m where i is the *ith* node of layer m. All nodes in the same layer have the same functionality. The functionality of the nodes in each layer is described now [(Jang 1993) and (Hynes 1997)].

Layer 1: Generate the membership grades

$$O_i^1 = \mu^{A_i}(x_1) \tag{4.11}$$

O_i^1 is the membership function of A_i and it specifies the degree to which the input x_1 is a member of the fuzzy set A_i. If $\mu^{A_i}(x_1)$ is chosen to be a triangular membership function, for example, with the antecedent parameter set $\{a, b, c\}$, then as the training proceeds and the parameters change, the triangular shape also varies accordingly.

Layer 2: Generate the firing strengths

Each node in this layer applies a fuzzy operator to the inputs (the membership grades outputted from layer 1) with the output, w_i, representing the firing strength of each rule. The generalised *AND* operation can be performed using the *min* function as follows:

$$O_i^2 = w_i = min\left(\mu^{A_i}(x_1), \mu^{B_i}(x_2)\right) \tag{4.12}$$

Layer 3: Normalise the firing strengths

Each node in this layer calculates the ratio of the firing strength of the *ith* rule to the sum of all the rules' firing strengths. The output is called the normalised firing strength.

$$O_i^3 = \overline{w}_i = \frac{w_i}{w_1 + w_2} \tag{4.13}$$

Layer 4: Calculate the rule outputs based on the consequent parameters

The consequent part of each rule is described by a nonfuzzy equation of the input variables x_1 and x_2. In layer 4, the rule outputs are calculated using the consequent parameters $\{p_i, q_i, r_i\}$.

$$O_i^4 = y_i = \overline{w}_i f_i = \overline{w}_i(p_i x_1 + q_i x_2 + r_i) \tag{4.14}$$

Layer 5: Sum all the inputs from layer 4

In layer 5, the overall output is computed as the summation of all the rule outputs from layer 4 (linear combination of the consequent parameters), i.e.,

$$O_1^5 = y = \sum y_i = \sum \overline{w}_i f_i \tag{4.15}$$

$$O_1^5 = y = (\overline{w}_1 x_1)p_1 + (\overline{w}_1 x_2)q_1 + \overline{w}_1 r_1 + (\overline{w}_2 x_1)p_2 + (\overline{w}_2 x_2)q_2 + \overline{w}_2 r_2 \tag{4.16}$$

It is the last layer (layer 5) that enables solution of the consequent parameters using a least squares algorithm. Equation (4.16) can be expressed in matrix form as:

$$y = \begin{bmatrix} \overline{w}_1 x_1 & \overline{w}_1 x_2 & \overline{w}_1 & \overline{w}_2 x_1 & \overline{w}_2 x_2 & \overline{w}_2 \end{bmatrix} \begin{bmatrix} p_1 \\ q_1 \\ r_1 \\ p_2 \\ q_2 \\ r_2 \end{bmatrix} = \mathbf{X}\,\mathbf{W} \tag{4.17}$$

A least squares regression technique is used to solve for the weight vector, **W**. Thus, for each training epoch, $\overline{w}_1$ and $\overline{w}_2$ are calculated. Equation (4.17) is then used to solve for the consequent parameters. The rule outputs are then calculated using the new updated consequent parameters and the error signals are propagated back through the layers to update the antecedent parameters (using a gradient descent algorithm) (Hynes 1997).

4.4 Basics of the proposed torque ripple minimisation approach

For servo-type applications or smooth control of the SRM at low speeds, torque ripple minimisation is desired. Consider then a current-regulated speed control loop implemented using a PI controller. During steady-state operation of the SRM, if the speed is constant and equal to the reference speed then the current reference control signal produced by the PI controller, I_{PI}, will be a constant current value. However, due to the inherent nonlinearity of the SRM's magnetic characteristics, a constant current reference produces an output torque profile with considerable ripple. Thus,

any method employed to reduce the torque ripple requires careful profiling/shaping of the phase current waveforms.

One possible approach is to add a compensating signal, I_{COMP}, to the constant current reference produced by the PI controller. Thus, the final reference signal employed in the current control stage (current hysteresis, delta modulation etc.) should be such that the torque ripple is minimised. Figure 4.7 illustrates the basic idea. In the method outlined in this chapter, the ANFIS system is used to determine the compensating current signal. Three distinct approaches for training the compensator and its subsequent incorporation into the SR drive are described. The efficacy of each approach is tested through simulation.

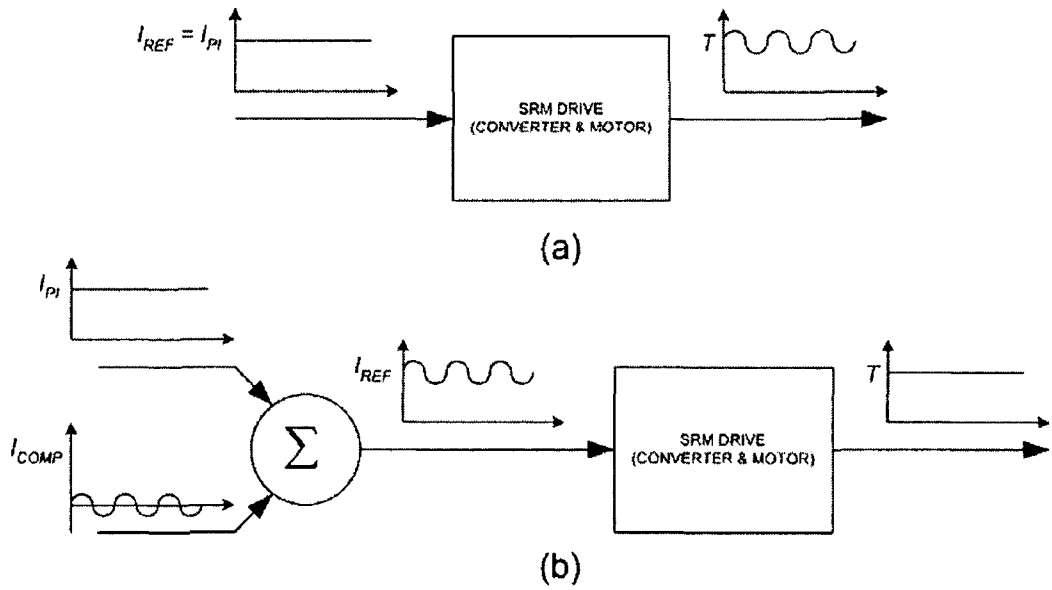

Figure 4.7: Effect of adding a compensating current signal to the output reference signal produced by the PI controller. **(a)** Constant $I_{REF} = I_{PI}$ produces significant torque ripple. **(b)** I_{REF} consisting of constant I_{PI} and the compensating signal I_{COMP} produces a ripple-free torque profile.

4.5 Neuro-fuzzy control strategy no. 1

As described in Section 4.4, the control approach involves the addition of a compensating signal to the output of a PI controller in a current-regulated speed control loop. It is known that the torque ripple can be reduced by accurately controlling the shape of the current pulse applied to each phase of the SRM. Thus, the

compensating signal is the required modification to the current control signal from the PI controller necessary to produce a reduced-ripple torque profile. The compensating signal is necessary because, in steady-state operation with a constant output from the PI controller, the torque profile will have significant ripple. The compensating signal profile is trained via the ANFIS neuro-fuzzy system prior to normal SRM operation.

For this control strategy, it is proposed to train the compensator off-line by passing three parameters obtained from steady-state operation of the SRM to the ANFIS system - torque, T, PI controller output current signal, I_{PI}, and rotor position information, θ. The aim of the compensator training is to enable determination of the current required to produce a specific torque at a specific position. Hence, the data is passed to the ANFIS system in such a manner that the torque and rotor position information are interpreted as inputs and the PI controller current signal is interpreted as an output as shown in Figure 4.8. The data is subsequently modeled until an acceptable error limit is reached.

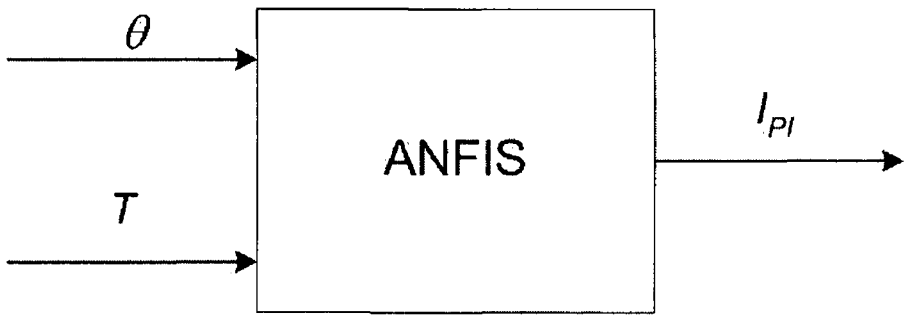

Figure 4.8: Block diagram of the neuro-fuzzy compensator training method.

Once trained, the neuro-fuzzy compensator is incorporated into the SR drive. During subsequent operation of the SR drive, the torque ripple (i.e. the torque signal with the dc component removed), T_{RIPPLE}, and the rotor position, θ, are inputted to the compensator, which produces the required compensating current signal to be added to the PI controller current signal. A block diagram of the proposed neuro-fuzzy torque ripple minimisation control strategy is shown in Figure 4.9.

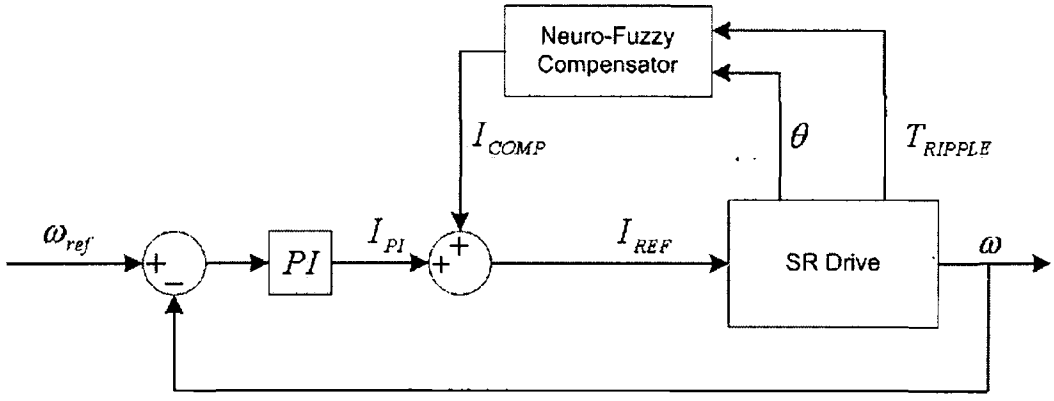

Figure 4.9: Block diagram of the neuro-fuzzy torque ripple minimisation control strategy no. 1.

This neuro-fuzzy torque ripple minimisation control strategy is suitable for use with SRMs whose torque-current-position characteristics are mildly nonlinear. This is because, for any particular combination of torque ripple and rotor position, the compensator outputs the same compensating current signal value regardless of the average torque value. Furthermore, a high sampling rate is required to enable the compensator to react to the constantly changing torque ripple and output the appropriate compensating current signal.

4.6 Simulation results for control strategy no. 1

MATLAB/Simulink was used for all of the simulation work. A 6/4 three-phase SRM model and a 12/8 three-phase SRM model (both of which were based on the model developed by Roux et al. (Roux 2000)) were used to verify the efficacy of the proposed torque ripple minimisation approach. The 6/4 three-phase SRM model was first introduced in Chapter Three. The nominal parameters of the 12/8 three-phase SRM model are shown in Table 4.2. These parameters are identical to those of the experimental SRM, which is described in detail in Section 5.1. The control strategy was implemented for two SRMs to demonstrate its ability to reduce torque ripple in machines with different configurations and magnetic characteristics. For the control implementations described in the following sections, two modes of control were employed for the production of the gate signals for the power converter. These were current control and voltage control. Each phase conduction interval is divided into three regions. During the torque production interval, the current is regulated using delta modulation control, a variation of hysteresis control. With delta modulation, the

phase winding is demagnetised when the phase current rises above the current reference value and is energised when the phase current falls below the current reference value. During the commutation stage (of which there are two intervals), voltage control of the phase is employed. During the first commutation interval, a zero voltage is applied to the phase. This enables torque to build up in the next phase. During the second commutation interval, a negative voltage is applied to the phase. This rapidly suppresses the current to zero thereby avoiding the production of negative torque.

Parameter	Value
model number	H55BMBJL
R_{phase}	2.5Ω
$L_{aligned}$	52 mH
$L_{unaligned}$	9 mH
inertia	1.07×10^{-3} kg-m^2
rated current	2.5 amp
rated voltage	120 volt d.c. bus
stator / rotor poles	12/8
phases	3

Table 4.2: Nominal parameters of the 12/8 three-phase experimental SRM.

4.6.1 6/4 three-phase SRM results for control strategy no. 1

Training data was obtained from simulations of the steady-state operation of a 6/4 three-phase SR drive system. The rule set for the neuro-fuzzy system was initially generated using the grid partition technique. This technique partitions the domains of the input variables into a number of fuzzy sets. A rule is formed by a combination of these fuzzy sets. When the grid partition technique is employed, the rule set covers the entire input space by using all possible combinations of the input fuzzy sets. Five triangular membership functions were chosen for each of the two inputs giving a total of ten antecedent membership functions. Hence, the total number of rules is 5x5 = 25. The torque, PI controller current signal and rotor position information were then passed to the ANFIS system and the neuro-fuzzy system was optimised using the hybrid training technique that incorporates the backpropagation algorithm and the least-mean-squares algorithm. As outlined in Section 4.3, it is the parameters associated with the membership functions that are updated during the learning process. When the training was complete, the membership functions for the rotor

position and the torque were as shown in Figure 4.10 and Figure 4.11. As can be seen in Figure 4.10, the rotor position was in the range 0 - 2π radians.

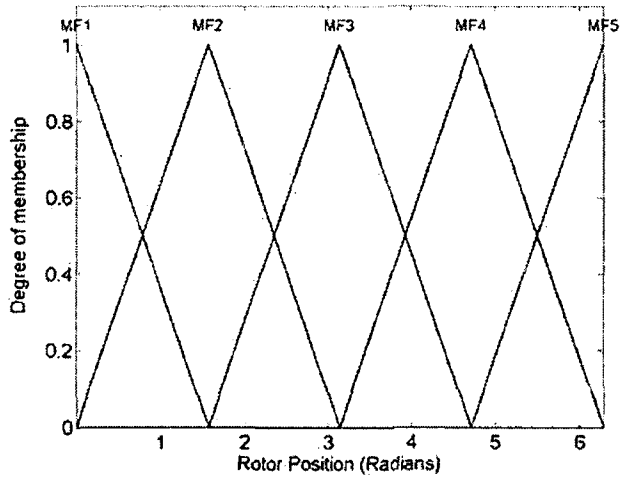

Figure 4.10: Rotor position membership functions.

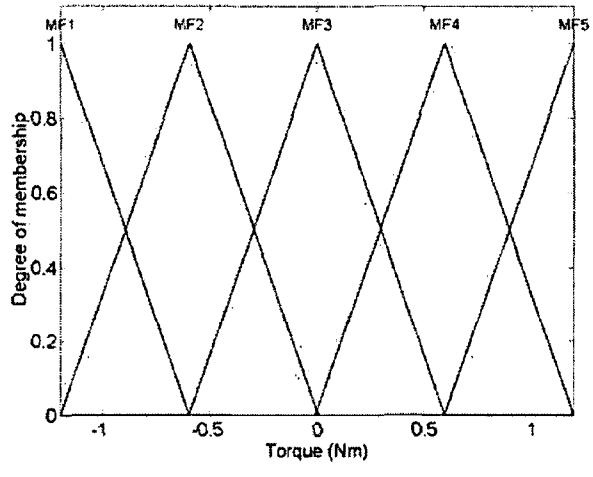

Figure 4.11: Torque membership functions.

Once the neuro-fuzzy compensator was trained, it was incorporated into the SR drive system. For comparison purposes, the system was simulated with and without current compensation for a wide range of values of rotor position and torque ripple. For SR drive operation with current compensation, the compensating current signal produced by the neuro-fuzzy compensator followed the curve shown in Figure 4.12.

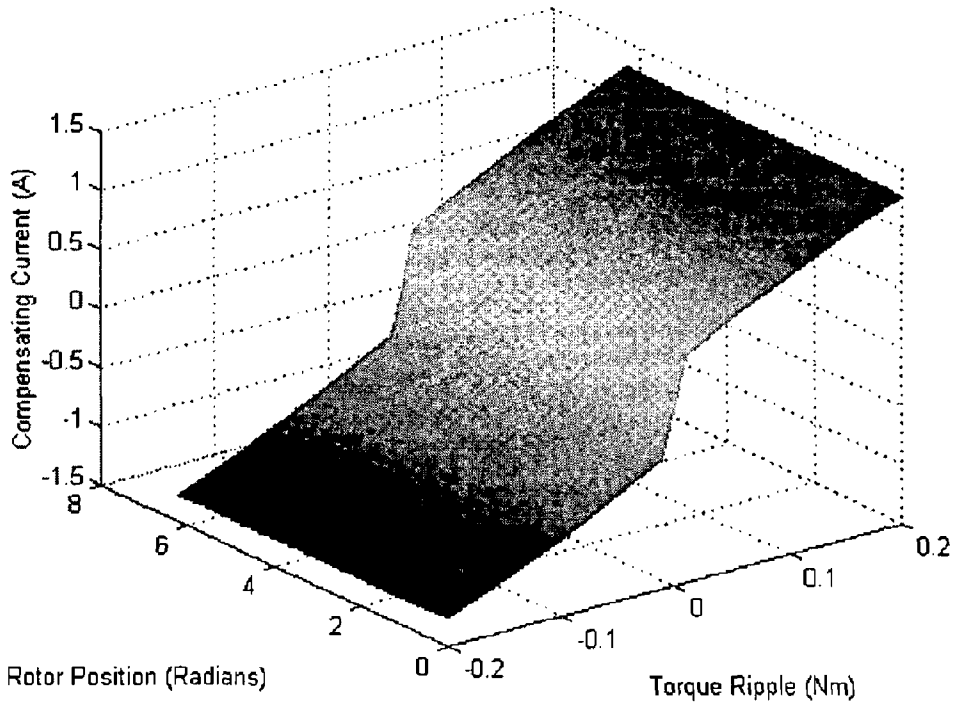

Figure 4.12: Current compensation curve for the 6/4 three-phase SRM

The neuro-fuzzy control strategy was tested for operation under current-regulated speed control implemented using a PI controller. Figure 4.13 shows the currents in phases A and B when the SR drive system was simulated without current compensation. As expected, the current profiles are flat-topped. Figure 4.13 also shows the currents in phases A and B when the neuro-fuzzy compensator was incorporated into the system. As can clearly be seen, the phase current shape is modified due to the addition of the I_{COMP} current compensating signal to the constant PI controller current signal.

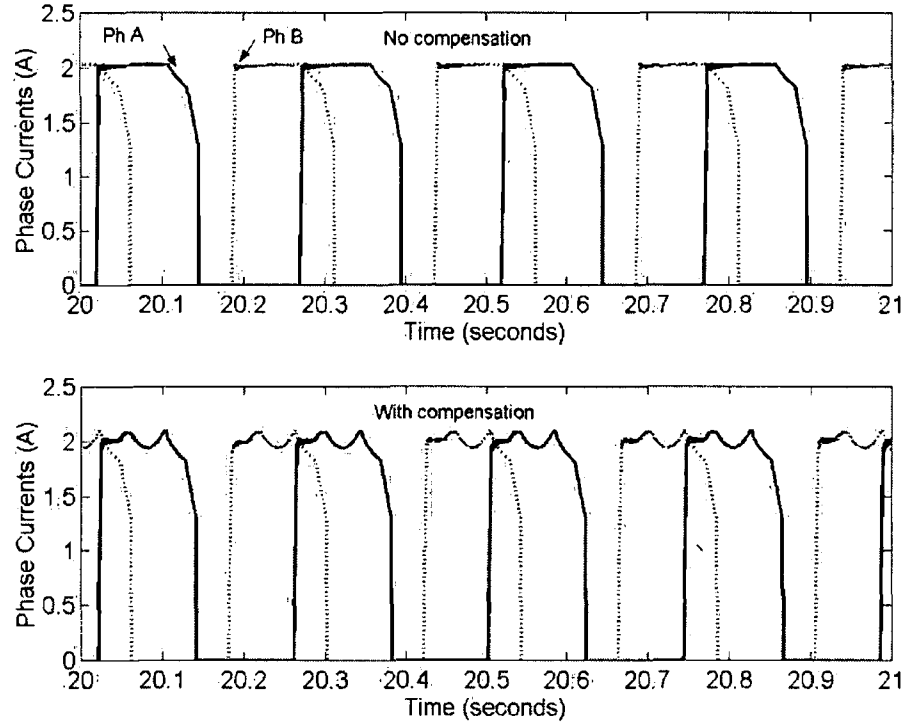

Figure 4.13: Phase currents A and B for steady-state motoring at 60rpm with a 0.5Nm load with and without current compensation.

Figure 4.14 shows the torque produced by each of the three phases of the 6/4 SRM for a load torque of 0.5Nm when there is no current compensation and when the neuro-fuzzy compensator is incorporated into the SR drive. The profiles of the phase torques change when the compensator is employed.

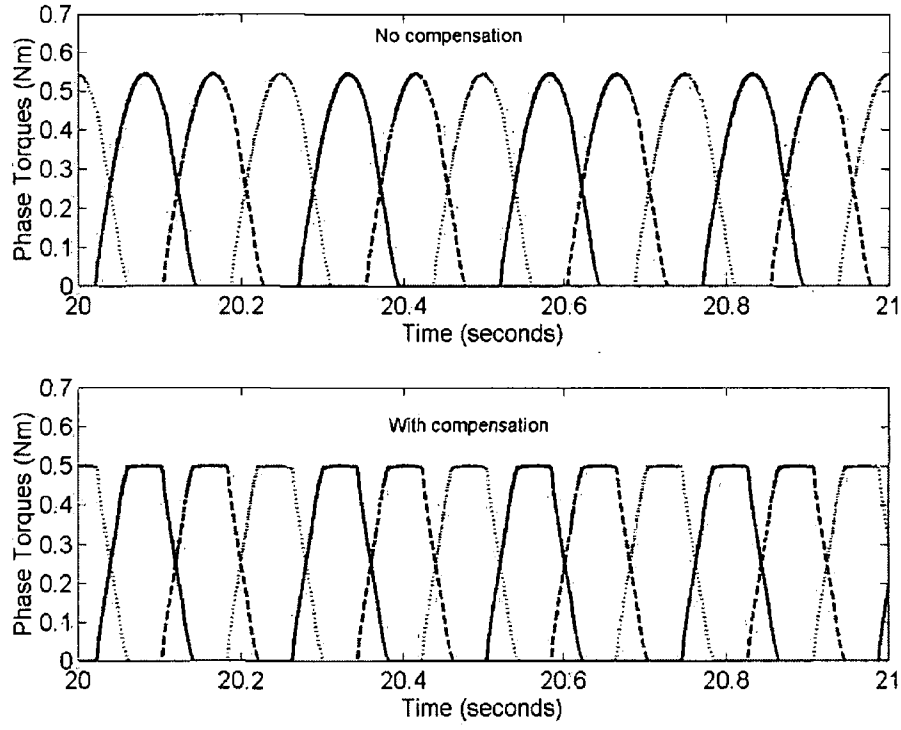

Figure 4.14: Torque in the individual phases for steady-state motoring at 60rpm with a 0.5Nm load with and without current compensation.

The total torque produced by the SRM is the algebraic sum of the individual phase torques. Thus, Figure 4.15 shows the steady-state torque produced by the 6/4 SRM (for a load torque of 0.5Nm) when there is no current compensation. Figure 4.15 also shows the steady-state torque produced by the 6/4 SRM when the neuro-fuzzy compensator is incorporated into the drive. As can clearly be seen, there is a very significant reduction in the torque ripple when the neuro-fuzzy compensator is employed.

A numerical comparison of the ripple on the torque outputs with and without compensation is desired. In (Miller 2001), the variance of the ripple is employed as the performance gauge. In this thesis, the root-mean-squared (rms) error (which is the square root of the variance) is calculated for both sets of data. The rms error is defined as:

$$rms\ error = \sqrt{\frac{\sum_{i=1}^{n} Tripple_i^2}{n}} \tag{4.18}$$

where $Tripple_i$ is the torque ripple at each sample point and n is the total number of samples. $Tripple_i$ is calculated from $T_i - \overline{T}$ where T_i is the torque at each sample point and $\overline{T}$ is the mean torque value. For a load torque of 0.5Nm, the rms error is reduced by slightly less than an order of magnitude, from 0.0242 to 0.0025, when compensation is employed.

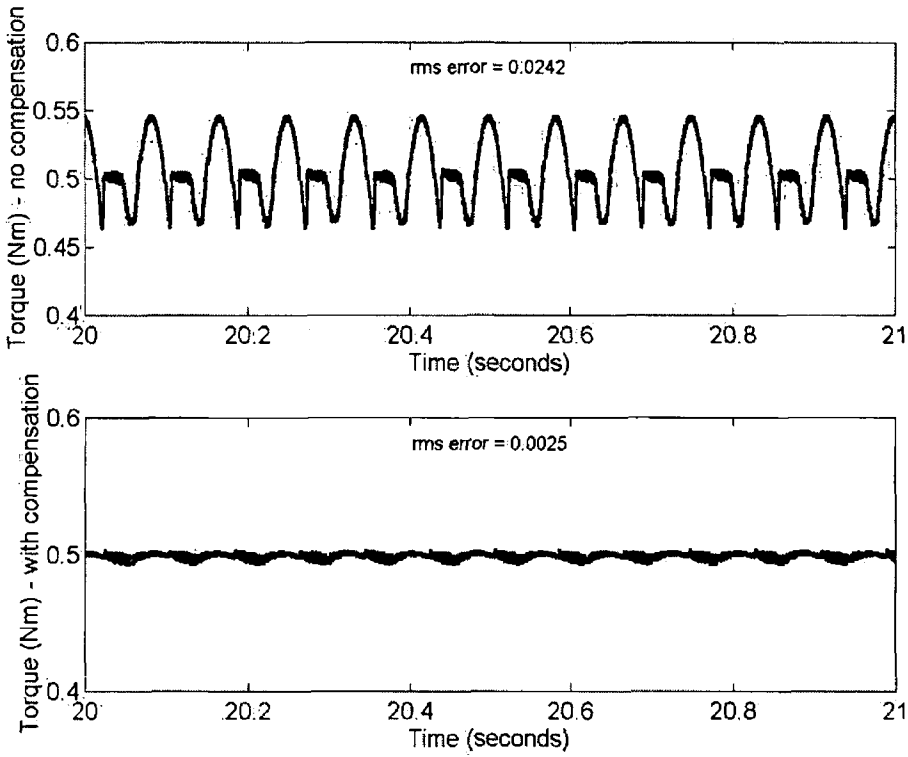

Figure 4.15: Torque produced by the 6/4 SRM for steady-state motoring at 60rpm with a 0.5Nm load with and without current compensation.

4.6.2 12/8 three-phase SRM results for control strategy no. 1

Training data was obtained from simulations of the steady-state operation of the 12/8 three-phase SR drive system. As with the compensator used in the 6/4 SR drive system, the rule set for the neuro-fuzzy system was initially generated using the grid partition technique. Five triangular membership functions were chosen for each input. The torque, PI controller current signal and rotor position information were then passed to the ANFIS algorithm and, as for the 6/4 SRM, the neuro-fuzzy system was optimised using the hybrid training technique that incorporates the backpropagation algorithm and the least-mean-squares algorithm.

Once the neuro-fuzzy system was trained, it was incorporated into the SR drive system. For comparison purposes, the system was simulated with and without current compensation for current-regulated speed control implemented using a PI controller. Figure 4.16 shows the steady-state torque produced by the 12/8 three-phase SRM with and without current compensation for operation at 180rpm with a load of 0.25Nm. As for the 6/4 SRM, there is a very significant reduction in the torque ripple in the 12/8 SRM when the neuro-fuzzy compensator is employed. The rms error, defined in equation (4.18), is reduced from 0.0131 to 0.0017.

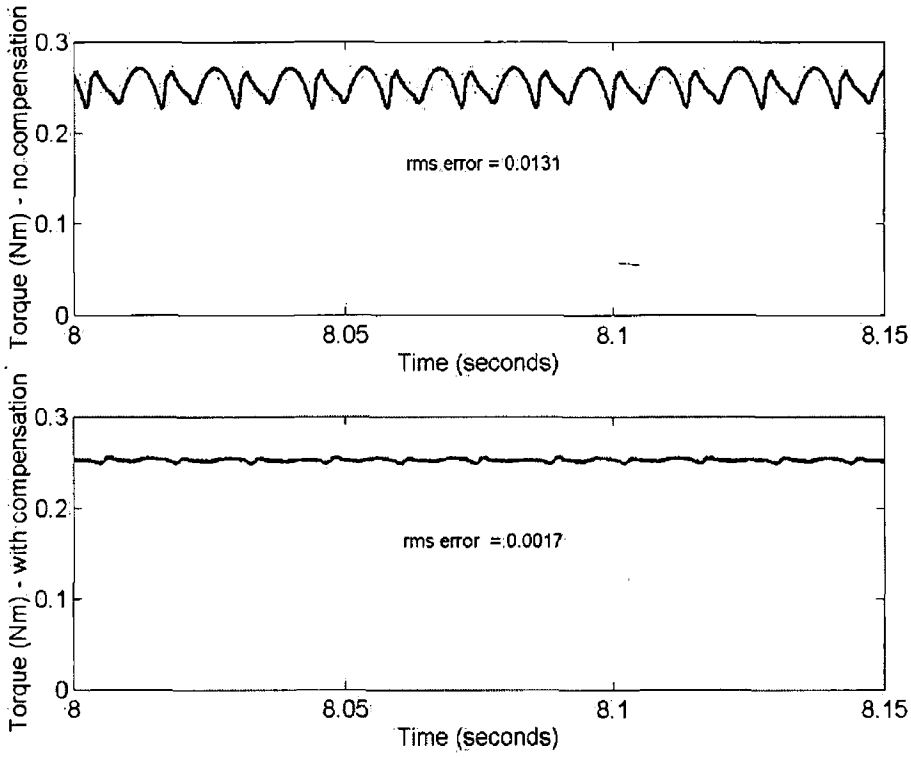

Figure 4.16: The steady-state torque produced by the 12/8 three-phase SRM with and without current compensation for motoring operation at 180rpm with a 0.25Nm load.

4.7 Neuro-fuzzy control strategy no. 2

As with the first torque ripple reduction control scheme, the second neuro-fuzzy control strategy involves the addition of a compensating current signal to the output of the PI controller in a current-regulated speed control loop. The second control scheme also employs the ANFIS system to train the compensating current signal profile. However, the parameters employed in the training are different to those employed in the first control scheme and the manner in which the training is conducted is also

different. Figure 4.17 shows a block diagram of the neuro-fuzzy torque ripple minimisation control strategy no. 2. As can be seen, the neuro-fuzzy compensator selects the appropriate compensating current signal, I_{COMP}, based on the average torque, $T_{AVERAGE}$, and the rotor position, θ.

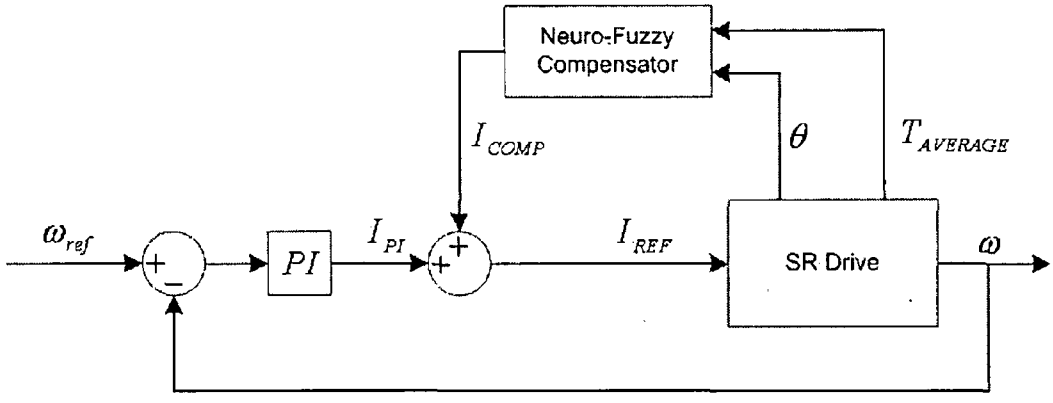

Figure 4.17: Block diagram of neuro-fuzzy torque ripple minimisation control strategy no. 2.

As before, it is proposed to train the neuro-fuzzy compensator using data obtained from steady-state operation of the SR drive. Figure 4.18 shows a basic block diagram of the ANFIS training method.

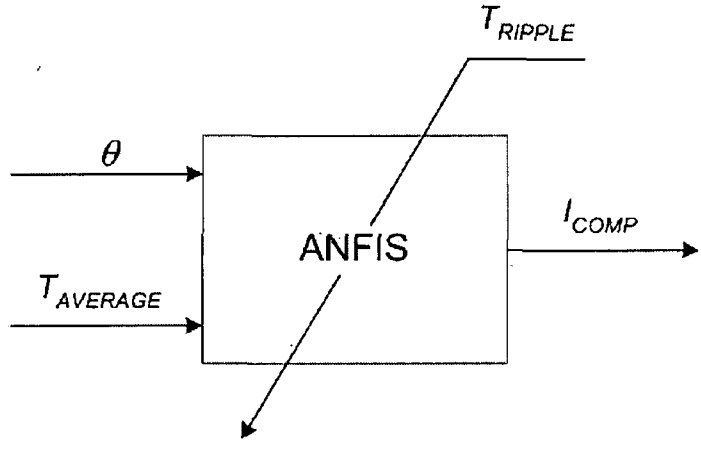

Figure 4.18: Basic block diagram of the ANFIS training method for neuro-fuzzy control strategy no. 2.

The training procedure is initiated by simulation of the SR drive operation in open-loop motoring mode with a constant current reference value and no compensating

current signal. On completion of the first simulation, the following steady-state data is recorded - the average torque, $T_{AVERAGE}$, the rotor position, θ, and the torque ripple, T_{RIPPLE}. The torque ripple is obtained by simply removing the dc component from the total torque value. A vector, whose length is equal to that of each of the three recorded parameter vectors, is then created and initialised to zero. This vector is used to hold the compensating current signal values, I_{COMP}. These are updated throughout the training.

The torque ripple at each rotor position sample point is accurately known. Therefore, at each sample point, the compensating current value is decremented if the torque ripple is greater than zero while the compensating current value is incremented if the torque ripple is less than zero. This produces an updated I_{COMP} data vector that can be employed in the ANFIS training. Essentially then, the torque ripple is the error information that is used to update the compensating current signal. The average torque, rotor position and compensating current signal data is passed to the ANFIS system in such a manner that the average torque and rotor position are interpreted as inputs and the compensating current interpreted as an output as shown in Figure 4.18. The data is modeled and an appropriate FIS is generated. The generated FIS is then incorporated into the SR drive as the neuro-fuzzy compensator. The SR drive is simulated with the compensating current signal generated by the neuro-fuzzy compensator added to the same constant current reference value employed in the original system simulation. The average torque, rotor position and torque ripple are once again recorded. The compensating current signal data vector is further updated according to the T_{RIPPLE} information. The neuro-fuzzy compensator is then trained again using ANFIS and the trained compensator is incorporated into the SR drive for use during the next training iteration. Thus, each training iteration refines the compensating current signal further, resulting in a reduction in the torque ripple during each subsequent SR drive simulation. This training process is repeated until the torque ripple has been reduced below some desired minimum value.

When the torque ripple has been brought within the desired error limits at each rotor position for a particular average torque value, the current reference is incremented, thereby increasing the average torque produced by the SRM, and the entire training

procedure is repeated. This is done for several discrete values of the average torque. The desired compensating current signal is then known for every rotor position at each discrete average torque value. The entire data set is then combined and passed to the ANFIS system and the final neurofuzzy compensator is trained. Figure 4.19 shows a flowchart describing the neuro-fuzzy compensator training procedure. In Figure 4.19, N is an integer that refers to the Nth training iteration. For N=1 (first iteration), the SR drive is simulated without any compensating current signal. However, for N>1, the neuro-fuzzy compensator trained during the previous training iteration is incorporated into the SR drive for system simulation. When the torque ripple is sufficiently small, the current reference is incremented and the training procedure is repeated.

Unlike neuro-fuzzy control strategy no. 1, this control strategy is suitable for employment with an SRM that has strongly nonlinear torque-current-position characteristics. This is because the compensating current signal outputted by the compensator at each rotor position changes with the average torque operating point.

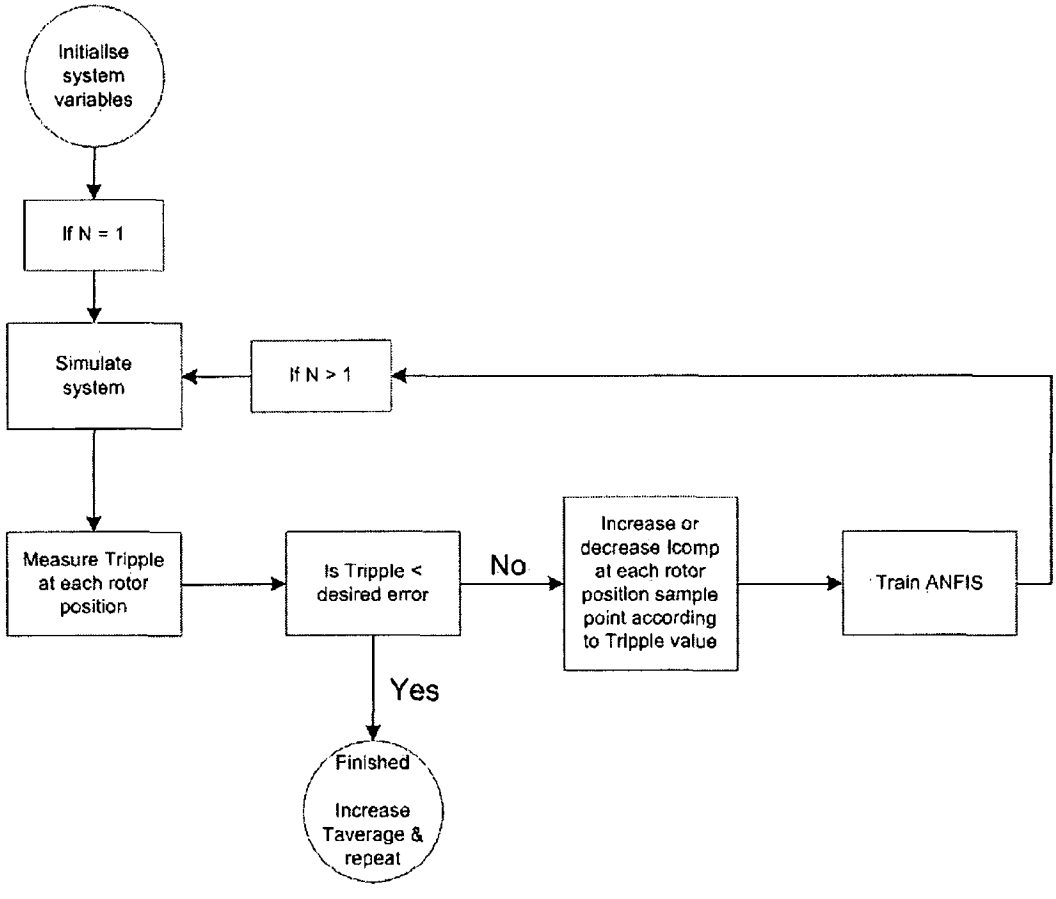

Figure 4.19: Neuro-fuzzy compensator training procedure.

4.8 Simulation results for control strategy no. 2

The control strategy was implemented and tested using the 6/4 three-phase SRM model and the model of the 12/8 three-phase experimental SRM. The method of phase conduction and commutation control described in Section 4.6 was employed in both SRM control implementations.

4.8.1 6/4 three-phase SRM results for control strategy no. 2

The neuro-fuzzy compensator training procedure was implemented for the 6/4 three-phase SR drive. Each phase of a 6/4 three-phase SRM receives four current pulses per revolution. Therefore, the rotor position, θ, employed in the compensator training process was confined to the range 0°-90° (mechanical degrees) and referenced to phase A where 0° represents alignment of a pair of rotor poles with phase A. As the rotor turns through 90°, the next pair of rotor poles reach alignment with phase A and hence the rotor position can be reset to 0°. The average torque was varied by incrementing the current reference in discrete steps of 0.25A between 1A and 2.5A. At each constant average torque value, the appropriate compensating current for each rotor position was determined and the neuro-fuzzy compensator was trained to ensure minimisation of the torque ripple in the manner described in Section 4.7. Finally, all the data was combined to produce an overall neuro-fuzzy compensator. The rule set for the neuro-fuzzy compensator was initially generated using the grid partition technique with fifty trapezoidal membership functions chosen for the rotor position and two trapezoidal membership functions chosen for the average torque. The variation of the compensating current signal with changing rotor position was strongly nonlinear. The nonlinearity in the variation of the compensating current signal with changing average torque was less pronounced. Hence, more membership functions were required to accurately model the variation of the compensating current signal with changing rotor position than with changing average torque. However, it was essentially a process of trial and error in determining the optimal number of membership functions to be used for each input. If the number of membership functions is too small, important relationships contained in the dataset may not be captured in the training process. Alternatively, too many membership functions can lead to overfitting of the data. The neuro-fuzzy compensator was trained using the

hybrid training technique that incorporates the backpropogation algorithm and the least-mean-squares algorithm.

4.8.1.1 Initial tests – constant current reference

For comparison purposes, the system was simulated with and without current compensation for open-loop SR motoring operation with a constant current reference of 1.75A. Figure 4.20 shows the torque produced by the 6/4 three-phase SRM without current compensation, with current compensation after two training iterations and with current compensation after eight training iterations. As can be seen, after just two training iterations, the torque ripple was drastically reduced with the rms error decreasing from 0.0181 to 0.0051. After eight training iterations, the torque ripple had decreased below the error limits and the training was halted. It is clear that using the neuro-fuzzy compensator results in a large reduction in the torque ripple with the final rms error measurement for the fully trained compensator equal to 0.0024.

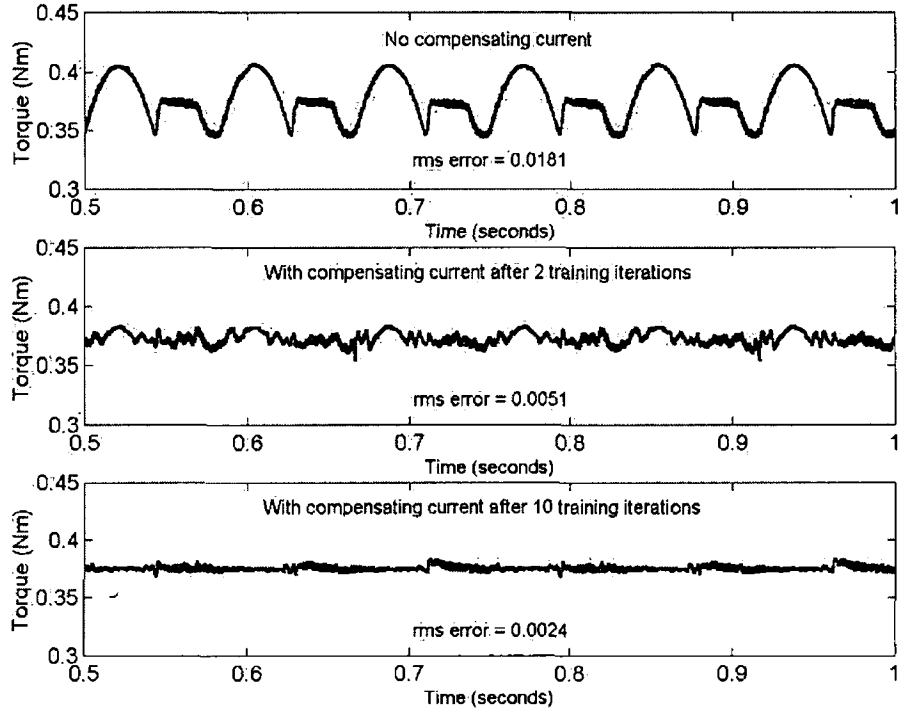

Figure 4.20: The torque produced by the 6/4 three-phase SRM without current compensation, with current compensation after two training iterations and with current compensation after eight training iterations for open-loop motoring operation with a constant current reference of 1.75A.

Figure 4.21 shows the phase currents and corresponding phase torques produced by the 6/4 SRM for open-loop motoring operation with a constant current reference of 1.75A without current compensation while Figure 4.22 shows the same waveforms with current compensation. When the neuro-fuzzy compensator is employed, the phase current shape is no longer flat-topped. As can be seen in Figure 4.22, the addition of a suitable compensating current results in flat-topped phase torque profiles. The compensating current signal that is added to the 1.75A constant reference during steady-state operation is plotted against rotor position in Figure 4.23.

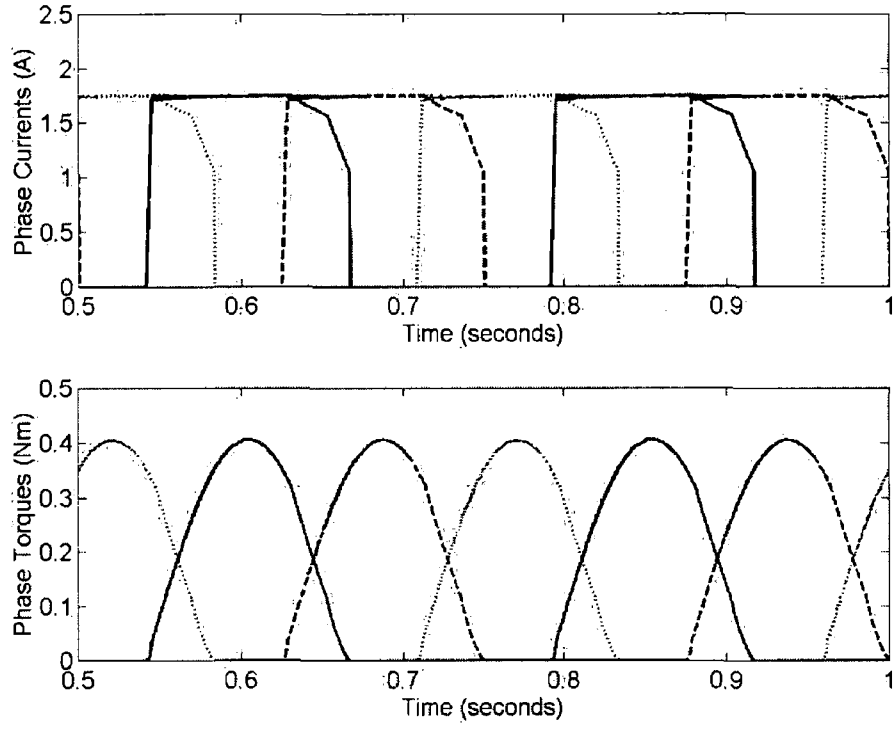

Figure 4.21: The phase currents and corresponding phase torques produced by the 6/4 SRM for open-loop motoring operation with a constant current reference of 1.75A without current compensation.

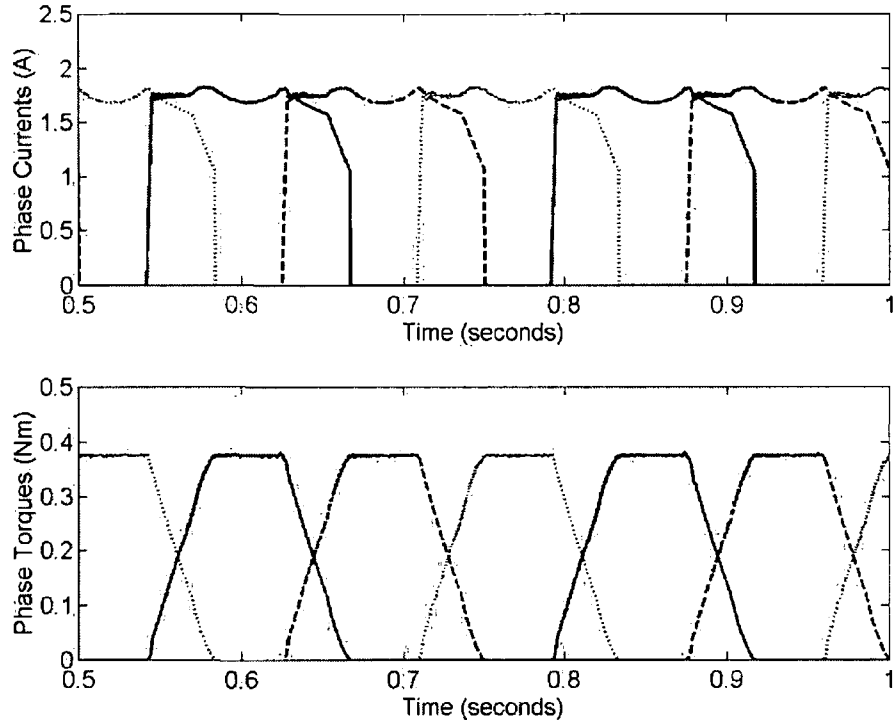

Figure 4.22: The phase currents and corresponding phase torques produced by the 6/4 SRM for open-loop motoring operation with a constant current reference of 1.75A with current compensation.

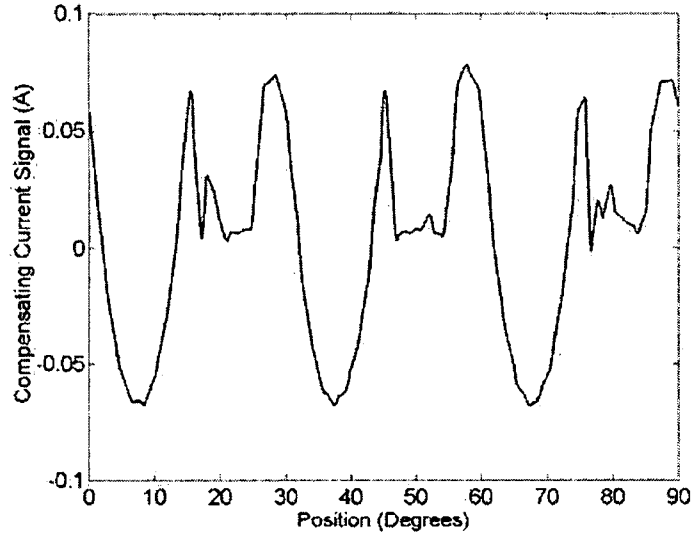

Figure 4.23: The compensating current signal produced by the neuro-fuzzy compensator for open-loop motoring operation of the 6/4 SRM with a constant current reference of 1.75A.

4.8.1.2 PI speed control tests

In Section 4.8.1.1, the neuro-fuzzy compensator was tested with the SR drive operating in open-loop motoring mode with a constant current reference. For further testing, the neuro-fuzzy compensator was incorporated into the SR drive operated under current-regulated speed control implemented using a PI controller. The PI controller was tuned manually. The resultant constants were P = 0.3 and I = 0.1. Once again, the system was simulated with and without current compensation to enable suitable comparison. For SR drive operation with current compensation, the compensating current signal produced by the neuro-fuzzy compensator followed the curve shown in Figure 4.24.

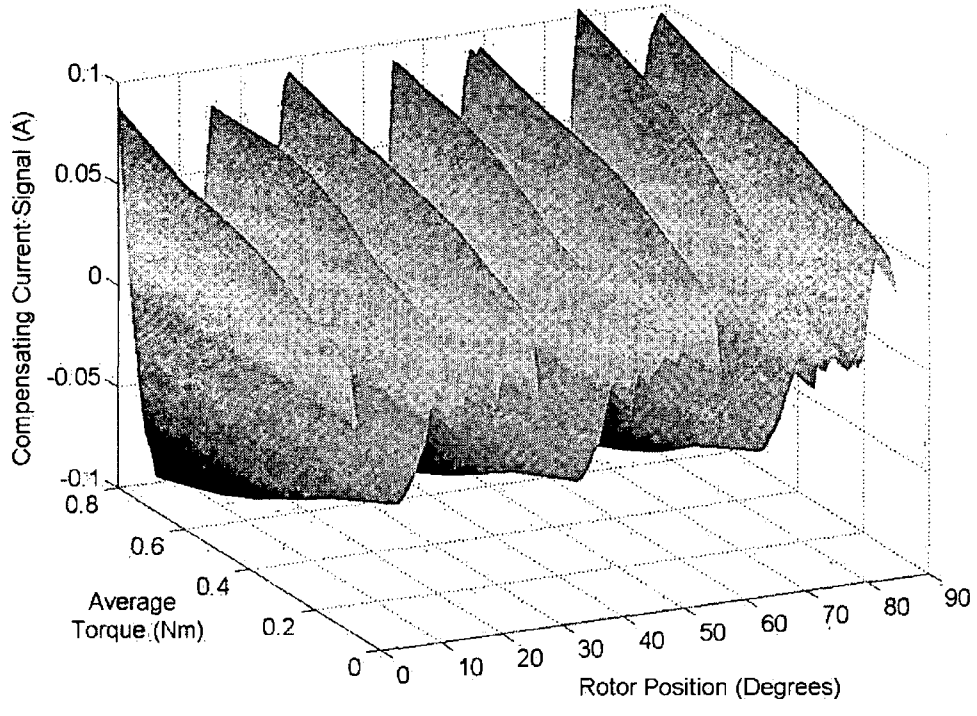

Figure 4.24: Current compensation curve for the 6/4 three-phase SRM.

The SR drive system was simulated with and without compensation for a load torque of T_L = 0.5Nm and with a reference speed of ω_{ref} = 60rpm. Figure 4.25 shows the steady-state torque produced by the 6/4 SRM with and without current compensation. As expected, when the neuro-fuzzy compensator is employed, a significant decrease in the torque ripple is observed. Figure 4.26 shows the phase currents and phase torques without current compensation during steady-state motoring operation. The

phase currents are controlled around the almost constant PI controller output signal using delta modulation current control. The torque profile has considerable ripple. Figure 4.27 shows the phase currents and phase torque profiles when the neuro-fuzzy compensator is incorporated into the SR drive. The shape of the current waveforms is such that flat-topped phase torques are produced. The torque ripple rms error is reduced from 0.0242 to 0.0033 when compensation is employed.

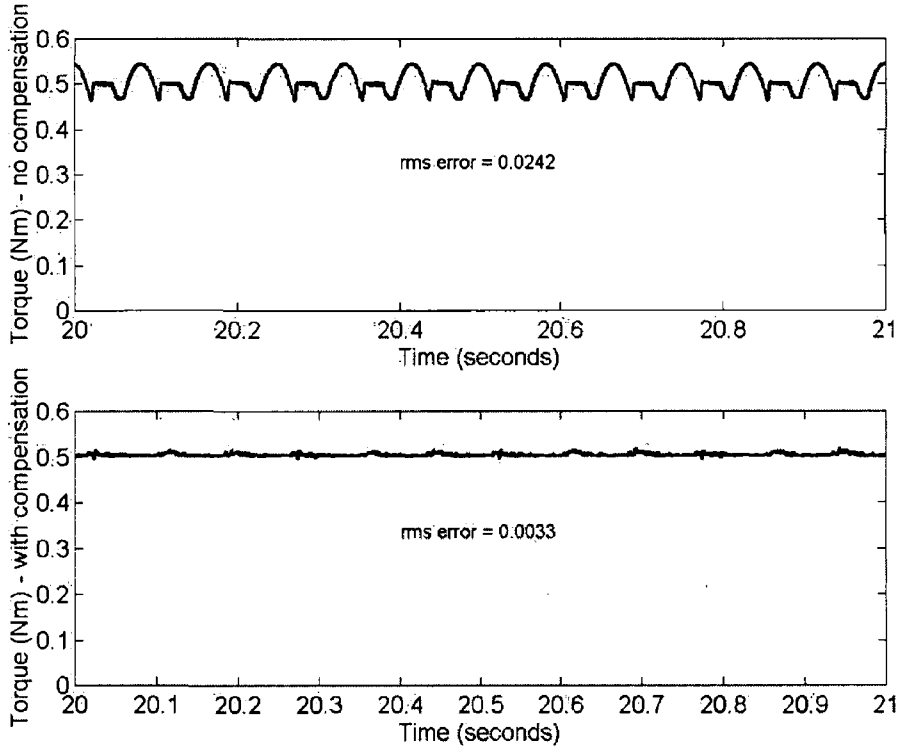

Figure 4.25: Torque produced by the 6/4 SRM with and without compensation for operation at 60rpm with a load torque of 0.5Nm.

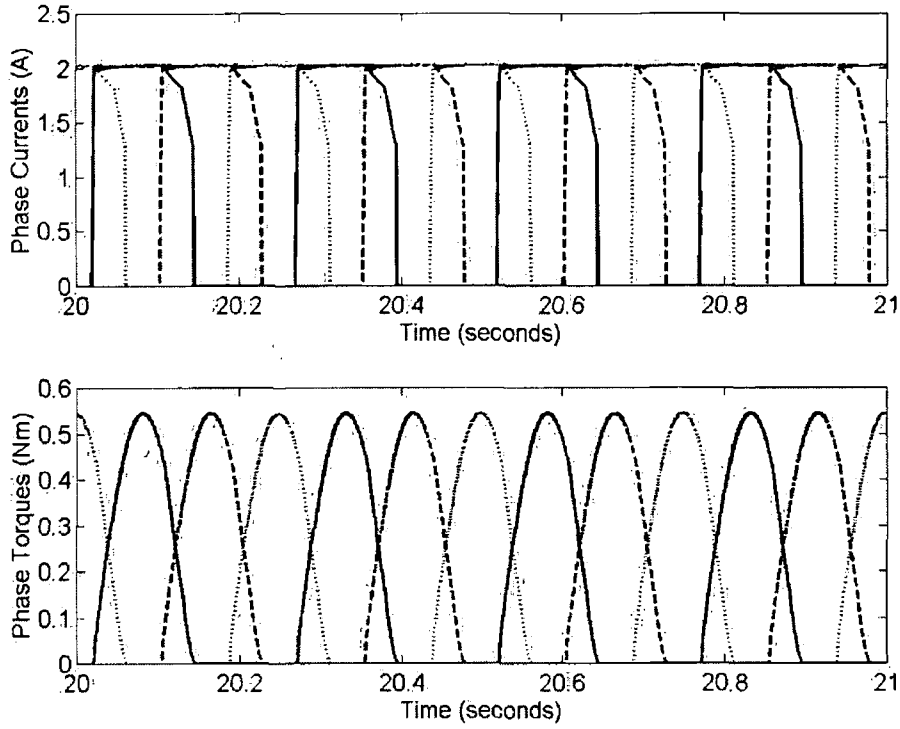

Figure 4.26: The phase currents and phase torque profiles for steady-state motoring operation at 60rpm with a 0.5Nm load without current compensation.

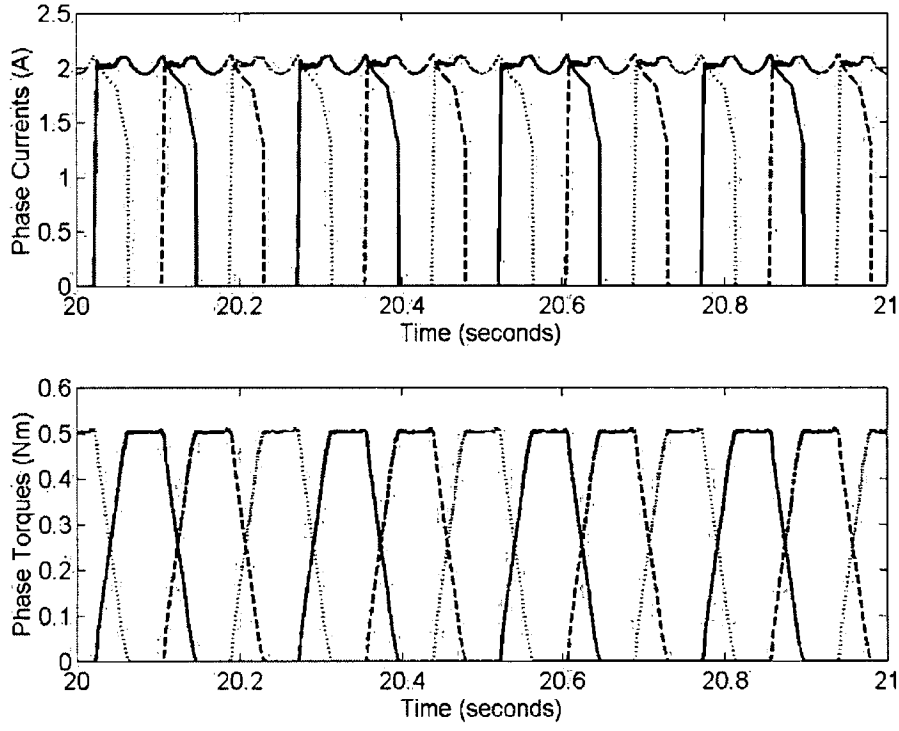

Figure 4.27: The phase currents and phase torque profiles for steady-state motoring operation at 60rpm with a 0.5Nm load with current compensation.

Figure 4.28 shows the PI controller output signal, the compensating current signal produced by the neuro-fuzzy compensator and the current reference used by the delta modulation current controller for steady-state motoring operation at 60rpm with a 0.5Nm load. The PI controller output signal is approximately constant in steady-state since the motor speed is essentially constant and equal to the reference speed. However, there is a small speed ripple and hence there is a small ripple on the PI controller output signal as well. The final current reference is the sum of the PI controller output current signal and the compensating current signal from the neuro-fuzzy compensator.

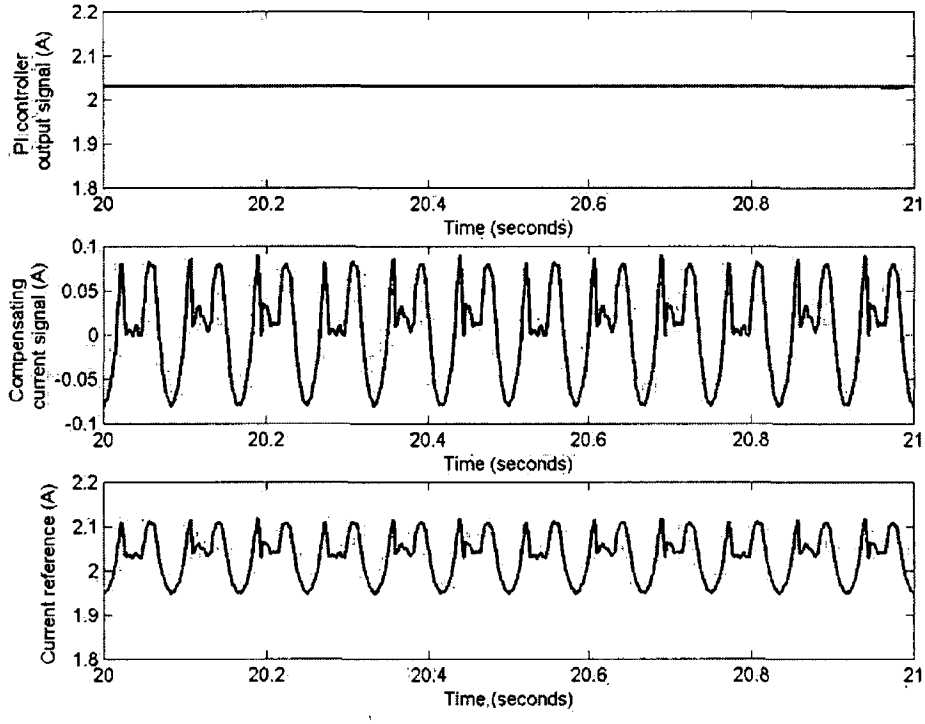

Figure 4.28: The PI controller output current signal, the compensating current signal produced by the neuro-fuzzy compensator and the final current reference used by the delta modulation current controller for steady-state motoring operation at 60rpm with a 0.5Nm load.

4.8.2 12/8 three-phase SRM results for control strategy no .2

The neuro-fuzzy control strategy was implemented in MATLAB/Simulink for the 12/8 three-phase SRM model whose parameters are shown in Table 4.2. The rotor position, θ, employed in the compensator training process was confined to the range 0°-45° (mechanical degrees) since each phase of the 12/8 three-phase SRM is excited eight times per revolution. The rotor position was referenced to phase A with 0° representing alignment of a pair of rotor poles with phase A. The average torque was varied by incrementing the current reference in discrete steps of 0.5A between 1A and 3A and the compensating current signal was trained. The training data obtained at each average torque setpoint was then integrated into an overall data set, which was employed in the training of the neuro-fuzzy compensator. The rule set for the neuro-fuzzy compensator was initially generated using the grid partition technique with one hundred trapezoidal membership functions chosen for the rotor position and two

trapezoidal membership functions chosen for the average torque. The neuro-fuzzy compensator was trained using the hybrid training technique that incorporates the backpropogation algorithm and the least-mean-squares algorithm.

4.8.2.1 Initial tests – constant current reference

The 12/8 SR drive was simulated with and without current compensation for open-loop SR motoring operation with a constant current reference of 2A. Figure 4.29 shows the torque produced by the 12/8 three-phase SRM without current compensation (rms error = 0.017), with current compensation after two training iterations (rms error = 0.0062) and with current compensation after ten training iterations (rms error = 0.0016). Figure 4.29 clearly demonstrates the reduction of the torque ripple as the training of the neuro-fuzzy compensator advances. After the tenth training iteration, the torque ripple had reduced below the desired error limit and the training was halted. Figure 4.30 shows the compensating current signal produced by the neuro-fuzzy compensator for open-loop motoring operation of the 12/8 SRM with a constant current reference of 2A. This compensating current signal is the required modification to the 2A constant reference necessary to produce flat-topped phase torque profiles and, consequently, a ripple-free total torque profile. The effect of the compensating current signal on the phase current waveform and on the phase torque produced is demonstrated in Figures 4.31 and 4.32. Figure 4.31 shows the phase currents and corresponding phase torques produced by the 12/8 SRM for open-loop motoring operation with a constant current reference of 2A without current compensation while Figure 4.32 shows the same waveforms for operation with current compensation. As can be seen, the addition of the compensating current signal alters the phase current shape from a flat-topped waveform to a fluctuating current waveform profile that results in flat-topped phase torques.

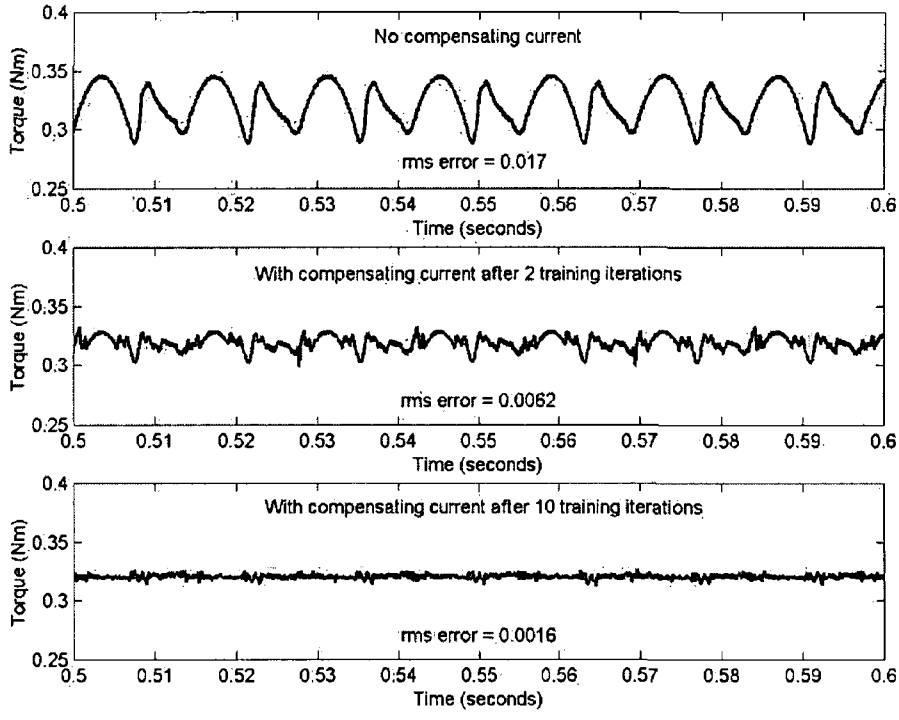

Figure 4.29: The torque produced by the 12/8 three-phase SRM without current compensation, with current compensation after two training iterations and with current compensation after ten training iterations for open-loop motoring operation with a constant current reference of 2A.

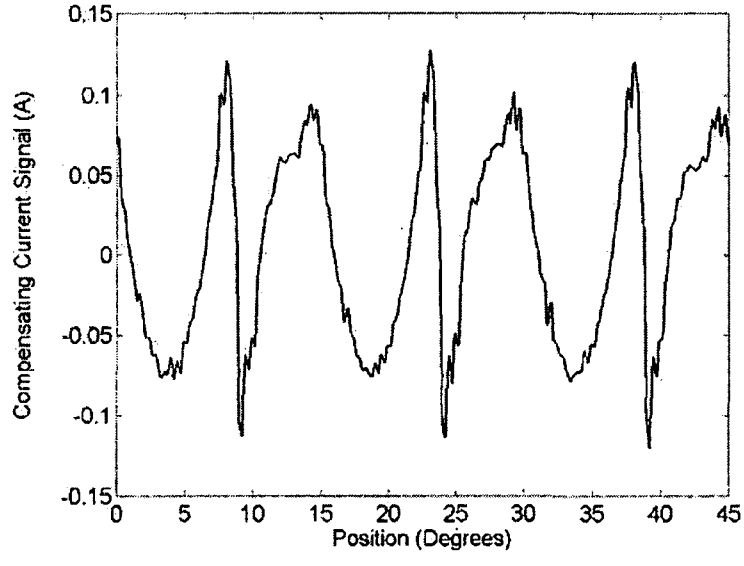

Figure 4.30: The compensating current signal produced by the neuro-fuzzy compensator for open-loop motoring operation of the 12/8 SRM with a constant current reference of 2A.

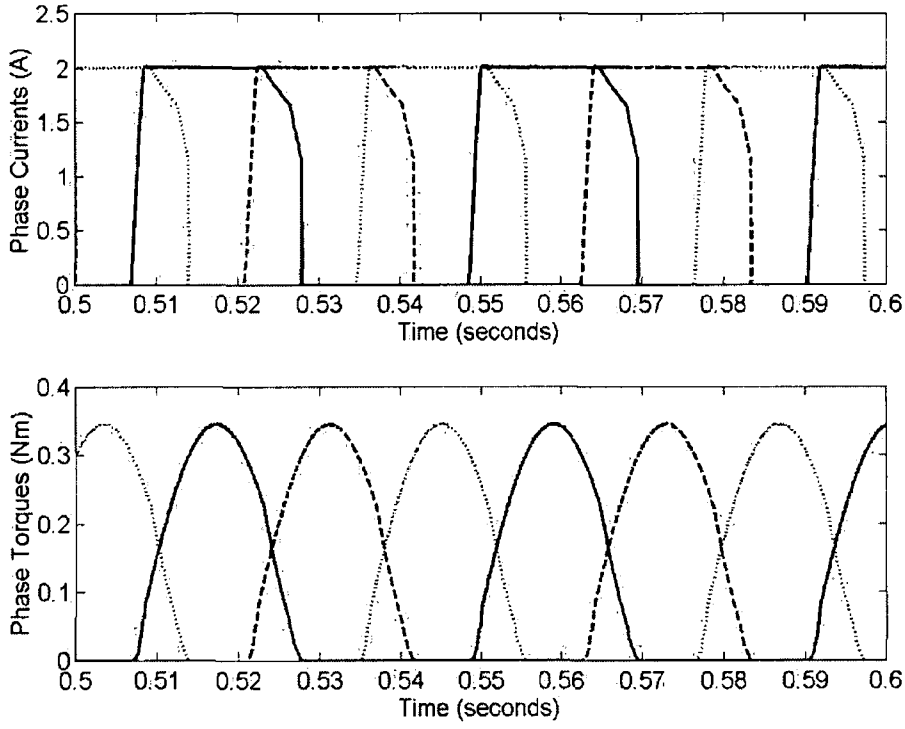

Figure 4.31: The phase currents and corresponding phase torques produced by the 12/8 SRM for open-loop motoring operation with a constant current reference of 2A without current compensation.

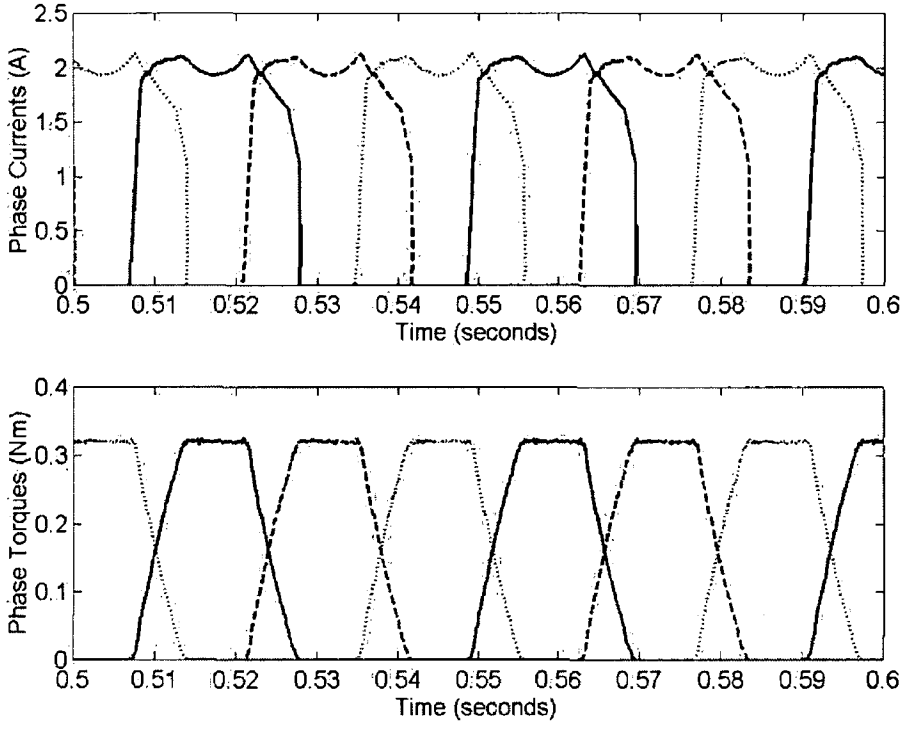

Figure 4.32: The phase currents and corresponding phase torques produced by the 12/8 SRM for open-loop motoring operation with a constant current reference of 2A with current compensation.

4.8.2.2 PI speed control tests

The PI controller constants employed in the speed controller for the SRM (obtained by manual tuning) were P = 0.1 and I = 0.1. For the purposes of comparison, the system was simulated initially with no compensation. It was then simulated with the trained neuro-fuzzy compensator incorporated. The compensating current signal produced by the compensator followed the curve shown in Figure 4.33.

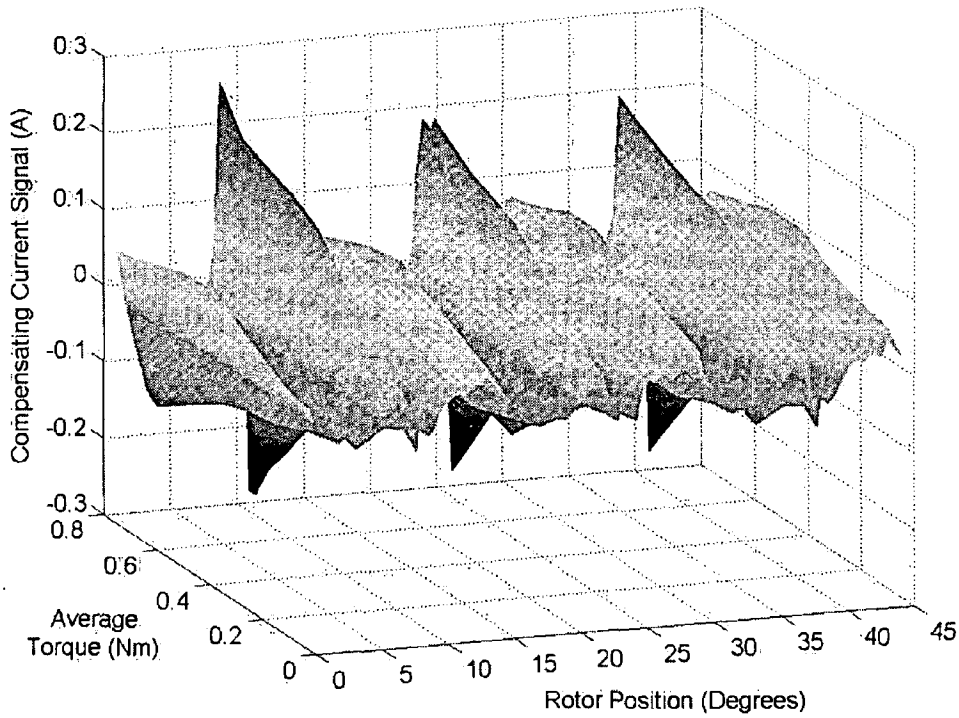

Figure 4.33: Current compensation curve for the 12/8 three-phase SRM.

The SR drive system was simulated with and without compensation for a load torque of T_L = 0.25Nm and with a reference speed of ω_{ref} = 180rpm. Figure 4.34 shows the steady-state torque produced by the 12/8 SRM with and without current compensation. The rms error is reduced from 0.0131 to 0.0016 when current compensation is employed. Figure 4.35 shows the phase currents and phase torques without current compensation during steady-state motoring operation while Figure 4.36 shows the same waveforms when the neuro-fuzzy compensator is incorporated into the SR drive.

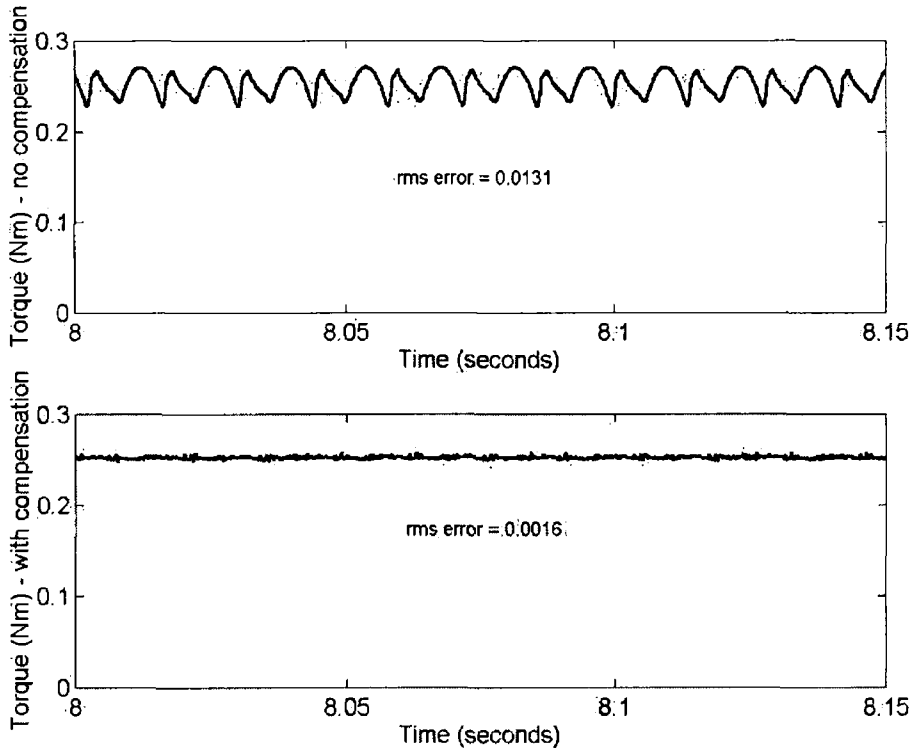

Figure 4.34: Torque produced by the 12/8 three-phase SRM with and without compensation for operation at 180rpm with a load torque of 0.25Nm.

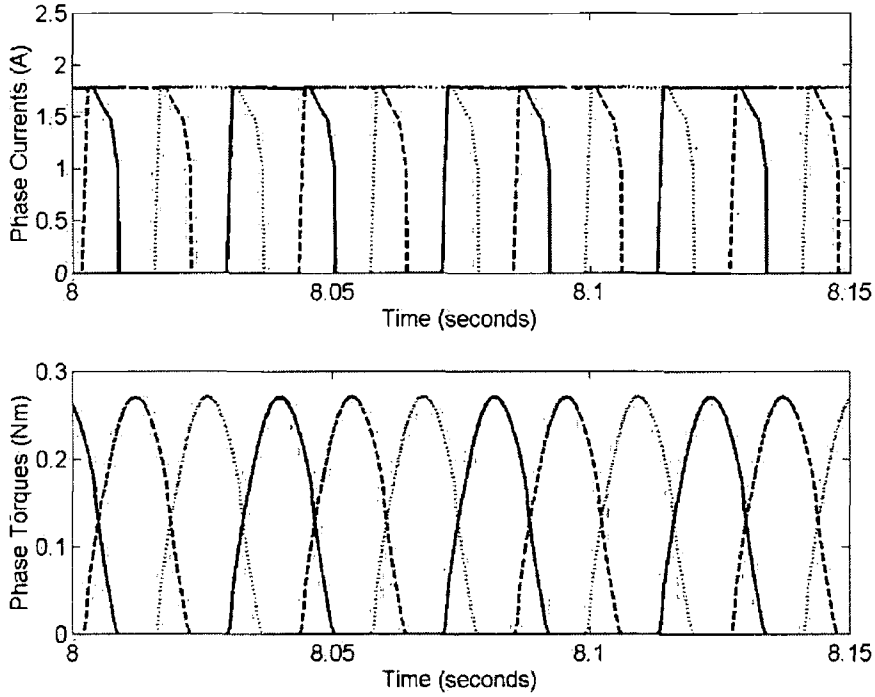

Figure 4.35: The phase currents and phase torque profiles for steady-state motoring operation at 180rpm with a 0.25Nm load without current compensation.

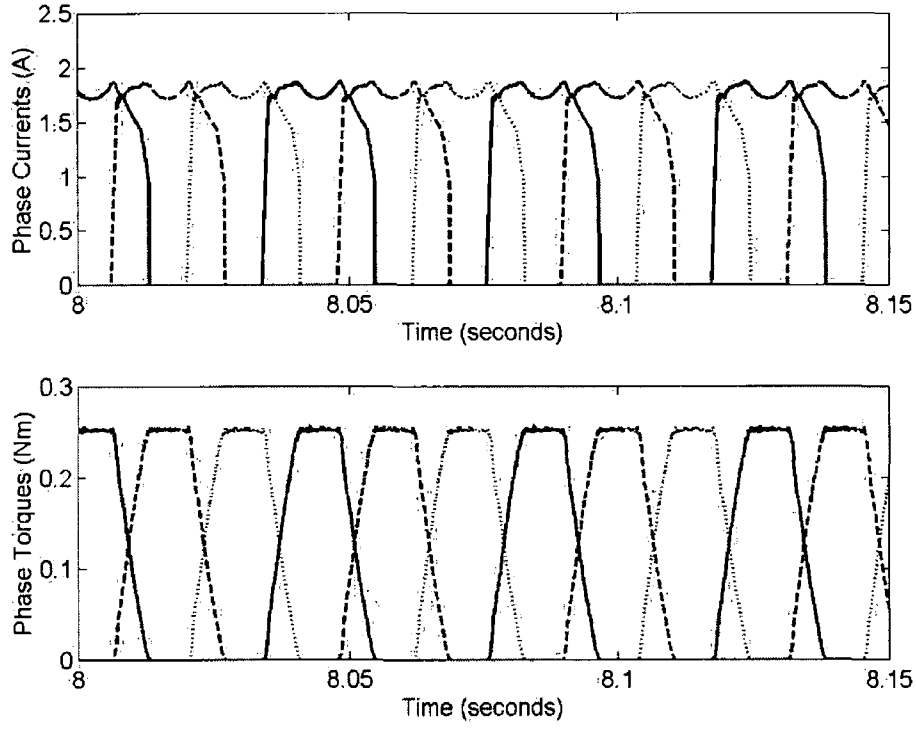

Figure 4.36: The phase currents and phase torque profiles for steady-state motoring operation at 180rpm with a 0.25Nm load with current compensation.

Figure 4.37 shows the PI controller output signal, the compensating current signal produced by the neuro-fuzzy compensator and the current reference employed by the delta modulation current controller for steady-state motoring operation at 180rpm with a 0.25Nm load. The final current reference is the sum of the PI controller output current signal and the compensating current signal.

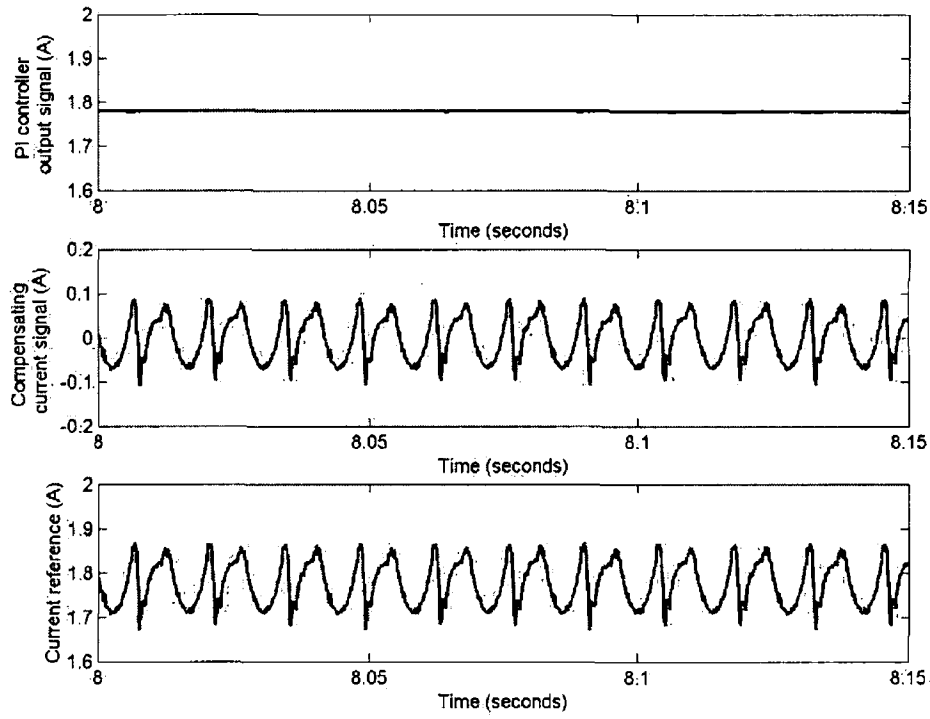

Figure 4.37: The PI controller output signal, the compensating current signal produced by the neuro-fuzzy compensator and the current reference employed by the delta modulation current controller for steady-state motoring operation at 180rpm with a 0.25Nm load.

4.9 Neuro-fuzzy control strategy no. 3

The third torque ripple reduction control strategy is similar to neuro-fuzzy control strategy no. 2. Once again, a compensating current signal, trained using the ANFIS system, is added to the PI controller output in a current-regulated speed control loop. The main differences between the two control schemes are in the parameters employed during the compensator training process and in the data required for operation of the drive when the trained compensator is incorporated. Figure 4.38 shows a block diagram of neuro-fuzzy control strategy no. 3. The neuro-fuzzy compensator determines the correct compensating current signal, I_{COMP}, based on the PI controller current signal, I_{PI}, and the rotor position, θ. This control strategy was first proposed in (Henriques 1999). Figure 4.39 shows a basic block diagram of the ANFIS training method, which uses data obtained from steady-state operation of the SR drive.

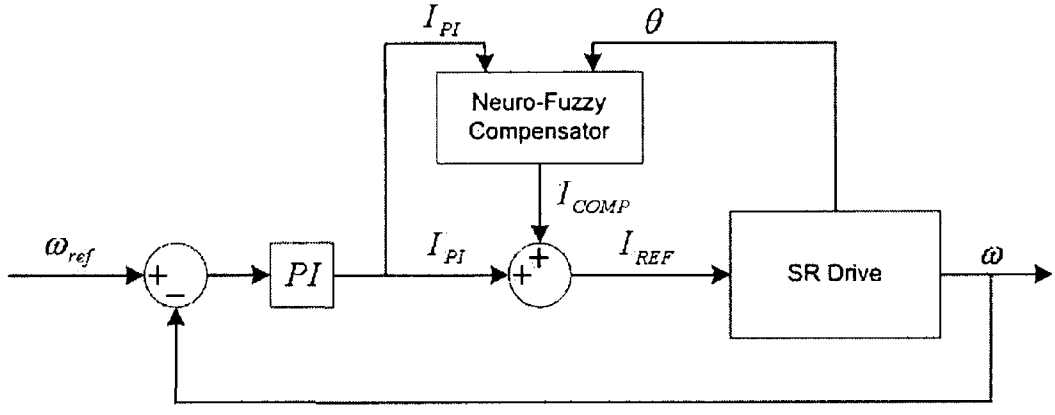

Figure 4.38: Block diagram of neuro-fuzzy control strategy no. 3.

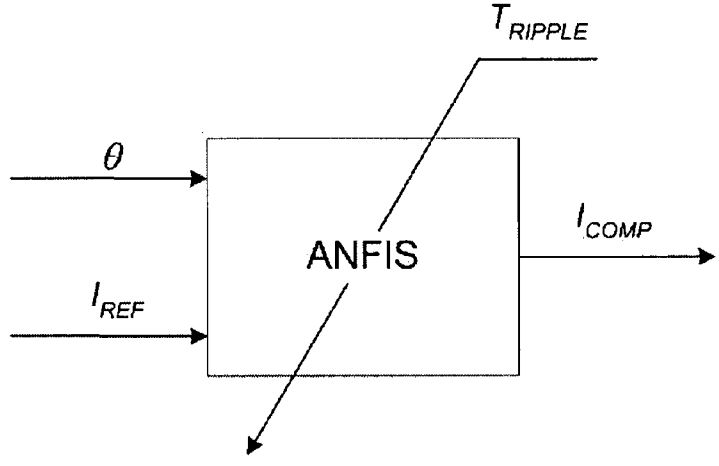

Figure 4.39: Basic block diagram of the ANFIS training method for neuro-fuzzy control strategy no. 3.

Figure 4.40 shows a flowchart detailing the training procedure for the neuro-fuzzy compensator employed in neuro-fuzzy control strategy no. 3. The only difference in the compensator training procedure for neuro-fuzzy control strategies 2 and 3 is in the inputs to the ANFIS system. For neuro-fuzzy control strategy no. 3, the current reference, I_{REF}, the rotor position, θ, and the torque ripple, T_{RIPPLE}, are recorded for each training iteration when the SR drive is operating in open-loop motoring mode. Before the first training iteration begins, a vector is created to hold the compensating current values and is initialised to zero. The torque ripple, obtained by removing the dc component from the total torque value, is used to update the compensating current signal data vector, I_{COMP}, in the same manner as for the neuro-fuzzy control strategy

no. 2. Hence, for each training iteration, the compensating current value at each sample point is decremented if the torque ripple is greater than zero while the compensating current value is incremented if the torque ripple is less than zero. The updated I_{COMP} data is then passed to the ANFIS system along with the current reference and rotor position data for training. This data set is used to generate an updated FIS that is incorporated into the SR drive as the neuro-fuzzy compensator. The process of updating the I_{COMP} data vector, generating a new FIS and incorporating the new FIS into the SR drive as the neuro-fuzzy compensator is repeated until the torque ripple is reduced below the desired error limits at each rotor position for the particular constant current reference. The training is performed for several discrete values of the current reference. The final overall neuro-fuzzy compensator is obtained by combining the data acquired at each current reference setpoint into a single data set and passing it to the ANFIS system for training. Neuro-fuzzy control strategy no. 3 is suitable for use with an SRM that has strongly nonlinear torque-current-position characteristics.

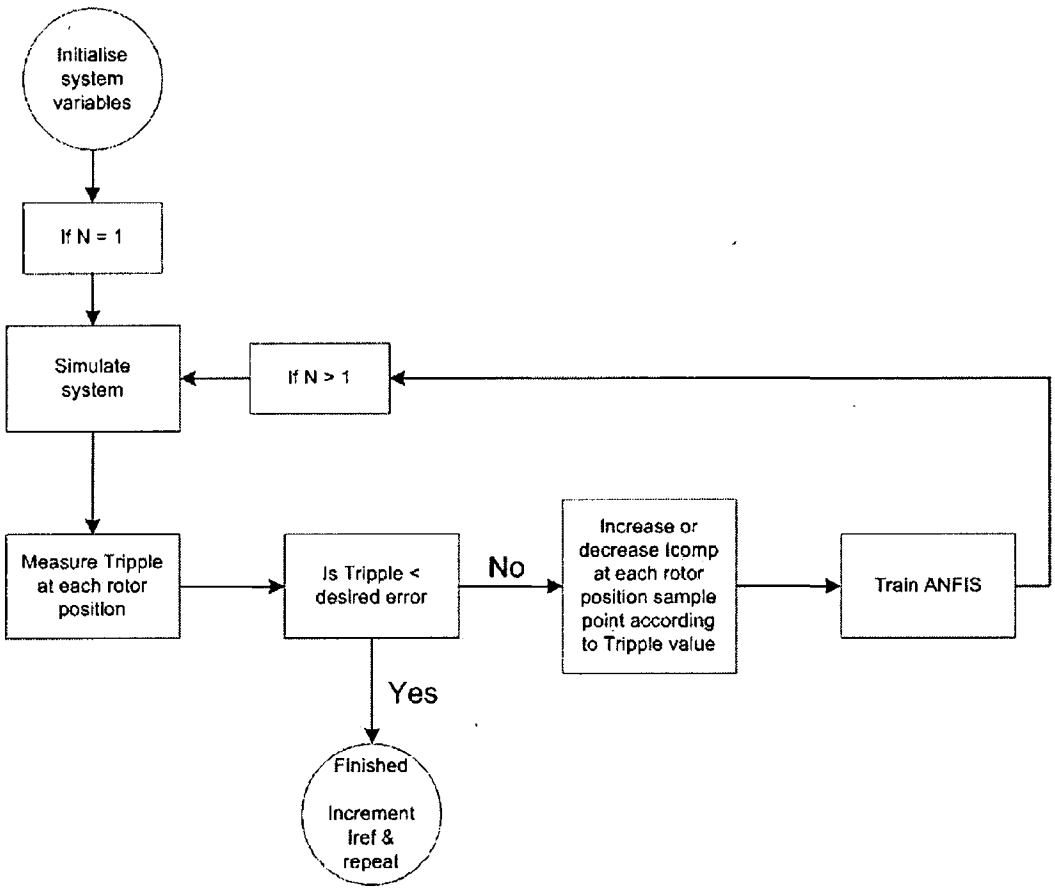

Figure 4.40: Compensator training procedure for neuro-fuzzy control strategy no. 3.

4.10 Simulation results for control strategy no. 3

The control strategy was implemented and tested in MATLAB/Simulink using the 6/4 three-phase SRM model and the 12/8 three-phase experimental SRM model. The method of phase conduction and commutation control described in Section 4.6 was employed in both SRM control implementations.

4.10.1 6/4 three-phase SRM results for control strategy no. 3

The neuro-fuzzy compensator training procedure was implemented for the 6/4 three-phase SR drive. The rotor position, θ, employed in the compensator training process was confined to the range 0°-90° (mechanical degrees). The current reference was varied in discrete steps of 0.25A between 1A and 2.5A. At each constant current reference value, the appropriate compensating current value was determined for every rotor position. All of the data was combined to produce the overall neuro-fuzzy compensator. The rule set for the neuro-fuzzy compensator was initially generated using the grid partition technique with fifty trapezoidal membership functions chosen for the rotor position and two trapezoidal membership functions chosen for the current reference. The neuro-fuzzy compensator was trained using the hybrid training technique that incorporates the backpropogation algorithm and the least-mean-squares algorithm.

4.10.1.1 Initial tests – constant current reference

For comparison purposes, the system was simulated with and without current compensation for open-loop SR motoring operation with a constant current reference of 1.75A. Figure 4.41 shows the torque produced by the 6/4 three-phase SRM without current compensation (rms error = 0.0181), with current compensation after two training iterations (rms error = 0.0056) and with current compensation after eight training iterations (rms error = 0.0024). After eight training iterations, the torque ripple had decreased below the error limits and the training was complete. This compares well with the result for control strategy no. 2 shown in Figure 4.20. As can be seen by comparing the two figures, the rms error was lower after two training iterations for control strategy no. 2 than it was for strategy no. 3. However, control strategy no. 2 required ten training iterations for full compensator training compared to eight for control strategy no 3. The final rms error for the two strategies is identical

(rms error = 0.0024), a result which is purely coincidental. The compensating current signal that is added to the 1.75A constant current reference during steady-state operation is plotted against rotor position in Figure 4.42.

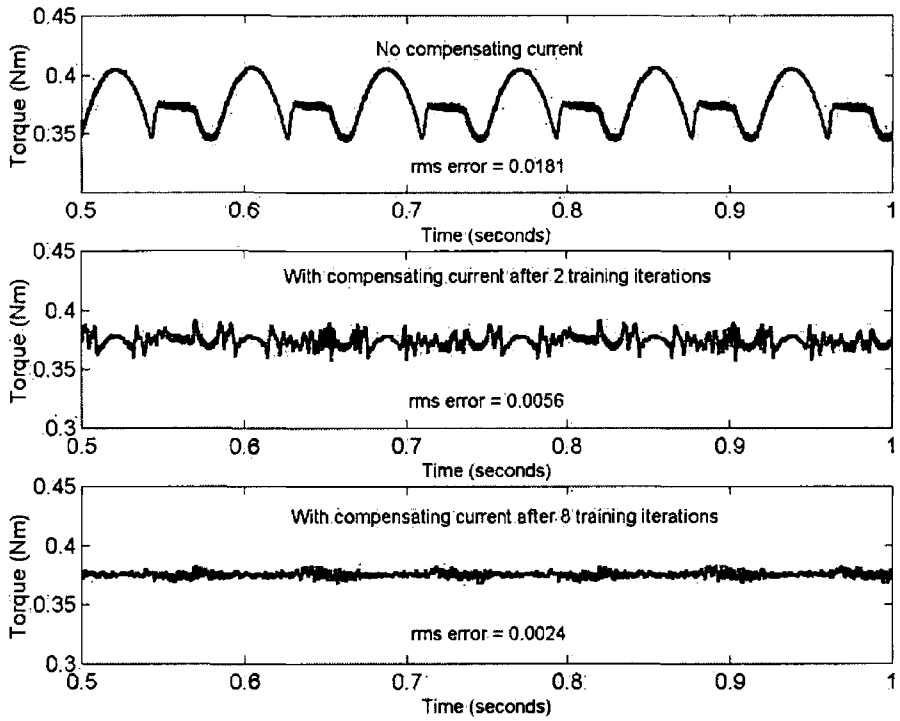

Figure 4.41: The torque produced by the 6/4 three-phase SRM without current compensation, with current compensation after two training iterations and with current compensation after eight training iterations for open-loop motoring operation with a constant current reference of 1.75A.

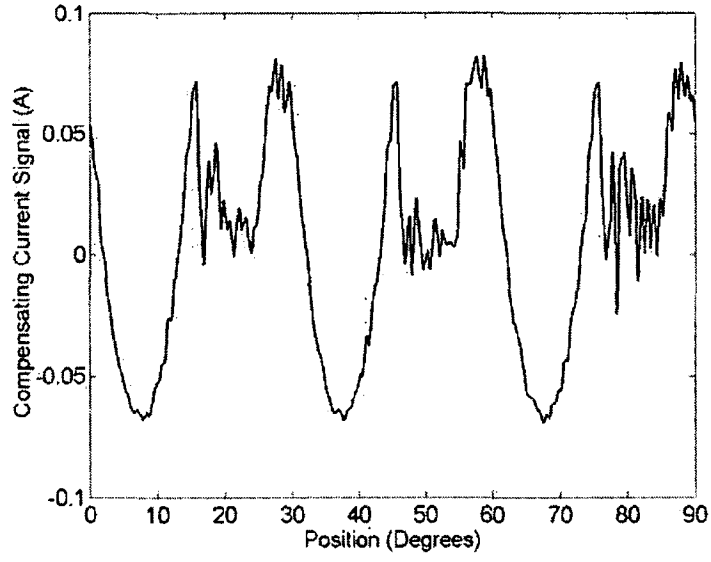

Figure 4.42: The compensating current signal produced by the neuro-fuzzy compensator for open-loop motoring operation of the 6/4 SRM with a constant current reference of 1.75A.

4.10.1.2 PI speed control tests

For further testing of the neuro-fuzzy control strategy no. 3, the compensator was incorporated into the SR drive operated under current-regulated speed control implemented using a PI controller. The PI controller was tuned manually. The resultant constants were P = 0.3 and I = 0.1. For SR drive operation with current compensation, the compensating current signal produced by the neuro-fuzzy compensator followed the curve shown in Figure 4.43.

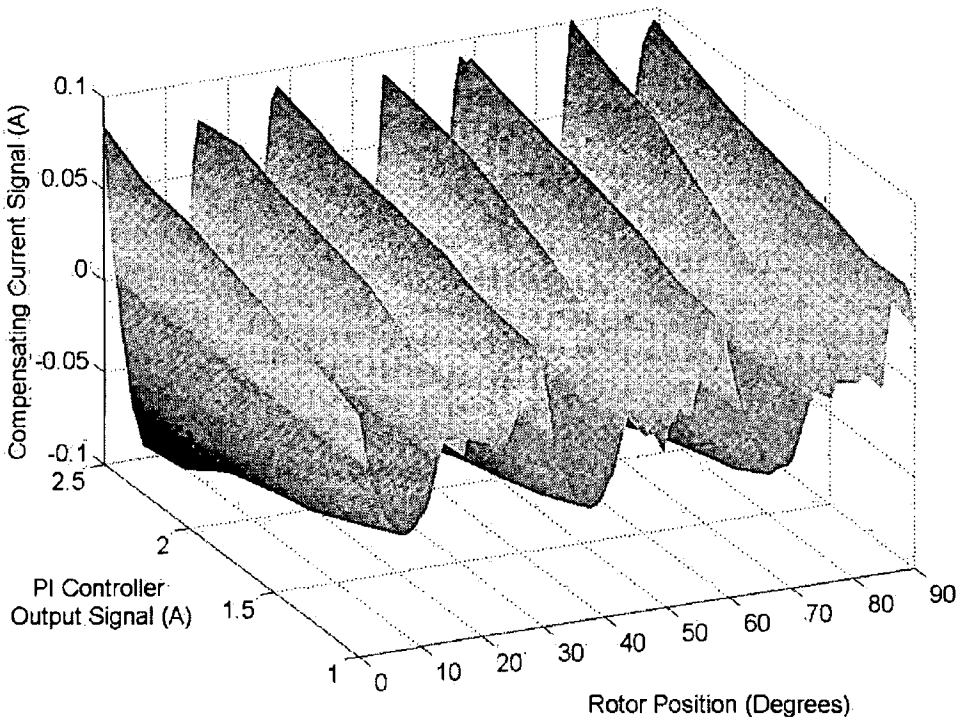

Figure 4.43: Current compensation curve for the 6/4 three-phase SRM.

The SR drive system was simulated with and without compensation for a load torque of T_L = 0.5Nm and with a reference speed of ω_{ref} = 60rpm. Figure 4.44 shows the steady-state torque produced by the 6/4 SRM with and without current compensation. As expected, when the neuro-fuzzy compensator is employed, a significant decrease in the torque ripple is observed. The torque ripple rms error is reduced from 0.0242 to 0.0033 when compensation is employed.

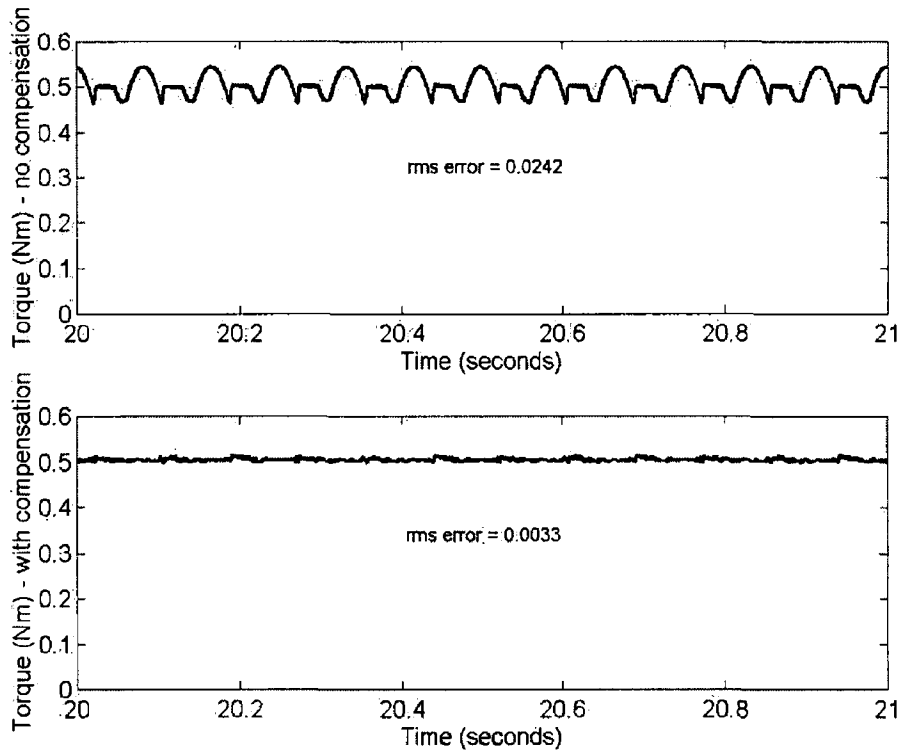

Figure 4.44: Torque produced by the 6/4 SRM with and without compensation for operation at 60rpm with a load torque of 0.5Nm.

Figure 4.45 shows the PI controller output signal, the compensating current signal produced by the neuro-fuzzy compensator and the final current reference used by the delta modulation current controller for steady-state motoring operation at 60rpm with a 0.5Nm load.

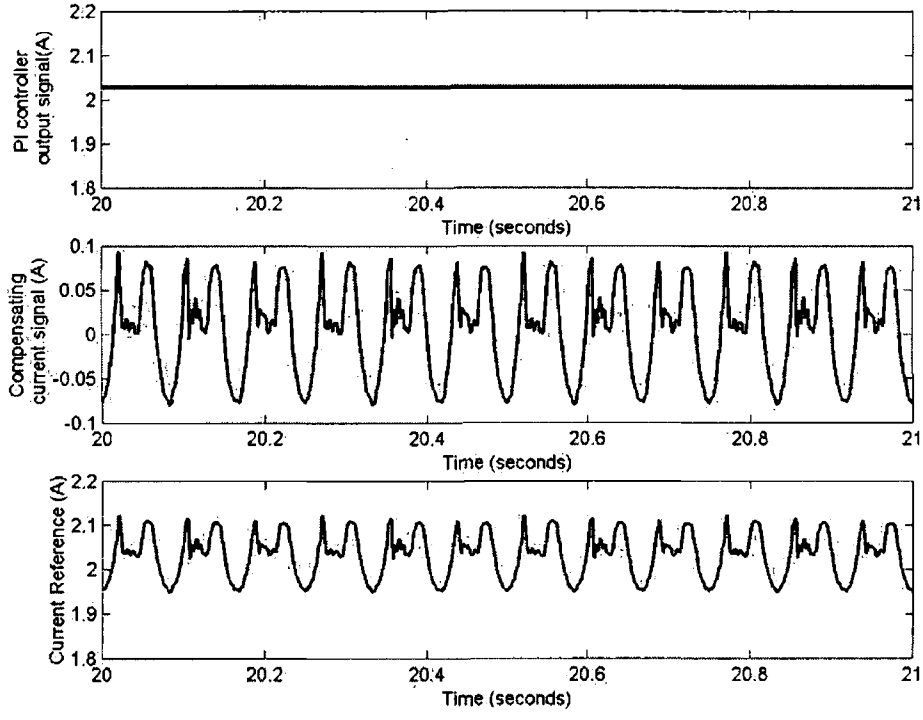

Figure 4.45: The PI controller output current signal, the compensating current signal produced by the neuro-fuzzy compensator and the final current reference used by the delta modulation current controller for steady-state motoring operation at 60rpm with a 0.5Nm load.

4.10.2 12/8 three-phase SRM results for control strategy no .3

The neuro-fuzzy control strategy was implemented in MATLAB/Simulink for the 12/8 three-phase SRM model whose parameters are shown in Table 4.2. The rotor position, θ, employed in the compensator training process was confined to the range 0°-45° (mechanical degrees). The current reference was varied in discrete steps of 0.5A between 1A and 3A and the compensating current signal was trained. The training data obtained at each current reference setpoint was then integrated into an overall data set, which was employed in the training of the final neuro-fuzzy compensator. The rule set for the neuro-fuzzy compensator was initially generated using the grid partition technique with one hundred trapezoidal membership functions chosen for the rotor position and two trapezoidal membership functions chosen for the current reference. The neuro-fuzzy compensator was trained using the hybrid training

technique that incorporates the backpropogation algorithm and the least-mean-squares algorithm.

4.10.2.1 Initial tests – constant current reference

The 12/8 SR drive was simulated with and without current compensation for open-loop SR motoring operation with a constant current reference of 2A. Figure 4.46 shows the torque produced by the 12/8 three-phase SRM without current compensation (rms error = 0.017), with current compensation after two training iterations (rms error = 0.0055) and with current compensation when the training was complete after ten iterations (rms error = 0.0017). The reduction of the torque ripple as the training of the neuro-fuzzy compensator advances is clearly visible in Figure 4.46. The compensating current signal produced by the neuro-fuzzy compensator for open-loop motoring operation of the 12/8 SRM with a constant current reference of 2A is shown in Figure 4.47. This compensating current signal is the required modification to the 2A constant current reference that is necessary to produce phase torque profiles that sum to produce a ripple-free total torque profile.

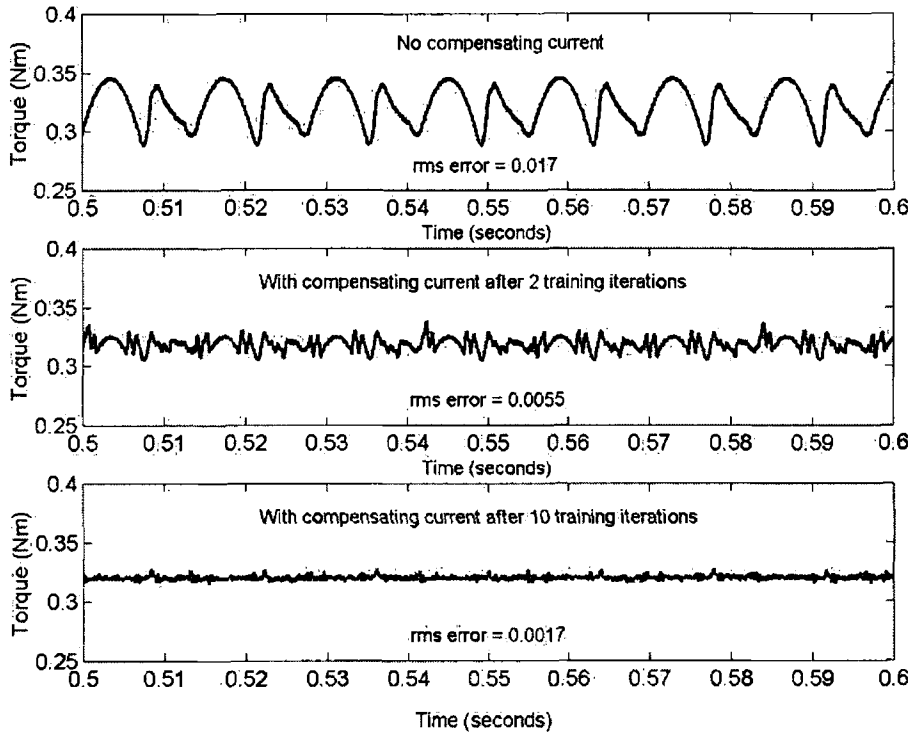

Figure 4.46: The torque produced by the 12/8 three-phase SRM without current compensation, with current compensation after two training iterations and with current compensation after ten training iterations for open-loop motoring operation with a constant current reference of 2A.

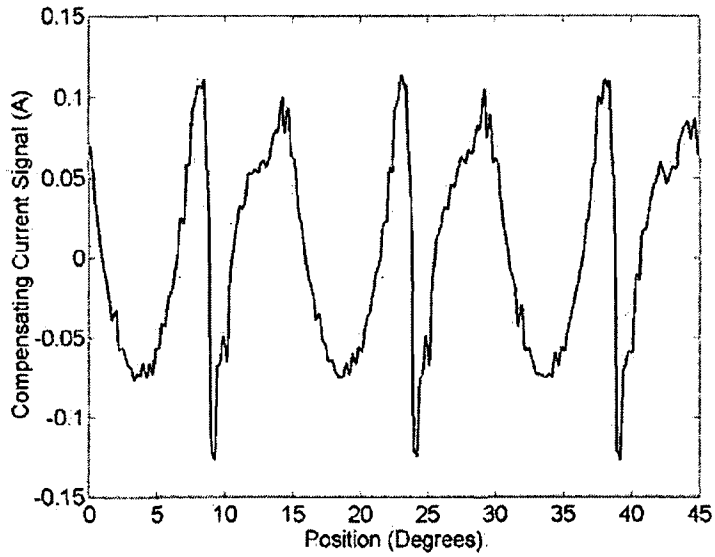

Figure 4.47: The compensating current signal produced by the neuro-fuzzy compensator for open-loop motoring operation of the 12/8 SRM with a constant current reference of 2A.

4.10.2.2 PI speed control tests

The PI controller constants employed in the speed controller for the SRM (obtained by manual tuning) were P = 0.1 and I = 0.1. The compensating current signal produced by the trained neuro-fuzzy compensator followed the curve shown in Figure 4.48.

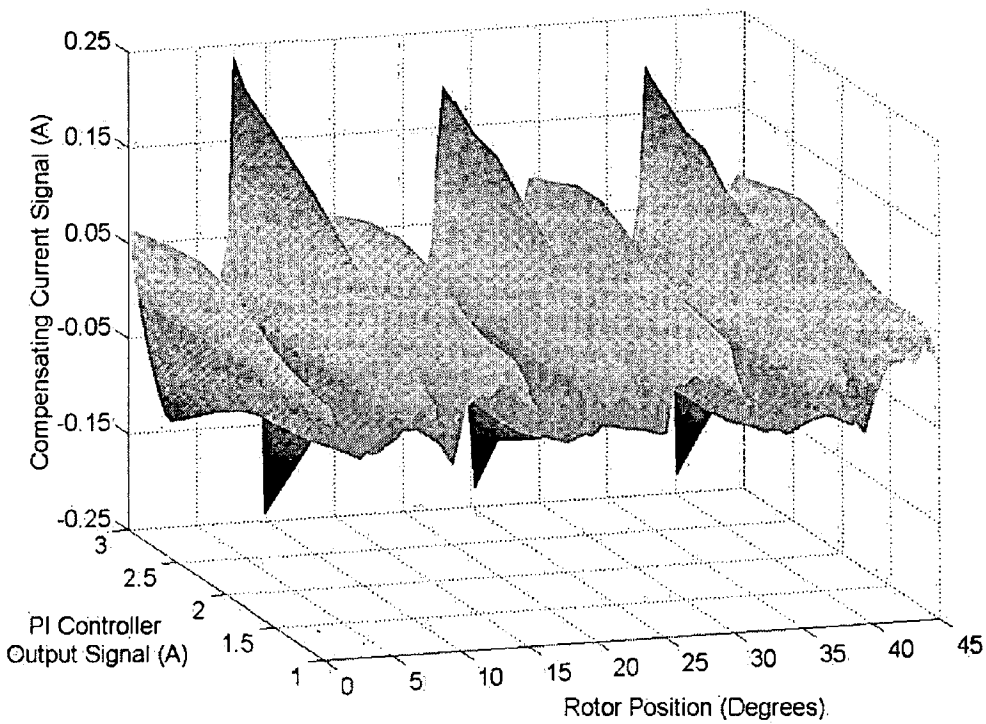

Figure 4.48: Current compensation curve for the 12/8 three-phase SRM.

The SR drive system was simulated with and without compensation for a load torque of T_L = 0.25Nm and with a reference speed of ω_{ref} = 180rpm. Figure 4.49 shows the steady-state torque produced by the 12/8 SRM with and without current compensation. The rms error is reduced from 0.0131 to 0.0017 when current compensation is employed. Figure 4.50 shows the PI controller output signal, the compensating current signal produced by the neuro-fuzzy compensator and the current reference employed by the current controller during steady-state operation.

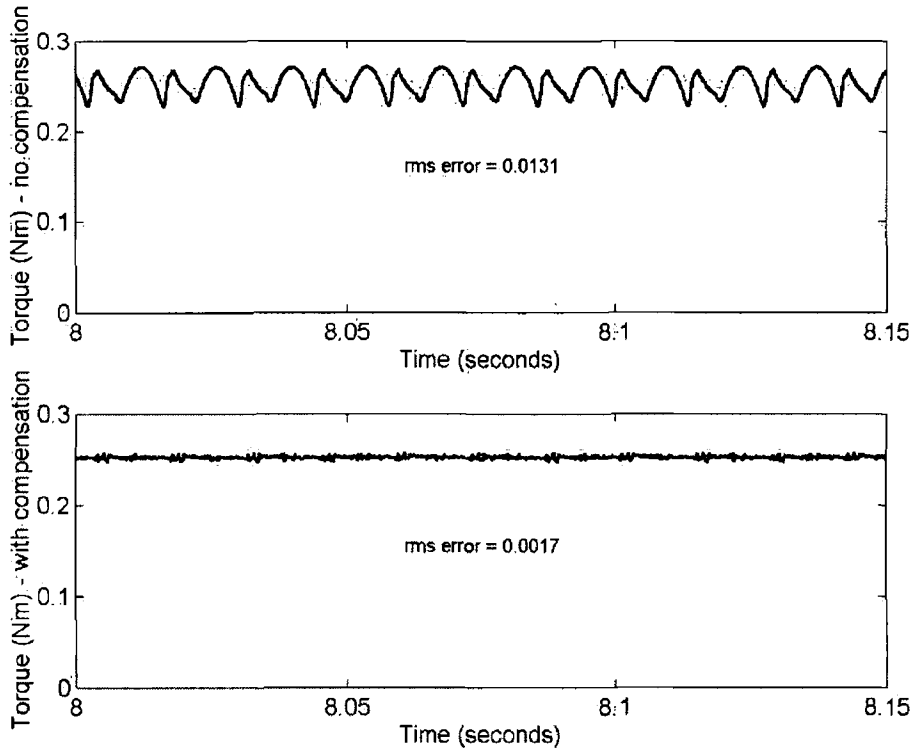

Figure 4.49: Torque produced by the 12/8 three-phase SRM with and without compensation for operation at 180rpm with a load torque of 0.25Nm.

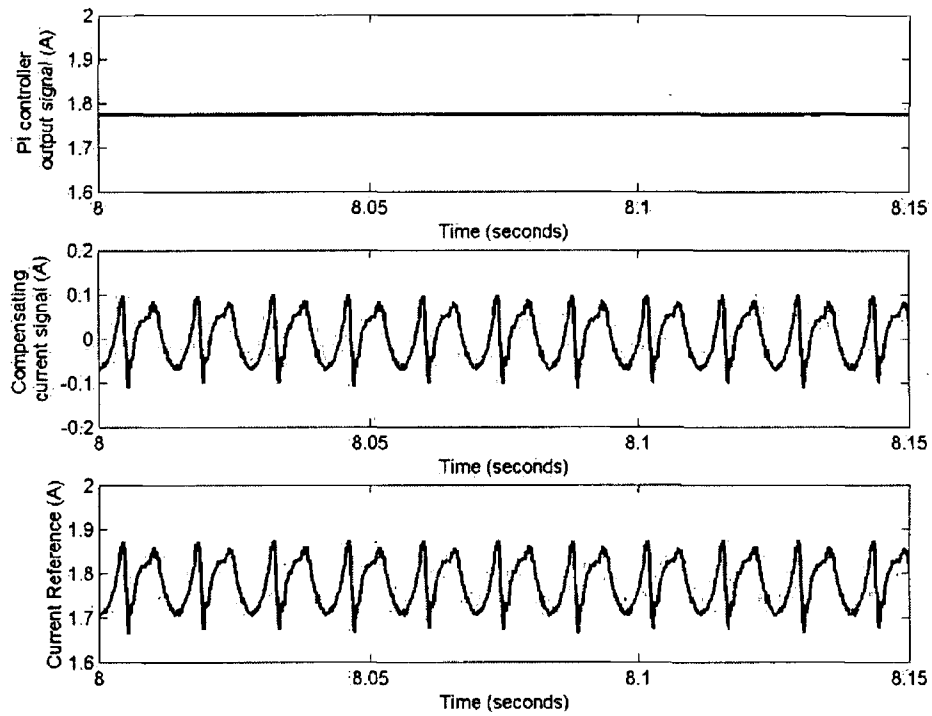

Figure 4.50: The PI controller output signal, the compensating current signal produced by the neuro-fuzzy compensator and the current reference employed by the delta modulation current controller for steady-state motoring operation at 180rpm with a 0.25Nm load.

4.11 Torque estimation

The three neuro-fuzzy controllers described in this chapter are trained using parameters obtained during steady-state operation of the SRM. All three control strategies require knowledge of the torque profile for the training of the compensating current signal. However, both neuro-fuzzy control strategy no. 1 and no. 2 require knowledge of the torque produced by the SRM for subsequent correct operation of the current compensated system. Therefore, accurate torque information is a fundamental requirement for these strategies.

An obvious method for obtaining the torque information is to employ a torque sensor but, in the majority of industrial applications, this is not economically viable. One possible alternative to using a physical torque sensor is to employ a torque observer that can calculate the total torque as well as the individual phase torques. Such an

observer is the nonlinear model with on-line parameter estimation developed for SRMs by Mir (Mir 1998). This torque observer is described in Section 3.3 and the results from simulations verify its efficacy. The observer involves using the recursive least squares technique to continuously update the parameters of a nonlinear mathematical model for a SRM using terminal measurements of the phase currents and voltages. Thus, the model can adapt itself and tune itself to any SRM. An example of this self-tuning ability can be seen in Figure 4.51. Figure 4.51 shows the torque produced by phase A of the 12/8 three-phase SRM model when neuro-fuzzy current compensation is employed (solid line). It also shows the estimated torque produced by the self-tuning nonlinear model tuned to match the characteristics of the SRM (dotted line). As can be seen, the two torque profiles match almost exactly. Hence, the torque observer could be employed for estimation of the torque both during the compensator training process (for all three neuro-fuzzy control strategies) and during subsequent on-line operation of neuro-fuzzy control strategies no. 1 and no. 2.

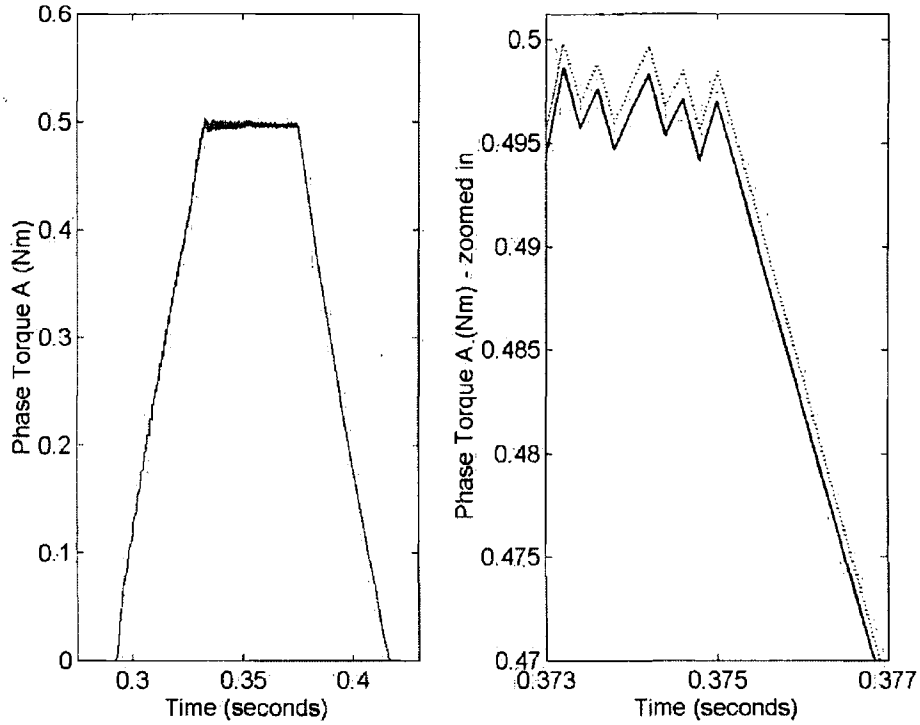

Figure 4.51: Torque produced by phase A of the 12/8 three-phase SRM when torque ripple minimisation is employed (solid line) and the estimated torque produced by the self-tuning nonlinear model tuned to match the characteristics of the SRM (dotted line).

4.12 Summary and conclusions

In this chapter, three control strategies for torque ripple minimisation in SR motors were presented and simulation results are given for both a 6/4 three-phase SRM and a 12/8 three-phase SRM. The three control schemes involve the addition of a compensating current signal to the current control signal produced by the PI controller in a current-regulated speed controlled SR drive. The compensating current signal is the required modification to the current control signal from the PI controller necessary to produce a torque profile with minimum ripple. In all three control strategies, the compensating current signal profile is trained off-line using the ANFIS system from parameters obtained during steady-state operation of the SRM. However, the parameters employed in the neuro-fuzzy compensator training are different for the three control strategies and the manner in which the compensator training is conducted also differs.

Neuro-fuzzy control strategy no. 1 uses the torque, T, the PI controller output current signal, I_{PI}, and rotor position information, θ, for the compensator training. When the training is complete and the neuro-fuzzy compensator is incorporated into the SR drive, the torque ripple, T_{RIPPLE}, and the rotor position, θ, are required by the compensator to produce the required compensating current signal. Simulation results indicate that this control strategy is very effective in minimising the torque ripple. However, this strategy suffers from the disadvantage of requiring knowledge of the torque signal for both the compensator training as well as for subsequent operation of the SR drive (with the trained compensator included). A torque sensor could be employed but this would greatly increase the overall cost of the drive. Alternatively, a torque estimation algorithm could be employed. This is the preferred option but the estimation algorithm must be highly accurate. In addition, implementation of such an estimation algorithm results in an increased control cycle time for real-time operation. Undoubtedly, the main drawback with using this control strategy in an experimental set-up is that it is only suitable for SRMs with relatively linear torque-current-position characteristics. Also, it requires a high sampling rate for effective operation. An additional, more obvious, disadvantage of neuro-fuzzy control strategy no. 1 is the extensive training process required in obtaining the compensating current function.

Neuro-fuzzy control strategy no. 2 uses the average torque, $T_{AVERAGE}$, the rotor position, θ, the torque ripple, T_{RIPPLE}, and the compensating current signal, I_{COMP}, in the compensator training process. The torque ripple is the error information used to update the compensating current signal in each training iteration. During subsequent operation of the SR drive system with the compensator included, the inputs are the average torque value and rotor position. The correct compensating current signal is returned by the neuro-fuzzy compensator. Simulation results prove the efficacy of this control approach in minimising the torque ripple. Neuro-fuzzy control strategy no. 2 is suitable for use with highly nonlinear SRMs. Hence, it is clearly superior to neuro-fuzzy control strategy no. 1. However, like neuro-fuzzy control strategy no. 1, knowledge of the torque signal is required both during the compensator training process and during subsequent on-line operation. As before, the instantaneous torque can be measured using a torque sensor or calculated using an estimation algorithm.

The iterative and hence, time-consuming, nature of the training is an obvious drawback.

Neuro-fuzzy control strategy no. 3 uses the current reference, I_{REF}, the rotor position, θ, the torque ripple, T_{RIPPLE}, and the compensating current signal, I_{COMP}, in the compensator training. As for the neuro-fuzzy control strategy no. 2, the torque ripple is the error information used to update the compensating current signal in each training iteration. During subsequent operation of the current-compensated SR drive system, the inputs to the neuro-fuzzy compensator are the PI controller current signal and rotor position. Like neuro-fuzzy control strategy no. 2, this control strategy is suitable for use with highly nonlinear SRMs with simulation results proving its efficacy in reducing the torque ripple. Neuro-fuzzy control strategy no. 2 proved to be marginally better than neuro-fuzzy control strategy no. 3 at reducing the torque ripple. For example, for operation of the 12/8 three-phase SRM at 180rpm with a load of 0.25Nm, the rms error was 0.0016 for control strategy no. 2 compared to 0.0017 for control strategy no. 3. In spite of this, neuro-fuzzy control strategy no. 3 is the best of the three strategies examined in this chapter for one reason in particular. Although knowledge of the torque signal is required during the compensator training process, the torque signal doesn't need to be known during on-line operation. Thus, the means of obtaining the torque signal (a torque sensor or computationally intensive torque estimation algorithm) can be eliminated once the compensator training is complete. However, like neuro-fuzzy control strategy no. 2, neuro-fuzzy control strategy no. 3 has the disadvantage of having a lengthy iterative training process.

Chapter Five – Experimental set-up

5.0 Introduction

In this chapter, the experimental set-up used in the development and testing of the control strategies is described. Firstly, the SRM employed is introduced and its characteristics and parameters are described. An overview of the various power converter configurations is included prior to a description of the actual converter circuit employed. The relevant features of the DSP development board used in the control of the SRM are then presented. The current sensing and voltage measurement electronics are described as well as the method for deriving accurate rotor position information. Accurate position information is essential for smooth control of the machine. Finally, the overall experimental SRM system is presented. The complete system comprises the SRM, the DSP development board, the power converter, the measurement electronics, a dc machine, an electronic load, power supplies and so on.

5.1 The SRM

The machine employed in the experimental set-up is a 12/8 three-phase SRM with a power rating of 300W. The SRM was manufactured by the Emerson Electric Company for use in the Maytag Neptune direct-drive front-loading washing machine and its nominal parameters are shown in Table 5.1. Figure 5.1 (Nagel 1999) shows the flux-linkage versus current for one phase of the SRM over one electrical revolution. The flux-linkage versus current plot is highly linear. The machine does not saturate even at 2A above its rated current of 2.5A.

Parameter	Value
model number	H55BMBJL
R_{phase}	2.5Ω
$L_{aligned}$	52 mH
$L_{unaligned}$	9 mH
inertia	1.07 x 10^{-3} kg-m^2
rated current	2.5 amp
rated voltage	120 volt d.c. bus
stator / rotor poles	12/8
phases	3

Table 5.1: Nominal parameters of the SRM.

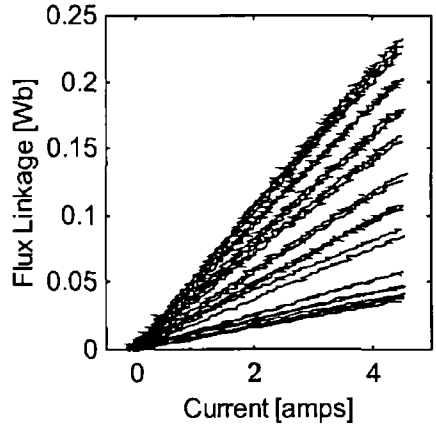

Figure 5.1: Flux-linkage versus current for one phase of the SRM over one electrical revolution.

The three-phase Emerson SRM is a suitable choice for the experimental work for a number of reasons. Firstly, three-phase machines have good starting capability in addition to enabling bi-directional operation (three phases are the minimum requirement for bi-directional rotation). As the number of phases increases however, the number of converter phase units and associated electronics also increases proportionally. Thus, a three-phase drive is the cheapest drive, in terms of converter components, that has bi-directional capability. The efficiency of a three-phase 6/4 machine is superior to that of a four-phase machine at high-speed operation. This is as a result of reduced core losses due to a lower number of phase excitations per revolution (Krishnan 2001). However, for a 12/8 three-phase machine with 24 strokes per revolution, the losses are identical to that of an 8/6 four-phase SRM.

The cross-section of a 12/8 three-phase machine is shown in Figure 5.2. A single phase consists of the series connection of stator windings on each of four stator poles that are situated at 90 mechanical degree intervals around the stator. According to (Miller 2001), the 12/8 machine is probably the most popular configuration for three-phase machines. The magnetic field in the 12/8 machine has shorter flux-paths than the 6/4 three-phase machine because of the four-pole configuration. In addition, the four-pole magnetic circuit of the 12/8 machine exhibits reduced acoustic noise when compared to the two-pole configuration of the 6/4 machine (Miller 2001).

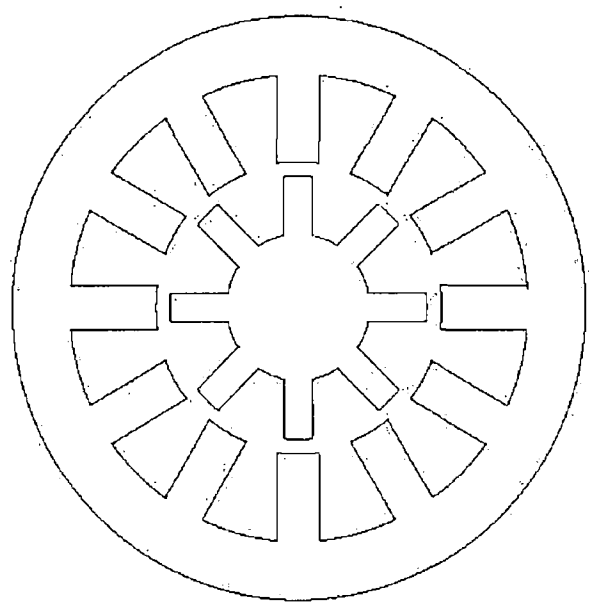

Figure 5.2: Cross-section of a 12/8 three-phase SRM.

5.2 Power electronic converter

For motor drives operating with sinusoidal voltages or currents, the power converter topology is independent of the motor design. However, in the case of an SRM drive, the motor geometry as well as the intended drive application affect the choice of a particular converter design. The number of stator/rotor poles and phases, the presence of current overlap in the phases and the way in which the motor is wound (monofilar or bifilar) influence the choice of converter topology (Vukosovic 1990). A monofilar phase winding is wound with a single wire whereas a bifilar winding implies that each phase is wound with two wires in parallel.

Power converters used to feed SRMs need to satisfy certain basic criteria to be considered as realistic candidates for employment in SRM applications. Energy conversion in SRMs occurs in discrete cycles called strokes. For each stroke of the motor, the power converter is required to first provide a positive voltage across the phase winding that enables the current to rise in the minimum time. Secondly, the converter must have the ability to reduce the applied voltage if the desired current level is reached. Finally, at commutation, the stored energy must be removed rapidly by reducing the current to zero as quickly as possible to avoid the production of negative torque. Hence, the converter must apply a negative voltage across the phase at turn off (Barnes 1998).

Since the converter needs only to carry unipolar or unidirectional current, the possibility of operating with only one switch in series per phase arises. This compares favourably from a cost viewpoint with converters for ac motors, which require at least two switches per phase. In addition, the problem of shoot-though faults is eliminated as the phase winding is always in series with a switch.

Several different converter topologies have been described in the literature, each with its own merits and drawbacks. They differ from each other by the manner of phase excitation as well as the means by which the stored magnetic field energy is recovered during commutation. Several converter circuits that have received widespread interest in the literature are now briefly outlined. This is followed by a description of the actual power converter employed in the experimental work described in this thesis.

5.2.1 Converter topologies

The 'asymmetric half-bridge' converter, also known as the 'classic' converter has already been described in detail in Section 2.4 of this thesis. A three-phase 'classic' converter is shown in Figure 5.3. Each phase winding is connected in series with two switches with both these switches being turned on at the start of the stroke, resulting in the supply voltage being placed across the winding. During the conduction period the current can be controlled by either hard or soft chopping. Both switches are turned off at the turn-off angle placing the negative of the supply voltage across the winding with the stored magnetic energy returning to the supply through the two freewheeling diodes. The major advantage of the 'classic' converter is that current can be supplied to one phase while another phase is simultaneously demagnetised. This allows operation with any degree of phase current overlap (enabling completely independent control). Clearly, the main disadvantage is the two switches and two diodes per phase requirement.

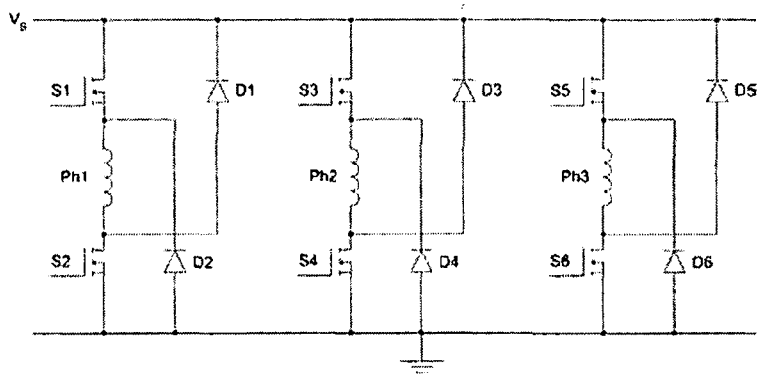

Figure 5.3: Three-phase 'classic' converter.

In (Miller 1988), a circuit configuration that reduces the number of switches and diodes to N+1 for an N phase motor is described. Figure 5.4 shows a three-phase 'Miller' converter. This converter has three operating states (magnetisation, freewheeling and forced demagnetisation) that are analogous to those of the 'classic' converter. This topology offers the lowest kVA rating of the converter circuits examined in (Vukosovic 1990). However, control of the converter is restricted. When switch SA is conducting, a forced demagnetisation of any of the phases is impossible with the result that two phases cannot conduct concurrently. In addition, the switch SA and diode DA have higher power ratings than the other semiconductor devices.

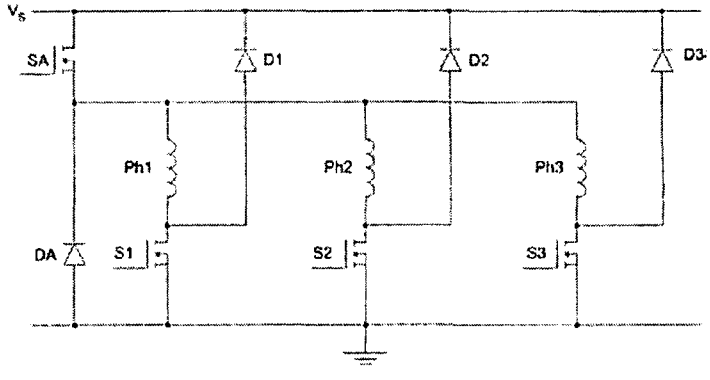

Figure 5.4: Three-phase 'Miller' converter.

The three-phase bifilar converter circuit shown in Figure 5.5 uses the fact that energy stored in the magnetic field of the phase winding can be transferred to a closely coupled second winding. It is the simplest converter circuit that achieves operation with only one switch per phase (thereby minimising switch conduction losses and reducing cost) and has been used extensively in stepper motor drives (Ehsani 1987).

To use this circuit, each phase stator pole pair requires a bifilar winding to be connected with opposing polarity. Current builds up in the primary phase winding when the switch turns on while the diode in series with the secondary is reverse biased. When the switch turns off, flux continuity ensures current flow transfers from the primary to the secondary with energy returning to the supply until the winding is completed demagnetised. One disadvantage of the bifilar converter is that the coupling between the primary and secondary windings is always imperfect leading to voltage spikes at switch turn off (Ehsani 1987). In addition, bifilar windings require additional slot volume reducing the power density of the SRM (Krishnan 2001) and the number of connections between the motor and the converter is doubled (Ehsani 1987).

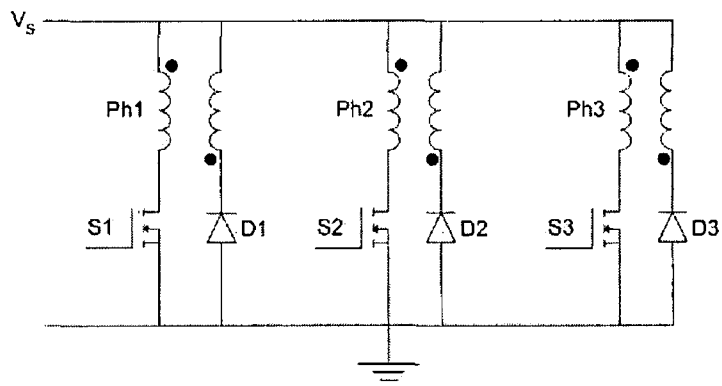

Figure 5.5: Three-phase bifilar converter.

Another converter configuration that requires only one switch and one diode per phase is the split dc supply converter and a two-phase example of this topology is shown in Figure 5.6. The circuit operation is as follows: phase 1 is energised by turning on S1 with the current circulating through S1, phase 1 and capacitor C1. When S1 is turned off the current flows through D1, phase 1 and into the capacitor C2 charging it in the process. A similar operation follows for phase 2. This converter configuration has the disadvantage of derating the supply voltage by utilising only half of its value at any time (Krishnan 2001). Also, in order to balance the charge across capacitors C1 and C2, an even number of phases is necessary. A fault in any phase would unbalance the upper and lower levels. The consequence of this is that the phases are less independent of each other than is the case with the converters previously described (Ehsani 1987).

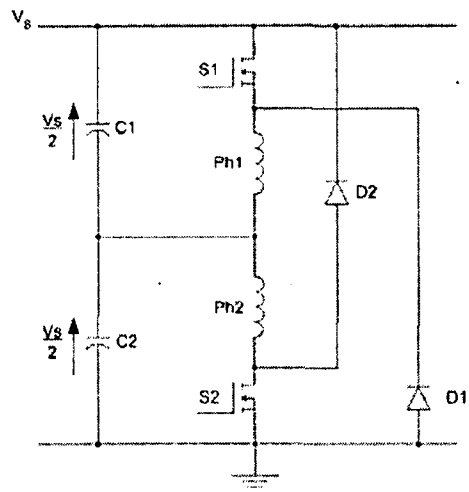

Figure 5.6: Two-phase split dc supply converter.

The last circuit shown in Figure 5.7 is known as the C-dump converter and was first described by Ehsani et al. (Ehsani 1987). The name is derived from its operation whereby stored magnetic energy is dumped into a capacitor (C1 in Figure 5.7) before being returned to the supply using a chopper circuit (consisting of SA, L1 and DA in Figure 5.7). It is an N+1 switch converter that has the advantage of having the minimum number of switches enabling independent phase control (Krishnan 2001). The voltage across C1 can be maintained at a higher level than the supply voltage. The main disadvantage of the C-dump converter is that the rate of demagnetisation is limited by the difference between the voltage across capacitor C1 and the supply voltage. In addition, losses in the chopper components decrease the efficiency of the drive (Krishnan 2001).

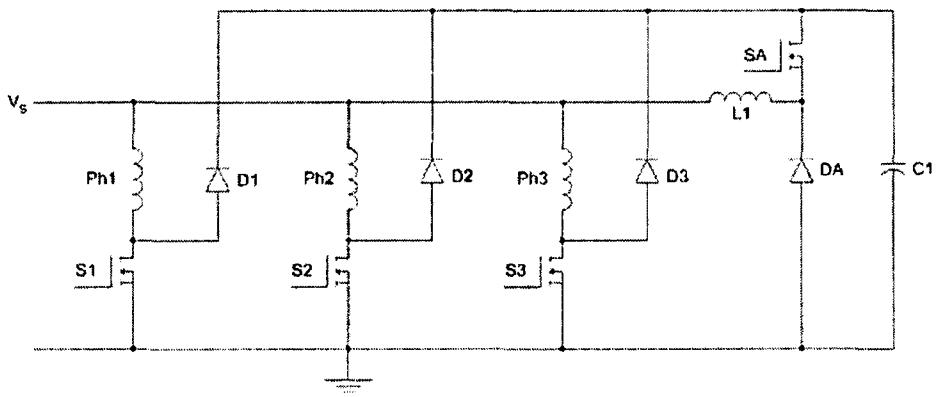

Figure 5.7: Three-phase C-dump converter.

5.2.2 Power converter circuit employed

The goal in this research was the development of control strategies for the SRM operating as a motor and as a generator. For this reason, the 'classic' converter was chosen as the converter topology because it provides excellent phase independent control capability. In one converter review paper (Barnes 1998), the 'classic' converter is described as being the benchmark topology against which all others should be compared. Similarly, another review paper (Vukosovic 1990) concludes that the 'classic' converter is the most attractive for industrial drives.

The SRM was obtained from a Maytag Neptune washing machine. The washing machine also contained a Printed Circuit Board (PCB) that integrated the electronics used to control the wash cycle of the washing machine (microprocessor etc.) with the SRM drive electronics. The converter topology used was that of a 'classic' converter. Rather than design a completely new converter circuit, it was decided to 'reverse-engineer' the PCB (which didn't have a schematic) and utilise only the relevant electronics on the PCB for the converter implementation. Figure 5.8 shows a diagram of the electronic circuit that accepts the input dc link supply voltage and uses it to derive the low voltage supplies for the drive electronics from the dc link voltage supply provided. Figure 5.9 shows a diagram of the electronic circuit for a single phaseleg (Phase A) of the SRM power converter. The electronic circuits used for phases B and C are identical.

Both Figure 5.8 and Figure 5.9 only show the relevant electronics. The PCB contained a vast amount of other electronic components that were isolated from the electronics employed in the project work by cutting tracks on the PCB. For example, the washing machine was originally designed to operate from a 120VAC USA standard mains supply. In this project, a dc power supply was employed instead. Therefore, the dc supply was connected to the output of the bridge rectifier B1 as shown in Figure 5.8. This rendered the input rectifier and filtering circuitry redundant.

As can be seen in Figure 5.9, IRF644 power MOSFETs (rated at 14A continuous drain current and 250V drain-to-source breakdown voltage) were used as the switching devices. These were driven using an IR2101 high voltage (600V), high

speed power MOSFET driver. The freewheeling diodes were high efficiency, fast recovery BYW98-200 diodes with a continuous current rating of 3A at 200V.

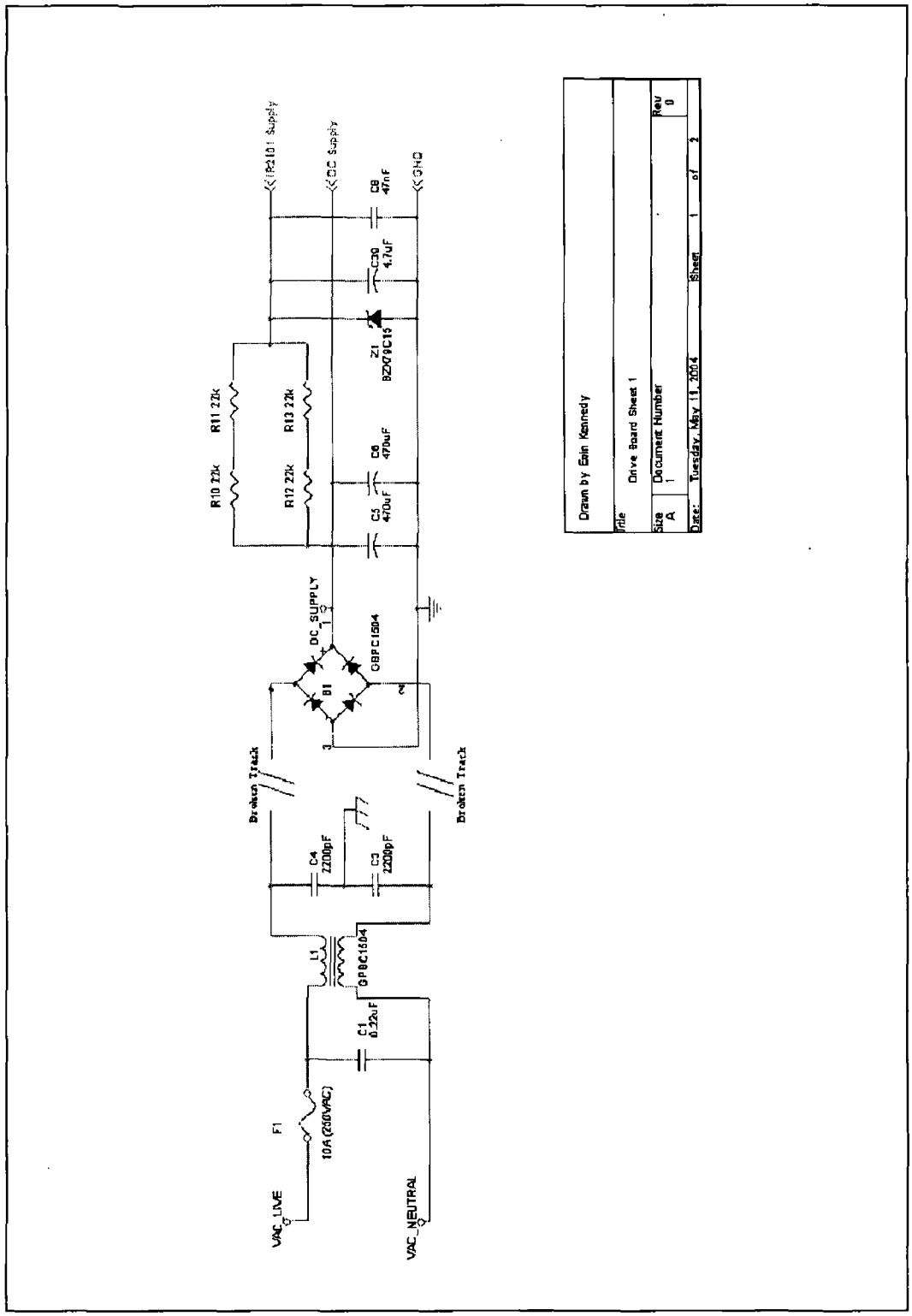

Figure 5.8: Diagram of the electronic circuit that takes the input dc link supply voltage and uses it to derive the low voltage supplies for the drive electronics.

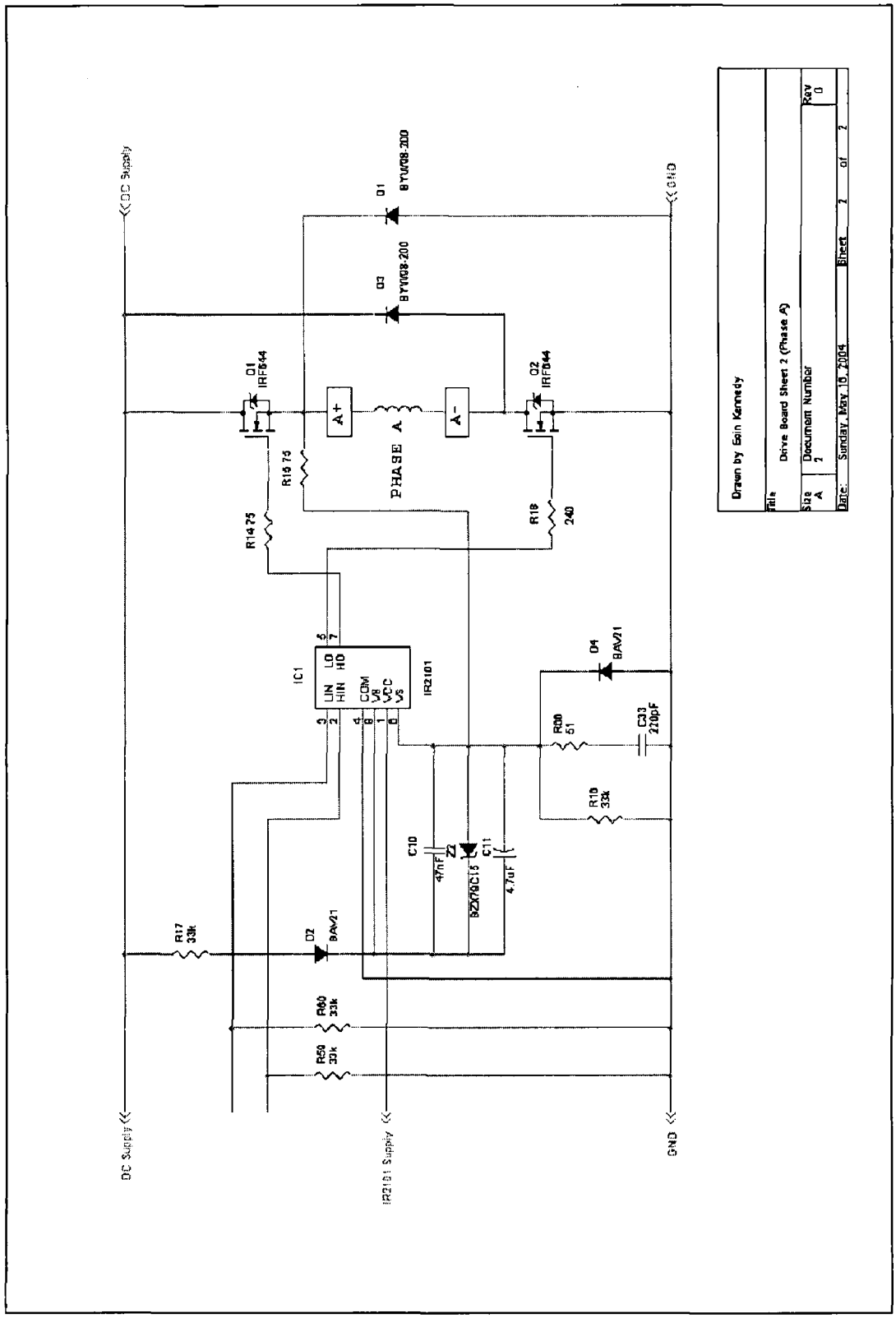

Figure 5.9: Diagram of the electronic circuit for a single phaseleg (Phase A) of the SRM power converter.

5.3 DSP controller

Two Analog Devices DSPs were employed in the experimental implementation of the SRM control strategies: the ADSP-21990 and the ADSP-21992. Both of these chips are mixed signal DSP controllers based on the ADSP-219x DSP Core and are suitable for a variety of high performance industrial motor control and signal processing applications. Essentially, the only difference between the two DSPs is that the ADSP-21992 has a substantially larger program memory (32K words compared to 4K words for the ADSP-21990). Hence, the rest of this section will only describe the performance and capabilities of the ADSP-21992. The ADSP-21990 was employed in the SR generator control while the SR motor control (which required significantly more program memory) was implemented using the ADSP-21992.

The ADSP-21992 is a single-chip DSP-based controller, which integrates a 160 Million Instructions Per Second (MIPS) sustained performance, 16-bit fixed point DSP core with a complete set of motor control peripherals that permit fast control in an integrated environment. The ADSP-21992 costs approximately 18euro. Table 5.2 outlines the key features of the ADSP-21992 while a functional block diagram of the ADSP-21992 is shown in Figure 5.10 (ADSP-2199x chip info 2003). Appendix B provides information on the ADSP-21992 EZ-KIT Lite development board employed in the experimental set-up for development and testing of the control strategies. Appendix B also provides a brief description of the integrated special purpose and motor control peripherals employed in the SRM control including the Analog-to-Digital Converter (ADC), the Encoder Interface Unit (EIU), the Flag I/O peripheral unit and the general-purpose timers. In addition, a brief explanation of how the programmable clock generation circuit works is included in Appendix B.

- 16-bit fixed point ADSP-219x DSP core, 160Mhz
- 48K words of on-chip RAM (Configured as 32K Words on-chip 24-bit Program RAM and 16K Words on-chip 16-bit Data RAM)
- 8-Channel, 14-bit ADC with up to 20 MSPS sampling rate
- Three 32-bit general-purpose timers
- Three-phase 16-bit centre-based PWM generation unit with 12.5ns resolution
- Dedicated 32-bit Encoder Interface Unit with companion Encoder Event Timer
- Dual 16-bit auxiliary PWM outputs
- 16 general-purpose Flag I/O pins
- SPI communications port with Master or Slave operation
- Synchronous Serial Communications Port (SPORT)
- External Memory Interface
- Controller Area Network (CAN) module fully compliant with V2.0B standard
- Peripheral Interrupt controller
- Programmable PLL and flexible clock generation

Table 5.2: Key Features of the ADSP-21992.

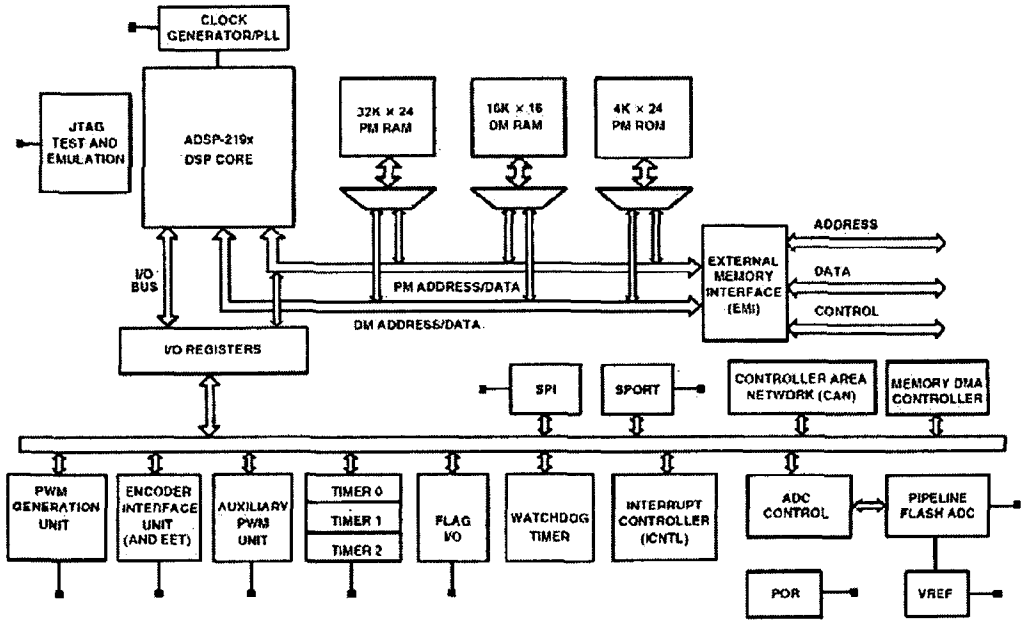

Figure 5.10: Functional block diagram of the ADSP-21992.

5.4 Current measurement

Accurate measurement of the three phase currents was achieved using Honeywell CSNP661 closed-loop current sensors. These sensors are based on the Hall effect and the zero magnetic flux method. The sensor has a transformer with a primary winding and a secondary winding. The sensor outputs a secondary measuring current that is proportional to the primary current. In this case, the primary current is the current flowing in one phase of the SRM. The current carrying conductor to be measured is placed through the aperture of the sensor. This produces a magnetic field that is proportional to the current. The amount of secondary current required to reduce the flux to zero in the sensor core is a measure of the primary current flowing in the conductor multiplied by the ratio of primary to secondary windings. Essentially, the secondary current (the output from the device) is a scaled duplicate, at any time instant, of the primary current. A photo of a sample of Honeywell CSN series current sensors including the CSNP661 is shown in Figure 5.11 (Honeywell CSN series datasheet).

Figure 5.11: Photo of the Honeywell CSN series of current sensors.

The CSNP661 provides 3.5kVrms electrical isolation between the primary (high current) and secondary (electronic) circuits and measures current over a large range of amplitudes and frequencies (dc to 150kHz). The nominal current rating of the CSNP661 is 50A. The CSNP661 has a turns ratio of 1:1000. Thus, with a primary current of 50A, a secondary current of 50mA is produced. For each phase, the wire carrying the phase current was passed through the aperture in the sensor five times. This meant that a phase current of 10A (50A/5 turns) resulted in a full-scale secondary current of 50mA. A measuring resistance of 20Ω was used to give an

output voltage range of 0 to ±1V, as required by the ADC on the EZ-KIT Lite board, for phase currents in the range 0 to ±10A. Figure 5.12 shows the current measurement circuit diagram for a single phase of the SRM. The CSNP661 was powered from ±12V supplies.

In addition to the three identical circuits built for measurement of the phase currents, another similar circuit was designed and built to measure the average dc link current. The average dc link current is required for certain generator control strategies described in Chapter Seven. This circuit diagram is shown in Figure 5.13. As can be seen, the 0 to ±1V output is now low pass filtered using LF353 op-amps to enable calculation of the average current. The wire carrying the dc link current was passed through the sensor aperture 15 times. Hence, a phase current of 3.33A (50A/15 turns) resulted in a full-scale secondary current of 50mA.

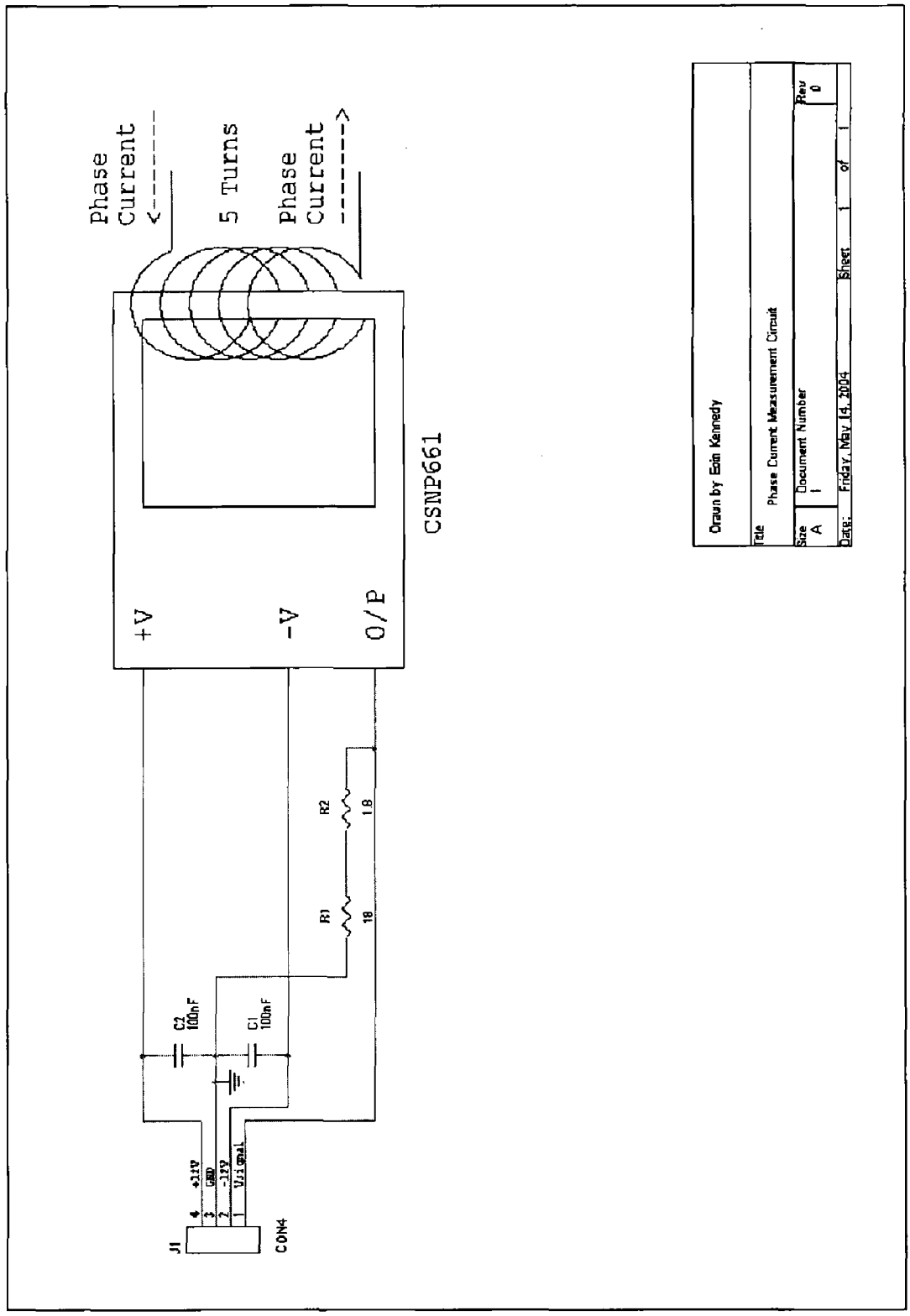

Figure 5.12: Phase current measurement circuit diagram.

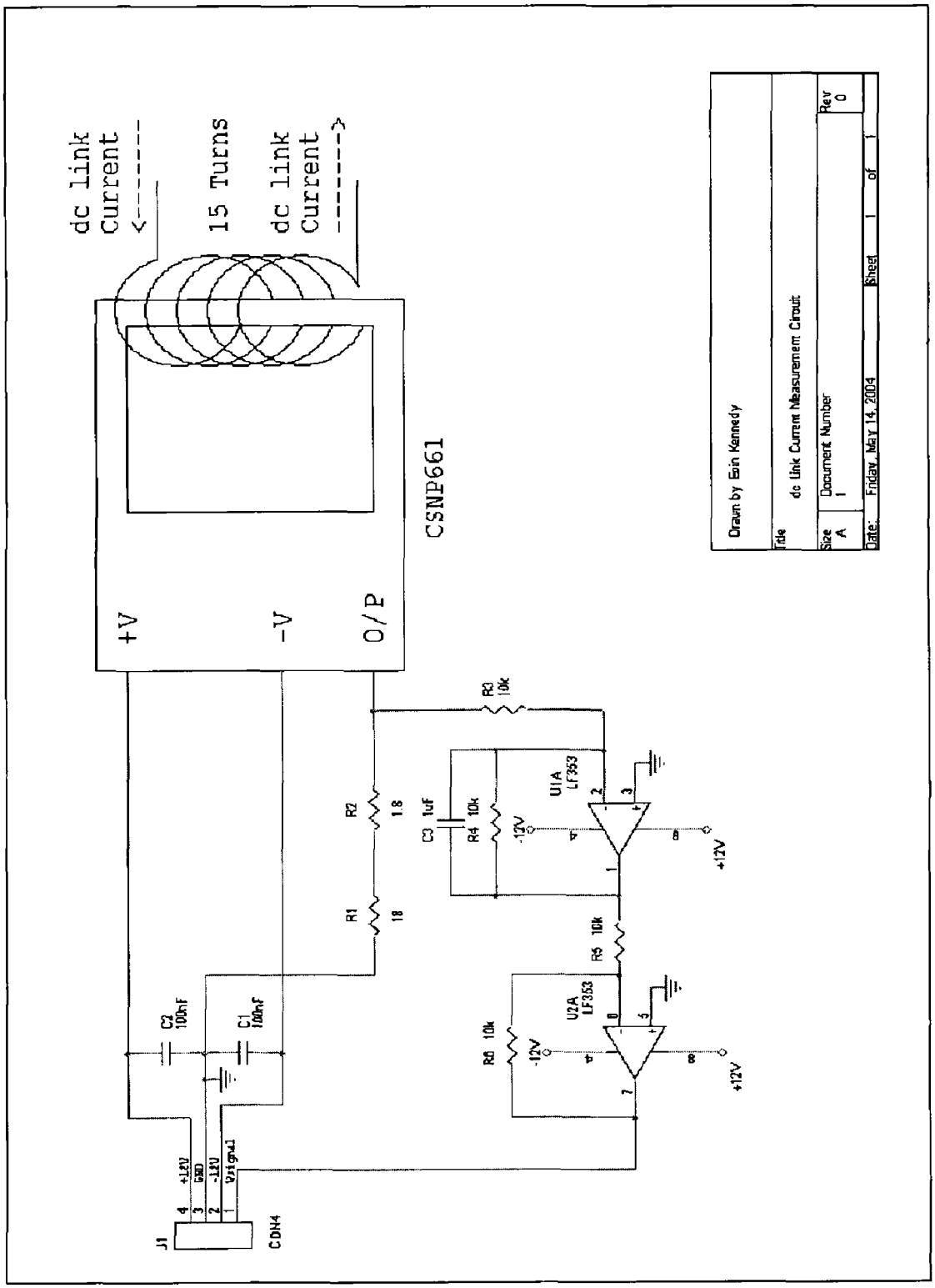

Figure 5.13: Dc link current measurement circuit diagram.

5.5 Voltage measurement

The control objective when the SRM is operating in generating mode is to maintain the dc link voltage at the desired value while achieving maximum efficiency. It is clear then that accurate measurement of the dc link voltage is a fundamental requirement for the successful implementation of any SR generator control strategy. A voltage measurement circuit was designed and built that outputs a voltage in the range 0 to 1V, as required by the ADC on the EZ-KIT Lite board, corresponding to dc link voltages in the range 0 to 100V. In addition, the circuit provides electrical isolation between the high voltage dc link and the low voltage ADSP-21992 EZ-KIT Lite board. The voltage measurement circuit diagram is shown in Figure 5.14.

The HCPL-7800 high Common-Mode Rejection (CMR) isolation amplifier is ideal for applications that require high accuracy, stability and linearity under severe noise conditions such as might be encountered in an SRM operating environment. A voltage divider reduces the 0 to 100V dc link voltage to a value between 0 and 0.375V at the input of the HCPL-7800. The HCPL-7800 has a mean gain value of eight resulting in a 0 to 3V differential voltage between pins 6 and 7 of the HCPL-7800. The differential output of the isolation amplifier is converted to a ground-referenced single-ended output using the simple differential amplifier circuit implemented using a LM358N op-amp. Finally, the 0 to 3V output of the differential amplifier circuit is reduced to a 0 to 1V output using a simple voltage divider. This signal is then routed to the ADC input signal connector on the EZ-KIT Lite board. Certain practical implementation factors had to be taken into account. The gain of the HCPL-7800 had a ±5% tolerance. In addition, the resistors used in the differential amplifier circuit were unequal due to manufacturing tolerances. This meant that a gain of 94 returned the correct dc link voltage in tests as opposed to the ideal value of 100.

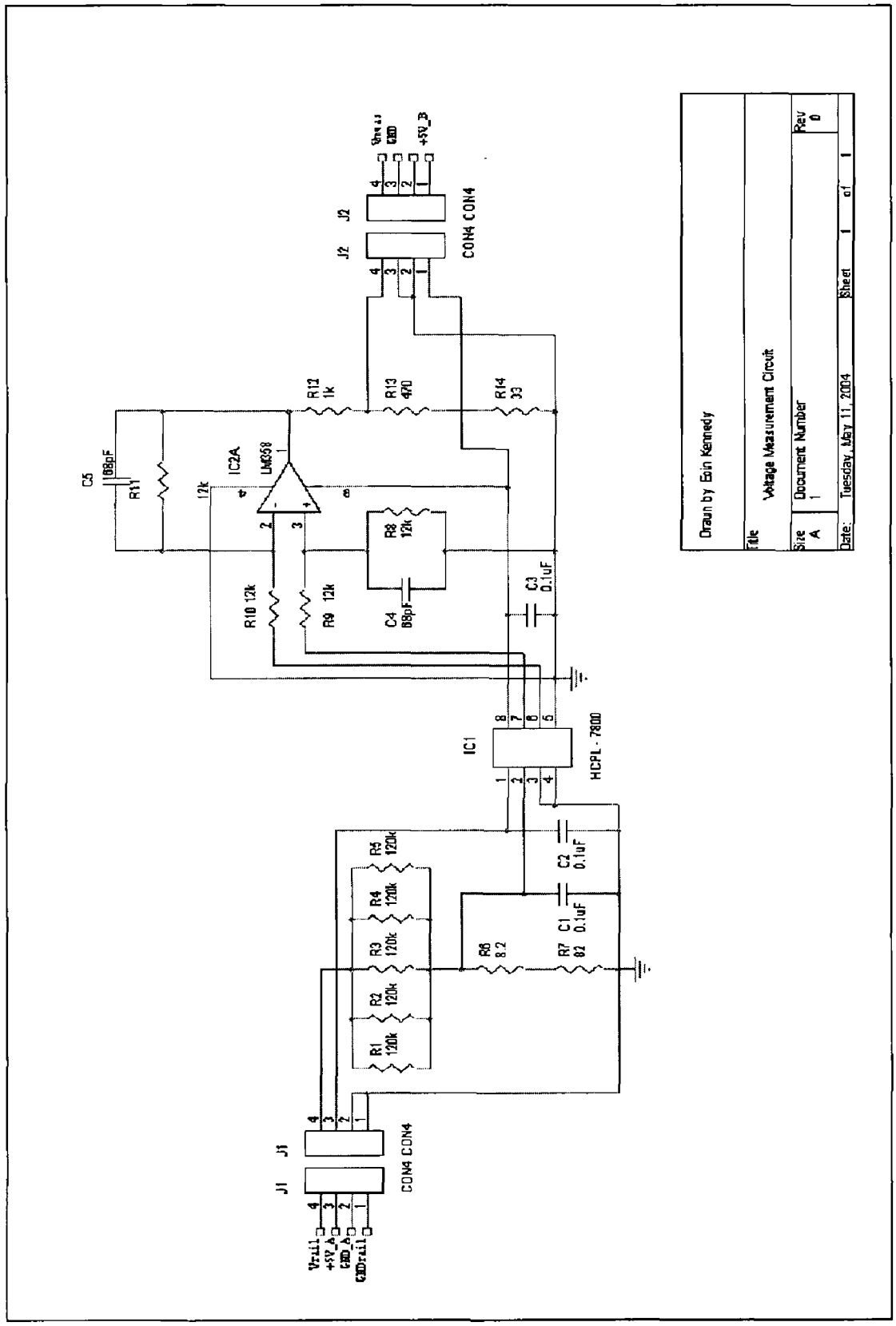

Figure 5.14: Dc link voltage measurement circuit diagram.

5.6 Position sensor and speed estimation

Accurate rotor position information is of extreme importance for the smooth control of the SRM when operating either as a motor or as a generator. The rotor position can be determined using either a shaft position transducer or by implementing a sensorless rotor position technique. Sensorless operation of SRMs has received considerable attention in the literature over the years (Husain 1996). Sensorless operation has the obvious advantage of reducing the overall cost of the SR drive by eliminating the shaft position transducer. However, the main drawback of sensorless operation is the often considerable real-time computation required and its effect on the starting and running performance of the drive over wide ranges of speed and load torque. In the work described in this thesis, rotor position information was derived independently from two shaft position transducers, a simple slotted optical disk encoder and an incremental encoder.

5.6.1 Simple slotted optical disk encoder

The 12/8 SRM employed in the experimental set-up had a position encoder attached to its rotor. This encoder employs a circular slotted disk which is used to determine rotor position in conjunction with an encoder interface circuit (incorporating an optocoupler). The circular disk is constructed with slots of various widths cut out of the disk. The particular slots/spacings are such that as the disk rotates past the optocoupler in the encoder interface circuit, the resultant electronic signal is a sequence of highs (8V) and lows (0V) corresponding to the position of the blades and slots on the disk itself.

Figure 5.15 shows the movement of the encoder disk when the SRM is rotating in the clockwise direction. The positions marked on the diagram, for example *Amin* and *Amax*, refer to the points on the blade pattern corresponding to certain physical values. The *max* values are the maximum inductance positions (in other words, complete phase alignment) while the *min* values refer to the minimum inductance positions. These positions were determined by using an inductance meter. The inductance on each phase with respect to the rotor position was measured as the rotor was rotated slowly. The maximum inductance positions for each phase were verified by pulsing each phase so that the rotor moved to alignment. The position of the disk with respect to the optocoupler was then recorded. The minimum inductance position is then 22.5

degrees from the maximum position (since this is a 12/8 SRM, the patterns repeat themselves every 45 degrees). Figure 5.15 also shows an end elevation of the SRM. Figure 5.16 shows the output signal from the encoder interface board as well as the inverted encoder signal inputted to the timer on the ADSP-21992 EZ-KIT Lite board.

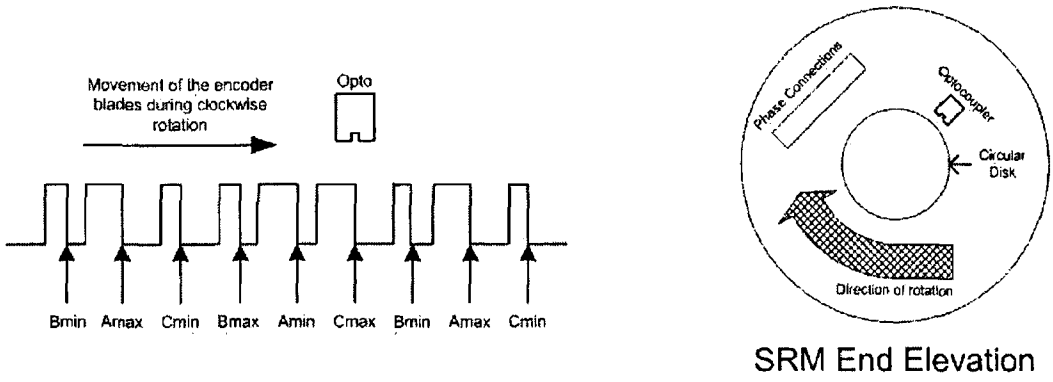

Figure 5.15: Movement of the encoder disk when the SRM is rotating in the clockwise direction. An end elevation of the SRM is also shown.

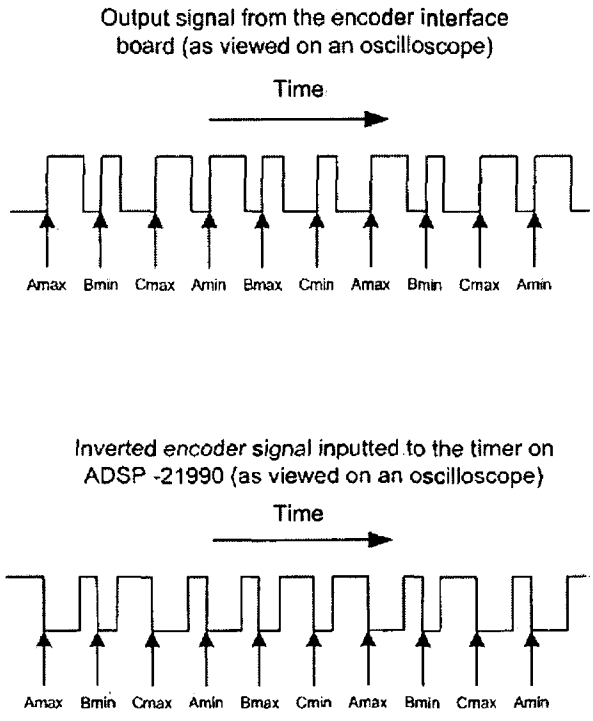

Figure 5.16: Output signal from the encoder interface board and the inverted encoder signal inputted to the timer on the ADSP-21992 board.

The widths of a succession of either high or low pulses were measured depending on the direction of rotation (high pulses if running clockwise, low pulses if running anti-clockwise) using a general-purpose timer on the ADSP-21992. Through the sequence of the last three 'results', the rotor position could be determined as shown in Table 5.3 where t1=last measured width, t2=second last measured width, t3=third last measured width, r1=last result, r2=second last result and r3=third last result.

	Running clockwise				Running anti-clockwise			
t1<t2 ⇒ r1=0 t1>t2 ⇒ r1=1 else if t1=t2: t2<t3 ⇒ r1=0 t2>t3 ⇒ r1=1	r1	r2	r3	Position	r1	r2	r3	Position
	1	1	0	Amax	1	0	1	Amax
	0	1	1	Bmin	0	1	0	Cmin
	1	0	1	Cmax	0	0	1	Bmax
	0	1	0	Amin	1	0	0	Amin
	0	0	1	Bmax	1	1	0	Cmax
	1	0	0	Cmin	0	1	1	Bmin

Table 5.3: Position determination.

However, this type of position determination was not adequate for the SRM control as the absolute angular position was desired. To achieve this, every time *Amax* was reached, a timer (TIMER1) was started. The next time *Amax* was reached the timer was stopped. The value of the timer was then read and the timer restarted. The absolute position in degrees was derived in the running program by reading the value of the running timer, dividing it by the period (the count value from *Amax* to *Amax*) and then multiplying it by 45. Thus, 0 degrees corresponds to phase A in alignment and 22.5 degrees corresponds to phase A unaligned. The angular position of the rotor with respect to phase A was easily related to phases B and C using a constant offset of 15 degrees for phase C and 30 degrees for phase B.

5.6.2 Incremental encoder

Derivation of position information using the simple slotted disk encoder in the manner outlined above proved to be computationally intensive. Therefore, it was decided to employ a rotary incremental encoder instead.

The incremental encoder has a circular track consisting of uniformly spaced alternating dark and clear lines. The incremental encoder outputs two square waves that are 90° out of phase with each other and these outputs are fed directly to the EIU on the ADSP-21992. The EIU can be programmed to decode their relative phase to determine the direction of rotation and count the quadrature states in each cycle. Thus, a resolution equal to four times the line count on the encoder disk is achieved. The shaft position at any instant is determined by the accumulated pulses from the starting position.

For this project, a Heidenhain ROD426 encoder with a 4096 line count was used. Thus, there are 16,384 increments per revolution of the rotating shaft (or 2048 increments every 45 degrees). This ensures very accurate position determination with a resolution of 0.022 degrees. Figure 5.17 shows the differential quadrature pulse signals outputted by the Heidenhain ROD426 encoder.

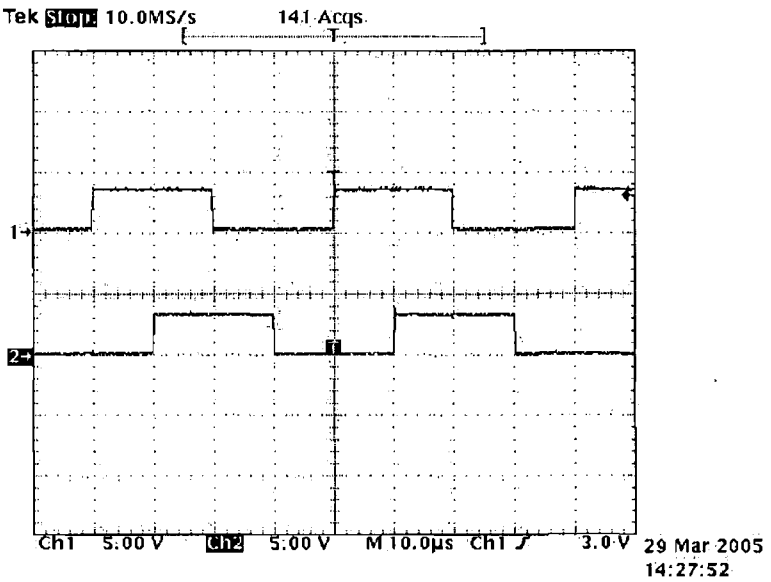

Figure 5.17: The differential quadrature pulse signals (Channel 1 – pulse output A) (Channel 2 – pulse output B) outputted by the Heidenhain ROD426 encoder.

Another track on the encoder disk is used to provide an index signal that occurs once per revolution called a zero marker. This is used to derive absolute position information. Figure 5.18 shows a typical incremental encoder (Optical encoders 2005).

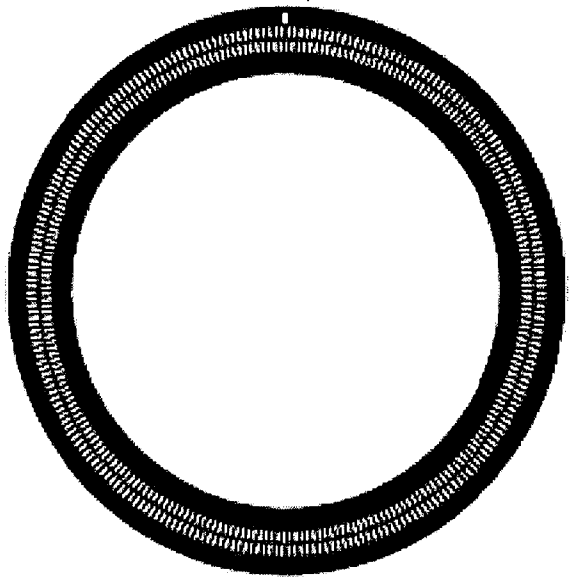

Figure 5.18: Typical incremental encoder.

The EIU was initialised by writing the value 2047 to the EIUMAXCNT register. As already mentioned, 2048 increments corresponds to 45 mechanical degrees. Thus, when the up/down counter reached 2047, the counter was reset to zero. The counter was also reset on the occurrence of the zero marker signal. This mode is selected by setting bit 1 of the EIUCTRL register. To return a position between 0 and 45, the running counter was read each control cycle. Its value was divided by 2048 and the result was multiplied by 45.

5.6.3 Speed estimation

Feedback from the incremental encoder was used to estimate the rotational speed of the SRM. The speed estimation was first implemented using a 32-bit general-purpose timer and then using the Encoder Event Timer (EET) module associated with the EIU.

5.6.3.1 Speed estimation using a general-purpose timer

The derived rotor position is in the form of a value between 0 and 45 degrees. A timer is started when the first position sample between 0 and 0.5 degrees is returned. The timer count is then read when the first position sample between 44.5 and 45 degrees is detected. This timer count value is converted into time (in seconds) and the timer stopped. Thus the time taken for the rotor to turn through 45 degrees approximately

(or one-eight of a revolution) is known. Since speed is distance/time, the speed in revs/second can be found by dividing the number of revolutions through which the rotor has rotated by the time taken to complete this distance. In this case, the number of revolutions completed is 0.125 (45 degrees/360 degrees). The speed measurement is extended to the standard revs/minute by multiplying the calculated speed in revs/second by 60.

5.6.3.2 Speed estimation using the EET

The EET can be used to accurately time the interval between encoder pulses enabling precise computation of the SRM rotational speed. The EET clock frequency was set equal to the HCLK frequency. The contents of the 16-bit encoder event timer register are incremented on the rising edge of the clock frequency. A pulse decimator output train at 1/8 of the quadrature signal frequency was produced by writing a value of 8 to the EETN register. The rising edge of this decimated signal is termed a velocity event. On each occurrence of a velocity event, the contents of the event timer are stored in an intermediate interval time register. The EET was programmed to latch the contents of this interval time register to the EETT register every time the EIUCNT register was read (every control cycle) by clearing bit 4 of the EIUCTRL register. The EETT register was then read and its contents converted to time (in seconds). The distance in revolutions travelled is equal to 8/16384 = 0.000488 revolutions. As before the speed in revolutions per second was found by dividing the distance travelled by the time taken. Finally, the speed in rpm was determined by multiplying the speed in revs/second by 60.

Figure 5.19 shows the estimated speed for the 512 values that were returned by both speed estimation methods when the rotor turned through ¼ of a revolution (90 mechanical degrees) at a speed of approximately 1000rpm. The solid line corresponds to the speed estimated by the EET while the broken line is the speed estimated when using the general-purpose timer.

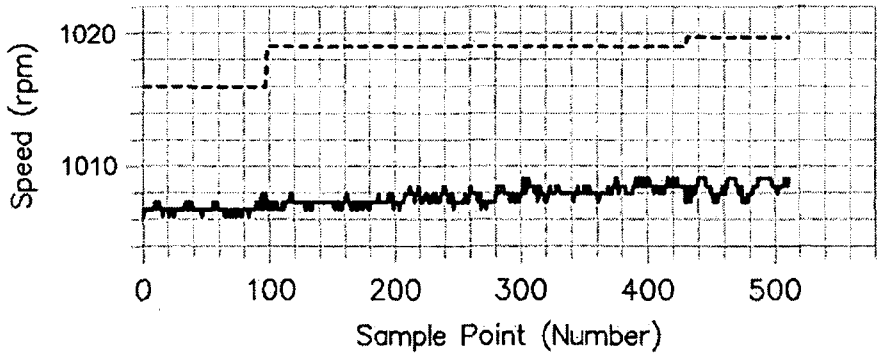

Figure 5.19: Estimated speed values returned by the EET estimation method (solid line) and the general-purpose timer estimation method (broken line) for operation at approximately 1000rpm.

Speed estimation using the EET is superior to the method employing the general-purpose timer for several reasons. Firstly, the speed measurement is updated far more frequently when the EET is employed. This is important if, for example, there is a sudden change in rotational speed in that it can be detected and dealt with more quickly. In addition, the general-purpose timer is started at the first sampled position between 0 and 0.5 degrees and stopped at the first sampled position between 44.5 and 45 degrees. Therefore, the exact distance travelled is likely to vary slightly (between 44 and 45 degrees), although any error will be relatively small. This isn't the case for the EET implementation where the distance travelled each time is identical.

5.7 Experimental SRM development set-up

A block diagram of the overall experimental set-up for the SRM control development is shown in Figure 5.20. As can be seen, the SRM was coupled to a permanent magnet dc motor that served a dual purpose: the dc motor acted as a load when the SRM was in motoring mode and as a prime mover when the SRM was in generating mode. The dc servomotor employed was a member of the TT series of motors built by Inland. It was controlled using a controller also designed by Inland. A tachometer on the dc servomotor was used to verify the accuracy of the speed estimation methods outlined in Section 5.6.3.

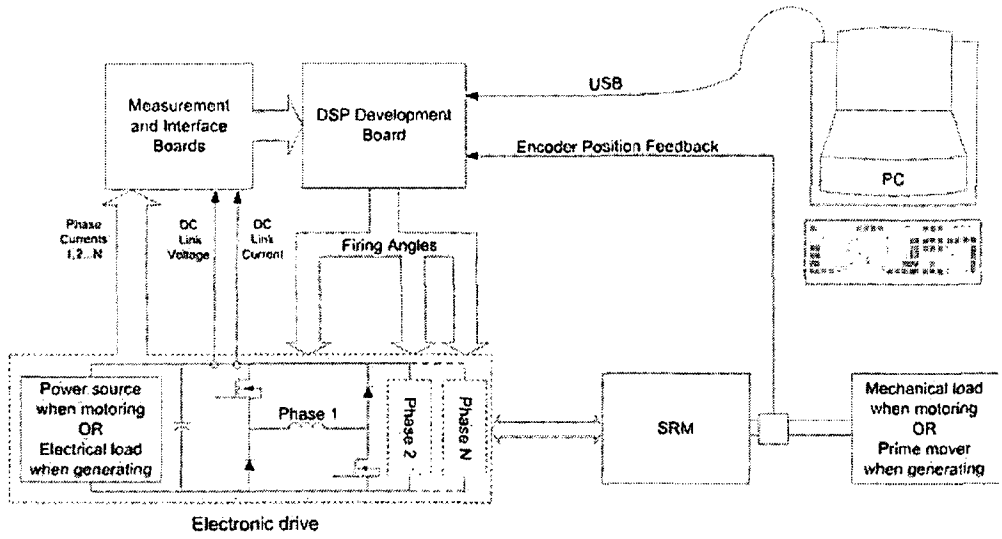

Figure 5.20: Block diagram of the overall experimental set-up for the SRM.

When motoring, a 70V, 4A power supply was used as the power source. When generating, the dc link capacitor bank (approximately 41mF; consisting of eight 5100uF capacitors connected in parallel) had a Kikusui PLZ1003W electronic load connected across it enabling exact control of the load current etc.

Originally, an interface circuit was designed and built that routed the measurement and encoder signals from the associated electronics to the DSP and routed the gate drive signals from the DSP to the power converter. This original interface board didn't optically isolate the DSP from the gate drive signals. As part of a project undertaken by another student, a new interface board that optically isolated the drive signals from the DSP and which provided a distribution point for the power supplies used by the various measurement electronics and encoder circuitry was designed and built. In addition, a power supply board that derived the various regulated power supplies for the DSP, measurement electronics, encoder circuitry and interface board was designed and built (described in the report (Murphy 2002)). This report also describes the incorporation of all the electronics into a prototype assembly. Appendix A shows the schematic drawings of both the original and updated interface boards, the schematic drawings of the power supply circuitry as well as photos of the experimental SRM development set-up.

Chapter Six – Experimental motor control

6.0 Introduction

In this chapter, the experimental implementation of several control strategies developed for SR motor operation is described. The 'start-up' algorithm employed in the experimental set-up for SR motor start-up is presented. Four simple SR motor speed control schemes for torque ripple-tolerant applications are described and experimental results are presented. Three of these control schemes are for low speed motoring operation while the fourth is aimed at high speed motoring in single pulse mode. This is followed by the implementation of the nonlinear self-tuning model of the SRM that can serve as a torque observer. This torque observer is then employed in the experimental implementation of the neuro-fuzzy control strategy no. 3 that was previously described and tested through simulation in Chapter Four. The results arising from the experimental implementation and testing of the SR motor torque ripple minimisation control strategy are presented.

6.1 SRM start-up algorithm

It is necessary to synchronise the excitation of the phase windings with rotor position for effective control of the SRM. Therefore, for motor start-up, the exact rotor position has to be identified. In the experimental SRM set-up, an incremental position encoder is employed for the rotor position determination as outlined in Section 5.6.2. The use of such an incremental encoder (as opposed to an absolute position encoder) requires that a start-up technique/algorithm be employed to determine the starting position of the rotor. A simple, but highly effective, method of starting the motor, which was implemented successfully on the experimental SRM system is now outlined.

The key idea behind this SRM start-up technique is to align one pair of rotor poles with a specific phase by excitation of that particular phase winding. This provides a reference position for motor start-up. In this implementation, phase A is excited by applying two current pulses in quick succession. It is important that the excitation period, T_{pulse}, be long enough to ensure a sufficiently large torque that can overcome the load and friction and guarantee that the rotor poles reach alignment with phase A. The aligned position of phase A is then assigned the 0 degree point on the SRM by

writing to the EIUCNT_LO register. As described in Section 5.6.2, a position between 0 and 45 degrees is returned every control cycle during subsequent SRM rotation after the start-up algorithm is finished.

With the initial position of the rotor known, the direction of subsequent rotor movement is determined by the firing sequence. For clockwise rotation of the SRM, the three phases are excited in the sequence A-C-B. Alternatively, if anti-clockwise rotation is desired, the phases are excited in the reversed sequence of A-B-C. To ensure that the rotor begins rotation in the desired direction, the start-up algorithm briefly excites either phase C (for clockwise rotation) or phase B (for anti-clockwise rotation) to ensure that the rotor starts to move in the desired direction. At this point, the start-up procedure is complete and the motor control algorithm takes over. Figure 6.1 shows a flowchart for the motor start-up procedure.

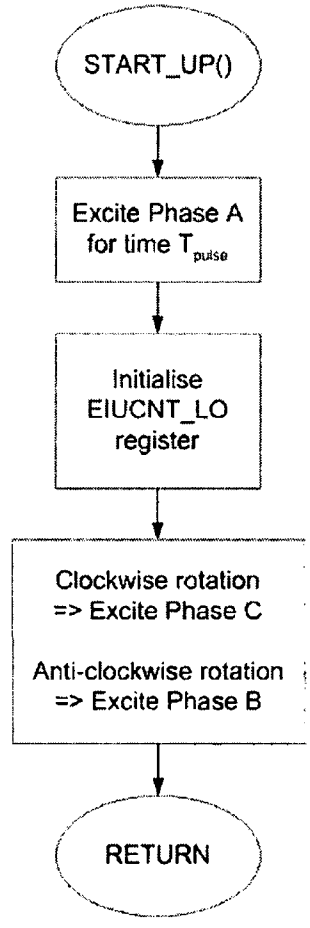

Figure 6.1: Flowchart of the SRM start-up procedure for motoring operation.

The start-up technique is relatively simple. However, the technique may not be applied to certain load configurations. For example, this technique could not be employed if the load can not tolerate reverse rotation during start-up. This is because, when phase A is excited, the rotor will move towards alignment with phase A but the direction of rotor movement is dependent on the initial position of the rotor poles with respect to phase A. Consequently, motion can not be guaranteed to be in the forward direction (Arefeen 1998).

6.2 Motor speed control for torque ripple-tolerant applications

When the motor start-up procedure is finished, an appropriate motor control algorithm is required to achieve the desired control objectives. For SR motor applications that are tolerant of torque ripple or nonservo-type applications (pumps, fans, compressor drives etc.), simple control strategies can be employed to excite the SRM and control the speed. Different control strategies are required for low speed motoring operation and high speed motoring operation. The design and implementation of simple control schemes that enable motoring operation over the entire speed range of the SRM is now described.

6.2.1 Low speed motoring – current regulation

As described in Section 2.5.1, at low motoring speeds the back-emf is small compared to the supply voltage necessitating a control scheme that can limit or regulate the current by chopping of the current waveform. The experimental implementation and testing of three SR motor speed control strategies for low speed operation is now described.

6.2.1.1 Simple control strategy

A very simple control scheme that requires no prior knowledge or characterisation of the SRM is that shown in block diagram form in Figure 6.2.

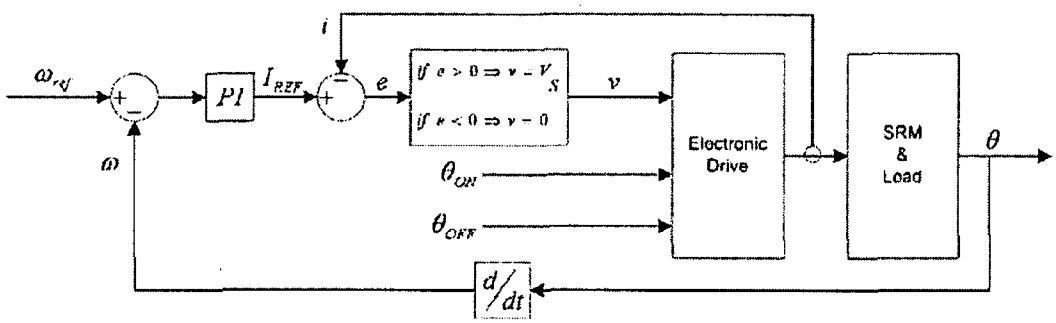

Figure 6.2: Block diagram of a simple control scheme for low speed motoring operation.

The speed, ω, is measured and compared to the reference speed, ω_{ref}. The speed error is then used by the PI controller to produce a current reference, I_{REF}, about which the phase currents are controlled using delta modulation current control. The control scheme shown in Figure 6.2 employs soft chopping in the delta modulation control throughout the entire conduction angle, θ_D, i.e. the voltage across the phase winding switches between V_S and 0. The initial turn-on angle, θ_{ON}, is selected by the user as is the turn-off angle, θ_{OFF}. At θ_{OFF}, both power switches are switched off placing $-V_S$ across the winding. This results in the current decreasing rapidly to zero.

The control strategy was implemented with the experimental 12/8 SRM set-up. The PI controller was tuned manually. The resultant constants, P and I, were P = 0.002 and I = 0.02. The control strategy was tested for different reference speeds with constant firing angles of θ_{ON} = 22.5 degrees before alignment (the unaligned position) and θ_{OFF} = 4 degrees before alignment. These firing angles result in an overlap of 3.5 degrees where two phases are controlled simultaneously before the phase that is approaching alignment is switched off (demagnetised). Figure 6.3 shows the current in phase A, the switch signals for phase A and a pulse waveform in which the pulse indicates the aligned position of phase A for a reference speed of 300rpm. Figure 6.4 shows the motor speed samples as calculated by the ADSP-21992 control program (using the general-purpose timer method outlined in Section 5.6.3.1) during steady-state operation for a reference speed of 300rpm. Each sample point in Figure 6.4 represents an updated speed estimate that is calculated approximately every 45 degrees. As described in Section 5.6.3.2, the exact distance travelled by the rotor between the

speed sample points varies slightly (between 44 and 45 degrees) and this results in ripple/difference in the speed estimates. Ideally, the speed samples would be constant.

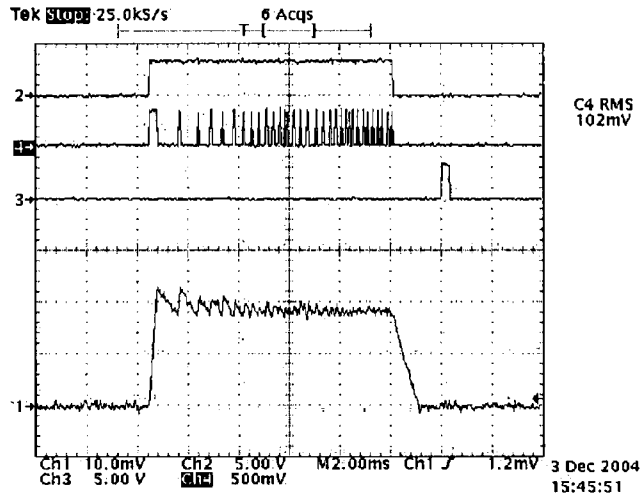

Figure 6.3: Current in phase A (Channel 1 – 1A/div), phase A switch signals (Channels 2 and 4) and pulse waveform indicating the aligned position of phase A (Channel 3) for the simple control strategy with a reference speed of 300rpm.

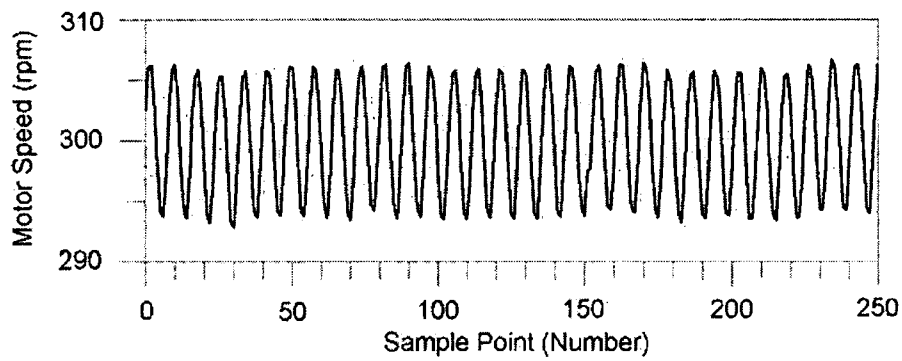

Figure 6.4: Calculated motor speed for the simple motor control strategy with ω_{ref} = 300rpm.

Figure 6.5 shows the current in phase A, the switch signals for phase A and a pulse waveform where a pulse indicates the aligned position of phase A for a reference speed of 650rpm. Figure 6.6 shows the three phase currents sampled by the ADC and used by the ADSP-21992 control program in the delta modulation current control for the same reference speed of 650rpm. Also shown in Figure 6.6 is the current reference (thick black line) outputted every control cycle by the PI controller. As can be seen,

the actual current waveform shown in Figure 6.5 and the sampled current waveforms shown in Figure 6.6 are very similar, verifying the accuracy of the ADC current measurement. Figure 6.7 shows the motor speed as calculated by the ADSP-21992 control program during steady-state operation for a reference speed of 650rpm.

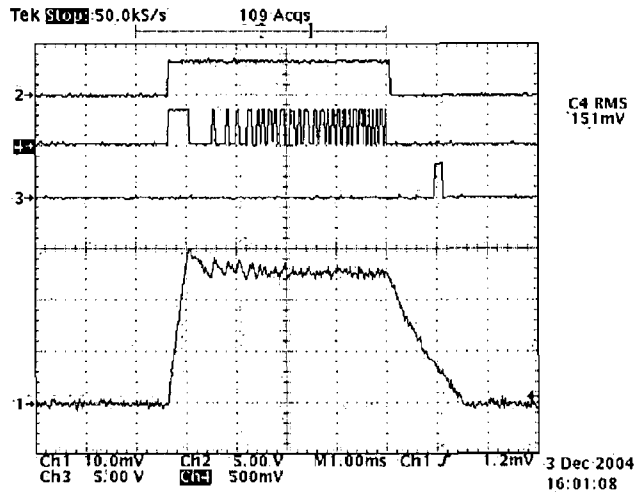

Figure 6.5: Current in phase A (Channel 1 – 1A/div), phase A switch signals (Channels 2 and 4) and pulse waveform indicating the aligned position of phase A (Channel 3) for the simple control strategy with a reference speed of 650rpm.

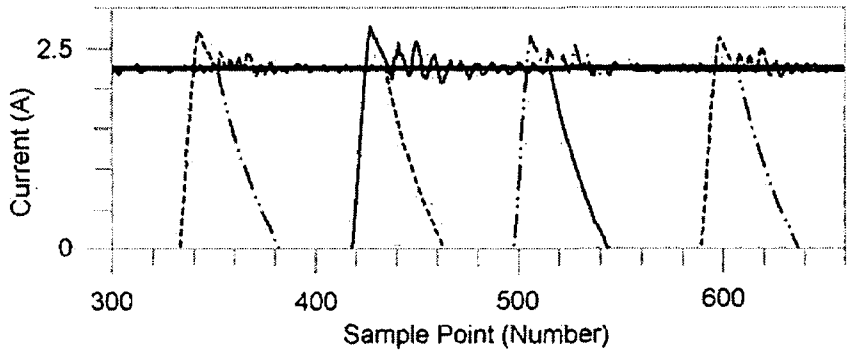

Figure 6.6: The three phase current waveforms sampled by the ADC and used by the ADSP-21992 in the delta modulation current control and the current reference (thick black line) outputted every control cycle by the PI controller for a reference speed of 650rpm.

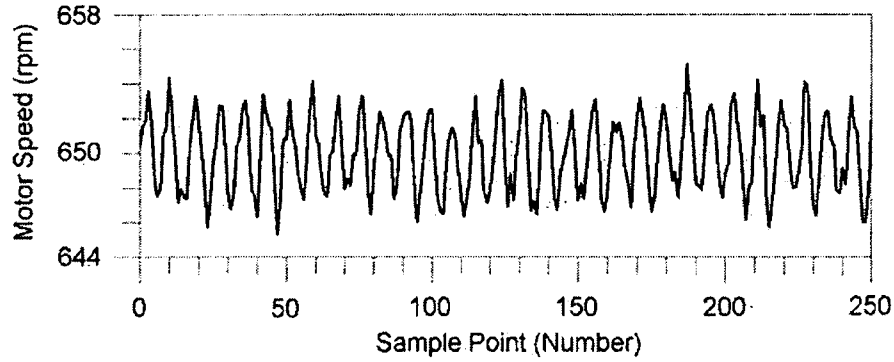

Figure 6.7: Calculated motor speed for the simple control strategy with ω_{ref} = 650rpm.

While this simple control strategy has the obvious advantage of requiring no characterisation or prior knowledge of the SRM (apart from geometrical machine information such as the number of poles, phases etc.), it has a number of disadvantages. Firstly, the employment of constant turn-on and turn-off angles results in poor efficiency levels. Also, on examining Figures 6.3 and 6.5, it can be seen that with a constant turn-off angle of θ_{OFF} = 4 degrees before alignment, the current in phase A when motoring at 300rpm reduces to zero in advance of the aligned position whereas when motoring at 650rpm, current continues to flow for some time after the rotor has passed alignment. To ensure higher positive torque production and to prevent the production of negative torque, the phase current should return to zero just as alignment is reached.

6.2.1.2 Automatic turn-off angle control strategy

Turning off the power switches too far in advance of the aligned position reduces the average torque produced by the SRM while the presence of current in the phase winding after alignment results in the production of negative torque, which also reduces the average torque. For this reason, a new control scheme was developed which automatically selects the turn-off angle (according to an algorithm based on the motor speed) to ensure that the phase current reduces to zero just before alignment.

The appropriate turn-off angle that results in the reduction of the phase current to zero at alignment was determined experimentally for motoring operation with a constant

mechanical load at several different speed setpoints. Figure 6.8 shows the relationship between the desired turn-off angle and the motor speed when a turn-on angle of 22.5 degrees before alignment was employed. Also shown in Figure 6.8 is a polynomial approximation to the experimental data. A second order polynomial was employed and it can be represented mathematically by equation (6.1) (where the speed, ω, is in hundreds of rpm).

$$\theta_{OFF} = 0.1339 * \omega^2 - 0.1196 * \omega + 0.9357 \qquad (6.1)$$

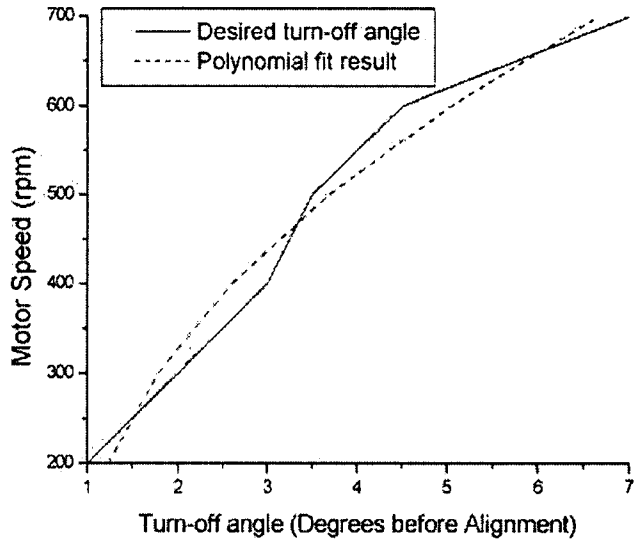

Figure 6.8: Actual and polynomial fit relationships between the motor speed and the turn-off angle for a constant mechanical load that results in phase current reduction to zero just before alignment.

A block diagram of the control scheme that enables the automatic selection of the appropriate turn-off angle for any given motoring speed is shown in Figure 6.9. The only difference in operation between the scheme shown in Figure 6.9 and that shown in Figure 6.2 is in the calculation of θ_{OFF}.

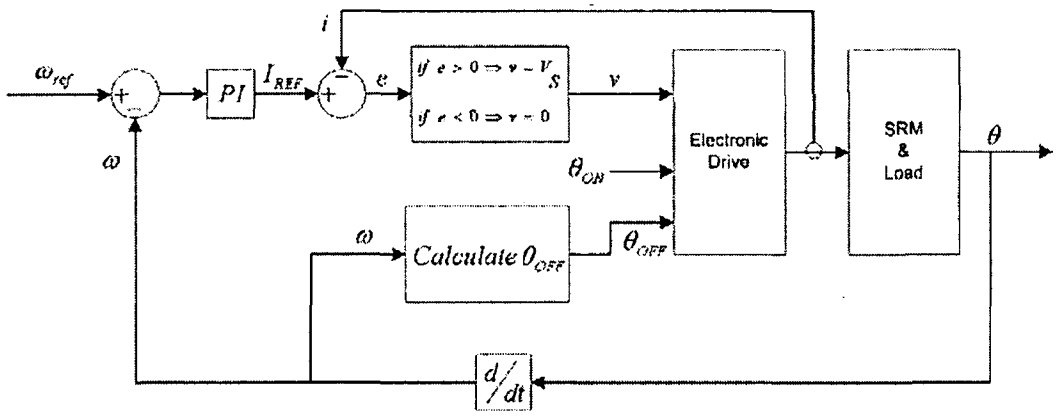

Figure 6.9: Block diagram of the control scheme that enables the automatic selection of the appropriate turn-off angle for low speed motoring operation that results in phase current reduction to zero just before alignment.

This control scheme was tested experimentally for various operating speeds with the PI controller constants unchanged from the simple control scheme (P = 0.002 and I = 0.02). Figure 6.10 shows the current in phase A, the switch signals for phase A and the pulse waveform that indicates the aligned position of phase A for a reference speed of 300rpm. θ_{ON} is chosen as 22.5 degrees before alignment and θ_{OFF} is determined from the relationship in equation (6.1). The same waveforms are shown in Figure 6.11 for a reference speed of 650rpm with constant θ_{ON} = 22.5 degrees before alignment and θ_{OFF} is determined automatically as before. Figure 6.12 shows the initial speed response of the experimental system to a 300rpm reference speed. The signal shown in the graph is derived from a tachometer on the dc servomotor. The shaft of the servomotor is coupled to the shaft of the 12/8 SRM in the experimental set-up. The tachometer outputs a signal whose amplitude is proportional to speed (12.5V per 1000rpm). As can be seen in Figure 6.12, the speed settles to 300rpm in under 3 seconds. The transient speed response of the system to a 650rpm speed reference is shown in Figure 6.13. The speed of the motor settles to 650rpm rapidly (approximately 4 seconds). By examining Figures 6.12 and 6.13, it is evident that there is a non-monotonic response at the start of the transient. This occurs for the following reason. At start-up, phase A is excited with a large current to ensure that the torque produced is sufficient to overcome the load and friction and guarantee that the rotor poles reach alignment for position initialisation. For the responses shown in Figures 6.12 and 6.13, the load is relatively small and hence the SRM accelerates very

quickly at start-up leading to the sudden large jump in speed that is clearly visible in the two figures. The motor control algorithm then takes over and controls the SRM speed as desired.

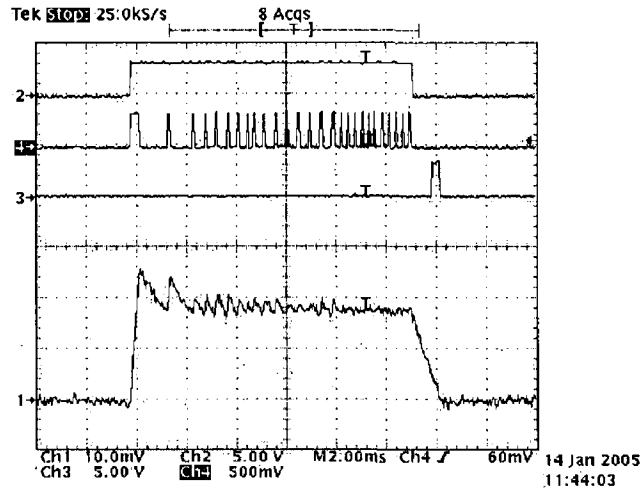

Figure 6.10: Current in phase A (Channel 1 – 1A/div), phase A switch signals (Channels 2 and 4) and pulse waveform indicating the aligned position of phase A (Channel 3) for a reference speed of 300rpm with constant θ_{ON} = 22.5 degrees before alignment and θ_{OFF} determined using equation (6.1).

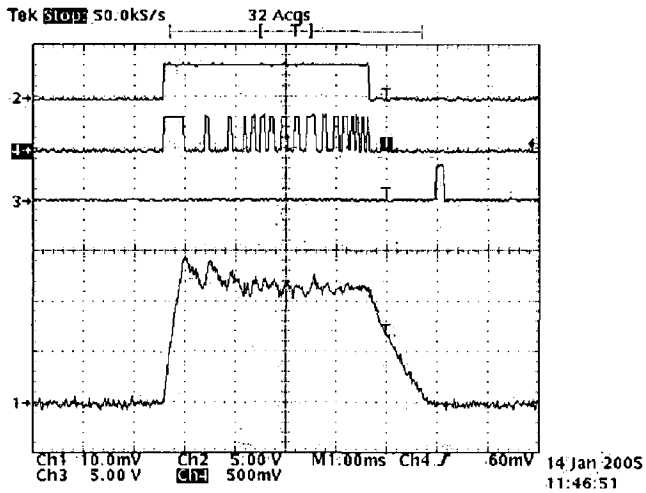

Figure 6.11: Current in phase A (Channel 1 – 1A/div), phase A switch signals (Channels 2 and 4) and pulse waveform indicating the aligned position of phase A (Channel 3) for a reference speed of 650rpm with constant θ_{ON} = 22.5 degrees before alignment and θ_{OFF} determined using equation (6.1).

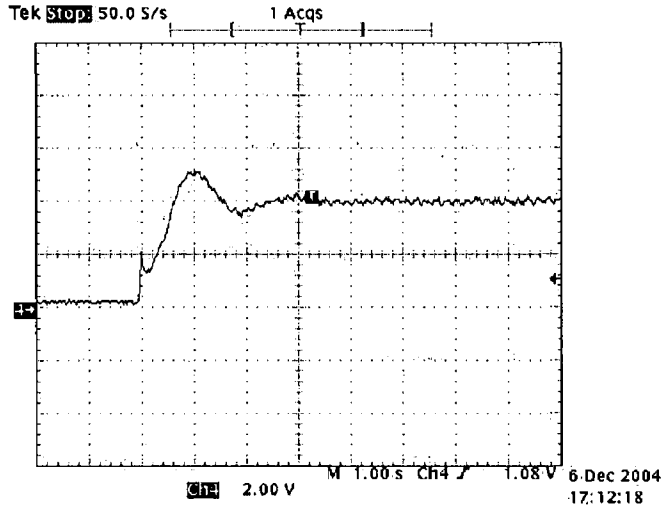

Figure 6.12: Transient speed response of the automatic turn-off angle control strategy for low speed motoring with a 300rpm speed reference (the amplitude of the tachometer signal is proportional to the speed - 12.5V/1000rpm).

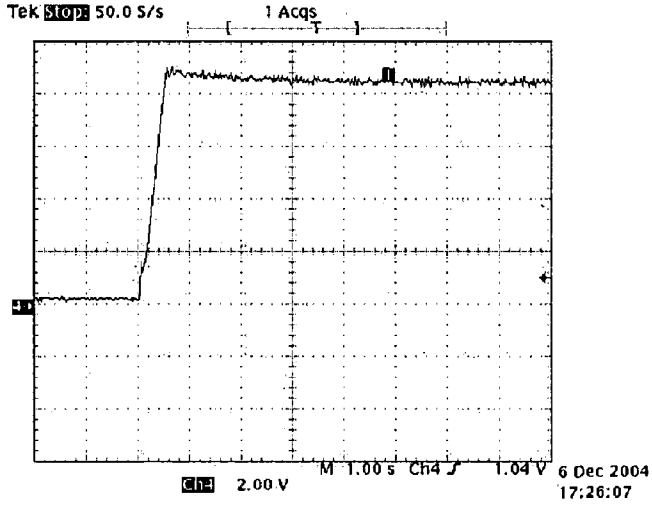

Figure 6.13: Transient speed response of the automatic turn-off angle control strategy for low speed motoring with a 650rpm speed reference reference (the amplitude of the tachometer signal is proportional to the speed - 12.5V/1000rpm).

Examining Figures 6.10 and 6.11 and comparing them with Figures 6.3 and 6.5, it is clear that at 300rpm, the current now flows until the aligned position while at 650rpm the current no longer flows past the point of alignment, thereby avoiding the production of negative torque. Thus, this control scheme results in improved operation over the very simplistic scheme described in Section 6.2.1.1. However, this particular control scheme is still limited. In its present form, a constant turn-on angle (22.5 degrees before alignment was used but there is no rationale for this choice) must

be employed and the mechanical load must be constant. It is possible, however, to extend this control scheme to operate with a changing load and variable turn-on angle.

6.2.1.3 Extended automatic turn-off angle control strategy

Figure 6.8 shows the relationship between the desired turn-off angle and the motor speed for one particular constant load, a relationship that may also be described mathematically by equation (6.1). However, for a given speed reference, the current reference signal outputted by the PI controller, I_{REF}, will increase if the mechanical load is increased and decrease if the mechanical load is reduced. Therefore, to extend the control scheme to handle a changing load, a mathematical model relating the desired turn-off angle to both motor speed and the current reference must be developed.

At five different speed setpoints ranging from 200rpm to 600rpm (in increments of 100rpm), the appropriate turn-off angle that results in the reduction of the phase current to zero at alignment was determined experimentally for motoring operation with different mechanical loads when a turn-on angle of 22.5 degrees before alignment was employed. Figure 6.14 shows the relationship between the desired turn-off angle and the PI controller current reference at each motor speed setpoint. The changing mechanical load is reflected in the PI controller current reference signal values.

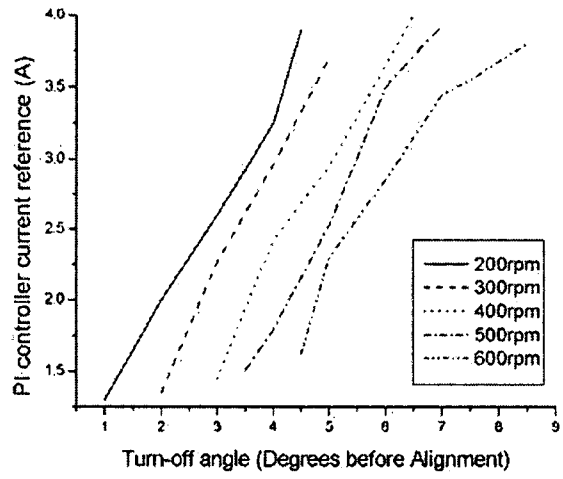

Figure 6.14: Relationship between the PI controller current reference and the turn-off angle that results in phase current reduction to zero at alignment for each motor speed setpoint.

At each motor speed setpoint, a second-order polynomial was employed to approximate the experimental data. These polynomial approximations can be represented mathematically by equations (6.2) – (6.6).

$$At\ 200rpm: \quad \theta_{OFF} = -0.1526 * I_{REF}^2 + 2.1891 * I_{REF} - 1.6467 \tag{6.2}$$

$$At\ 300rpm: \quad \theta_{OFF} = 0.0964 * I_{REF}^2 + 0.8020 * I_{REF} + 0.7293 \tag{6.3}$$

$$At\ 400rpm: \quad \theta_{OFF} = 0.1226 * I_{REF}^2 + 0.7368 * I_{REF} + 1.6406 \tag{6.4}$$

$$At\ 500rpm: \quad \theta_{OFF} = 0.0539 * I_{REF}^2 + 1.0618 * I_{REF} + 1.8577 \tag{6.5}$$

$$At\ 600rpm: \quad \theta_{OFF} = 0.7076 * I_{REF}^2 - 2.0923 * I_{REF} - 6.0593 \tag{6.6}$$

A block diagram of the control scheme that enables the automatic selection of the desired turn-off angle for different motor speeds and loads is shown in Figure 6.15. As can be seen, the calculation of θ_{OFF} requires knowledge of both the motor speed and the PI controller current reference value. At motor speeds other than those explicitly covered by equations (6.2) through (6.6), interpolation is employed. For example, at a motor speed of 250rpm, θ_{OFF} is calculated using linear interpolation of the angles returned by the polynomial approximations at 200rpm and 300rpm.

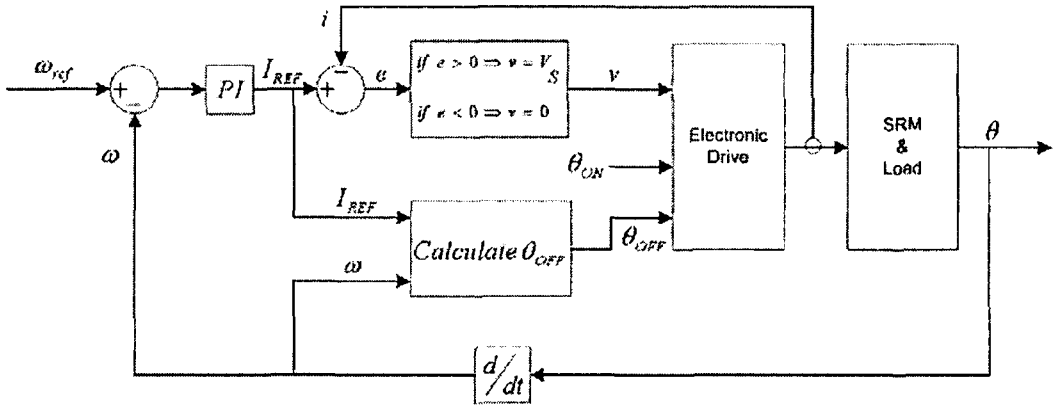

Figure 6.15: Block diagram of the extended automatic turn-off angle motor control strategy that results in phase current reduction to zero at alignment for operation at different motor speeds and with different mechanical loads.

The control strategy was tested experimentally for various operating speeds and mechanical loads with the PI controller constants unchanged from before (P = 0.002 and I = 0.02). θ_{ON} is chosen as 22.5 degrees before alignment and the initial value of θ_{OFF} is chosen to be 3 degrees before alignment. When the motor 'start-up' procedure is complete, the controller seeks to select the appropriate turn-off angle that results in the phase current reducing to zero at alignment.

Figure 6.16 shows the current in phase A, the switch signals for phase A and the pulse waveform that indicates the aligned position of phase A for a reference speed of 300rpm under a constant mechanical load. Figure 6.17 shows the turn-off angle selected by the controller during steady-state operation at 300rpm for that particular load. Figure 6.18 shows the current in phase A, the switch signals for phase A and the pulse waveform that indicates the aligned position of phase A for a reference speed of 300rpm when the load is increased. The increased load results in an increase in the PI controller current reference value and hence the controller must advance the turn-off angle to ensure phase current suppression at alignment. Figure 6.19 shows the turn-off angle selected by the controller during steady-state operation at 300rpm for the increased load. The turn-off angle is advanced from approximately 2 degrees before alignment with the original mechanical load to just over 4 degrees before alignment when the load is increased.

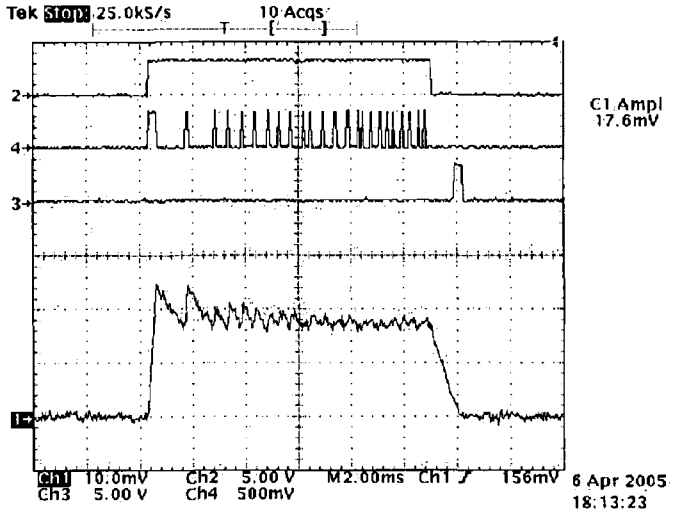

Figure 6.16: Current in phase A (Channel 1 – 1A/div), phase A switch signals (Channels 2 and 4) and pulse waveform indicating the aligned position of phase A (Channel 3) for a reference speed of 300rpm with constant θ_{ON} = 22.5 degrees before alignment and θ_{OFF} determined by the automatic turn-off angle controller.

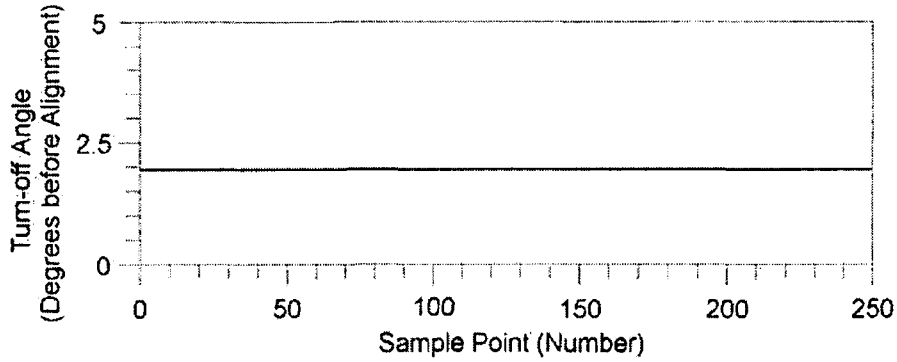

Figure 6.17: The turn-off angle selected by the automatic turn-off angle controller during steady-state operation at 300rpm.

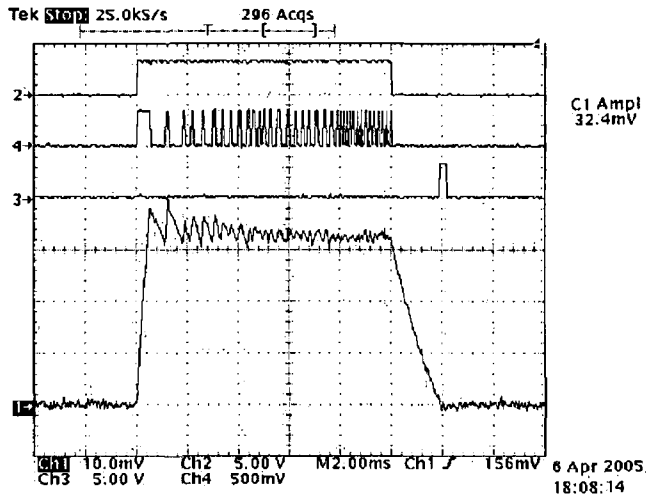

Figure 6.18: Current in phase A (Channel 1 – 1A/div), phase A switch signals (Channels 2 and 4) and pulse waveform indicating the aligned position of phase A (Channel 3) for a reference speed of 300rpm with constant θ_{ON} = 22.5 degrees before alignment and θ_{OFF} determined by the automatic turn-off angle controller when the mechanical load is increased.

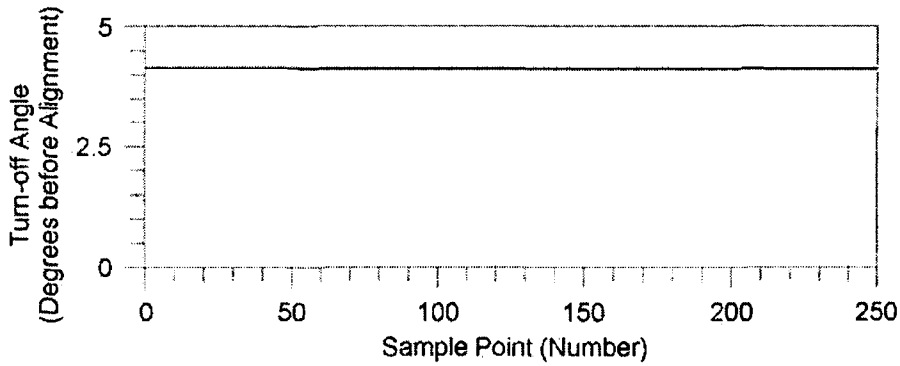

Figure 6.19: The turn-off angle selected by the automatic turn-off angle controller during steady-state operation at 300rpm when the mechanical load is increased.

Figure 6.20 shows the current in phase A, the switch signals for phase A and the pulse waveform that indicates the aligned position of phase A for a reference speed of 550rpm under a constant mechanical load. Figure 6.21 shows the same waveforms at a reference speed of 550rpm when the load is increased. In both instances, the controller selects the appropriate turn-off angle to reduce the current to zero at alignment. The turn-off angle for the operation shown in Figure 6.20 is approximately 4.5 degrees before alignment and when the load is increased, with a subsequent

increase in phase current (as shown in Figure 6.21), it is advanced to slightly less than 7 degrees before alignment.

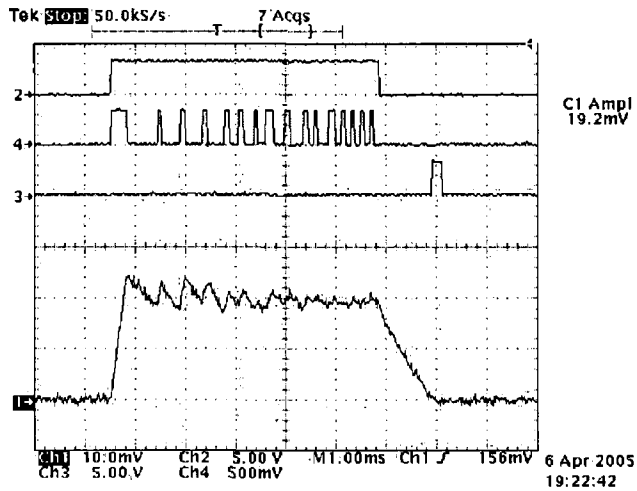

Figure 6.20: Current in phase A (Channel 1 – 1A/div), phase A switch signals (Channels 2 and 4) and pulse waveform indicating the aligned position of phase A (Channel 3) for a reference speed of 550rpm with constant θ_{ON} = 22.5 degrees before alignment and θ_{OFF} determined by the automatic turn-off angle controller.

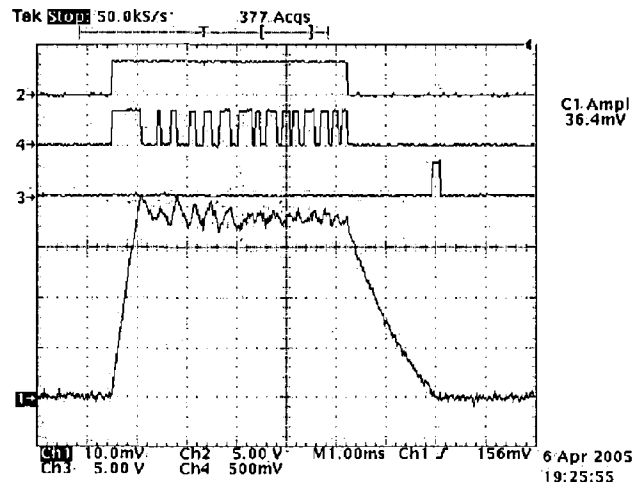

Figure 6.21: Current in phase A (Channel 1 – 1A/div), phase A switch signals (Channels 2 and 4) and pulse waveform indicating the aligned position of phase A (Channel 3) for a reference speed of 550rpm with constant θ_{ON} = 22.5 degrees before alignment and θ_{OFF} determined by the automatic turn-off angle controller when the mechanical load is increased.

The automatic turn-off angle control strategy described in Section 6.2.1.2 requires a constant turn-on angle to be employed. In addition, for accurate operation, a constant mechanical load is required. From Figures 6.16 through 6.21, it is clear that the extended automatic turn-off angle control strategy just described has the major advantage that it is capable of operating with a variable mechanical load. In addition, the extended automatic turn-off angle control strategy can be operated without a fixed turn-on angle. This is possible because the control strategy determines the appropriate turn-off angle based on the current reference value at the particular speed at which the motor is rotating. With a fixed turn-on angle and a constant motor speed, the current reference increases with increasing load. Similarly, with a constant mechanical load and a constant motor speed, the current reference changes with a change in the turn-on angle. The controller reacts to a change in the current reference value by adjusting the turn-off angle. The controller doesn't need to know if the shift in the current reference value is caused by a change in the mechanical load or a change in the turn-on angle.

Figure 6.22 shows the current in phase A, the switch signals for phase A and the pulse waveform that indicates the aligned position of phase A for a reference speed of 550rpm under a constant mechanical load when a turn-on angle of 16 degrees before alignment is employed. Figure 6.23 shows the same waveforms for operation at 550rpm when θ_{ON} = 16 degrees before alignment and the mechanical load is increased. In both cases, the controller selects the appropriate turn-off angle as expected.

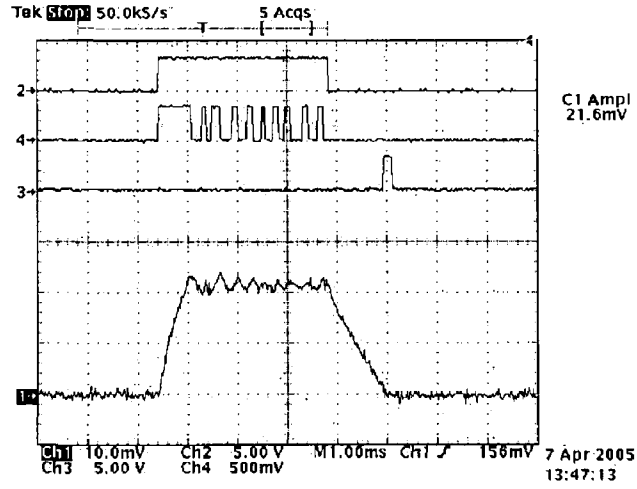

Figure 6.22: Current in phase A (Channel 1 – 1A/div), phase A switch signals (Channels 2 and 4) and pulse waveform indicating the aligned position of phase A (Channel 3) for a reference speed of 550rpm with constant θ_{ON} = 16 degrees before alignment and θ_{OFF} determined by the automatic turn-off angle controller.

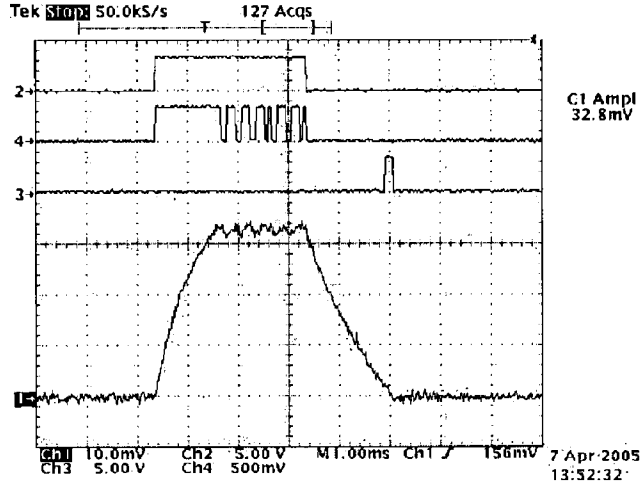

Figure 6.23: Current in phase A (Channel 1 – 1A/div), phase A switch signals (Channels 2 and 4) and pulse waveform indicating the aligned position of phase A (Channel 3) for a reference speed of 550rpm with constant θ_{ON} = 16 degrees before alignment and θ_{OFF} determined by the automatic turn-off angle controller when the mechanical load is increased.

6.2.1.4 Optimal efficiency control strategy

Although both the simple control strategy and the automatic turn-off angle control strategy succeed in accurately controlling the speed of the motor, neither strategy enables operation at the desired optimal efficiency level. For a given load, there are many sets of firing angles that enable the SRM to rotate at the reference speed. While each of these sets of firing angles produces the same amount of power, they draw different rms phase currents from the power converter. Clearly, it is preferable to choose firing angles that minimise the rms phase current, thereby achieving the goal of maximum mechanical output power from minimum electrical input. In other words, the objective is to maximise the torque per ampere produced by the SRM. A control strategy that enables automatic selection of the firing angles for achieving optimal efficiency is now described and experimental results are presented.

The reasoning behind the algorithm employed in this motor control strategy is best explained using the idealised inductance profile and phase current waveform shown in Figure 6.24. The angular interval where the inductance profile is at its minimum and is unchanging corresponds to the interval during which there is no overlap of the rotor and stator poles. At the angle θ_S, the leading edges of the rotor poles start to overlap with the first edges of the stator poles and the inductance starts to increase. For motoring operation, current must flow during this interval where the inductance is increasing, resulting in the production of positive torque. According to Sozer, the maximum torque for a given amount of current is produced at the start of pole overlap as the rotor moves out of the minimum inductance position (Sozer 2003a). For this reason, it is important to ensure that the phase current is at the reference value before the rotor reaches θ_S. This is achieved by choosing θ_{ON} in advance of θ_S. It is important however, not to turn on the current too far in advance since very little torque would be produced initially due to the low and unchanging inductance (lowering efficiency).

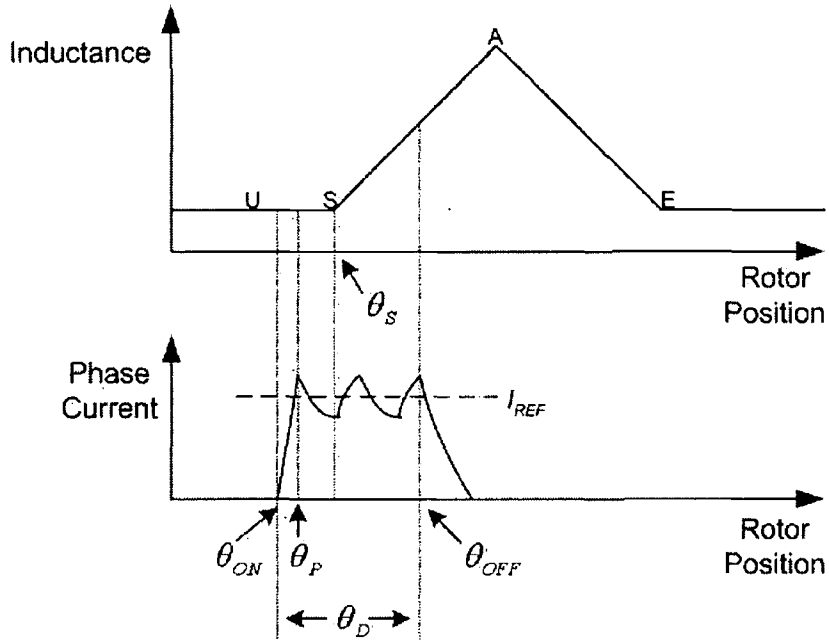

Figure 6.24: The idealised inductance profile and phase current waveform for low speed SR motoring operation.

Figure 6.25 shows the current reference versus turn-on angle for motor operation at 300rpm under a constant load and with a constant dwell angle of θ_D = 14 degrees. The same average torque is produced at each point on the graph. As can be seen however, the choice of turn-on angle has a major effect on the magnitude of the current reference outputted by the PI controller. Since the magnitude of the current reference is directly proportional to the rms phase current, the most efficient operating point is that with the lowest current reference. For the particular operating conditions used to obtain the data shown in Figure 6.25, a turn-on angle of 16 degrees before alignment is the most efficient. This turn-on angle provides sufficient time for the phase current to rise to the reference value by θ_S, which for the 12/8 experimental SRM is at approximately 15 degrees before alignment.

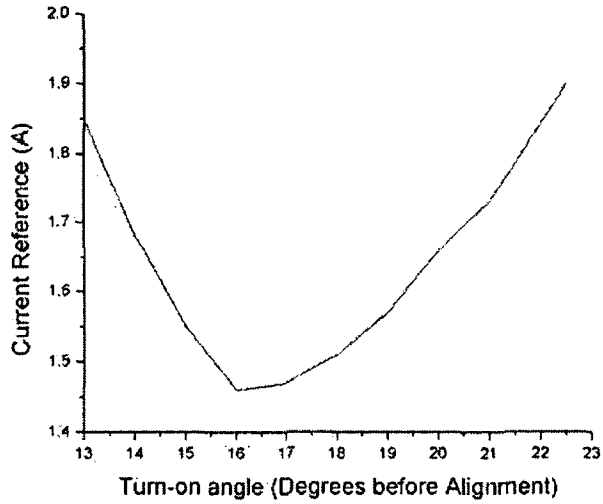

Figure 6.25: Current reference versus turn-on angle for operation at 300rpm under a constant load and with a constant dwell angle of $\theta_D = 14$ degrees.

The approach adopted for optimal efficiency control is the regulation of the turn-on angle to ensure that the first peak of the phase current, which occurs at angle θ_P, is aligned with the angle where the poles start to overlap, θ_S. The first peak of the phase current occurs when the phase current reaches the reference value, I_{REF}, for the first time. The controller continuously monitors θ_P and automatically advances or delays the turn-on angle to minimise the error between θ_P and θ_S. Examining the phase current waveform shown in Figure 6.24, it is clear that the turn-on angle would need to be delayed in order to move θ_P closer to θ_S. This approach is similar to that adopted in (Sozer 2003a). The dwell angle is kept constant for all operating conditions and during the conduction interval the current is controlled using delta modulation current control as before. A block diagram of the optimal efficiency motor control strategy is shown in Figure 6.26.

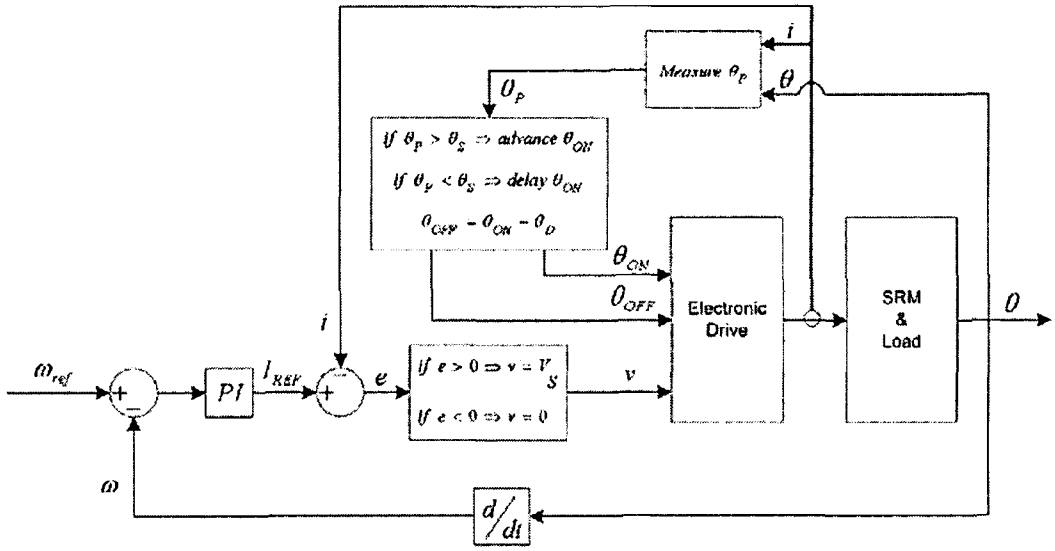

Figure 6.26: Block diagram of the optimal efficiency motor control strategy for low speed motoring operation.

The control strategy was implemented on the experimental 12/8 SRM rig with PI controller constants of P = 0.002 and I = 0.02. The increment/decrement in the turn-on angle was chosen to be 0.005 mechanical degrees and the dwell angle was held constant at θ_D = 14 degrees. The initial firing angles at start-up were θ_{ON} = 22.5 degrees before alignment and θ_{OFF} = 8.5 degrees before alignment with the controller seeking to select the optimal efficiency angles once the motor is running. A number of tests were performed to verify the efficacy of the control approach.

Figure 6.27 shows the current in phase A, the switch signals for phase A and a pulse waveform indicating the aligned position of phase A for a reference speed of 300rpm during steady-state operation of the optimal efficiency control strategy. Figure 6.28 shows the same waveforms for steady-state operation of the simple control strategy at 300rpm with constant firing angles of θ_{ON} = 22.5 degrees before alignment and θ_{OFF} = 8.5 degrees before alignment. From a visual inspection of the current waveforms in Figures 6.27 and 6.28, it is clear that the rms phase current is significantly smaller for the optimal efficiency control strategy than for the simple control strategy (as expected). In fact, the rms phase current is 1.1A for the optimal control strategy compared to 1.35A for the simple control strategy with the constant firing angles as outlined. Figure 6.29 shows the turn-on angle selected by the optimal efficiency controller during steady-state operation at **300rpm** to ensure that the first peak of the

current waveform is at θ_S. The turn-on angle converges from its initial value of 22.5 degrees before alignment at start-up to its steady-state value of approximately 16 degrees before alignment. It can be seen in Figure 6.25 that, at 300rpm, the lowest rms phase current value occurs at 16 degrees before alignment.

Figure 6.30 shows the current in phase A, the switch signals for phase A and a pulse waveform indicating the aligned position of phase A for a reference speed of **650rpm** during steady-state operation of the optimal efficiency control strategy. Figure 6.31 shows the turn-on angle selected by the controller during steady-state operation at 650rpm to ensure that the first peak of the current waveform is at θ_S. The turn-on angle converges from its initial value of 22.5 degrees before alignment at start-up to its steady-state value of approximately 17.5 degrees before alignment.

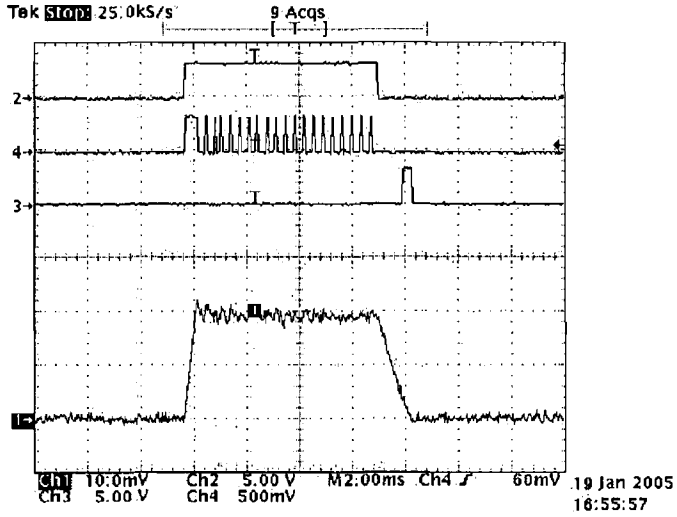

Figure 6.27: Current in phase A (Channel 1 – 1A/div), phase A switch signals (Channels 2 and 4) and pulse waveform indicating the aligned position of phase A (Channel 3) for the optimal efficiency control strategy at a reference speed of 300rpm and with constant θ_D = 14 degrees.

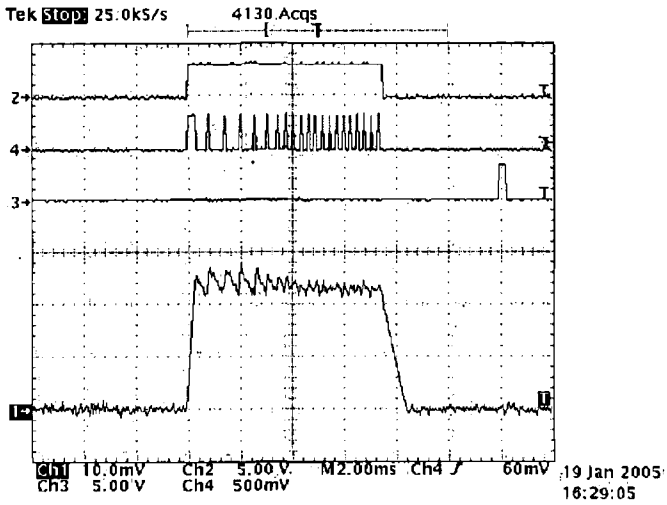

Figure 6.28: Current in phase A (Channel 1 – 1A/div), phase A switch signals (Channels 2 and 4) and pulse waveform indicating the aligned position of phase A (Channel 3) at a reference speed of 300rpm with constant firing angles of θ_{ON} = 22.5 degrees before alignment and θ_{OFF} = 8.5 degrees before alignment.

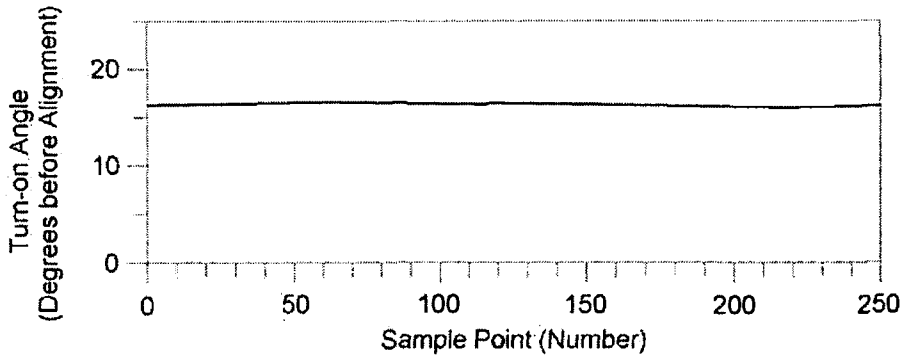

Figure 6.29: The turn-on angle selected by the optimal efficiency controller during steady-state operation at 300rpm to ensure that the first peak of the current waveform is at θ_S.

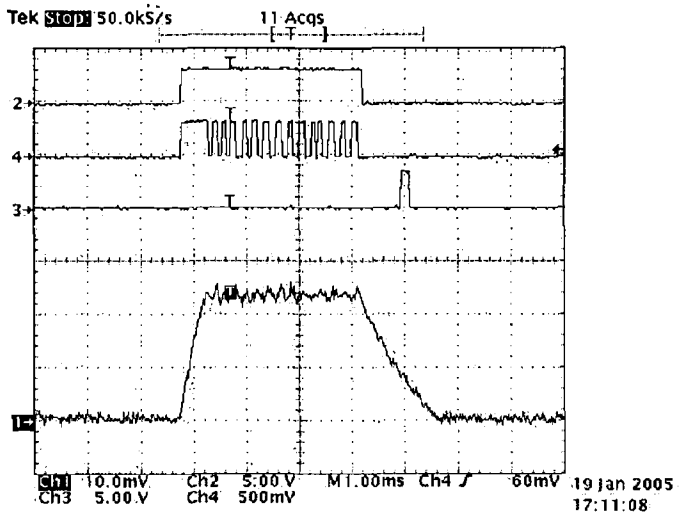

Figure 6.30: Current in phase A (Channel 1 – 1A/div), phase A switch signals (Channels 2 and 4) and pulse waveform indicating the aligned position of phase A (Channel 3) for the optimal efficiency control strategy at a reference speed of 650rpm and with constant θ_D = 14 degrees.

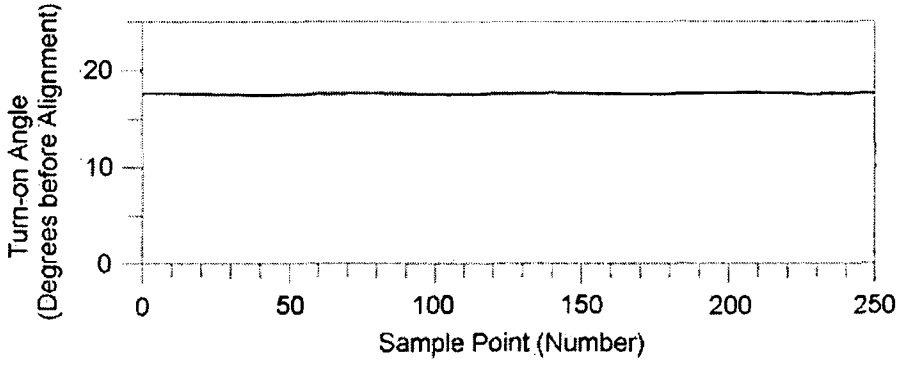

Figure 6.31: The turn-on angle selected by the optimal efficiency controller during steady-state operation at 650rpm to ensure that the first peak of the current waveform is at θ_S.

This control strategy selects the optimal efficiency turn-on angle thus ensuring that it is the most efficient SR motor control. In addition, no characterisation of the SRM is required. Hence, the optimal efficiency control strategy is clearly superior to the simple control strategy and the automatic turn-off angle control strategy.

6.2.2 High speed motoring – single pulse mode control

At higher motor speeds, the magnitude of the back-emf is sufficiently large to limit the phase current and negate the requirement for current regulation. Assuming a constant supply voltage, V_S, in single pulse mode, the SRM can only be controlled by variation of the control variables, θ_{ON} and θ_{OFF}. At θ_{ON}, both power switches are closed (placing the supply voltage across the winding) and remain closed throughout the entire conduction cycle. At θ_{OFF}, both switches are turned off and the phase is demagnetised by the negative supply voltage placed across the winding. At high speeds, θ_{OFF} must be advanced to ensure that the current has sufficient time to reduce to zero by alignment, avoiding the production of negative torque. It is possible to implement a very simple control scheme that requires no prior knowledge or characterisation of the SRM. The turn-off angle is fixed and the turn-on angle is used to control the rotational speed. A block diagram of this simple control scheme is shown in Figure 6.32.

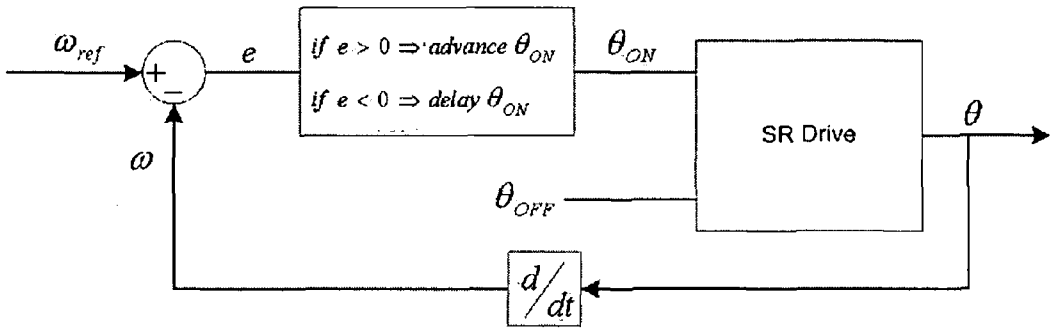

Figure 6.32: Block diagram of the single pulse mode motor control scheme.

Starting with θ_{ON} = 22.5 degrees before alignment (the unaligned position), θ_{ON} is advanced by a fraction of a degree (increasing the conduction angle) if the estimated speed is less than the reference value and is delayed (decreasing the conduction interval) if it is greater than the reference value. The increment/decrement in θ_{ON} should be chosen to be relatively small (to keep speed ripple to a minimum) but large enough to ensure a fast response of the controller to variation in the load or speed reference. The control scheme was implemented on the ADSP-21992 with a increment/decrement value of $\Delta\theta_{ON}$ = 0.001 degrees.

Figure 6.33 shows the current in phase A, the switch signals for phase A, the tachometer output signal and a pulse waveform that indicates the aligned position of phase A for a reference speed of 700rpm with a constant θ_{OFF} = 10 degrees before alignment. Figure 6.34 shows the turn-on angle for steady-state operation at 700rpm with a constant θ_{OFF} = 10 degrees before alignment. As can be seen, the turn-on angle is approximately 21 degrees before alignment. Figure 6.35 shows the motor speed calculated by the ADSP-21992 control program in the manner described in Section 5.6.3 during steady-state operation for a reference speed of 700rpm. Figure 6.36 shows the initial response of the experimental system to a 700rpm reference speed. The speed of the motor quickly settles to 700rpm in approximately 0.5 seconds.

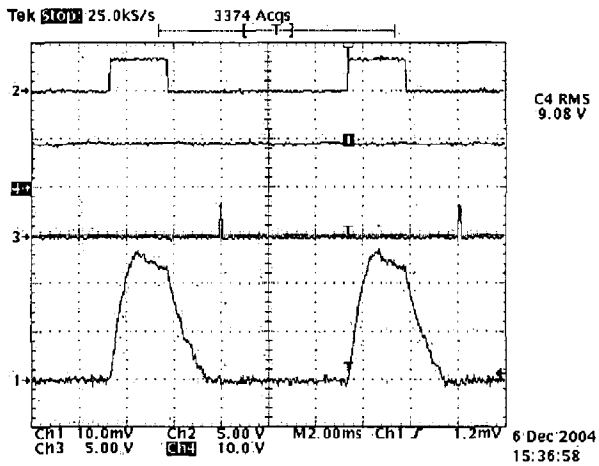

Figure 6.33: Current in phase A (Channel 1 – 2A/div), phase A switch signals (Channel 2), the tachometer output signal (Channel 4 – 12.5V/1000rpm) and a pulse waveform indicating the aligned position of phase A (Channel 3) for a reference speed of 700rpm with constant θ_{OFF} = 10 degrees before alignment.

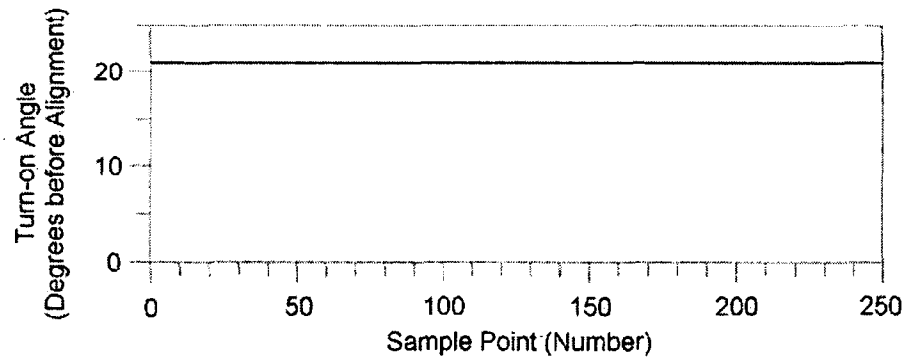

Figure 6.34: Turn-on angle for steady-state operation at 700rpm with constant θ_{OFF} = 10 degrees before alignment.

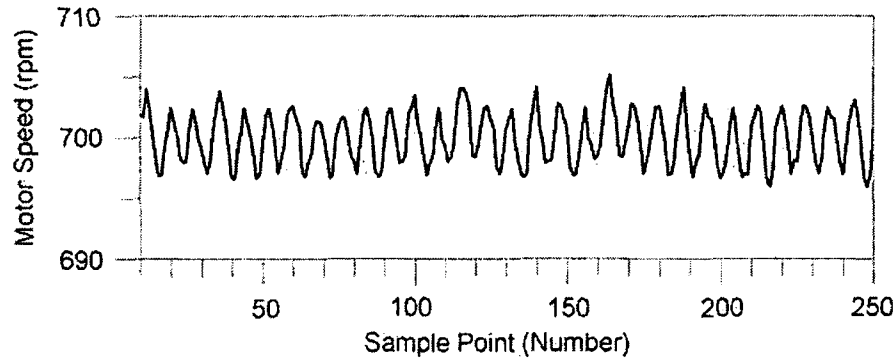

Figure 6.35: Motor speed as calculated by the ADSP-21992 control program during steady-state single pulse mode motoring operation for a reference speed of 700rpm.

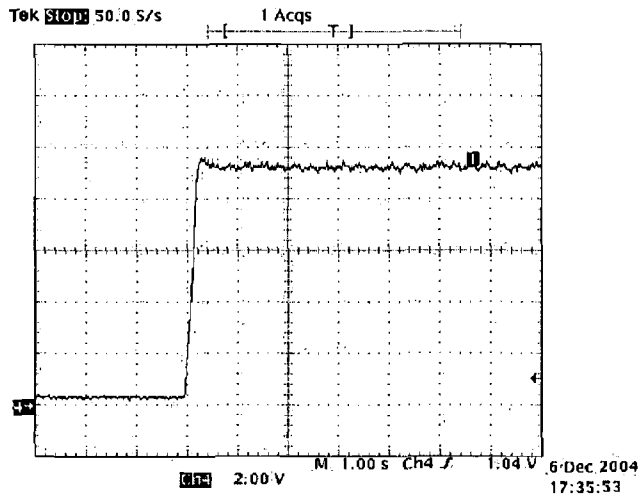

Figure 6.36: Transient speed response of the experimental system for high speed motoring with a 700rpm speed reference.

The simple control strategy succeeds in accurately controlling the rotational speed of the motor. However, in the outlined strategy, the turn-off angle was chosen rather randomly with the only criterion being that it should ensure current suppression before alignment. For any operating speed, there are many conduction angles that can be chosen to ensure operation at that particular speed. Possible future work could involve further development of the simple control strategy such that the maximum efficiency conduction angles are chosen for a particular operating speed and load. The maximum efficiency angles could be determined either through simulation or experimentation.

Finally, while both low speed motoring below the base speed and high speed single pulse mode control have been examined experimentally, the transition between the two modes of operation hasn't been investigated. However, it is expected that there would be a naturally smooth transition between, for example, the simple low speed control scheme described in Section 6.2.1.1 and the single pulse mode control scheme described above. The simple low speed motor control strategy controls the phase current around the reference current produced by the PI controller. As the speed increases, the phase currents may not be able to reach the demanded reference level and hence, the controller will automatically enter single pulse mode operation. The turn-on angle can then be used to control the speed as described for the high speed motor control strategy. It is recommended that the transition between low speed motoring control and single pulse mode control be investigated as part of future work.

6.3 Torque estimation

The four motor speed control schemes described and experimentally tested thus far in Chapter Six are designed for SR motor applications that can tolerate torque ripple. However, there are many applications where the torque ripple is troublesome and must be minimised. Chapter Four describes the performance of three neuro-fuzzy torque ripple minimisation control schemes that were examined with simulations. Neuro-fuzzy control strategy no. 3 was the best of the three strategies examined. Hence, it was decided to further test neuro-fuzzy control strategy no. 3 using the experimental set-up. During the neuro-fuzzy compensator training process, knowledge of the torque profile is required. However, the experimental set-up did not have a torque sensor incorporated. Hence, it was necessary to estimate the instantaneous torque using an estimation algorithm.

In Section 3.3, a nonlinear SRM mathematical model with on-line parameter identification is described and the simulated results for a 12/8 three-phase SRM are included. The torque estimation involves using the recursive least squares technique to continuously update the parameters of the mathematical model using actual terminal measurements of phase currents and voltages. The simulated results indicate the suitability of the nonlinear model for torque estimation purposes. Indeed, this nonlinear model is employed as a torque observer/estimator in the self-tuning torque ripple minimising controller whose operation is described and tested through

simulation in Section 3.4. In addition, the torque estimation capability of the nonlinear model is further verified in the simulation of the neuro-fuzzy torque ripple minimisation control strategies as described in Section 4.11. The model can adapt and tune itself to any SRM and enables estimation of the total torque as well as the individual phase torques. As described in Section 3.3, there are essentially two parts to the torque estimation algorithm.

(1) Flux-linkage calculation and parameter identification: The flux-linkage, ψ, is used as the state variable for the modeling approach and is represented by the continuous function:

$$\psi(\theta,i) = \psi_S\left(1 - e^{-i f(\theta)}\right) \tag{6.7}$$

where ψ_S is chosen equal to or greater than the saturation flux-linkage of the SRM and $f(\theta)$ is the Fourier series function:

$$f(\theta) = a + b\cos N\theta + c\cos 2N\theta + d\sin N\theta + e\sin 2N\theta \tag{6.8}$$

where N is the number of rotor poles and the parameters a,b,c,d and e are variables that are determined while the motor is running. The model parameters are determined using recursive least squares identification as outlined in Section 3.3 and they assume values that account for the particular characteristics of the SRM being modeled.

(2) Torque calculation: With the system identification algorithm returning the model parameters, knowledge of ψ_S, the rotor position, θ, and the measured phase current, i, enables estimation of the phase torque, T, from the following equation:

$$T = \frac{\psi_S \dfrac{df(\theta)}{d\theta}}{f(\theta)^2}\left[1 - \left(1 + if(\theta)\right)e^{-i f(\theta)}\right] \tag{6.9}$$

Alternatively, the phase torque can be calculated from:

$$T = \frac{1}{2} \frac{\psi^2 \frac{df(\theta)}{d\theta}}{\psi_S f^2(\theta)} \tag{6.10}$$

where ψ is calculated from equation (6.7) using the measured phase current and updated model parameter values.

For torque estimation using this nonlinear model, knowledge of the saturated flux-linkage, ψ_S, is necessary. In addition, the flux-linkage, ψ, is required to be known for system identification and thus it must be calculated every control cycle. The experimental method employed for determination of ψ_S and the algorithm for on-line real-time calculation of ψ are now outlined.

6.3.1 Saturated flux-linkage determination

For the torque estimation algorithm, the approximate saturated flux-linkage value, ψ_S, is required. An experiment was carried out to determine a value for ψ_S. A variac drawing power from the 220V 50Hz mains was directly connected to a single phase of the SRM. A variac enables the applied voltage to be varied from 0V to the maximum 220V. In addition, a current probe and an oscilloscope were employed to enable visualisation of the current waveform.

When a voltage is applied across a phase of the SRM, the rotor moves seeking alignment with the excited phase and 'locks' itself in the aligned position. To find the saturation point, the voltage across the phase was increased until a rapid increase in the phase current was observed. In a phase current versus time plot on an oscilloscope, the significant change in slope of the phase current would indicate that the phase under test has gone into saturation.

The instantaneous voltage across the terminals of a single phase of an SRM winding is related to the flux linked in the winding by:

$$v = iR + \frac{d\psi}{dt} \tag{6.11}$$

where v is the terminal voltage, i is the phase current, R is the phase resistance and ψ is the flux-linkage.

If the iR loss is ignored (permissable because only an approximate value for ψ_S is required), then equation (6.11) simplifies to:

$$v = \frac{d\psi}{dt} \tag{6.12}$$

The applied voltage can be represented by the equation:

$$v = V_{PEAK}\cos(\omega t) \tag{6.13}$$

where V_{PEAK} is the peak value of the applied voltage. Hence, the flux-linkage can be represented by the equation:

$$\psi = \frac{V_{PEAK}}{\omega}\sin(\omega t) \tag{6.14}$$

where $\omega = 2\pi f$ (in this case, f = 50Hz). Thus, the saturated flux-linkage may be approximated by the maximum value of equation (6.14) i.e.:

$$\psi_S = \frac{V_{PEAK}}{\omega} \tag{6.15}$$

Saturation occurred at an applied voltage of approximately 90Vrms. Thus, the saturated flux-linkage was calculated as:

$$\psi_S = \frac{90\sqrt{2}}{2\pi 50} \cong 0.4Wb \tag{6.16}$$

This approximate value for ψ_S was then employed in the torque estimation algorithm.

6.3.2 Flux-linkage estimation

The torque estimation algorithm requires continuous knowledge of the flux-linkage for all time. Equation (6.11) indicates that the flux-linkage for a particular phase can be estimated using knowledge of both the phase voltage and phase current. Rearranging equation (6.11) and integrating both sides results in the following:

$$\psi = \int (v - iR)dt \tag{6.17}$$

This integration operation is performed using an update law such as the Forward Euler to determine the flux-linkage:

$$\psi_N = \psi_{N-1} + (v_{N-1} - i_{N-1}R)\Delta t \tag{6.18}$$

Δt is a variable that is determined in each control cycle using a general-purpose timer.

While a classical flux-linkage estimator uses terminal measurements of both current and voltage, the estimator employed here relies on current measurement only and approximates the phase voltage, v, as described in what follows, rather than specifically measuring it. This reduces the amount of measurement electronics required.

Using the 'classic' converter, there are three possible states of operation (as outlined in Section 2.4) namely magnetisation, freewheeling and forced demagnetisation. If losses in the power switches and diodes are neglected, the voltage across the phase winding is V_S, 0 and $-V_S$ during magnetisation, freewheeling and forced demagnetisation, respectively. However, for more accurate flux-linkage estimation, it is important to take losses in the semiconductor devices into consideration. Thus, the voltage across the winding in each converter state can be approximated by the following equations:

$$v = V_S - 2V_{Transistor} \quad \text{Magnetisation} \tag{6.19}$$

$$v = -V_{Diode} - V_{Transistor} \quad \text{Freewheeling} \tag{6.20}$$

$$v = -V_S - 2V_{Diode} \quad \text{Forced demagnetisation} \tag{6.21}$$

where $V_{diode} \cong 0.7V$ and $V_{transistor} \cong iR_{DSon}$ where R_{DSon} is the on-resistance of the MOSFET. The on-resistance of the IRF644 MOSFETs employed in the experimental 'classic' power converter is $R_{DSon} = 0.28\Omega$. Since the maximum phase current is 4A, the voltage drop, $V_{transistor}$, is never more than 1.12V. For simplicity, the value for $V_{transistor}$ is permanently set to 0.5 volts thereby avoiding the calculation of iR_{DSon} every cycle. Although there is a subsequent loss in accuracy, the percentage error will be small due to the relative magnitude of the error (<0.5V) when compared to the supply voltage magnitude of 70V.

At low speed operation, the current is controlled around the PI controller current reference value by soft chopping with the switch signals being generated by the ADSP-21992 control program. Hence, the switching states are known at all times and therefore, the mode of converter operation is also known. The voltage across the phase at any time can be derived from these known switch states. The voltage, v, is therefore estimated in each control cycle during the chopping and/or commutation control stages.

Once the phase voltage is estimated and the current measured, the flux-linkage estimate can be updated. The phase resistance is a known parameter and the integration time-step, Δt, can be found by starting and stopping a timer. Hence, the flux-linkage estimation can be implemented in C code on the ADSP-21992 in the manner shown in Appendix C4.

Figure 6.37 shows the estimated flux-linkage for experimental operation of the SRM at 400rpm under current-regulated speed control implemented using a PI controller when the flux-linkage estimation method described above is employed. The current is controlled using software-implemented delta modulation control. The firing angles were $\theta_{ON} = 22.5$ degrees before alignment and $\theta_{OFF} = 4$ degrees before alignment.

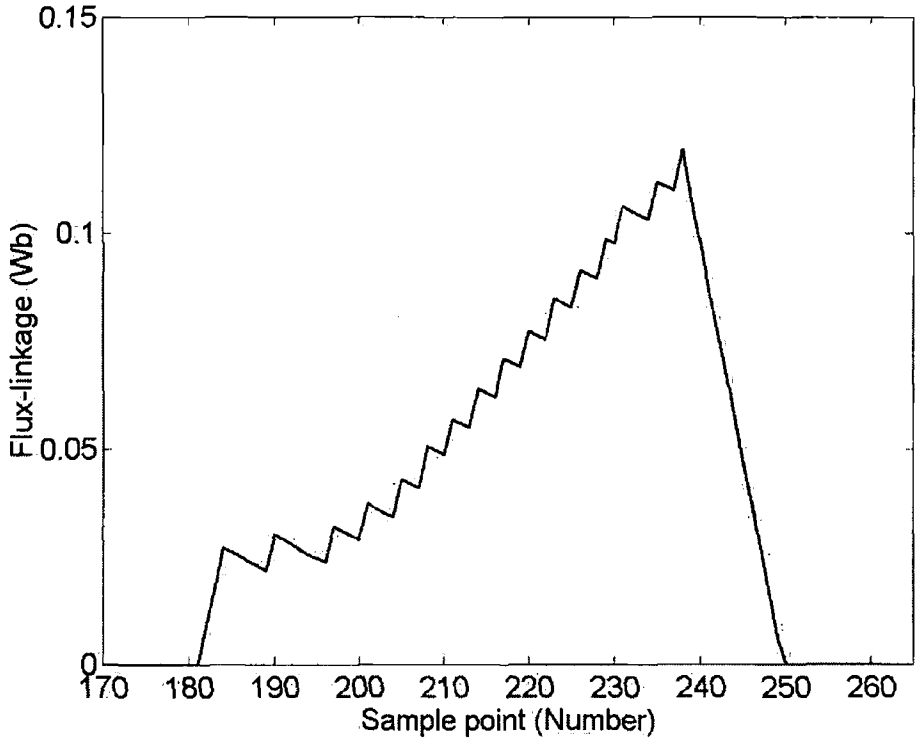

Figure 6.37: Estimated flux-linkage for experimental operation of the SRM at 400rpm.

6.3.3 Parameter identification

Using the self-tuning nonlinear model as a torque observer for the experimental SRM significantly increases the overall motor control cycle time. This cycle time also incorporates the time taken for the speed/torque control, commutation control etc. In particular though, the time-consuming nature of the recursive least squares model parameter identification routine must be acknowledged and every effort must be made to minimise its execution time.

Hence, a number of steps were taken to minimise the impact of the identification routine on the control cycle time. The nonlinear model described in the series of mathematical equations in Section 3.3 employs five parameters. However, simulation results indicate that there is minimal loss in accuracy if a three-parameter model is employed. Thus, the Fourier series function of equation (6.8) becomes:

$$f(\theta) = a + b\cos N\theta + c\cos 2N\theta \tag{6.22}$$

The reduction in the number of parameters results in faster implementation. While there is a subsequent loss in torque estimation accuracy, it is minimal. In addition, identification was performed only for a single phase of the SRM (phase A) and the results were utilised for all of the phases. This was validated through simulation where little degradation in the performance of the control strategy was observed. The validity of single-phase identification was also verified experimentally in (Mir 1998) and (Russa 2000). Furthermore, the identification algorithm was split into fifteen smaller constituent sections (all approximately equal in terms of execution time) that are executed during consecutive control cycles. Therefore, the SRM model that is employed for the torque estimation is updated only once in every fifteen control cycles. This greatly reduces computation. The phase torques, however, are estimated every control cycle. Figure 6.38 shows the *a*, *b* and *c* parameter values during steady-state operation. Figure 6.38 also shows the values of the parameters *a*, *b* and *c* during the first 250 control cycles as they start to diverge from their initial, arbitrarily chosen, values of one. As can clearly be seen in Figure 6.38, the parameters are updated every fifteen control cycles as expected.

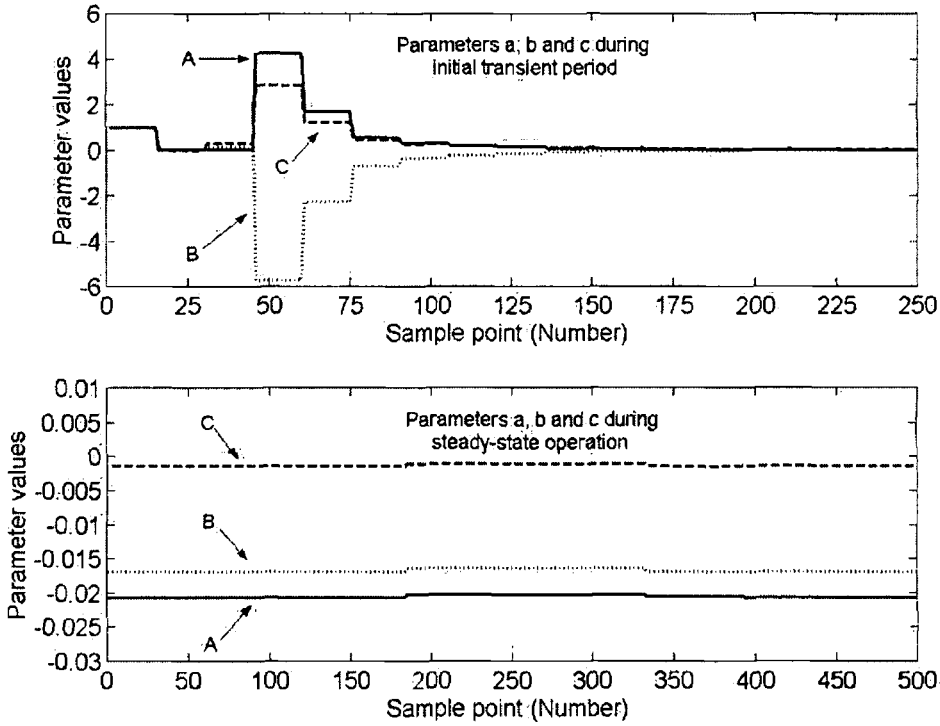

Figure 6.38: Values of parameters *a*, *b* and *c* during the first 250 control cycles and during subsequent steady-state operation.

6.3.4 Flux-linkage comparison and nonlinear model verification

Since the parameter identification is only implemented for a single phase of the SRM, the flux-linkage also needs only to be estimated using the measured phase current and estimated phase voltage (in the manner outlined in Section 6.3.2) for that one particular phase. To confirm the validity of the nonlinear model, the flux-linkage can be calculated using equation (6.7). This can then be compared to that obtained with the method outlined in Section 6.3.2. Figure 6.39 shows experimental results for the actual flux-linkage estimated using the method described in Section 6.3.2 and the flux-linkage estimated using the nonlinear model for phase A at 400rpm under current-regulated speed control. As can be seen, the actual flux-linkage value and the flux-linkage value estimated when the nonlinear model is employed are closely matched, thereby verifying the accuracy of the parameter identification. Figure 6.40 shows the current in phase A that produced the flux-linkage waveform shown in Figure 6.39 as well as the phase A switch signals. The current reference outputted by the PI controller for operation at 400rpm under software-implemented delta

modulation current control was approximately 2.25A. The flux-linkage for phases B and C can be estimated using the nonlinear model from the measured current in each phase and the parameters calculated from the system identification performed on phase A.

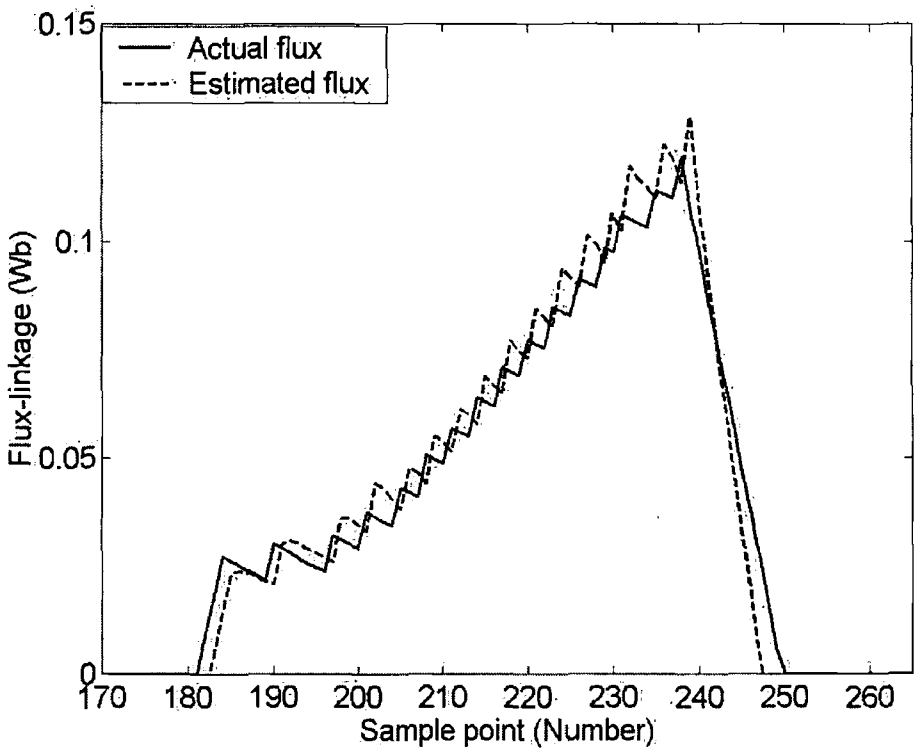

Figure 6.39: Experimental results showing the actual flux-linkage estimated using the method described in Section 6.3.2 as well as the flux-linkage estimated using equation (6.7) for phase A when the nonlinear model is employed at 400rpm.

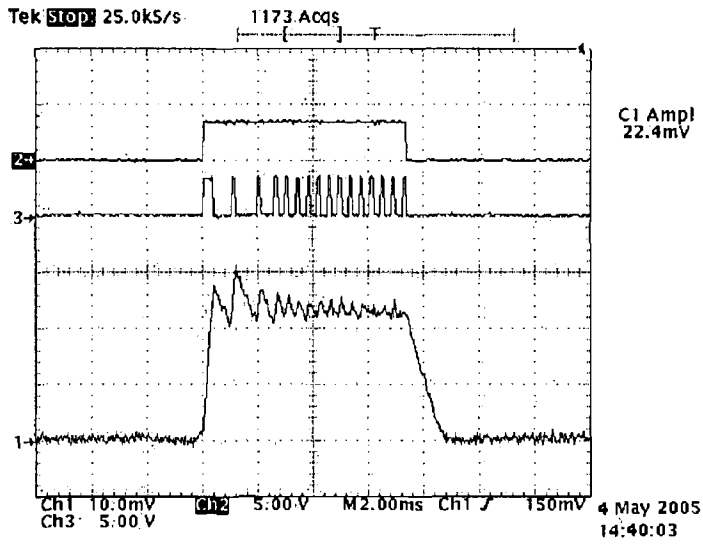

Figure 6.40: Current in phase A (Channel 1 – 1A/div) that produced the flux-linkage waveform shown in Figure 6.39 and the phase A switch signals (Channels 2 and 3) for operation at 400rpm.

6.3.5 Calculation of phase torque

The torque produced by each of the three phases can be calculated either using equation (6.9) or equation (6.10). Using equation (6.10) requires the calculation of the phase flux-linkage prior to the calculation of the phase torque. Both methods of torque estimation were implemented on the ADSP-21992 and the torque for each phase was estimated online for motor speed control operation.

Figure 6.41 shows the experimental results for the torque (produced by phase A) estimated using both equation (6.9) and equation (6.10) at 400rpm under software-implemented delta modulation control. As can be seen, both expressions for the estimation of the phase torque yield nearly identical results.

The total torque produced by the motor is the algebraic sum of the individual phase torques. Figure 6.42 shows the estimated phase torques and the estimated total torque for experimental operation at 400rpm under software-implemented delta modulation control.

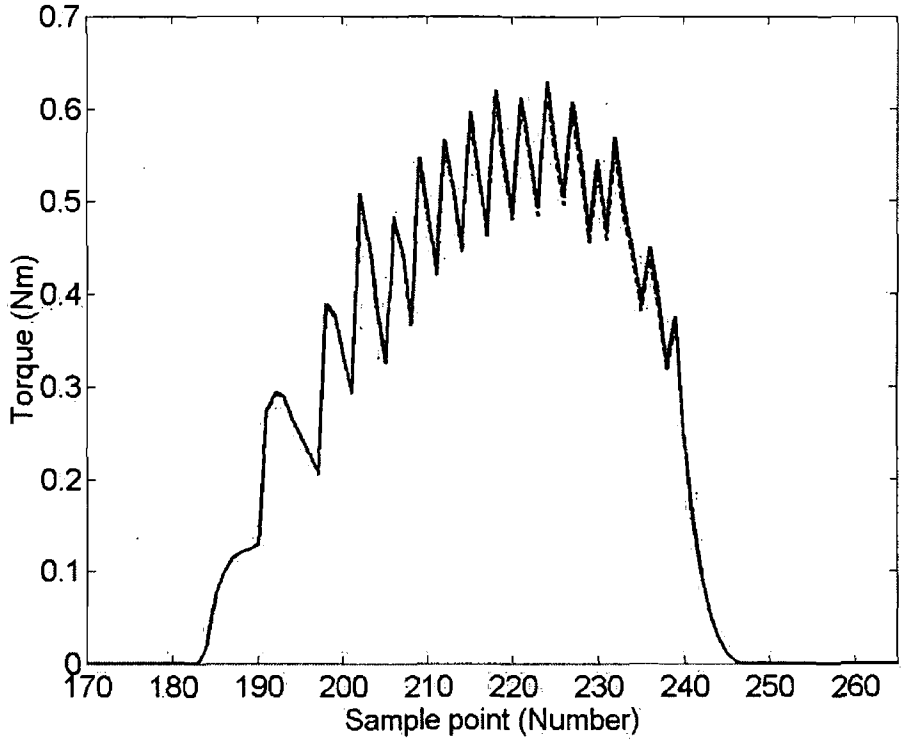

Figure 6.41: Experimental results showing the estimated torque (produced by phase A) calculated using both equation (6.9) (dotted line) and equation (6.10) (solid line) for motoring operation at 400rpm.

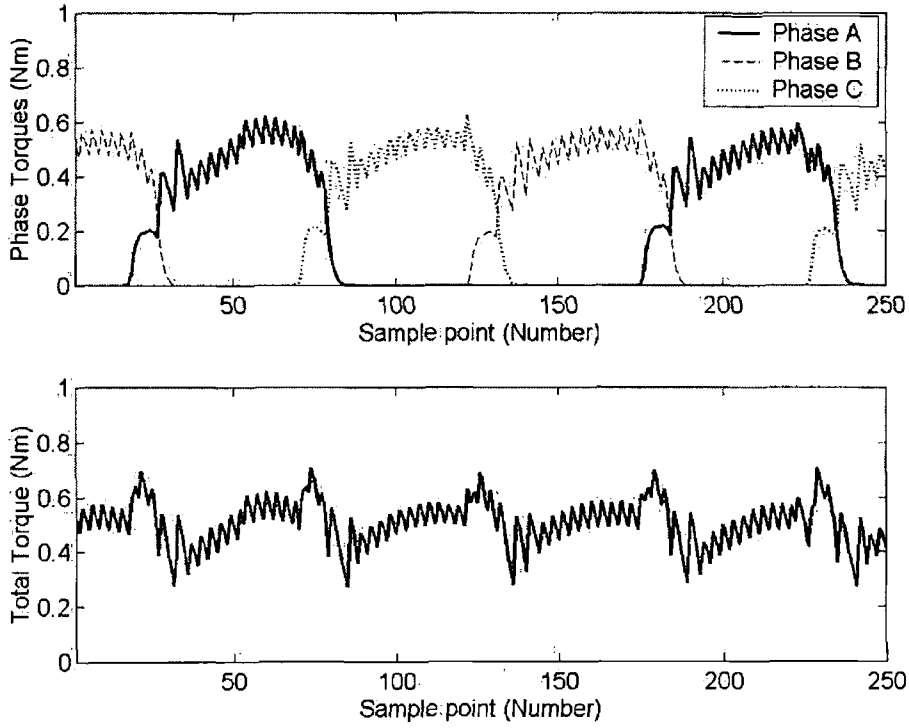

Figure 6.42: Experimental results showing the estimated phase torques and the estimated total torque for motoring operation at 400rpm.

6.4 Neuro-fuzzy control strategy no. 3

Neuro-fuzzy control strategy no. 3 is described in Section 4.9 and simulation results for both a three-phase 6/4 SRM and a three-phase 12/8 SRM are presented in Section 4.10. This section describes the experimental implementation of neuro-fuzzy control strategy no. 3. A full set of experimental results is included to verify the efficacy of the control approach in reducing the torque ripple.

Figure 6.43 shows a block diagram of neuro-fuzzy control strategy no. 3. During normal operation, the compensator selects the appropriate compensating current signal, I_{COMP}, based on the PI controller current signal, I_{PI}, and the rotor position, θ. The ANFIS system is used to train the current compensator. Figure 6.44 shows a basic block diagram of the ANFIS training approach.

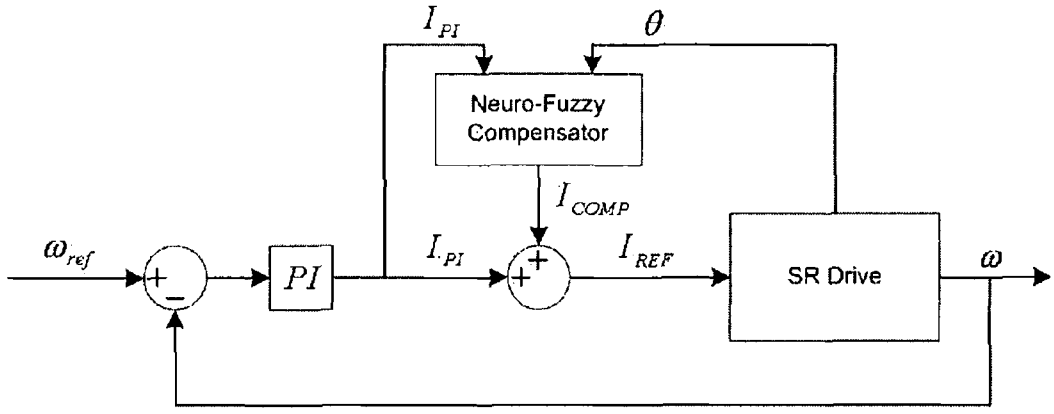

Figure 6.43: Block diagram of neuro-fuzzy control strategy no. 3.

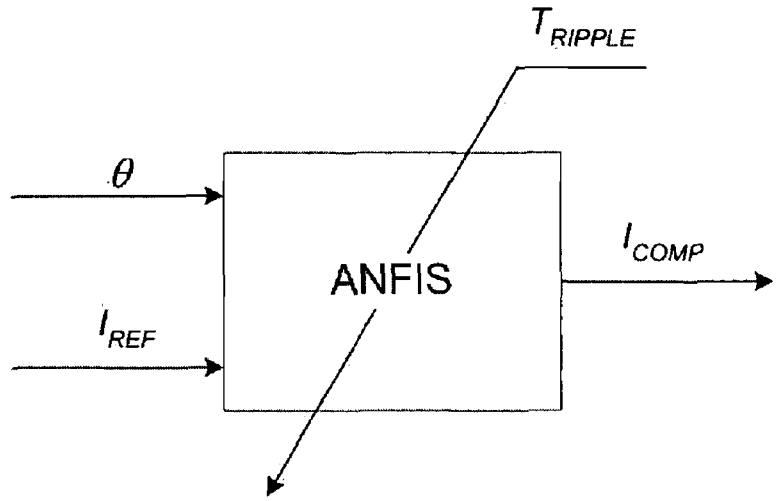

Figure 6.44: Basic block diagram of the ANFIS training approach.

Training of the neuro-fuzzy compensator is initiated by operation of the SR drive in open-loop motoring mode with a constant current reference value and no compensating signal. The following steady-state data is recorded – the current reference, I_{REF}, the rotor position, θ, and the torque ripple, T_{RIPPLE}. The torque ripple is the error information used to update the compensating current signal. With the I_{COMP} data vector initialised to zero, it is then updated according to whether the torque ripple at each rotor position sample point is greater than or less than zero. The data is then passed to the ANFIS system for training and an appropriate FIS is created. The generated FIS is incorporated into the SR drive as the neuro-fuzzy compensator. The SR drive is then operated in open-loop motoring mode once again with the compensating current signal added to the same constant current reference employed

during the initial operation of the SR drive. The required data is recorded and the I_{COMP} data vector is further updated. This procedure is repeated until the torque ripple is reduced below some error threshold. The current reference is then incremented and the entire training procedure is repeated.

The control strategy was first proposed in (Henriques 1999). In that paper, the torque signal for the training procedure was obtained using a torque sensor. In the experimental implementation described here, the torque is estimated using the method described in Section 6.3. The torque is estimated off-line using data obtained during steady-state operation of the SR drive. The identification parameters (a, b and c), the three phase currents (I_A, I_B and I_C) and the rotor position, θ, are buffered and saved in the memory of the ADSP-21992. The data is then exported and the torque information is estimated off-line using the MATLAB/Simulink package. The torque ripple is easily calculated once the total torque information is known. The neuro-fuzzy compensator is also trained off-line using the estimated torque ripple in addition to the current reference, rotor position and compensating current data, which is exported along with the data employed in the torque estimation.

6.4.1 Experimental results for neuro-fuzzy control strategy no. 3

The rotor position, θ, employed in the compensator training procedure was in the range 0 - 45 mechanical degrees. The current reference was varied in discrete steps of 0.25A between 1.75A and 3A. At each constant current reference setpoint, the appropriate compensating current for each rotor position was determined and the neuro-fuzzy compensator was trained. Finally, the training data obtained at each current setpoint was integrated into a single data set, which was employed in the training of the overall neuro-fuzzy compensator. The rule set for the neuro-fuzzy compensator was initially generated using the grid partition technique with fifteen generalised bell-shaped membership functions chosen for the rotor position and two generalised bell-shaped membership functions chosen for the current reference. The neuro-fuzzy compensator was trained using the hybrid training technique that incorporates the backpropogation algorithm and the least-mean-squares algorithm.

The FIS representing the neuro-fuzzy compensator was initially implemented in C code on the ADSP-21992. Thus, each control cycle, the appropriate compensating current was calculated using the rotor position and current reference values. However, this proved to be very computationally intensive and seriously degraded the performance of the SR drive. Hence, it was decided to implement the neuro-fuzzy compensator in the form of a look-up table. The look-up table uses the rotor position and current reference as indices, thereby returning the correct compensating current with minimal impact on the control cycle time.

6.4.1.1 Initial tests – constant current reference

The control strategy was tested for open-loop SR motoring operation with a constant current reference of 2.5A. Figure 6.45 shows the torque produced by the 12/8 three-phase SRM without current compensation and with current compensation after only two training iterations. As can be seen, the torque ripple is reduced with the rms error decreasing from 0.0945 to 0.0625. As the training of the neuro-fuzzy compensator advances, further reduction in the torque ripple is observed. Figure 6.46 shows the torque produced without current compensation and with current compensation when the training is completed after six iterations. The rms error decreases from 0.0945 to 0.0371, a reduction of over sixty per cent. The compensating current signal produced by the neuro-fuzzy compensator after two training iterations and the compensating current signal produced by the neuro-fuzzy compensator after six training iterations are plotted against rotor position in Figure 6.47.

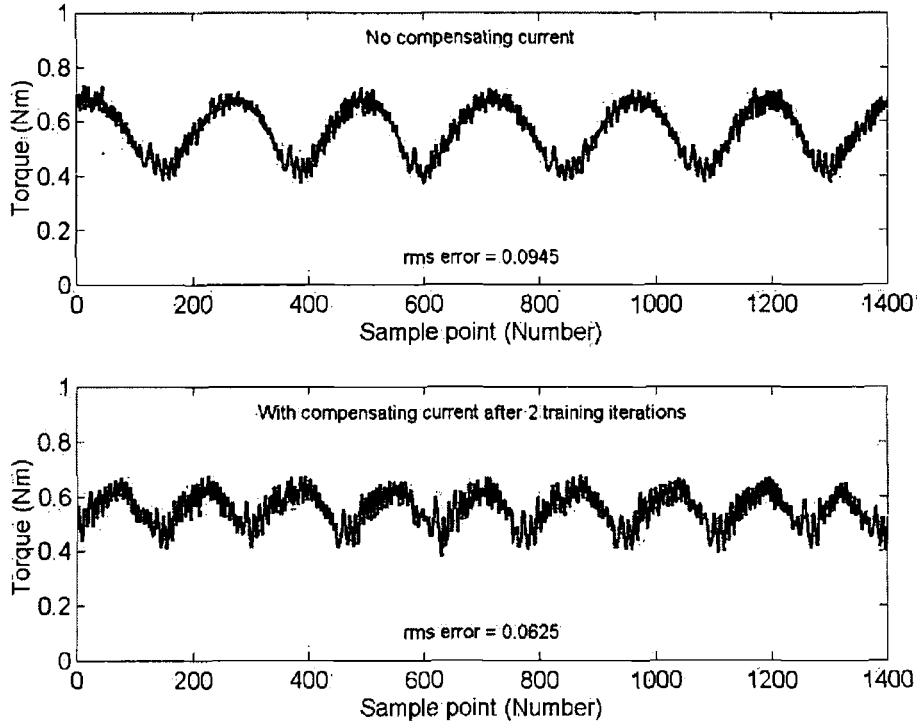

Figure 6.45: The torque produced by the 12/8 three-phase SRM without current compensation and with current compensation after only two training iterations for open-loop motoring operation with a constant current reference of 2.5A.

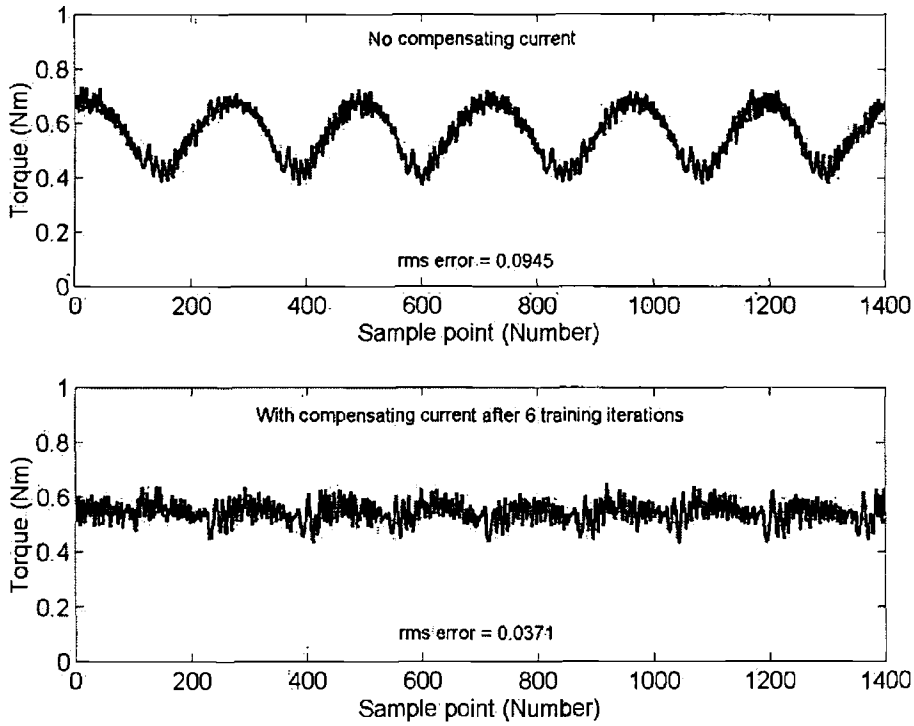

Figure 6.46: The torque produced by the 12/8 three-phase SRM without current compensation and with current compensation after six training iterations for open-loop motoring operation with a constant current reference of 2.5A.

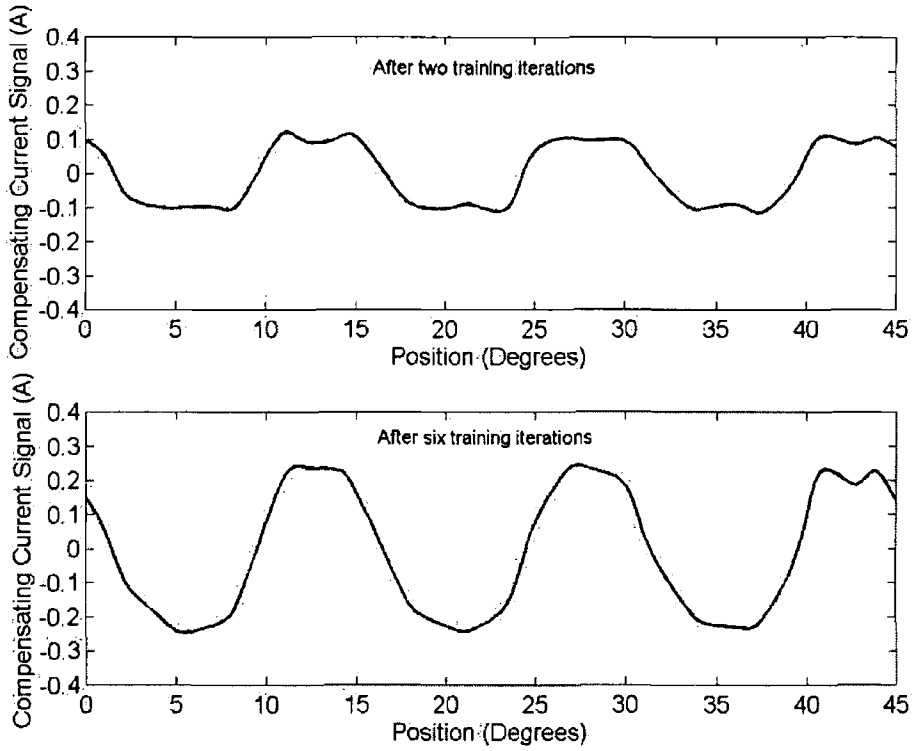

Figure 6.47: The compensating current signal produced by the neuro-fuzzy compensator after two training iterations and the compensating current signal produced by the neuro-fuzzy compensator after six training iterations for open-loop motoring operation with a constant current reference of 2.5A.

The compensating current signal is added to the constant current reference of 2.5A. The effect of the compensating current signal on the phase current waveform is demonstrated in Figures 6.48, 6.49 and 6.50. When no current compensation is employed the phase current waveform is flat-topped as shown in Figure 6.48. The phase current is controlled around the constant 2.5A reference. Figure 6.49 shows the phase current waveform with current compensation after only two training iterations. As can be seen, the phase current shape is altered from a flat-topped wavefrom to a slightly fluctuating wavefrom profile. Figure 6.50 shows the phase current waveform with current compensation when the fully-trained neuro-fuzzy compensator is employed i.e. after six training iterations. The fluctuation in the current waveform shape is more pronounced in Figure 6.50 when the fully-trained compensator is employed than in Figure 6.49. The modified phase current waveforms result in phase torques which sum to produce a reduced-ripple torque profile. Figure 6.51 shows the

torque produced by each of the three phases of the SRM for open-loop motoring with a 2.5A constant current reference when there is no current compensation and when the neuro-fuzzy compensator is incorporated into the SR drive.

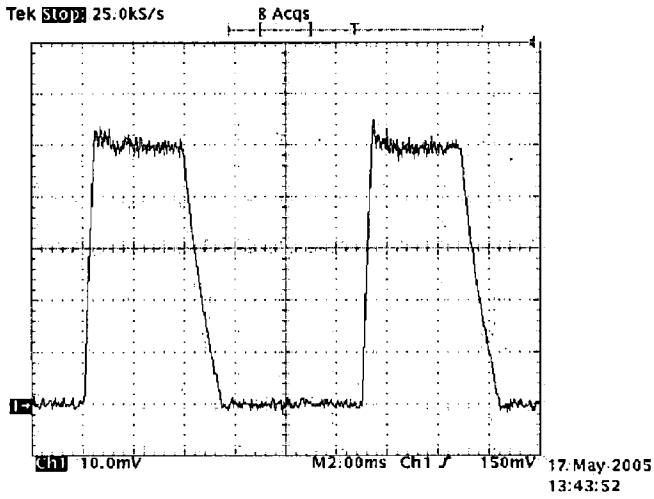

Figure 6.48: Phase A current (0.5A/div) without current compensation.

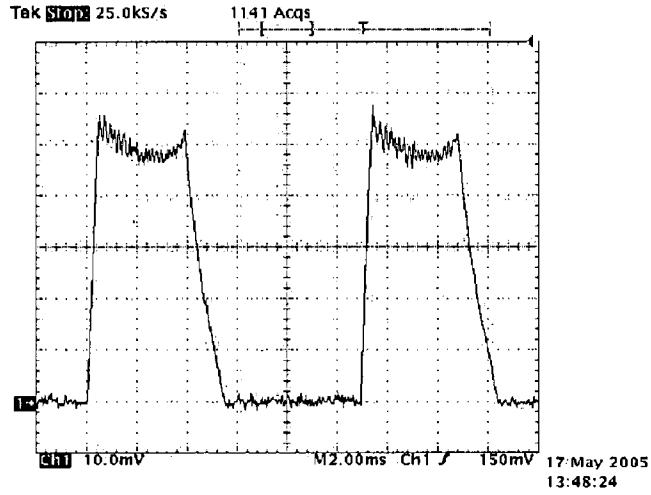

Figure 6.49: Phase A current (0.5A/div) with current compensation after two training iterations.

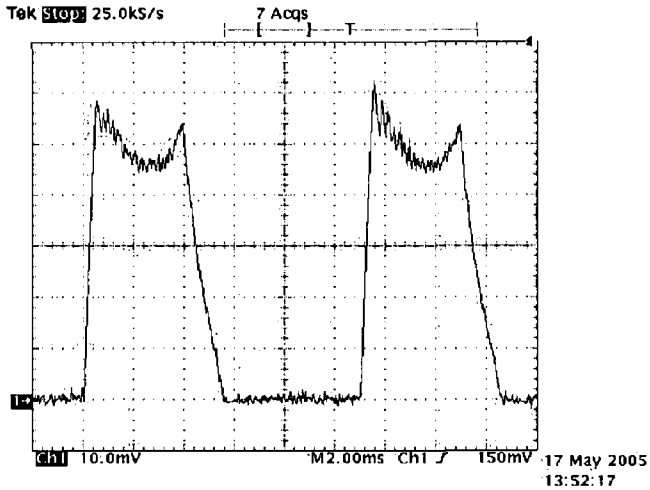

Figure 6.50: Phase A current (0.5A/div) when the fully-trained neuro-fuzzy compensator is employed i.e. after six training iterations.

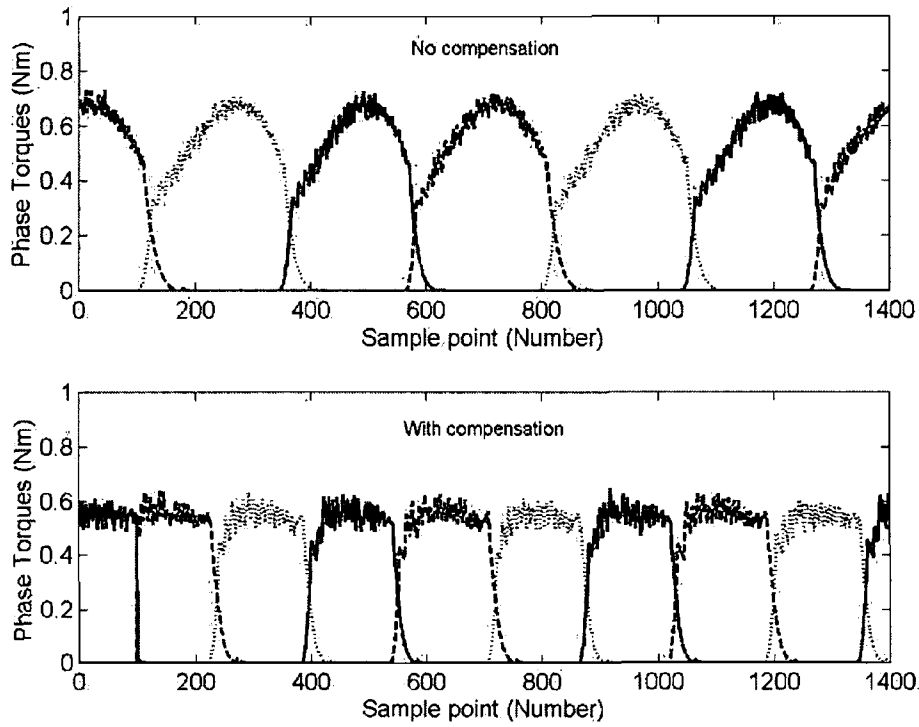

Figure 6.51: The torque produced by the individual phases for open-loop motoring operation with a 2.5A constant current reference with and without current compensation.

6.4.1.2 PI speed control tests

In Section 6.4.1.1, the neuro-fuzzy compensator was tested with the SR drive operating in open-loop motoring mode with a constant current reference of 2.5A. To

further test the control strategy, the neuro-fuzzy compensator was incorporated into the SR drive operated under current-regulated speed control implemented using a PI controller. The PI controller constants were P = 0.002 and I = 0.02. For SR drive operation with current compensation, the compensating current signal produced by the neuro-fuzzy compensator followed the curve shown in Figure 6.52.

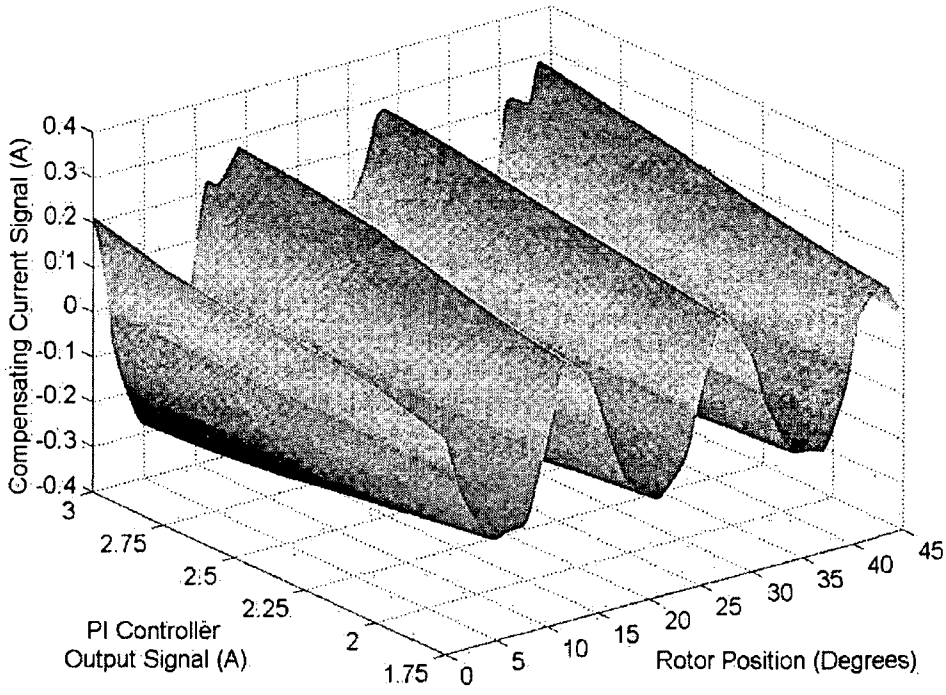

Figure 6.52: Current compensation curve for the 12/8 three-phase experimental SRM.

Figure 6.53 shows the steady-state torque produced by the SRM with and without compensation for operation with a reference speed of 600rpm and with a constant mechanical load. The almost constant PI controller output signal was approximately 2.75A. As expected, when the neuro-fuzzy compensator is employed, a significant decrease in the torque ripple is observed. In fact, the rms error is approximately halved from 0.1206 to 0.0615 when the neuro-fuzzy compensator is employed. However, this reduction in the torque ripple is only a fraction of the reduction observed when the control strategy is tested through simulation as described in Chapter Four. In the simulations, the small sampling time employed results in the phase current being controlled very precisely about the current reference. For the experimental implementation, the current control is implemented on the ADSP-21992

using delta modulation. This has the advantage that no external analog/digital hysteresis control circuit is required. However, the ADSP-21992 is also responsible for the speed/torque control, commutation control etc. in addition to the delta modulation current control. The implementation of the torque estimation algorithm to enable visualisation of the phase torques further increases the control cycle time. Consequently, there is ripple on each phase current waveform being controlled around the reference value. This ripple on the phase current waveform produces torque ripple. Figure 6.54 shows the PI controller output signal, the compensating current signal produced by the neuro-fuzzy compensator and the current reference used by the delta modulation current controller for steady-state motoring operation at 600rpm with a constant mechanical load. The current reference employed by the current controller is the sum of the PI controller output signal and the compensating current signal.

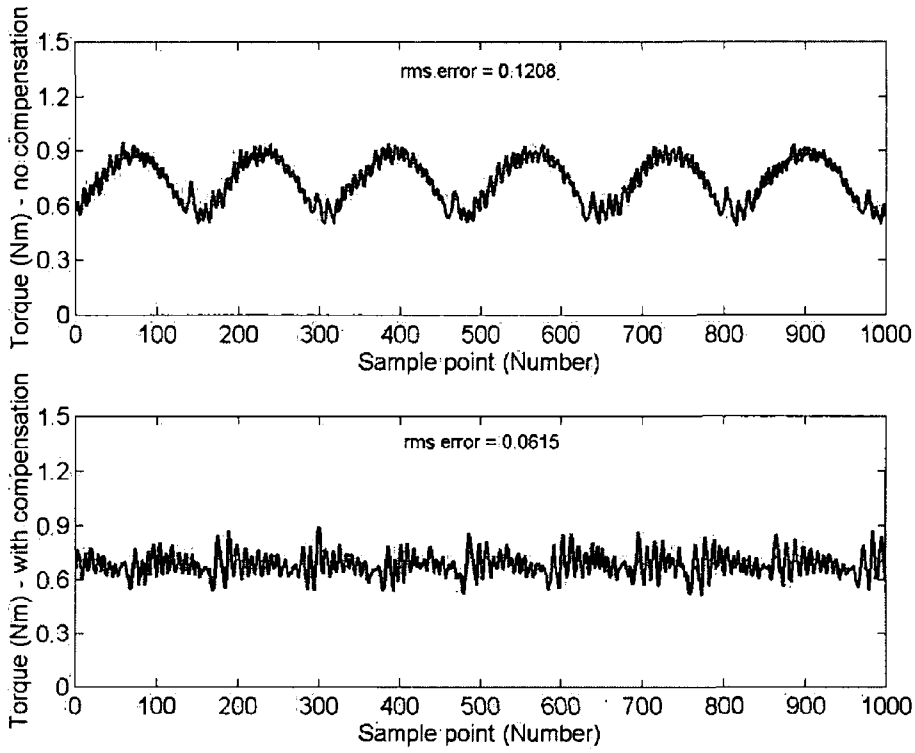

Figure 6.53: Steady-state torque produced by the SRM with and without compensation for operation at 600rpm with a constant mechanical load.

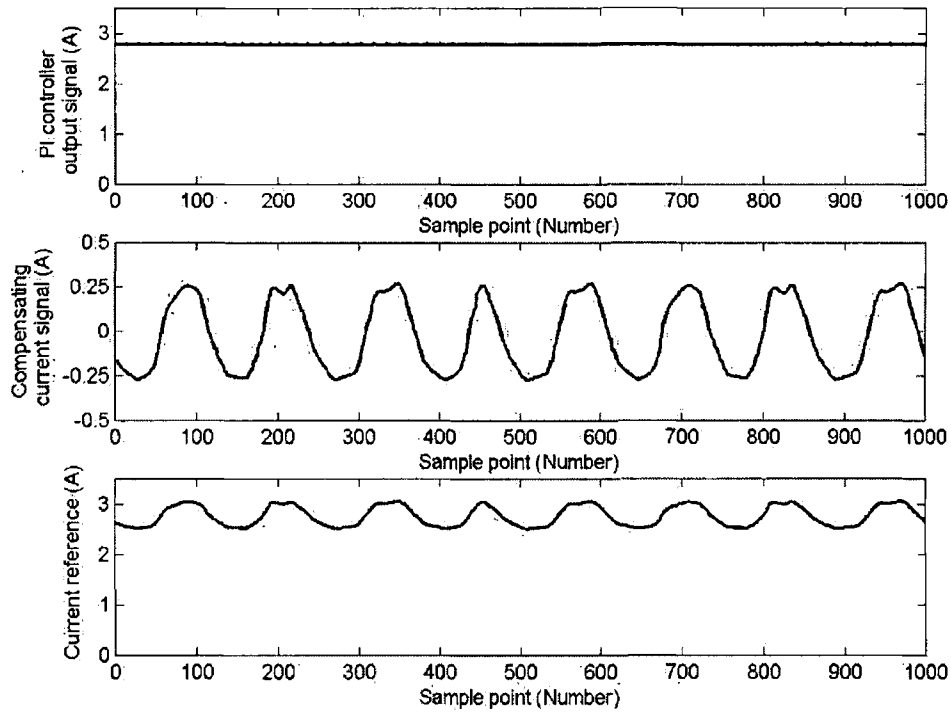

Figure 6.54: The PI controller output signal, the compensating current signal produced by the neuro-fuzzy compensator and the current reference used by the delta modulation current controller for steady-state motoring operation at 600rpm with a constant mechanical load.

Figure 6.55 shows the phase A current when no current compensation is employed. The phase current is controlled around the approximately constant PI controller output current signal of approximately 2.75A. Figure 6.56 shows the phase A current when the neuro-fuzzy compensator is incorporated into the SR drive. The effect of the compensating current signal on the phase current waveform shape is clearly visible by comparing Figures 6.55 and 6.56. The resultant phase torques produced in the individual phases with and without current compensation are shown in Figure 6.57.

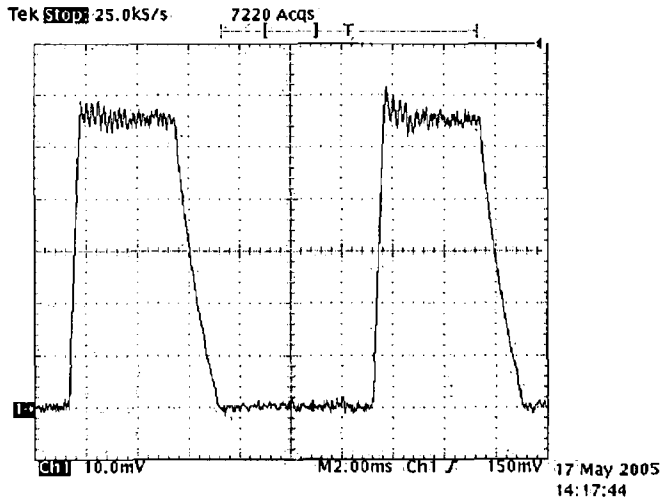

Figure 6.55: Phase A current (0.5A/div) without current compensation for operation at 600rpm with a constant mechanical load.

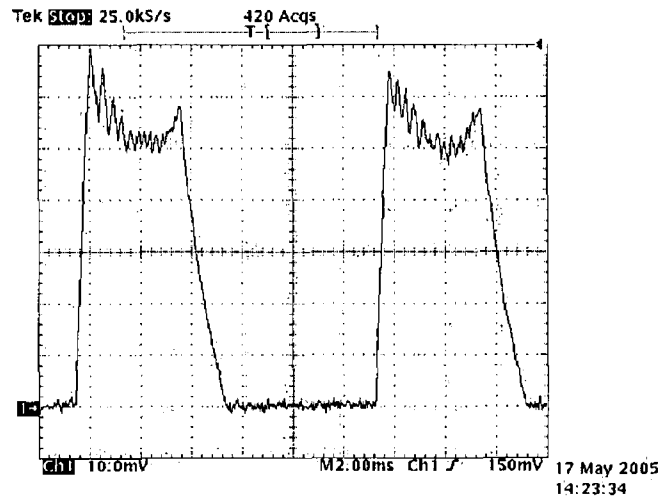

Figure 6.56: Phase A current (0.5A/div) for operation at 600rpm with a constant mechanical load when the neuro-fuzzy compensator is incorporated into the SR drive.

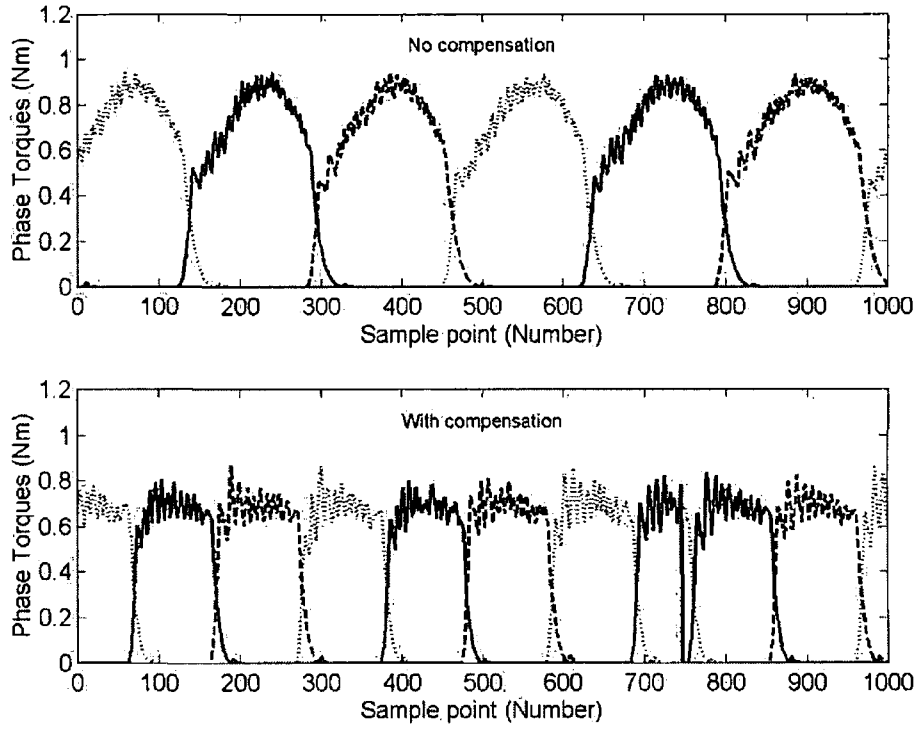

Figure 6.57: Phase torque profiles for steady-state motoring operation at 600rpm with and without current compensation.

6.5 Summary and conclusions

In this chapter, several SR motor control strategies are described and experimental results are given for a 12/8 three-phase SRM. Four of the implemented control strategies are aimed at applications that can tolerate a certain amount of torque ripple. However, there are numerous applications for which torque ripple is troublesome and for which it must be reduced. Therefore, the neuro-fuzzy control strategy no. 3, described in Chapter Four, is tested experimentally.

Three of the four motor speed control strategies for torque ripple-tolerant applications are aimed at low speed motoring. The fourth is intended for high speed motoring operation in single pulse mode. The first low speed motor control scheme involves the selection of fixed firing angles and the employment of a PI controller to control the speed. The PI controller uses the speed error to produce a current reference about which the phase currents are controlled using delta modulation current control. The main advantage of this simple scheme is that no prior knowledge or characterisation

of the machine is required. Its main disadvantage is its poor efficiency levels as a result of the employment of fixed firing angles. In addition, depending on the motor speed and the mechanical load, the phase current may reduce to zero in advance of the aligned position or some time after the rotor has passed alignment. This reduces the average torque produced by the SRM.

The second low speed motor control strategy involves the experimental determination of the turn-off angle that results in phase current reduction to zero at alignment for different motor speeds and mechanical loads. At a given motor speed, any change in the mechanical load is reflected in the current reference outputted by the PI controller. A mathematical model of the experimental data is created that enables the controller to automatically select the appropriate turn-off angle to ensure current suppression at alignment based on the motor speed and the PI controller current reference signal. This automatic turn-off angle control strategy can be operated without a fixed turn-on angle. It enables large positive torque production. However, like the first simple control strategy, it also suffers from the disadvantage of operation at non-optimum efficiency levels. An additional disadvantage is the requirement of measurement and curve fitting for determination of the mathematical model.

The final low speed motor control strategy for torque ripple-tolerant applications enables operation at the desired optimal efficiency level. The control approach involves the regulation of the turn-on angle to ensure that the first peak of the phase current is aligned with the angle where pole overlap begins. This maximises the torque per ampere produced by the SRM. The dwell angle is kept constant for all operating conditions and the current is controlled using delta modulation control. The main advantage of this control strategy is the improvement in efficiency. In addition, no characterisation of the SRM is required. Thus, the optimal efficiency control strategy is far superior to the first simple control strategy and the automatic turn-off angle control strategy.

The high speed motor control strategy is simple to implement and requires no prior knowledge or characterisation of the machine. The turn-off angle is fixed and the turn-on angle is varied to control the rotational speed. The turn-off angle is chosen to ensure current suppression before alignment. A disadvantage of this simple control

strategy is its operation at non-optimum efficiency levels. Future work could include the experimental determination of the maximum efficiency conduction angles.

The lack of a torque sensor in the experimental set-up necessitated the employment of another method for determination of the instantaneous torque. The nonlinear mathematical model of the SRM with on-line parameter identification previously tested through simulation was employed to estimate the instantaneous phase torques and total torque. This torque estimator was employed in the experimental implementation and testing of neuro-fuzzy control strategy no. 3.

Neuro-fuzzy control strategy no. 3 is aimed at minimisation of the torque ripple. The control strategy employs a neuro-fuzzy compensator to select an appropriate compensating current signal to be added to the PI controller output signal. The ANFIS system is employed to train the compensator. The training procedure requires knowledge of the torque ripple. However, neuro-fuzzy control strategy no. 3 doesn't require on-line torque estimation. For training, the torque is estimated off-line using data obtained during steady-state operation of the SR drive. The torque ripple is easily calculated from the estimated torque information. The neuro-fuzzy compensator was initially tested for open-loop motoring operation with a constant current reference. Further testing involved incorporating the compensator into the SR drive operating under current-regulated speed control implemented using a PI controller. A significant reduction in the torque ripple is observed when the neuro-fuzzy compensator is employed.

Chapter Seven – Experimental generator control

7.0 Introduction

In this chapter, the experimental implementation and testing of three closed-loop SR generator control strategies is described. Initially, the generating characteristics of the 12/8 three-phase SRM employed in the experimental set-up are described. The three control schemes for SR generator control are then outlined and their performance is examined by testing on the experimental SRM. Finally, a comparison of the three control strategies in terms of the efficiency and peak current produced by each is presented.

7.1 Generating characteristics of the experimental 12/8 three-phase SRM

The SRM employed in the experimental implementation and testing of the SR generator control strategies was that described in Section 5.1. Each phase of this 12/8 three-phase SR generator draws excitation current and returns generated current eight times per revolution. Figure 7.1 shows the load power versus turn-on angle and turn-off angle for a rotational speed of 900rpm when the Kikusui PLZ1003W electronic load is used to maintain the dc link voltage at 60V. Similarly, Figure 7.2 shows the load power versus turn-on angle and turn-off angle for a rotational speed of 1500rpm when the electronic load is used to maintain the dc link voltage at 50V. It is clear from the experimental results displayed in Figure 7.1 and Figure 7.2 that many combinations of turn-on angle and turn-off angle exist that yield the same output power.

Figure 7.3 shows the load power versus dc link voltage for operation at 1500rpm with constant firing angles of θ_{ON} = 7.5 degrees before alignment and θ_{OFF} = 7.5 degrees after alignment. The electronic load was employed to maintain the dc link voltage at the desired level for each sample point used in the graph. In Figures 7.1, 7.2 and 7.3 the load power is effectively equivalent to the net generated power as the voltage across the dc link capacitor is held constant by the electronic load. This follows from the capacitor equation:

$$i_C = C\frac{dV}{dt} \tag{7.1}$$

which indicates that for a constant dc link voltage, $i_C = 0$. Hence, the average dc link current, I_O, is equal to the average load current, I_L.

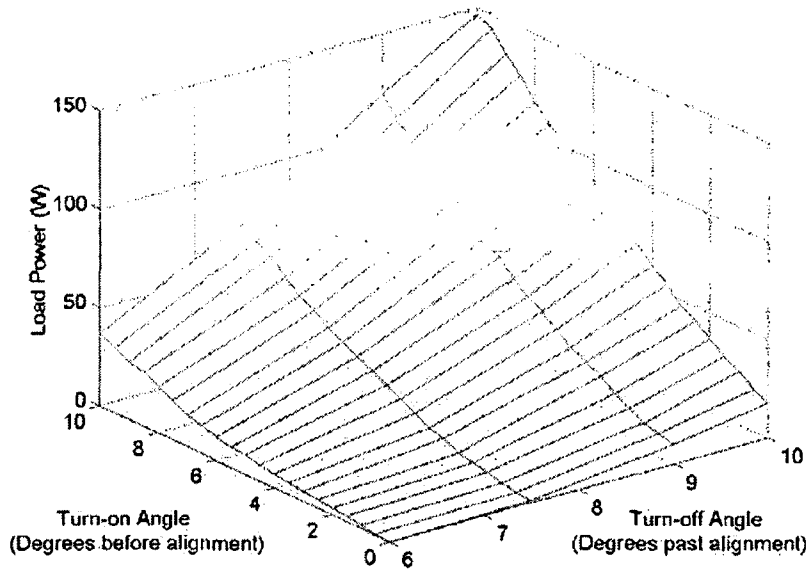

Figure 7.1: Load power versus turn-on angle and turn-off angle for a rotational speed of 900rpm with the electronic load used to maintain the dc link voltage at 60V.

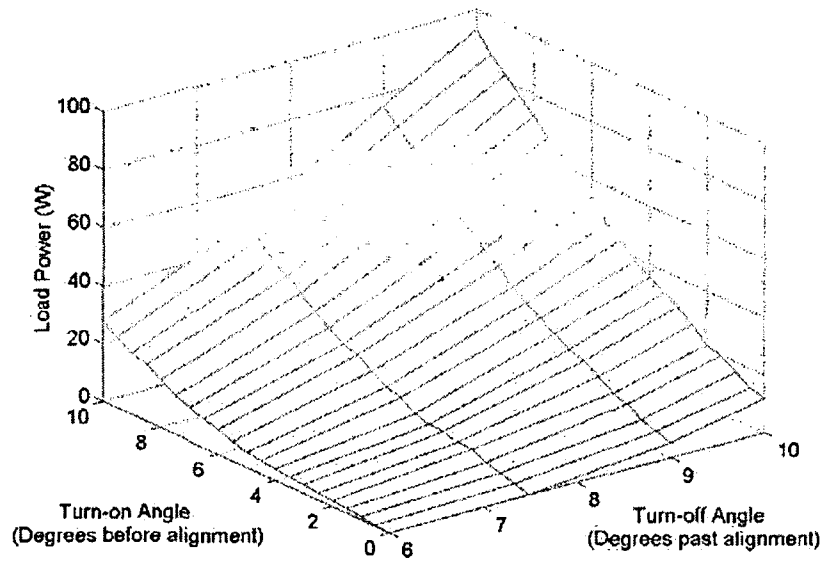

Figure 7.2: Load power versus turn-on angle and turn-off angle for a rotational speed of 1500rpm with the electronic load used to maintain the dc link voltage at 50V.

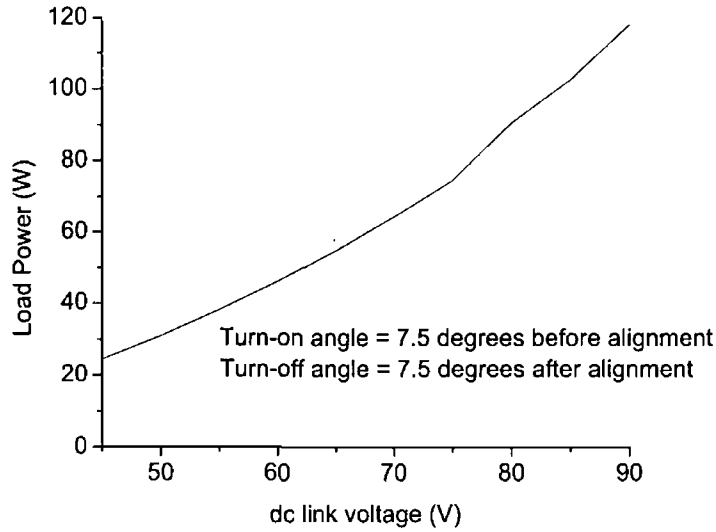

Figure 7.3: Load power versus dc link voltage for operation at 1500rpm with constant firing angles of θ_{ON} = 7.5 degrees before alignment and θ_{OFF} = 7.5 degrees after alignment.

Figure 7.4 shows both the phase A switch signal and the phase A current waveform for operation at 900rpm at a dc link voltage of 60V (controlled using the electronic load) and with fixed firing angles of θ_{ON} = 1.5 degrees before alignment and θ_{OFF} = 10 degrees after alignment. The current waveform resembles that of Figure 2.18(c) whereby the current decreases immediately after θ_{OFF} is reached due to a small back-emf value. Figure 7.5 shows the same two signals under the same operating conditions with θ_{ON} advanced to 4 degrees before alignment. As can be seen, the current waveform now resembles the flat-topped waveform of Figure 2.18(b) as a result of the back-emf balancing with the dc link voltage. Figure 7.6 shows the same two signals with the turn-on angle advanced even further such that θ_{ON} = 10 degrees before alignment. The current waveform now resembles that of Figure 2.18(a) due to the back-emf in the phase winding having a larger magnitude than the dc link voltage. The net generated power for operation with θ_{ON} = 1.5, 4 and 10 degrees before alignment was 33W, 59.9W and 146.4W respectively. Figure 7.7 shows the switch signals for all three phases of the machine for operation at 900rpm and with θ_{ON} = 7.5 degrees before alignment and θ_{OFF} = 7.5 degrees after alignment.

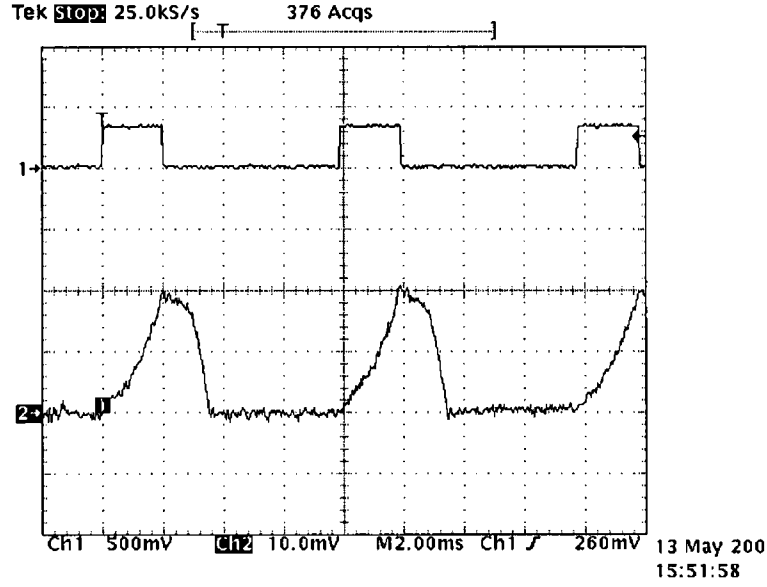

Figure 7.4: Phase A switch signal (Channel 1) and phase A current waveform (Channel 2 – 2A/div), speed = 900rpm, dc link voltage = 60V, θ_{ON} = 1.5 degrees before alignment and θ_{OFF} = 10 degrees after alignment.

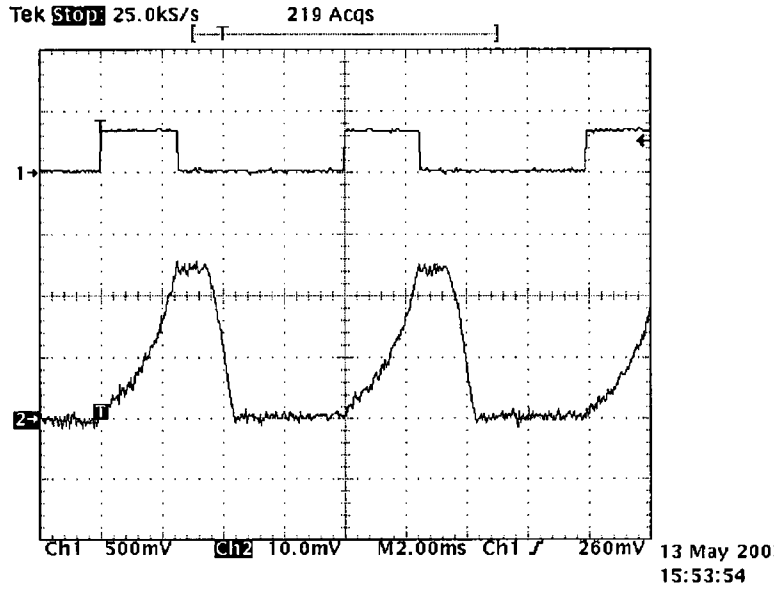

Figure 7.5: Phase A switch signal (Channel 1) and phase A current waveform (Channel 2 – 2A/div), speed = 900rpm, dc link voltage = 60V, θ_{ON} = 4 degrees before alignment and θ_{OFF} = 10 degrees after alignment.

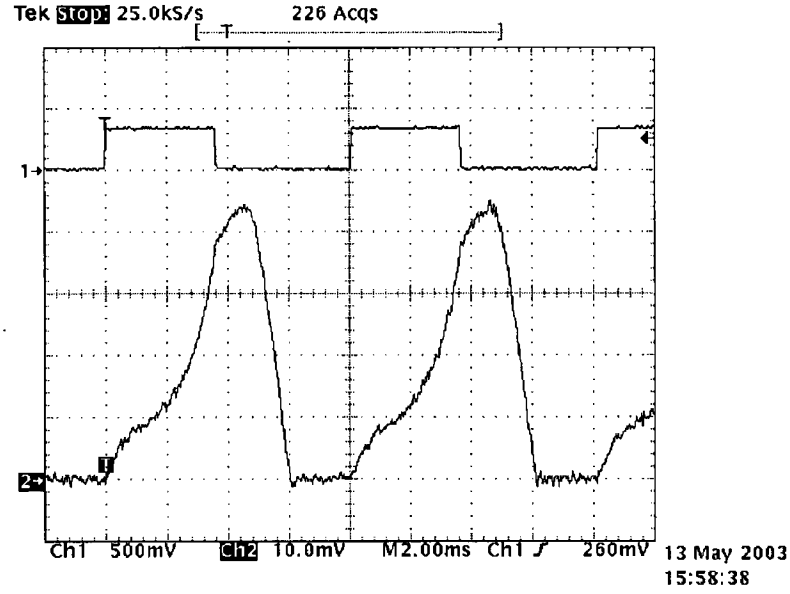

Figure 7.6: Phase A switch signal (Channel 1) and phase A current waveform (Channel 2 – 2A/div), speed = 900rpm, dc link voltage = 60V, θ_{ON} = 10 degrees before alignment and θ_{OFF} = 10 degrees after alignment.

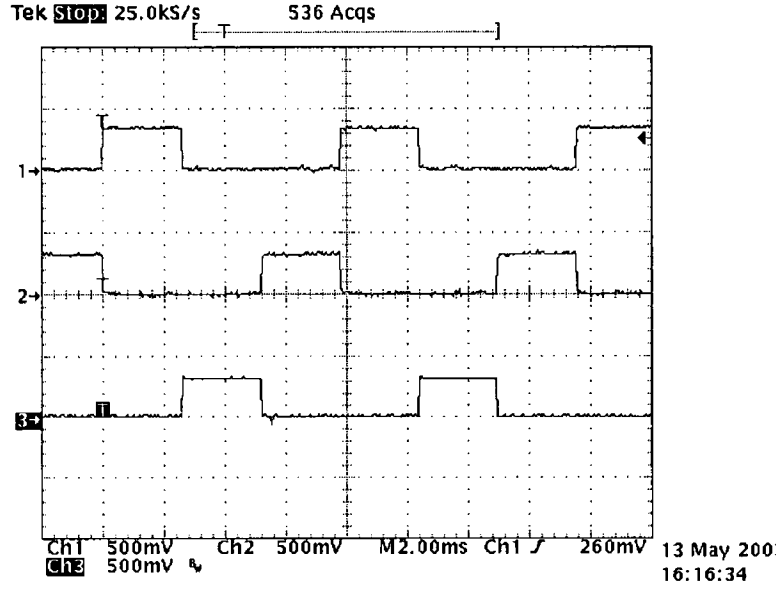

Figure 7.7: Switch signals for all three phases of the machine for operation at 900rpm and with θ_{ON} = 7.5 degrees before alignment and θ_{OFF} = 7.5 degrees after alignment.

Figure 7.8 shows both the phase A switch signal and the phase A current waveform for operation at 1500rpm at a dc link voltage of 50V (controlled using the electronic load) and with fixed firing angles of θ_{ON} = 7.5 degrees before alignment and θ_{OFF} = 10 degrees after alignment. Figure 7.9 shows the same waveforms for operation under identical conditions apart from the firing angles which were fixed at θ_{ON} = 14 degrees before alignment and θ_{OFF} = 7.5 degrees after alignment. The net generated power was 69.4W for the operation shown in Figure 7.8 and 85.4W for the operation shown in Figure 7.9. Figure 7.10 shows the phase A switch signal as well as the summation of the three phase currents for operation at 1500rpm at a dc link voltage of 50V with fixed firing angles of θ_{ON} = 7.5 degrees before alignment and θ_{OFF} = 7.5 degrees after alignment.

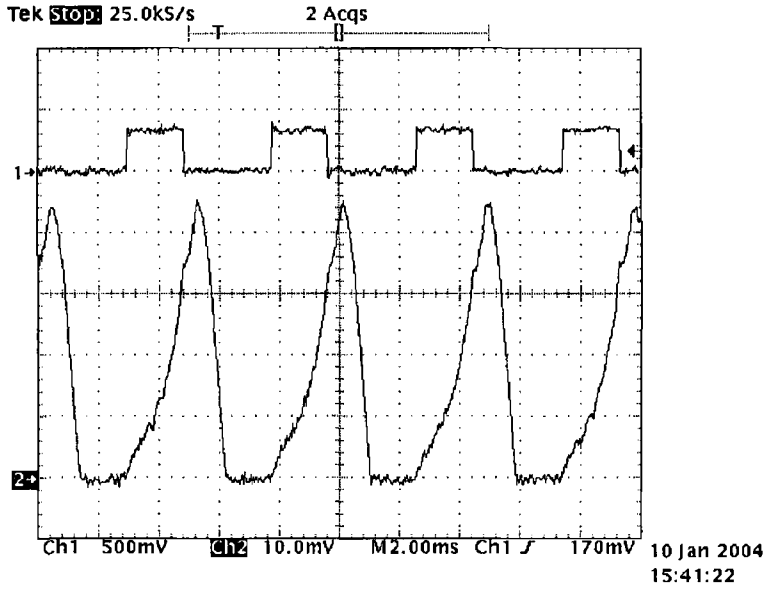

Figure 7.8: Phase A switch signal (Channel 1) and phase A current waveform (Channel 2 – 1A/div), speed = 1500rpm, dc link voltage = 50V, θ_{ON} = 7.5 degrees before alignment and θ_{OFF} = 10 degrees after alignment.

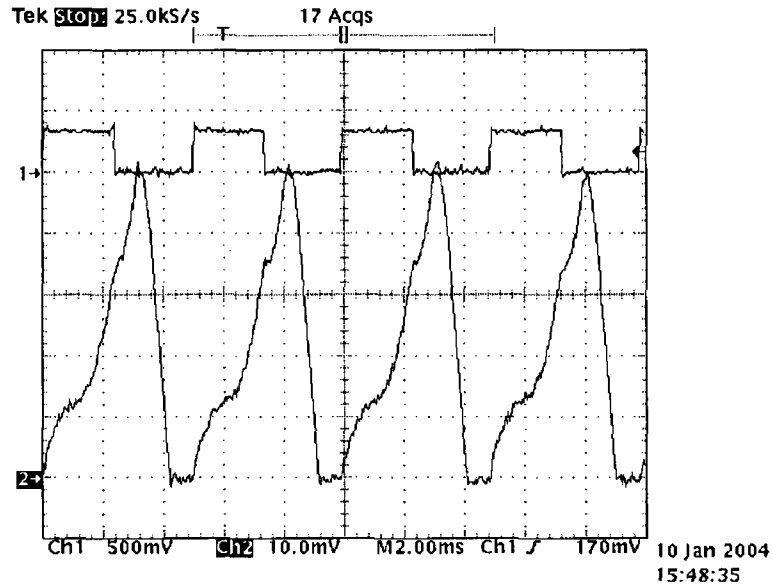

Figure 7.9: Phase A switch signal (Channel 1) and phase A current waveform (Channel 2 – 1A/div), speed = 1500rpm, dc link voltage = 50V, θ_{ON} = 14 degrees before alignment and θ_{OFF} = 7.5 degrees after alignment.

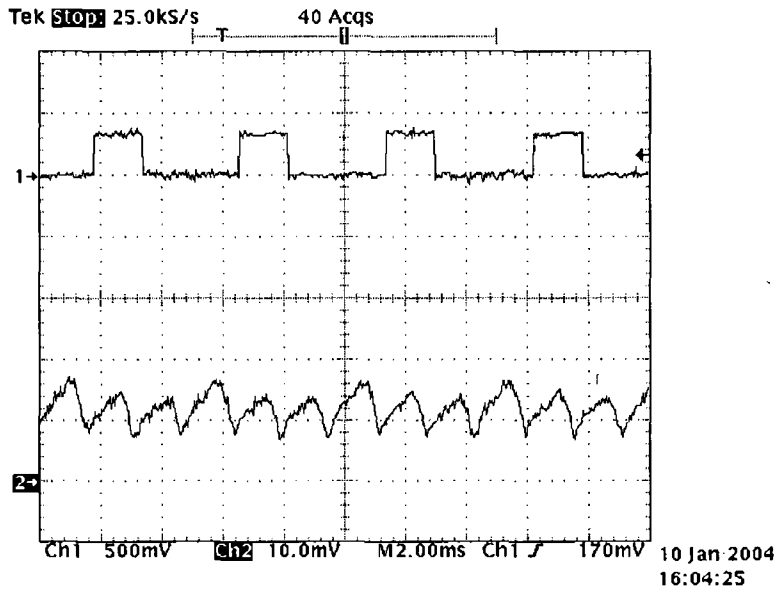

Figure 7.10: Phase A switch signal (Channel 1) and the waveform representing the summation of all three phase currents (Channel 2 – 2A/div), speed = 1500rpm, dc link voltage = 50V, θ_{ON} = 7.5 degrees before alignment and θ_{OFF} = 7.5 degrees after alignment.

The SR generator controller is required to maintain the average dc link voltage constant. However, the dc link capacitance has an integrating or smoothing effect on the dc link voltage. Therefore, the generator controller requires a lower bandwidth to control the dc link voltage than is required by the motor controller to control the phase current (and the torque that is subsequently produced) (Miller 2001). For this reason, it is possible to implement the generator control strategies described in this chapter using the ADSP-21990 operating at 32MHz as opposed to the high-bandwidth motor control that was implemented at 160MHz using the ADSP-21992. All of the control strategies described in the following sections are aimed at SR generator operation in single pulse mode.

7.2 Simple control strategy

With the SR generator operating at a sufficiently high speed such that it operates under single pulse control, the only two parameters that enable regulation of the voltage on the link are the turn-on and turn-off angles. It is possible to implement a very simple control scheme that requires no prior knowledge or characterisation of the SRM. The turn-off angle is fixed and the turn-on angle is used to control the dc link voltage. The chosen turn-off angle should be large enough to ensure that the dc link voltage can be maintained under maximum load conditions. No current measurement is required and the dc link voltage measurement is used to determine the turn-on angle according to a simple algorithm.

Starting with some initial selected turn-on angle, the turn-on angle is advanced by a fraction of a degree (increasing the conduction interval) if the measured dc link voltage is less than the reference voltage level and is delayed (decreasing the conduction interval) if the voltage is greater then the reference level. The initial turn-on angle should be chosen relatively close to the alignment position i.e. 2-3 degrees before alignment. This prevents any possibility of the system generating such a large current that overshoot of the dc link voltage could occur (as might be the case with a large initial turn-on angle and a small load). The increment/decrement in the turn-on angle should be chosen to be relatively small (to keep voltage ripple on the dc link to an acceptable level) but large enough to ensure the fast response of the controller to changes in the load or speed. It is also necessary to set maximum and minimum turn-

on angles for safety purposes. A block diagram of this simple generator control strategy is shown in Figure 7.11.

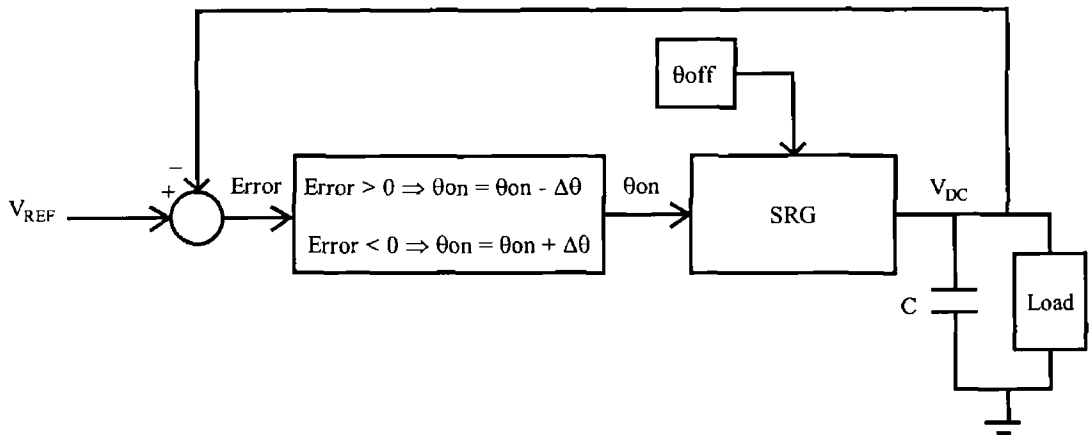

Figure 7.11: Block diagram of the simple generator control strategy.

This control scheme was implemented on the ADSP-21990 with an initial selected turn-on angle of 2.5 degrees before alignment, a turn-on angle increment/decrement value of 0.05 mechanical degrees and a turn-off angle of 7.5 degrees after alignment. Figure 7.12 shows the dc link voltage and the dc link current with a step in the load from 0.3A to 2A at 1.2s followed by a step back down to 0.3A after 3.5s for a voltage reference of 50V. Figure 7.13 shows the response of the system to a step in the operating speed from 1000rpm to 1400rpm after 1.6s. The dc link current, dc link voltage and the generator speed are shown.

The main advantage of this simple control scheme is that no prior knowledge or characterisation of the machine is required apart from, obviously, the number of rotor/stator poles and the number of phases etc. Also, there is no need for dc link current measurement. Its main disadvantage is its relatively low efficiency levels as a result of the constant turn-off angle (although it will be efficient at the power level for which the selected turn-off angle is the optimal angle from an efficiency viewpoint).

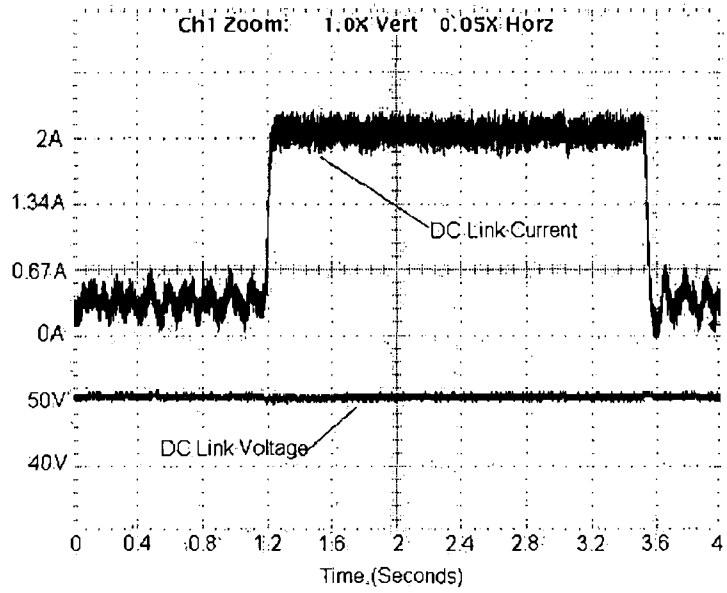

Figure 7.12: The dc link voltage and the dc link current with a step in the load from 0.3A to 2A at 1.2s followed by a step back down to 0.3A after 3.5s for a voltage reference of 50V.

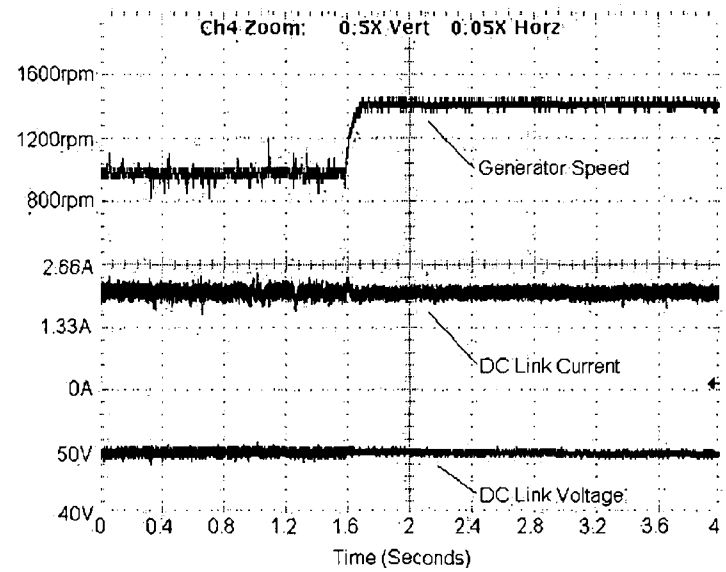

Figure 7.13: Response of the experimental system to a step in the operating speed from 1000rpm to 1400rpm after 1.6s. The dc link current, dc link voltage and the generator speed are shown.

7.3 Inverse model control strategy

In Section 3.5 of this thesis, a SR generator control strategy based on an inverse model approach was tested through simulation. The suggested approach described in that section built on that previously outlined in (Kjaer 1994). In that paper, Kjaer et al. derive an inverse model of the SR generator which relates the firing angles for single pulse operation to the average dc link current (also referred to as the average net generated current), the dc link voltage and the generator speed. In Kjaer's closed-loop generator controller, a voltage controller outputs the required average dc link current to account for the voltage mismatch and the inverse model is then used to select the correct firing angles to produce the necessary current. A limitation of the approach described in (Kjaer 1994), however, is that the inverse model is obtained on the basis of a linear inductance profile. Under this assumption, it is shown in (Kjaer 1994) that there is a quadratic relationship between the turn-on firing angle, θ_{ON}, and the average dc link current, I_O, i.e.:

$$I_O = \frac{V_{dc}}{\omega}(A\theta_{ON}^{\ 2} + B\theta_{ON} + C) \tag{7.2}$$

where ω is the rotational speed, V_{dc} is the dc link voltage and the expressions for A, B and C are as given in (Kjaer 1994). Thus, the required average dc link current can be used to deduce the turn-on angle, θ_{ON}, analytically using equation (7.2).

As for the simulation work described in Section 3.5, the assumption of a linear inductance profile is not made here. Instead, the relationship between the turn-on angle and the average dc link current is obtained by experimental means. Figure 7.14 shows the relationship between the average dc link current and the turn-on angle for a fixed turn-off angle of 7.5 degrees after alignment. Also shown in Figure 7.14 is an approximation to the real data curve that was obtained using a polynomial fit. This is a first-order polynomial representation of the real data and as can be seen, the approximation is quite good. In the simulation work described in Section 3.5, a second order polynomial was employed as a curve fit. The reason that it is possible to use a first order polynomial is because, as shown in Figure 5.1, the particular characteristics of the 12/8 SRM employed are such that there is no saturation over the operating current range. Using a first-order polynomial fit (as opposed to a second-

order polynomial fit as was employed in the simulation work and which would be more accurate) reduces DSP control cycle time due to a reduction in the computational requirements. The polynomial fit to the curve in Figure 7.14 is represented by equation (7.3) where A = 2.278 and B = -3.042.

$$I_0 = \frac{V_{dc}}{\omega}(A\theta_{ON} + B) \tag{7.3}$$

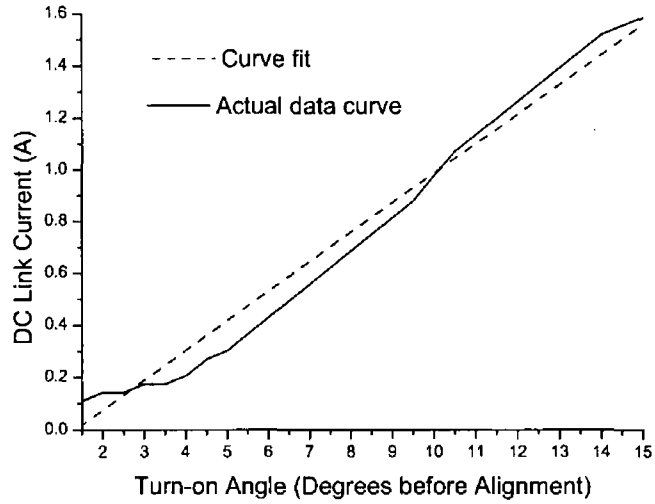

Figure 7.14: Actual and curve fit relationships between the turn-on angle and the dc link current for a turn-off angle of 7.5 degrees after alignment and V_{dc} = 50V.

Having established the mathematical relationship between the turn-on angle and average dc link current for a fixed turn-off angle, the generator control system shown in Figure 7.15 is applicable. $F(\theta)$ is the approximation to the exact relationship between the turn-on angle and the average dc link current.

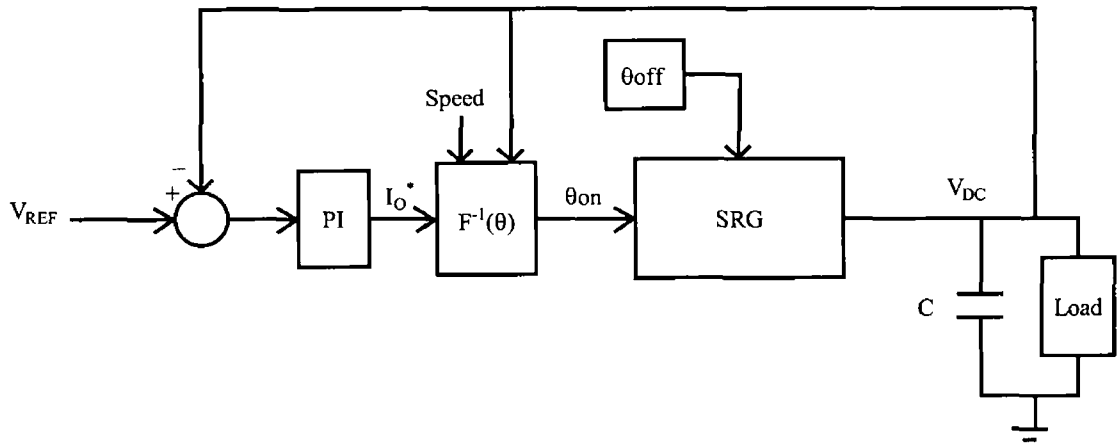

Figure 7.15: Block diagram of the inverse model control strategy.

The voltage controller (in this case a PI controller) outputs the required average generated current, I_O^*, required to bring the dc link voltage, V_{dc}, to the demanded level. The inverse machine model described by $F^{-1}(\theta)$ then selects the appropriate turn-on angle to produce the necessary current.

The control strategy was implemented using the experimental set-up for a voltage reference of 50V and a fixed turn-off angle of 7.5 degrees after alignment. The PI controller was tuned manually. The resultant constants were P = 0.25 and I = 0.1. The control strategy was then tested under different conditions to verify the control algorithm.

Figure 7.16 shows the response of the experimental system to a sudden switch in the load from 0.3A to 2A after 1.6s and back to 0.3A after 2.7s. The SR generator was operating at 1400rpm and at a 50V reference voltage. Figure 7.17 shows the response of the experimental system to a sudden step in generator speed from 1000rpm to 1400rpm after 1.4s under a load of 2A and at a 50V reference level. Figure 7.18 shows the response of the experimental system to changes in the load current at a generator speed of 1400rpm. The load is increased from 1A to 2A at 0.4s and reduced to 0.3A after 1.5s. Figure 7.19 shows the response of the system when starting from an initial dc link voltage of 40V to a reference voltage of 50V under a 0.3A load at a speed of 1000rpm. The overshoot in the dc link current is in part due to supplying the load current but also, during the transient, the SR generator must charge the dc link

capacitor to the higher voltage level. The new voltage level is reached in approximately 0.4s.

Although operation was quite good this control strategy suffers from operation at non-optimum efficiency levels in a similar manner to the simple control strategy. It also has the additional disadvantage of requiring some measurement and curve fitting for determination of the inverse model. This strategy also requires operation at a constant voltage reference for accurate operation.

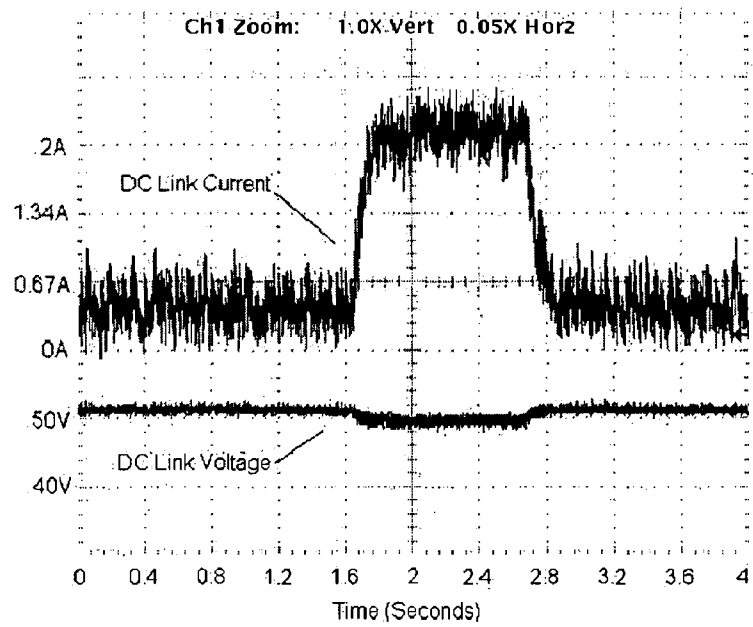

Figure 7.16: Response of the experimental system to sudden switches in the load from 0.3A to 2A and back to 0.3A for a speed of 1400rpm and at a 50V reference voltage.

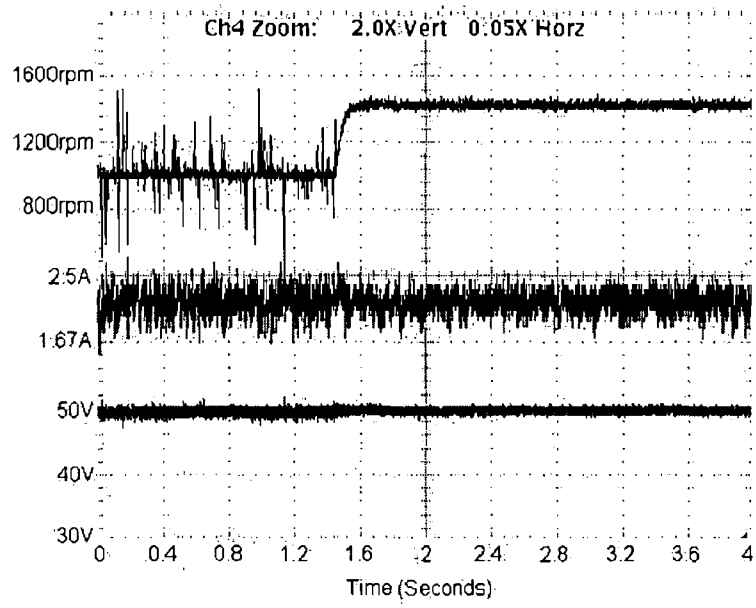

Figure 7.17: Response of the experimental system to a sudden step in generator speed from 1000rpm to 1400rpm under a load of 2A and at a 50V reference level.

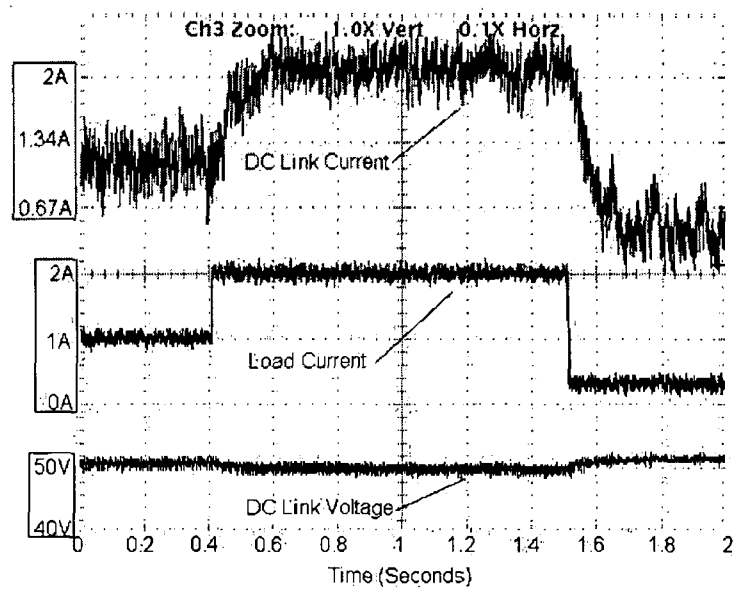

Figure 7.18: Response of the experimental system to changes in the load current at a generator speed of 1400rpm. The load is increased from 1A to 2A at 0.4s and reduced to 0.3A after 1.5s.

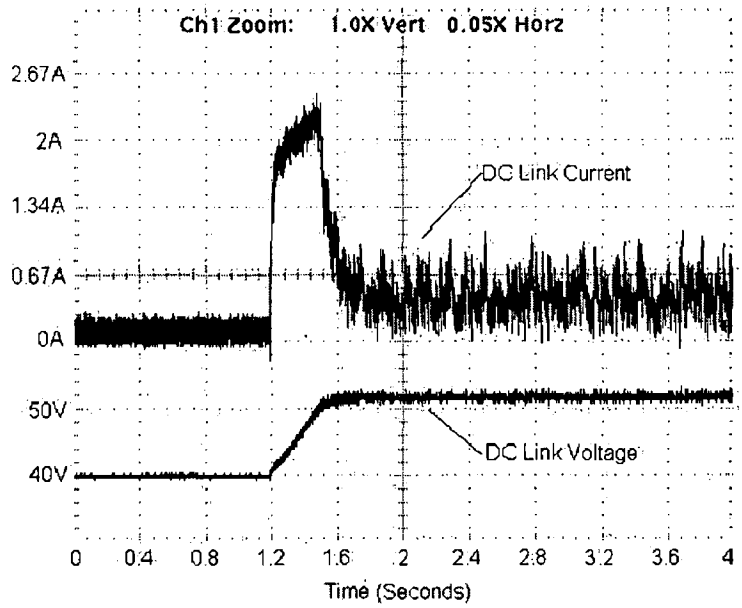

Figure 7.19: Response of the experimental system when starting from an initial dc link voltage of 40V to a reference voltage of 50V under a 0.3A load and at a speed of 1000rpm.

7.4 Optimal control strategy

Although both the simple and inverse model control strategies succeed in regulating the dc link voltage as required, neither strategy enables SR generator operation at a preferred optimum efficiency level. In single pulse mode operation, the magnitude and shape of the phase current is dependent on the choice of turn-on and turn-off angles. It is well known that for a particular operating speed there are many conduction angles that will provide the same average dc link current. However, each of these different conduction angles, while producing equal amounts of power, will have different rms phase currents. It is clear that a lower rms phase current will result in lower conduction and switching losses. According to Torrey, a reduction in the rms phase current also implies a reduction in the peak flux in the SR generator with a subsequent reduction in the core losses (Torrey 2002). In addition, Torrey states that minimisation of rms phase currents tends to reduce the current peaks and positive torque production thereby reducing both rms dc link current and torque ripple (Torrey 2002). Consequently, a higher level of efficiency can be attained by minimising the rms phase current. Both (Torrey 2002) and (Mese 2000) employ the rms phase current as a gauge of efficiency. That approach is also adopted here. Thus, for single pulse mode operation it makes sense to choose the conduction angles that result in operation

with minimum rms phase current and hence, with maximum efficiency, for a particular generator speed and dc link current.

It is possible, either through simulation or experimentation, to develop a three-dimensional map relating the optimum turn-off angle to the average dc link current and generator speed for a particular dc link voltage (in the majority of applications the reference voltage is a constant). For a variety of speed and dc link current operating points, the optimum efficiency turn-off angle is found by varying the turn-off angle and determining that with the lowest corresponding rms phase current. While the turn-off angle is varied in pursuit of the optimum efficiency point, the turn-on angle is used to ensure closed-loop voltage control of the dc link (as for the simple control strategy). As stated, the rms phase current value is used to select the optimal efficiency turn-off angle. However, future work might include using full efficiency measurements performed on the SR generator, taking both copper losses and iron losses into account, to confirm that the optimal turn-off angles are correct.

Using the experimental set-up, the optimum turn-off angle was determined for various generator speed (ranging from 800rpm to 1500rpm) and dc link current (ranging from 0.3A to 2A) operating points. The voltage reference was 50V. Figure 7.20 shows the optimum turn-off angle as a function of generator speed and average dc link current.

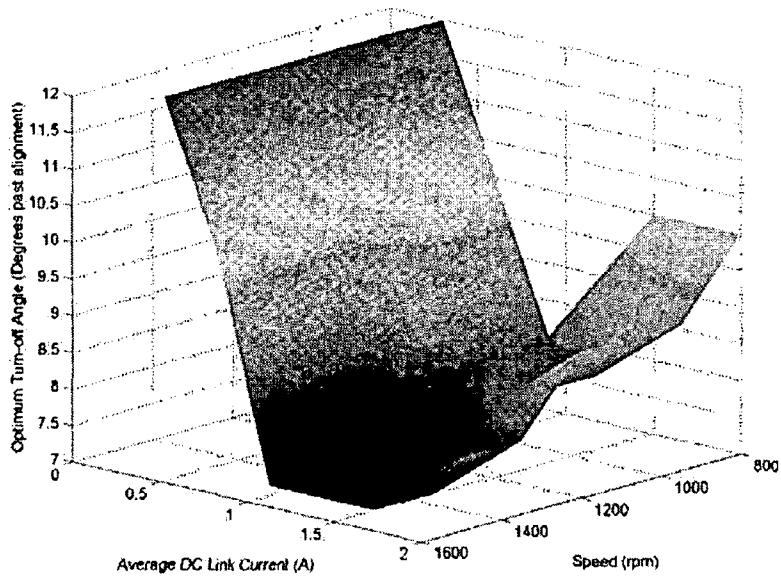

Figure 7.20: Optimum turn-off angle as a function of generator speed and average dc link current.

It is possible to generate a mathematical model of the data represented in Figure 7.20 using multiple regression. The data was fitted using least squares to the following model:

$$\theta_{OFF} = 14.8568 - 0.0006 * \omega - 7.7778 * I_{dc\,link} \quad \textit{for average dc link current} < 1A \quad (7.3)$$

and

$$\theta_{OFF} = 8.9158 - 0.0026 * \omega + 1.4264 * I_{dc\,link} \quad \textit{for average dc link current} > 1A \quad (7.4)$$

where ω is the speed and $I_{dc\,link}$ is the average dc link current.

Figure 7.21 shows the optimum turn-off angle versus speed and average dc link current for the least squares fitted mathematical model of the experimental data (model represented by equations (7.3) and (7.4)). As can be seen, the curve is similar to that of Figure 7.20 and produces turn-off angles very close to the actual optimal turn-off angles.

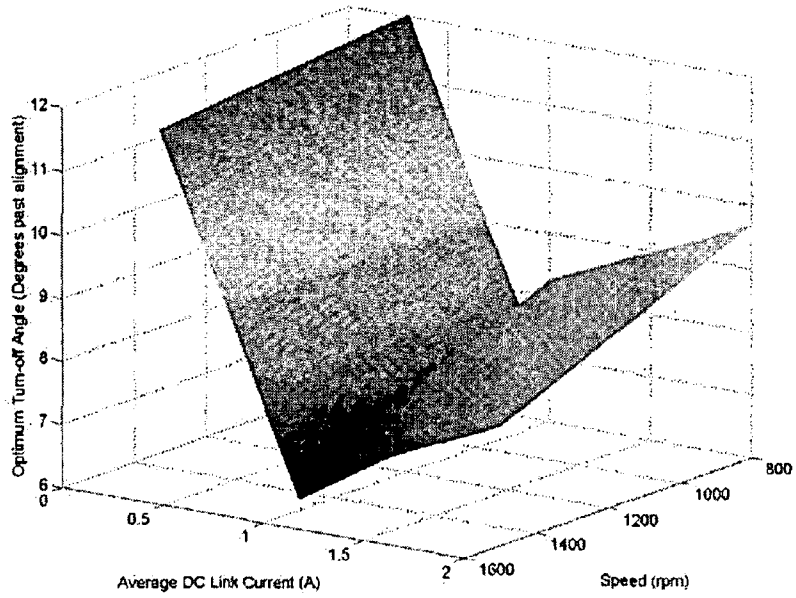

Figure 7.21: Optimum turn-off angle versus speed and average dc link current for the least squares fitted mathematical model of the experimental data.

Figure 7.22 shows a block diagram of the proposed optimal turn-off angle closed-loop voltage control strategy. The average dc link current and dc link voltage are measured and are inputted to the DSP. The position information is used to calculate the operating speed. The dc link current measurement and speed are then used to calculate the optimum turn-off angle from the least squares model. The measured dc link voltage is compared to the reference voltage and the turn-on angle is advanced by a fraction of a degree (increasing the conduction interval) if the measured dc link voltage is less than the reference voltage level and is delayed (decreasing the conduction interval) if it is greater then the reference level. As with the simple control strategy, the increment/decrement in the turn-on angle should be chosen to be relatively small (to keep voltage ripple on the dc link to an acceptable level) but large enough to ensure a fast response of the controller to changes in the load or speed. Because the turn-off angle is optimal for a given speed and dc link current, the turn-on angle is then also guaranteed to give optimal efficiency (ensuring overall optimal efficiency control).

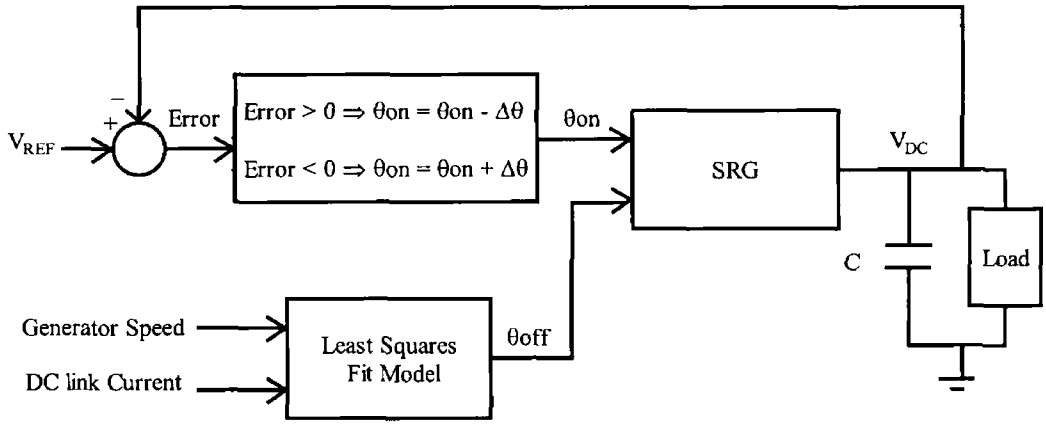

Figure 7.22: Block diagram of the optimal turn-off angle SR generator control strategy.

The control strategy was implemented for a voltage reference of 50V and a turn-on angle increment/decrement value of 0.2 mechanical degrees was chosen. Equations (7.3) and (7.4) were used to calculate the optimal turn-off angle. A number of tests were performed to verify the efficacy of this control approach. The tests were designed to examine the system's ability to react to sudden large deviations in both the load current and generator speed when the optimal control strategy is employed. If the dc link voltage recovers quickly after the system experiences an extreme change in either load or speed (or both), then it is safe to assume that it will cope well with smaller variations and/or more slowly varying conditions. The response of the system when generating first begins (with the dc link voltage considerably lower than the desired reference value) is also examined.

Figure 7.23 shows the response of the experimental system to a sudden switch in the load from 0.3A to 2A after 0.9s and back to 0.3A after 3s. The SR generator was operating at 1400rpm and at a 50V reference voltage. Figure 7.24 shows the response of the experimental system to a sudden step in generator speed from 1000rpm to 1400rpm after 1.6s under a load of 0.3A and at a 50V reference level. Figure 7.25 shows the response of the experimental system to changes in the load current at a generator speed of 1400rpm. The load is increased from 1A to 2A at 1.6s and reduced to 0.3A after 3.5s. Figure 7.26 shows the response of the system when starting from an initial dc link voltage of 40V to a reference voltage of 50V under a 0.3A load at a

speed of 1000rpm. As for the inverse model strategy, the overshoot in the dc link current is because, apart from supplying the load current, during the transient, the SR generator must also charge the dc link capacitor to the higher voltage level. The new voltage level is reached in under 0.4s. Figure 7.27 shows the response of the system to a step in the speed from 1000rpm to 1400rpm after 0.6s followed by a step in the load current from 1A to 2A after 2.2s.

Because the optimal efficiency turn-off angle is always selected, this control scheme offers the most efficient power generation possible. Like the inverse model method, the scheme is dependent on operation at a constant reference voltage (which is the case for the majority of generator applications). The control scheme also has the disadvantage of requiring characterisation of the SRM.

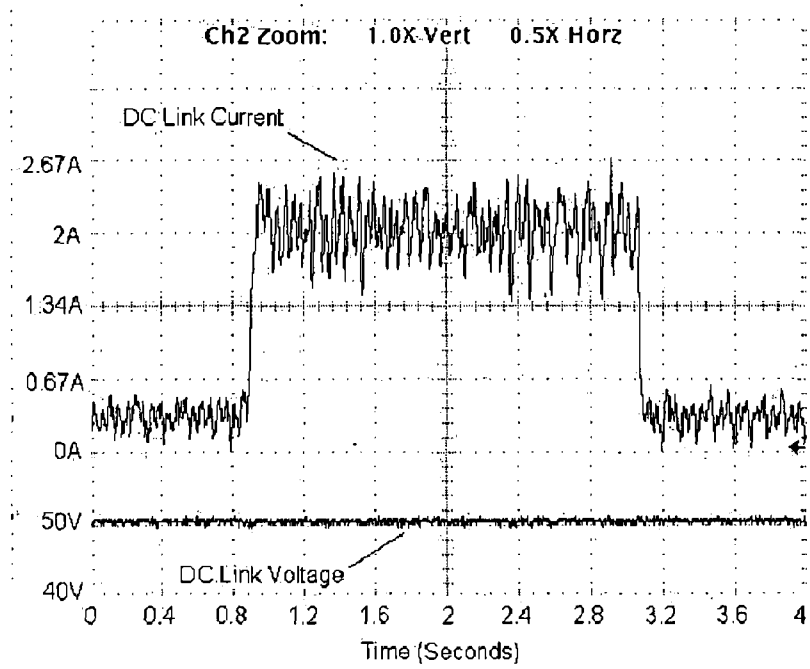

Figure 7.23: Response of the experimental system to a sudden switch in the load from 0.3A to 2A after 0.9s and back to 0.3A after 3s. The SR generator was operating at 1400rpm and at a 50V reference voltage.

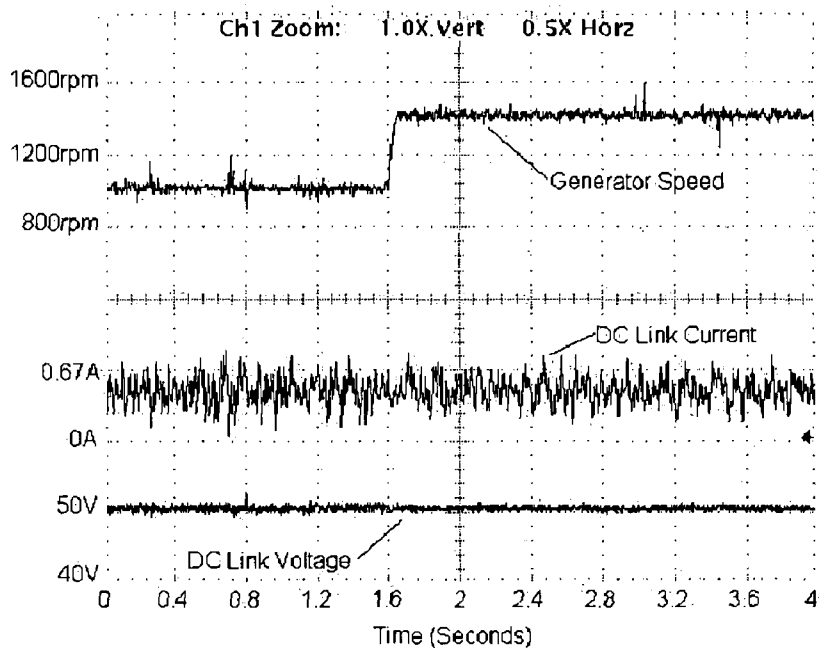

Figure 7.24: Response of the experimental system to a sudden step in generator speed from 1000rpm to 1400rpm after 1.6s under a load of 0.3A and at a 50V reference level.

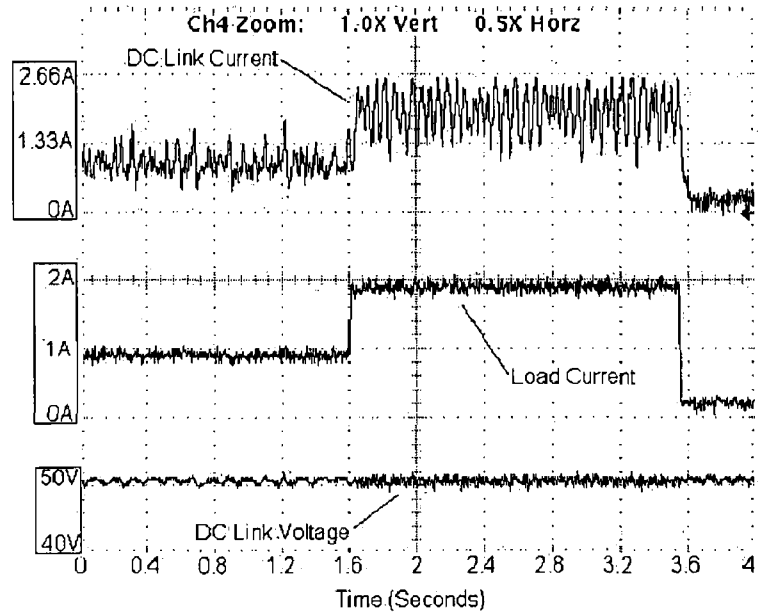

Figure 7.25: Response of the experimental system to changes in the load current at a generator speed of 1400rpm. The load is increased from 1A to 2A at 1.6s and reduced to 0.3A after 3.5s.

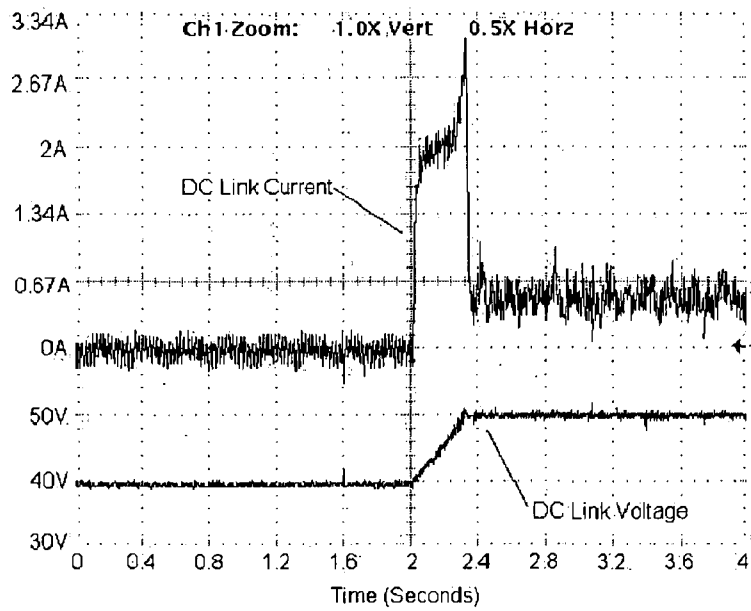

Figure 7.26: Response of the experimental system when starting from an initial dc link voltage of 40V to a reference voltage of 50V under a 0.3A load and at a speed of 1000rpm.

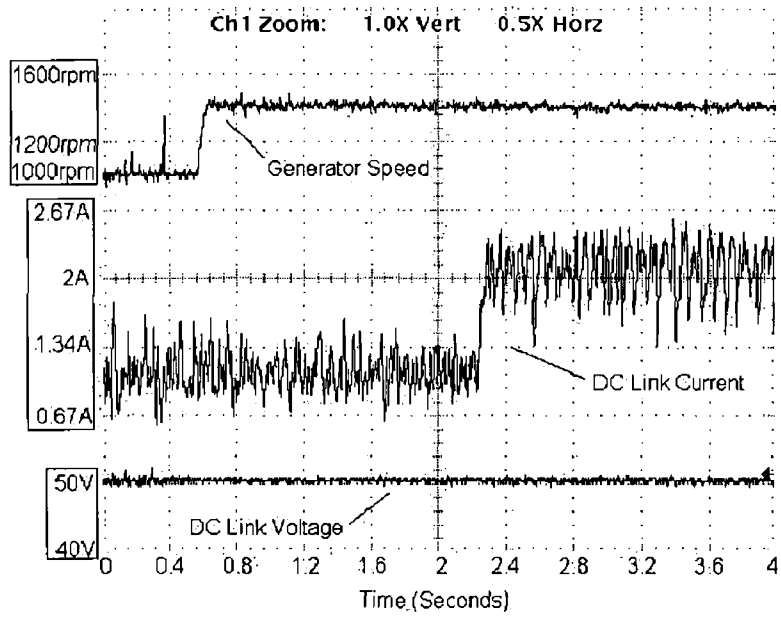

Figure 7.27: Response of the experimental system to a step in the speed from 1000rpm to 1400rpm after 0.6s followed by a step in the load current from 1A to 2A after 2.2s.

The method for selecting the optimal turn-off angle that results in the waveforms shown in Figures 7.23-7.27 is similar to that described in (Sozer 2003). In (Sozer 2003), an optimal turn-off angle selection based on a mapping of the optimum turn-off angle versus generator speed and dc power is described. Thus, the turn-off angle is found using a curve fit to the collection of optimal angles for all speed and power operating points. The control strategy employs a power control loop that operates inside an outer voltage control loop. A PI controller uses the voltage error signal to produce a reference power value. Another PI controller is then employed to produce the turn-on angle from the error between the reference power value and the measured power. This strategy was the result of the continuation of the work first described in (Mese 2000). It has the advantage that it can operate accurately at different voltage references. However, it does require considerably more measurement and characterisation of the SRM than the optimal efficiency control strategy presented in this thesis.

7.5 Efficiency comparison

To enable an efficiency comparison, the rms phase current was measured for various dc link current operating points for each of the control strategies described in this

chapter. The rms phase current is a good gauge of efficiency, as a lower rms phase current will result in lower conduction and switching losses and consequently a higher level of efficiency. Figure 7.28 shows the rms phase current as a function of dc link current at a generator speed of 1500rpm for the three control strategies. Figure 7.29 shows the phase current waveform for the optimal efficiency control strategy at a generator speed of 1500rpm and an average dc link current of 1A. Figure 7.30 shows the phase current waveform for the simple control strategy with a turn-off angle of 12 degrees after alignment at a generator speed of 1500rpm and an average dc link current of 1A while Figure 7.30 shows the phase current waveform for the same simple control strategy with a turn-off angle of 7.5 after alignment. Figure 7.31 shows the phase current waveform for the inverse model control strategy at a generator speed of 1500rpm and an average dc link current of 1A.

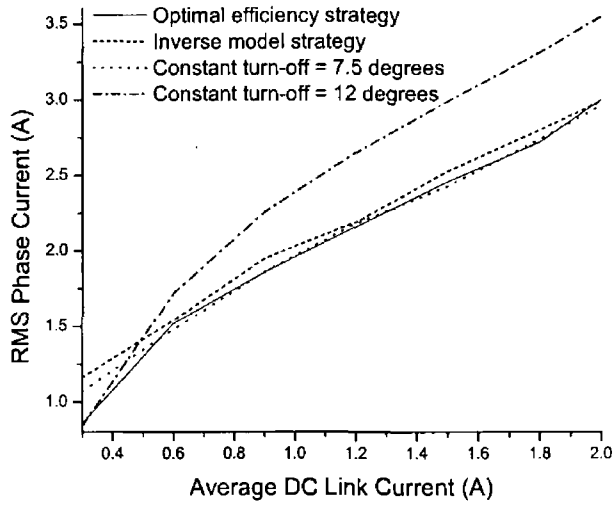

Figure 7.28: rms phase current versus average dc link current for the three control strategies at a generator speed of 1500rpm.

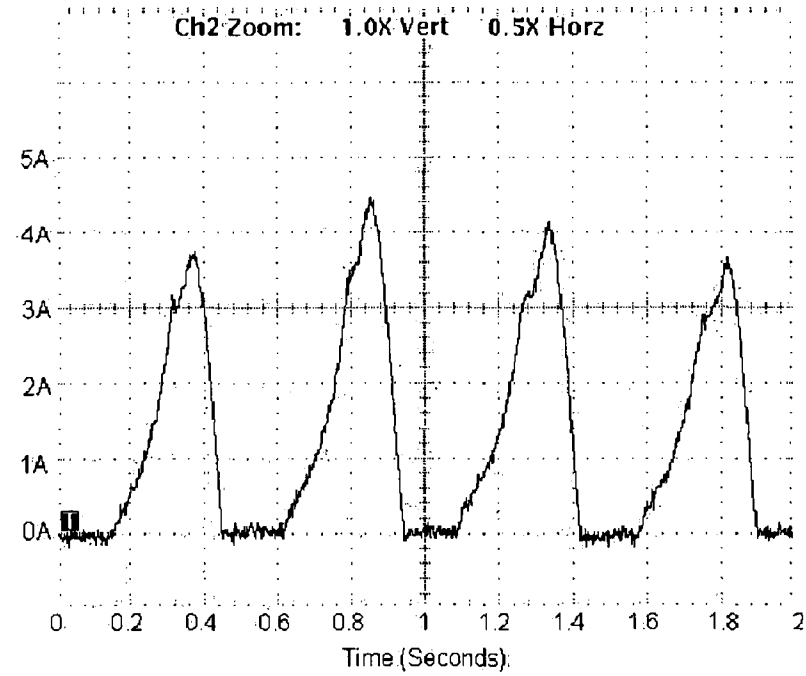

Figure 7.29: Phase current for the optimal efficiency control strategy at a generator speed of 1500rpm and an average dc link current of 1A.

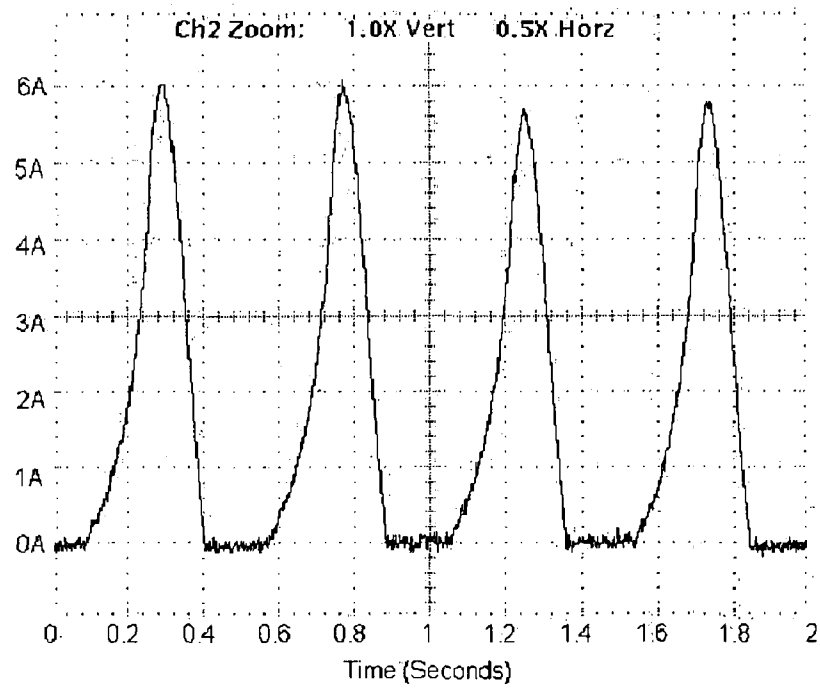

Figure 7.30: Phase current for the simple control strategy with a turn-off angle of 12 degrees after alignment at a generator speed of 1500rpm and an average dc link current of 1A.

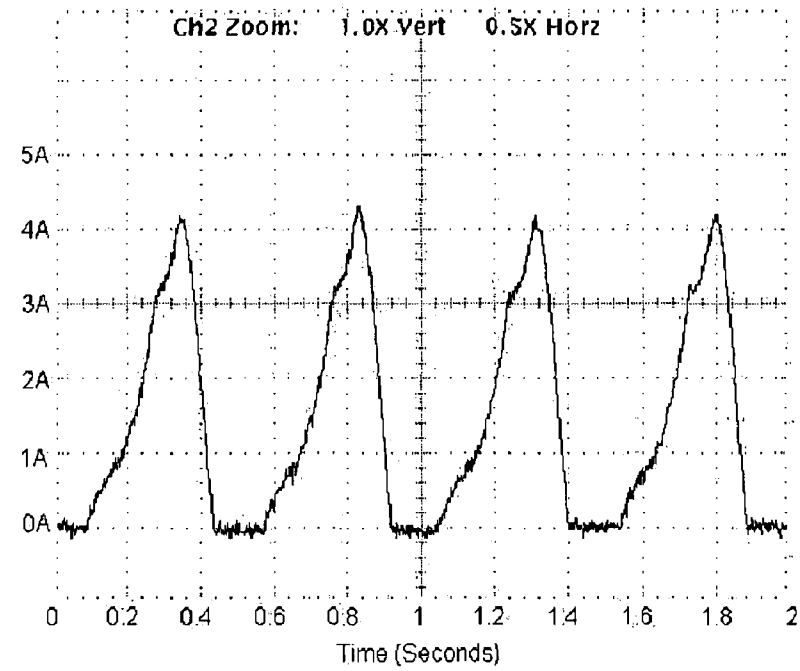

Figure 7.31: Phase current for the simple control strategy with a turn-off angle of 7.5 degrees after alignment at a generator speed of 1500rpm and an average dc link current of 1A.

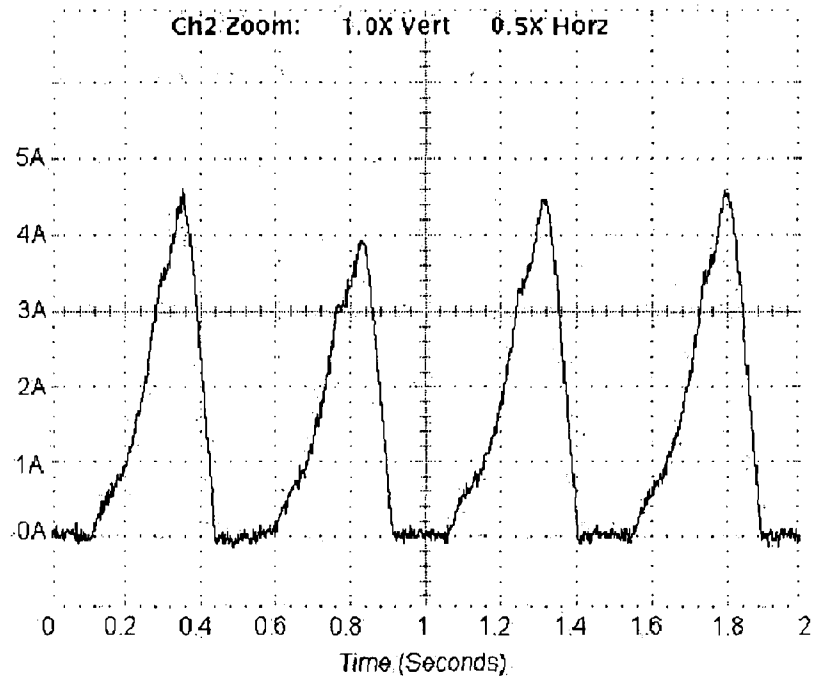

Figure 7.32: Phase current for the inverse model control strategy at a generator speed of 1500rpm and an average dc link current of 1A.

From the results shown in Figure 7.28, it is clear that the optimal control strategy is the most efficient over the majority of the range of average dc link currents at a generator speed of 1500rpm. However, at some dc link current values, the simple control strategy with a constant turn-off angle of 7.5 degrees after alignment proves to be marginally more efficient. This is because a turn-off angle of 7.5 degrees after alignment transpires to be the optimal efficiency turn-off angle for these particular dc link current operating points at a generator speed of 1500rpm. The least squares fitted mathematical model of the experimental data employed by the optimal control strategy produces turn-off angles very close to the actual optimal efficiency angles but there is obviously a slight error between the actual optimal angle and the one outputted by the model. It is important to note that, for example, at lower speeds where 7.5 degrees isn't close to the optimum efficiency angle, the optimal control strategy proves to be far more efficient than the simple strategy with a turn-off angle of 7.5 degrees after alignment. As can clearly be seen from the graph, with a turn-off angle of 12 degrees after alignment, the optimal control strategy would prove far more efficient than the simple control strategy for the entire range of operation. The inverse model control strategy (which has a constant turn-off angle of 7.5 degrees after alignment) is the least efficient strategy at low dc link currents. However, as the dc link current increases, its efficiency improves greatly and is only marginally less efficient than the optimal control strategy and the simple control strategy (with a turn-off angle of 7.5 degrees after alignment) for dc link current values above 0.6A. The inverse model strategy and simple control strategy with a turn-off angle of 7.5 degrees would be expected to give similar rms current readings due to the fact that they have the same turn-off angle of 7.5 degrees after alignment. Figures 7.29-7.32 show that with an average dc link current of 1A and at a generator speed of 1500rpm, the optimal control strategy current waveform has a similar shape to the current waveforms of both the simple control strategy with a turn-off angle of 7.5 degrees after alignment and the inverse model control strategy. This is the expected result, as from inspection of Figure 7.20, 7.5 degrees is very close to the optimum turn-off angle. The simple control strategy with a turn-off angle of 12 degrees after alignment has a higher rms current value and this is reflected in its current waveform.

7.6 Peak current comparison

While achieving high efficiency is clearly extremely desirable, another important aspect of SR generator control is its effect on the peak value of the phase current waveform. Higher peak current values require the power converter to have a higher VA rating, which consequently results in an increase in the cost of the converter. Figure 7.33 shows the peak phase current versus average dc link current for the three control strategies at a generator speed of 1500rpm. The test was carried out at 1500rpm, the upper level of the generating speed range, because for a given average dc link current, the peak current tends to increase with speed. As can be seen, the simple control strategy with a turn-off angle of 12 degrees after alignment has the highest peak current values over the entire range of operation. The optimal efficiency strategy, whose turn-off angle varies with average dc link current has relatively high peak current values at lower and higher average dc link currents but has the lowest peak values for the mid-range of the average dc link current. The simple control strategy with a turn-off angle of 7.5 degrees after alignment and the inverse model strategy have low peak current values purely as a result of the coincidental choice of 7.5 degrees as their constant turn-off angle. With a different turn-off angle, this is not necessarily the case as evidenced by the result when a turn-off angle of 12 degrees is used.

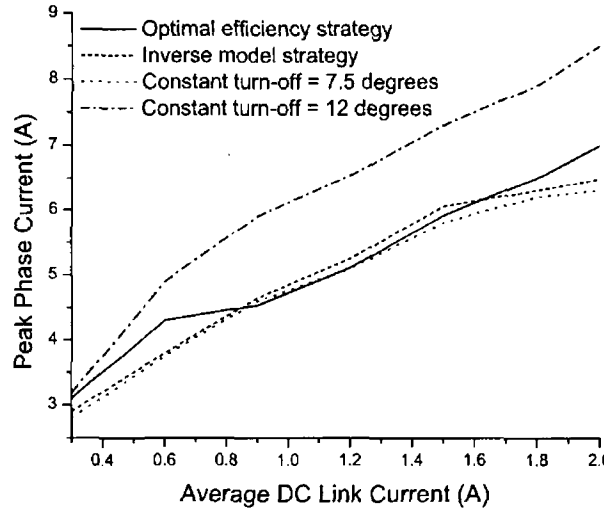

Figure 7.33: Peak phase current versus average dc link current for the three control strategies at a generator speed of 1500rpm.

7.7 Summary and conclusions

In this chapter, three separate strategies for closed-loop voltage control of a SR generator were presented and experimental results are given for a 300W 12/8 3-phase SRM. The first control scheme involves the selection of a fixed turn-off angle and the subsequent adjustment of the turn-on angle during operation to regulate the dc link voltage. The main advantage of this simple scheme is that no prior knowledge or characterisation of the machine is required apart from some simple geometrical information regarding the number of phases etc. Its main disadvantage is its relatively low efficiency levels (over most of its range of operation) as a result of the turn-off angle being held constant (although high efficiency may be achieved at certain dc link current operating points for which the turn-off angle is the optimal efficiency turn-off angle).

The second control scheme is based on the use of an inverse machine model that relates the firing angles to the average dc link current, the dc link voltage and the rotational speed. A mathematical relationship between the turn-on angle and average dc link current for a fixed turn-off angle was obtained experimentally. This relationship was then used to select the appropriate turn-on angle to produce the necessary dc link current required to keep the dc link voltage, V_{dc}, at the reference value. The required average dc link current value, I_O^*, used in the turn-on angle selection algorithm was the output of a manually tuned PI controller. Although operation was satisfactory, it suffers from the disadvantage of operation at non-optimum efficiency levels as well as the additional disadvantage of requiring some measurement and curve fitting for determination of the inverse model. The strategy also requires operation at a constant voltage reference for accurate operation.

The final control scheme involves the experimental determination of the optimum turn-off angle for various generator speed and dc link current operating points. A least squares curve fit to the experimental data produces a mathematical model that outputs the optimum efficiency turn-off angle for a particular speed and dc link current. The turn-off angle is varied to obtain optimum efficiency and the turn-on angle is used to ensure closed-loop voltage control of the dc link. The obvious advantage of this method of SR generator control is the improvement in efficiency. Like the inverse model method however, the scheme is dependent on operation at a constant reference

voltage (which is the case for the majority of generator applications). This scheme is the best for efficient power generation.

It should be noted that the machine employed in the testing of the three control strategies is a low power machine (300W). By virtue of this fact, the resistive voltage drop would be more significant than in medium/high power machines. However, this does not complicate the implementation of any of the control strategies. The simple control strategy requires no previous characterisation of the machine and is easily implemented. The inverse model control strategy and the optimal control strategy both require a certain number of measurements to be taken to enable design and implementation of the controller. However, these measurements obviously include the inherent effect of the voltage drop and therefore, its effects are automatically taken into account by the controller. Thus, all three control strategies can be used on low, medium and high power machines.

Finally, the results arising from the work described in this chapter form the basis of a paper published in *COMPEL: The International Journal for Computation and Mathematics in Electrical and Electronic Engineering* in 2005. This paper provides a good overview of SRG operation and details the development and experimental implementation of three separate closed-loop voltage control schemes. The abstract of the published paper is included in Appendix D.

Chapter Eight – Summary and conclusions

The SRM is a rugged, low-cost machine that has a simple mechanical construction. However, in spite of these advantages, the SRM has yet to see widespread acceptance in industry. The primary reason for this is the complexity of control required to achieve high performance levels for servo-type applications. The behaviour of an SRM is such that it has strong nonlinear magnetic characteristics. This results in torque production that is nonlinearly dependent on both rotor position and phase current. Hence, sophisticated electronic control of the SRMs is required to produce a smooth torque output with minimum torque ripple. Consequently, the topic of torque ripple reduction in SR motors has been the subject of considerable research activity over the years. Presently, the ever-improving DSP and microprocessor technology is enabling the implementation of more complex control algorithms than was previously possible. In this thesis, the development of three neuro-fuzzy torque ripple minimisation control strategies for SR motoring has been described. In addition, a number of simpler control strategies suitable for torque ripple-tolerant applications have been developed and tested.

The SRM is suitable for variable speed generator applications where reliability, fault tolerance and the ability to operate at high speeds are important. The lack of windings and magnets on the rotor enables high speed operation. The simple rotor construction coupled with the absence of brushes results in a robust and reliable machine that requires little maintenance. In addition, the possibility of generating into a shorted winding can be avoided by simply removing the excitation. Despite this, the control of SR generators has received considerably less attention in the literature to date than that of SR motors. This thesis contributes to the area of SR generator control through the development and testing of several control strategies.

In Chapter One, the motivation for the work described in this thesis was outlined. In addition, the reasons behind the resurgence of interest in SR motors and generators in recent years were fully explained.

In Chapter Two, the fundamental principles of operation of the SRM were introduced

and the electromagnetic characteristics of the machine were described. The basic operation of the SRM in both motoring and generating modes was also described.

In Chapter Three, the two SRM models that were employed throughout the simulation work described in this thesis were introduced. The first was a simple SRM model that was derived from the nonlinear magnetic characteristics of an SRM. The second model employed was a self-tuning nonlinear model with on-line parameter estimation that can serve as a torque observer. Two control strategies, one for motoring and one for generating, described in the literature were tested through simulation using MATLAB/Simulink. For both control strategies, the simple SRM model was used to represent a 'real' SRM.

The self-tuning nonlinear model was employed as a torque observer/estimator in the simulation of the torque ripple minimisation motor control scheme described in (Russa 2000). This was the first motor control strategy implemented. It was chosen to enable testing of the torque estimation capability of the self-tuning nonlinear model. The control scheme proved to be very effective in reducing the torque ripple. However, a disadvantage of this control strategy is that knowledge of the phase torques is required for the production of the phase current command.

The second control strategy that was implemented and tested was concerned with SR generation. It employed an inverse machine model. This followed a similar approach to that outlined in (Kjaer 1994) whereby a voltage controller outputs the required average net generated current to bring the dc link voltage to the desired value and the inverse model is then used to select the correct firing angles to produce the necessary current. In (Kjaer 1994), the inverse model relating the firing angles for single pulse mode operation to the average net generated current, the dc link voltage and the rotational speed is derived on the basis of a linear inductance profile using geometrical information and knowledge of the unsaturated aligned and unaligned phase inductances. In the implementation described in Chapter Three, however, the assumption of a linear inductance profile wasn't made and the inverse model was obtained by means of simulation. While the use of a nonlinear model is clearly advantageous, this particular implementation has the disadvantage of requiring some measurement and curve fitting for determination of the inverse model.

In Chapter Four, three neuro-fuzzy torque ripple minimisation control strategies were developed and simulation results were presented for both a 6/4 three-phase SRM and a 12/8 three-phase SRM. For all three strategies, the approach adopted was the addition of a compensating current signal to the PI controller output current signal in a current-regulated speed controlled drive. In each case, the compensating current signal was trained off-line using the ANFIS system. However, the parameters employed in the training process were different for all three control strategies as was the manner in which the training was conducted.

Neuro-fuzzy control strategy no. 1 outputted the required compensating current signal based on knowledge of the torque ripple and the rotor position. While this control strategy proved effective in reducing the torque ripple, it is limited to use with SRMs that have mildly nonlinear torque-current-position characteristics. In addition, it required a high sampling rate for effective operation. A further disadvantage is the extensive training process that is required. Furthermore, knowledge of the torque signal for both the compensator training process and for subsequent operation of the SR drive with the compensator included is required.

For operation of neuro-fuzzy control strategy no. 2, the inputs to the neuro-fuzzy compensator were the average torque and the rotor position. A considerable reduction in the torque ripple was observed when this control strategy was employed. In addition, neuro-fuzzy control strategy no. 2 is suitable for use with highly nonlinear SRMs and, as such, it is clearly superior to neuro-fuzzy control strategy no. 1. However, like neuro-fuzzy control strategy no. 1, knowledge of the torque was required both during the compensator training and during subsequent on-line operation. A further disadvantage is the iterative and hence, time-consuming, nature of the training process.

For neuro-fuzzy control strategy no. 3, the neuro-fuzzy compensator inputs were the PI controller current signal and the rotor position with the resultant compensating current produced effecting a significant decrease in the torque ripple. Like neuro-fuzzy control strategy no. 2, this control strategy is suitable for use with highly nonlinear SRMs. However, this control strategy is clearly superior to both neuro-fuzzy control strategy no.1 and no. 2 in that knowledge of the torque signal isn't

required during *on-line* operation (although it is required during the compensator training process). However, as for neuro-fuzzy control strategy no. 2, neuro-fuzzy control strategy no. 3 requires a lengthy iterative training process.

In Chapter Five, the experimental set-up employed in the development and testing of the control strategies was described. The 12/8 three-phase SRM employed was introduced as well as the power converter circuit and DSP development board used in the control of the SRM. The various measurement electronics employed and the method for deriving the rotor position were also described. Finally, the overall set-up comprising the SRM, a dc machine, the electronic circuitry and test equipment was described.

In Chapter Six, several SR motor control strategies were described and experimental results were presented. Initially, the simple 'start-up' algorithm employed was described. Four simple SR motor speed control strategies aimed at applications that can tolerate a certain amount of torque ripple were then described and tested. Three of the four control strategies were intended for low speed motoring operation while the fourth was aimed at high speed motoring in single pulse mode. In addition, the self-tuning nonlinear model introduced in Chapter Three was tested experimentally. Finally, neuro-fuzzy control strategy no. 3 was implemented and tested with the experimental system.

The first low speed motor control strategy employed fixed firing angles with a PI controller controlling the speed by outputting a current reference about which the phase currents were controlled using delta modulation current control. This simple control scheme required no prior knowledge or characterisation of the machine. However, it suffers from poor efficiency levels as a result of the employment of constant firing angles.

The second low speed motor control strategy involved the experimental determination of the turn-off angle that results in phase current reduction to zero at alignment for different motor speeds and mechanical loads. A mathematical model of the data was then created to automatically select the appropriate turn-off angle. This ensures large positive torque production. However, this strategy suffers from operation at non-

optimum efficiency levels as well as the requirement of measurement and curve fitting for determination of the mathematical model.

The final low speed motor speed control strategy enabled operation at the desired optimal efficiency level by maximising the torque per ampere produced by the SRM. The dwell angle was kept constant and the turn-on angle was regulated to ensure that the first peak of the phase current was aligned with the angle where pole overlap begins. This control strategy is clearly superior to the other two strategies as a result of the improved efficiency and the fact that no characterisation of the machine was required.

The high speed motor speed control strategy was simple to implement and required no prior knowledge or characterisation of the SRM. The turn-off angle was fixed and the turn-on angle was varied to control the motor speed. While no effort was made to ensure operation at optimal efficiency levels, future work could involve the determination of the maximum efficiency conduction angles.

Finally, the self-tuning nonlinear SRM model that was tested through simulation in Chapter Three was implemented with the experimental system. Its torque estimation capability was then employed in the experimental implementation and testing of neuro-fuzzy control strategy no. 3. Neuro-fuzzy control strategy no. 3 was chosen for implementation as it was the best of the three torque ripple reduction control strategies examined in Chapter Four. The training of the neuro-fuzzy compensator was conducted off-line using data obtained during steady-state operation of the SR drive. Neuro-fuzzy control strategy no. 3 was tested in open-loop motoring mode with a constant current reference and again under current-regulated speed control implemented using a PI controller. A significant reduction in the torque ripple was observed when the neuro-fuzzy compensator was employed.

In Chapter Seven, three strategies for SR generator control were described and their performance was examined by testing on the experimental SRM. The first control scheme involved the selection of a fixed turn-off angle and the subsequent adjustment of the turn-on angle to regulate the dc link voltage. No prior knowledge or

characterisation of the SRM was required. However, the fixed turn-off angle resulted in relatively low efficiency levels.

The SR generator inverse model control strategy previously tested through simulation in Chapter Three was tested experimentally. Despite producing satisfactory results, it suffers from the disadvantage of operation at non-optimum efficiency levels as well as the additional disadvantage of requiring measurement and curve fitting to determine the inverse model. In addition, the strategy required operation at a constant voltage reference for accurate operation.

The final control strategy involved the determination of the optimum efficiency turn-off angle for different generator speed and dc link current operating points. A mathematical model was then produced that outputted the turn-off angle while the turn-on angle was used to ensure closed-loop voltage control of the dc link. Like the inverse model approach, this control strategy required extensive measurement and curve fitting and it was also dependent on operation at a constant reference voltage. However, it did demonstrate improved efficiency when compared to the other two strategies.

Overall, the thesis contributes to the area of SRM control through the development, implementation and testing of a wide variety of control strategies for SR operation in both motoring and generating modes. Three neuro-fuzzy control strategies were developed and tested through simulation with one of the strategies, neuro-fuzzy control strategy no. 3, also implemented and tested experimentally using the ADSP-21992. The powerful ADSP-21992 DSP controller enabled the entire control operation including speed/torque control, commutation control as well as chopping of the power switches for current control to be implemented in software. This eliminated the requirement for an external analog/digital hysteresis control circuit, which is clearly beneficial in the quest for a cost-effective drive. Owing to the lack of a torque sensor in the experimental system, a torque estimator was employed in the training of the neuro-fuzzy compensator and for verification of the control strategy's ability to reduce the torque ripple. It is recommended that future work include the implementation of the control strategy on an experimental system with a torque sensor

included to further validate the torque ripple reduction capability of the control strategy.

High speed SR generation was examined through the development and experimental implementation of three SR generator control strategies under single pulse mode control. A comparison of the performance of the three control strategies in terms of efficiency and peak phase current was presented. In Chapter Seven, the rms phase current was employed as the gauge of efficiency. However, future work could include the use of full efficiency measurements performed on the SR generator, taking both copper losses and iron losses into account, to verify the results obtained in Chapter Seven.

In addition to torque ripple reduction control at low motor speeds and high speed generator control, a number of motor control strategies were developed for ripple-tolerant applications. These control strategies cover both low speed and high speed motoring and they were implemented and tested experimentally. However, no work was conducted on low speed generator operation and as such it is an area that is suitable for future work. It would be interesting, for example, to examine the possibility of developing a low speed generator control strategy that would minimise the dc link current ripple through shaping of the phase currents. If the desired phase current waveforms could be determined, then the ANFIS system could be trained to produce them in a similar manner to the torque ripple reduction control implementations described in Chapter Four. Similarly, while a number of control strategies were developed covering various modes of operation, the transition between the different control strategies wasn't examined. Future work could involve the development of a 'management controller' that would guarantee that the correct mode of operation is selected and ensure a smooth transition between the different operating modes.

In conclusion, the results presented in this thesis indicate that it is possible to overcome the obstacle of the SRM's inherent nonlinearity and to produce reliable and efficient operation using complex control algorithms. The developed control strategies are suitable for independent motoring and generating applications as well as for dual-

purpose applications such as an integrated starter/alternator in automotive or aeronautical environments.

Bibliography

(Acarnley 1985) Acarnley P.P., Hill R.J. and Hooper C.W., Detection of rotor position in stepping and switched motors by monitoring of current waveforms, *IEEE Transactions on Industrial Electronics*, Vol. IE-32, No. 3, pp. 215-222, 1985.

(ADMC501 Specification 1.0 2001) Embedded DSP motor controller based on the ADSP-219x DSP core, Specification 1.0, Embedded Control Systems Group, Analog Devices Inc., January, 2001.

(ADSP-2199x chip info 2003) Mixed signal DSP controller with CAN: ADSP-21992, Analog Devices Inc., 2003.

(Arefeen 1998) Arefeen M.S., Implementation of a current controlled switched reluctance motor drive using TMS320F240, *Texas Instruments Application Report: SPRA282, Automotive/Industrial Applications, Digital Signal Processing Solutions*, September, 1998.

(Barnes 1998) Barnes M. and Pollock C., Power electronic converters for switched reluctance drives, *IEEE Transactions on Power Electronics*, Vol. 13, No. 6, pp. 1100-1111, 1998.

(Bass 1986) Bass J.T., Ehsani M. and Miller T.J.E., Robust torque control of a switched-reluctance motor without a shaft-position sensor, *IEEE Transactions on Industrial Electronics*, Vol. IE-33, No. 3, pp. 212-216, 1986.

(Besbes 2000) Besbes M., Gabsi M., Hoang E., Lecrivain M., Grioni B. and Plasse C., SRM design for starter-alternator system, *Proceedings of ICEM 2000, the 14th International Conference on Electrical Machines*, Espoo, Finland, Vol. 4, pp. 1931-1935, 28 - 30 August, 2000.

(Bizkevelci 2004) Bizkevelci E., Leblebicioðlu K. and Ertan H.B., A sliding mode controller to minimize SRM torque ripple and noise, *Proceedings of ISIE 2004, IEEE International Symposium on Industrial Electronics*, Ajaccio, Corsica, pp. 1333 – 1338, 4 - 7 May, 2004.

(Bolognani 1996) Bolognani S. and Zigliotto M., Fuzzy logic control of a switched reluctance motor drive, *IEEE Transactions on Industry Applications*, Vol. 32, No. 5, pp. 1063-1068, 1996.

(Bose 1986) Bose B.K., Miller T.J.E., Szczesny P.M. and Bicknell W.H., Microcomputer control of a switched reluctance motor, *IEEE Transactions on Industry Applications*, Vol. IA-22, No. 4, pp. 708-715, 1986.

(Byrne 1973) John Byrne and James Lacy, Electrodynamic system comprising a variable reluctance machine, Patent No. GB1321110, The Patent Office, London, 20 June 1973.

(Byrne 1976) Byrne J.V. and Lacy J.G., Characteristics of saturable stepper and reluctance motors, *Proceedings of the IEE Conference on Small Electrical Machines, IEE Conference Publication No. 136,* London, UK, pp. 93-96, 30 - 31 March, 1976.

(Byrne 1985) Byrne J.V., McMullin M.F. and O' Dwyer J.B., A high performance variable reluctance drive: a new brushless servo, *Proceedings of MOTOR-CON '85, SATECH '85, the 7th International Intelligent Motion Conference*, Chicago, IL, USA, pp. 147-160, 21 - 25 October, 1985.

(Cardenas 1995) Cardenas R., Ray W.F. and Asher G.M., Switched reluctance generators for wind energy applications, *PESC '95 Record, 26th Annual IEEE Power Electronics Specialists Conference,* Atlanta, USA, Vol. 1, pp. 559-564, 18 - 22 June, 1995.

(Cardenas 2004) Cárdenas R., Peña R., Pérez M., Asher G.M., Clare J.C. and Wheeler P.W., Control system for grid generation of a switched reluctance generator driven by a variable speed wind turbine, *Proceedings of IECON '04, the 30th Annual Conference of the IEEE Industrial Electronics Society*, Busan, Republic of Korea, CDROM Paper No. FB3-3, 2 - 6 November, 2004.

(Cossar 2004) Cossar C. and Sawata T., Microprocessor controlled DC power supply for the generator control unit of a future aircraft generator with a wide operating speed range, *Proceedings of PEMD '04, the 2nd International Conference on Power Electronics, Machines and Drives, Edinburgh, UK*, Vol. 2, pp. 458 – 463, 31 March - 2 April, 2004.

(Davidson 1843) 'Davidson's Electromagnetic Engine': *The Penny Mechanic and Chemist*, 23 September 1843, pp. 298-299 and 30 September 1843, p. 305.

(Davis 1981) Davis R.M., Ray W.F. and Blake R.J., Inverter drive for switched reluctance motor: circuits and component ratings, *IEE Proceedings, Part B, Electric Power Applications*, Vol. 128, No. 2, pp. 126-136, March, 1981.

(De Oliveira 1999) De Oliveira L.P.B., Da Silva E.R.C., Lima A.M.N. and Jacobina C.B., New soft-switched power converter topologies for variable reluctance machine drives, *PESC '99 Record, 30th Annual IEEE Power Electronics Specialists Conference, Charleston*, SC, USA, pp. 826-831, 27 June - 1 July, 1999.

(Deshpande 2000) Deshpande V.V. and Young L.J., New converter configurations for switched reluctance motors wherein some windings operate on recovered energy, *Conference Record of IAS 2000, the 2000 IEEE Industry Applications Society 35th Annual Meeting*, Rome, Italy, Vol. 3, pp. 1578-1585, 8 - 12 October, 2000.

(Dessouky 1998) Dessouky Y.G., Williams B.W. and Fletcher J.E., A novel power converter with voltage-boosting capacitors for a four-phase SRM drive, *IEEE Transactions on Industrial Electronics,* Vol. 45, No. 5, pp. 815-823, 1998.

(De Vries 2001) De Vries A., Bonnassieux Y., Gabsi M., d'Oliveira F. and Plasse C., Switched reluctance machine for a car starter/alternator system, *Proceedings of*

IEMDC 2001, IEEE International Electric Machines and Drives Conference, Cambridge, MA, USA, pp. 323-328, 18 - 20 June, 2001.

(Ehsani 1987) Ehsani M., Bass J.T., Miller T.J.E. and Steigerwald R.L., Development of a unipolar converter for variable reluctance motor drives, *IEEE Transactions on Industry Applications*, Vol. IA-23, No. 3, pp. 545-553, 1987.

(Ehsani 2002) Ehsani M. and Fahimi B.F., Elimination of position sensors in switched reluctance motor drives: state of the art and future trends, *IEEE Transactions on Industrial Electronics*, Vol. 49, No. 1, pp. 40-47, 2002.

(EZ-KIT manual 2003) ADSP-21992 EZ-KIT Lite evaluation system manual, Analog Devices Inc., October, 2002.

(Fahimi 2001) Fahimi, B., A switched reluctance machine based starter/generator for more electric cars, *Proceedings of IEMDC 2001, IEEE International Electric Machines and Drives Conference*, Cambridge, MA, USA, pp. 73-78, 18 - 20 June, 2001.

(Ferreira 1995) Ferreira C.A., Jones S.R., Heglund W.S. and Jones W.D., Detailed design of a 30kW switched reluctance starter/generator system for a gas turbine engine application, *IEEE Transactions on Industry Applications*, Vol. 31, No. 3, pp. 553-561, 1995.

(Filicori 1993) Filicori F., Guarino Lo Bianco C. and Tonielli A., Modeling and control strategies for a variable reluctance direct-drive motor, *IEEE Transactions on Industrial Electronics*, Vol. 40, No. 1, pp. 105-115, 1993.

(Fleadh Electronics 2004), Brivit SRM database, **http://www.brivit.com/**, Fleadh Electronics, Leeds, UK, 2004.

(Fuzzy Logic Toolbox User's Guide 2000) Fuzzy Logic Toolbox User's Guide, Version 2, September, 2000.

(Hancock 1990) Clyde Hancock and James Hendershot Jr, *Pacific Scientific Company, Newport Beach, CA, USA,* Electronically commutated reluctance motor, PCT International Patent No. W.O. 90/11641A1, 4 October, 1990.

(Hedlund 1991) Bengt Hedlund, *Aktiebolaget Electrolux, Stockholm, Swede,* A method and a device for sensorless control of a reluctance motor, PCT International Patent No. WO 91/02401A1, 21 February, 1991.

(Henriques 1999) Henriques L.O.A.P., Rolim L.G.B., Suemitsu W.I., Costa Branco P.J. and Dente J.A., Neuro-fuzzy compensation of torque ripple in a switched reluctance drive, *Proceedings of ElectrIMACS '99, the 6th International Conference on Modelling and Simulation of Electric Machines, Converters and Systems*, Lisbon, Portugal, Vol. 3, pp. 19-23, 14 - 16 September, 1999.

(Henriques 2000) Henriques L.O.A.P., Rolim L.G.B., Suemitsu W.I. and Costa Branco P.J., Torque ripple minimisation in a switched reluctance drive by neuro-fuzzy

compensation, *IEEE Transactions on Magnetics*, Vol. 36, No. 5, pp. 3592-3594, 2000.

(Henriques 2001) Henriques L.O.A.P., Costa Branco P.J., Rolim L.G.B. and Suemitsu W.I., Automatic learning of pulse current shape for torque ripple minimisation in switched reluctance machines, *Proceedings of ECC '01, European Control Conference*, Porto, Portugal, pp. 232-237, 4 - 7 September, 2001.

(Henriques 2001a) Henriques L.O.A.P., Costa Branco P.J., Rolim L.G.B. and Suemitsu W.I., Proposition of an offline learning current modulation for torque-ripple reduction in switched reluctance motors: design and experimental evaluation, *IEEE Transactions on Industrial Electronics*, Vol. 49, No. 3, pp. 665-676, 2002.

(Honeywell CSN series datasheet) Closed loop current sensors, CSN series, Sensing and Control, Honeywell Inc.

(Husain 1996) Husain I., Indirect rotor-position estimation techniques for switched reluctance motors - a review, *Electromotion*, Vol. 3, No. 2, pp. 94-102, 1996.

(Husain 2002) Husain I., Minimization of torque ripple in SRM drives, *IEEE Transactions on Industrial Electronics*, Vol. 49, No. 1, pp. 28-39, 2002.

(Hynes 1997) Wesley Hynes J., MATLAB supplement to fuzzy and neural approaches in engineering, *Book*, New York: Wiley, ISBN: 0471192473, 1997.

(Inanc 1997) Inanc N., Derdiyok A. and Ozbular V., Torque ripple minimisation of a switched reluctance motor including mutual inductances via sliding mode control technique, *Proceedings of ISIE '97, IEEE International Symposium on Industrial Electronics*, Guimarães, Portugal, Vol. 3, pp. 1024-1028, 7 - 11 July, 1997.

(Jang 1993) Jang J.S.R., ANFIS – Adaptive-Network-based Fuzzy Inference System, *IEEE Transactions on Systems, Man and Cybernetics*, Vol. 23, No. 3, pp. 665-685, 1993.

(Kjaer 1994) Kjær P.C., Cossar C., Gribble J.J., Li Y. and Miller T.J.E., Switched reluctance generator control using inverse machine model, *Proceedings of ICEM '94, International Conference on Electrical Machines*, Paris, France, Vol. 2, pp. 380-385, 5 - 8 September, 1994.

(Kjaer 1997) Kjær P.C., Gribble J.J. and Miller T.J.E., High-grade control of switched reluctance machines, *IEEE Transactions on Industry Applications*, Vol. 33, No. 6, pp. 1585-1593, 1997.

(Kokernak 1999) Kokernak J.M., Torrey D.A. and Kaplan M., A switched reluctance starter/alternator for hybrid electric vehicles, *Proceedings of INTELLIGENT MOTION '99, Powersystems World '99, 40th International Intelligent Motion Conference*, Chicago, IL, USA, pp. 74-80, 7 - 11 November, 1999.

(Krishnan 1990) Krishnan R. and Materu P.N., Design of a single-switch-per-phase converter for switched reluctance motor drives, *IEEE Transactions on Industrial Electronics*, Vol. 37, No. 6, pp. 469-476, 1990.

(Krishnan 1993) Krishnan R. and Materu P.N., Analysis and design of a low-cost converter for switched reluctance motor drives, *IEEE Transactions on Industry Applications*, Vol. 29, No. 2, pp. 320-327, 1993.

(Krishnan, 2001) Krishnan R., Switched reluctance motor drives: modeling, simulation, analysis, design and applications, *Book*, Industrial Electronics series, CRC Press LLC, ISBN: 0-8493-0838-0, 2001.

(Lawrenson 1980) Lawrenson P.J., Stephenson J.M., Blenkinsop P.T., Corda J. and Fulton N.N., Variable-speed switched reluctance motors, *IEE Proceedings, Part B, Electric Power Applications*, Vol. 127, No. 4, pp. 253-265, July, 1980.

(Lee 2004) Lee J.W., Kim H.S., Kwon B.I. and Kim B.T., New rotor shape design for minimum torque ripple of SRM using FEM, *IEEE Transations on Magnetics*, Vol. 40, No. 2, pp. 754 – 757, 2004.

(Le-Huy 1990) Le-Huy H., Viarouge P. and Francoeur B., A novel unipolar converter for switched reluctance motor, *IEEE Transactions on Power Electronics*, Vol. 5, No. 4, pp. 469-475, 1990.

(Lyons 1991) Lyons Jr J.P., MacMinn S.R. and Preston M.A., Flux/current methods for SRM rotor position estimation, *Conference Record of IAS '91, the 1991 IEEE Industry Applications Society 26th Annual Meeting*, Dearborn, Michigan, USA, Vol. 1, pp. 482-487, 30 September - 4 October, 1991.

(MacMinn 1989) MacMinn S.R and Sember J.W., Control of a switched reluctance aircraft starter-generator over a very wide speed range, *Proceedings of IECEC '89, IEEE 24th Intersociety Energy Conversion Engineering Conference*, Washington DC, USA, Vol. 1, pp. 631-638, 6 - 11 August, 1989.

(Mamdani 1975) Mamdani E.H. and Assilian S., An experiment in linguistic synthesis with a fuzzy logic controller, *International Journal of Man-Machine Studies*, Vol. 7, No. 1, pp. 1-13, 1975.

(Mese 2000) Mese E., Sozer Y., Kokernak J.M. and Torrey D.A., Optimal excitation of high speed switched reluctance generators, *Proceedings of APEC 2000, IEEE 15th Annual Applied Power Electronics Conference and Exposition*, New Orleans, LA, USA, Vol. 1, pp. 362-368, 6 - 10 February, 2000.

(Miller 1985) Miller T.J.E., Converter volt-ampere requirements of the switched reluctance drive, *IEEE Transactions on Industry Applications*, Vol. IA-21, No. 5, pp. 1136-1144, 1985.

(Miller 1988) Miller T.J.E., Bower P.G., Becerra R.C. and Ehsani M., Four-quadrant brushless reluctance motor drive, *Proceedings of PEVD '88, the 3rd International*

Conference on Power Electronics and Variable Speed Drives, IEE Conference Publication No. 291, London, UK, pp. 273-276, 13 - 15 July, 1988.

(Miller 1990) Miller T.J.E. and McGilp M.I., Nonlinear theory of the switched reluctance motor for rapid computer-aided design, *IEE Proceedings, Part B, Electric Power Applications*, Vol. 137, No. 6, pp. 337-347, November, 1990.

(Miller 1999) Miller T.J.E. and McGilp M.I., PC-SRD User's manual, Version 7.0, SPEED Laboratory, University of Glasgow, 1999.

(Miller 2001) Miller T.J.E., Electronic control of switched reluctance machines, *Book*, Newnes Power Engineering series, Reed Educational and Professional Publishing Ltd, ISBN: 0750650737, June, 2001.

(Miller 2002) Miller T.J.E., Optimal design of switched reluctance motors, *IEEE Transactions on Industrial Electronics*, Vol. 49, No. 1, pp. 15-27, 2002.

(Mir 1997) Mir S., Husain I. and Elbuluk M.E., Energy-efficient C-dump converters for switched reluctance motors, *IEEE Transactions on Power Electronics*, Vol. 12, No. 5, pp. 912-921, 1997.

(Mir 1998) Mir S., Husain I., and Elbuluk M.E., Switched reluctance motor modeling with on-line parameter identification, *IEEE Transactions on Power Electronics*, Vol. 34, No. 4, pp. 776-783, 1998.

(Mir 1999) Mir S., Elbuluk M.E. and Husain I., Torque-ripple minimisation in switched reluctance motors using adaptive fuzzy control, *IEEE Transactions on Industry Applications*, Vol. 35, No. 2, pp. 461-468, 1999.

(Moreira 1992) Moreira J.C., Torque-ripple minimisation in switched reluctance motors via b-cubic spline interpolation, *PESC '92 Record. 23rd Annual IEEE Power Electronics Specialists Conference*, Toledo, Spain, Vol. 2, pp. 851-856, 29 June - 3 July, 1992.

(Murphy 2002) Murphy A.J., WP5n – Hardware description, PEI Technologies, Dublin City University, Ireland, 2002.

(Nagel 1999) Nagel N.J. and Lorenz R.D., Complex rotating vector methods for smooth torque control of a saturated switched reluctance motor, *Conference Record of IAS '99, the 1999 IEEE Industry Applications Society 34th Annual Meeting*, Pheonix, AZ, USA, Vol. 4, pp. 2591-2598, 3 - 7 October, 1999.

(Nasar 1969) Nasar S.A., DC switched-reluctance motor, *Proceedings of the IEE*, Vol. 116, No. 6, pp. 1048-1049, June, 1969.

(Nedic 2000) Nedic V. and Lipo T.A., Experimental verification of induced voltage self-excitation of a switched reluctance generator, *Conference Record of IAS 2000, the 2000 IEEE Industry Applications Society 35th Annual Meeting*, Rome, Italy, Vol. 1, pp. 51-56, 8 - 12 October, 2000.

(O' Donovan 1994) O' Donovan J.G., Roche P.J., Kavanagh R.C., Egan M.G. and Murphy J.M.D., Neural network based torque ripple minimisation in a switched reluctance motor, *Proceedings of IECON '94, 20th IEEE International Conference on Industrial Electronics, Control and Instrumentation*, Bologna, Italy, Vol. 2, pp. 1226-1231, 5 - 9 September, 1994.

(Optical encoders 2005) Optical encoder types and how they function, http://www.encoders.us/, 2005.

(Pollock 1990) Pollock C. and Williams B.W., A unipolar converter for a switched reluctance motor, *IEEE Transactions on Industry Applications*, Vol. 26, No. 2, pp. 222-228, 1990.

(Radun 1994) Radun A.V., Generating with the switched reluctance motor, *Proceedings of APEC '94, IEEE 9th Applied Power Electronics Conference and Exposition*, Vol. 1, pp. 41-47, 13 - 17 February, 1994.

(Radun 1997) Radun A.V., Ferreira C.A. and Richter E., Two-channel switched reluctance starter/generator results, *Proceedings of APEC '97, IEEE 12th Annual Applied Power Electronics Conference and Exposition*, Atlanta, GA, USA, Vol. 1, pp. 546-552, 23 - 27 February, 1997.

(Radun 1998) Radun A.V., Ferreira C.A. and Richter E., Two-channel switched reluctance starter/generator results, *IEEE Transactions on Industry Applications*, Vol. 34, No. 5, pp. 1026-1034, 1998.
(Ray 1979) Ray W.F. and Davis R.M., Inverter drive for doubly salient reluctance motor: its fundamental behaviour, linear analysis and cost implications, *IEE Journal on Electrical Power Applications*, Vol. 2, No. 6, pp. 185-193, December, 1979.

(Reay 1993) Reay D.S., Green T.C.E. and Williams B.W., Applications of associative memory neural networks to the control of a switched reluctance motor, *Proceedings of IECON '93, 19th IEEE International Conference on Industrial Electronics, Control and Instrumentation*, Maui, HI, USA, Vol. 1, pp. 200-206, 15 - 18 November, 1993.

(Rochford 1993) Rochard C., Kavanagh R.C., Egan M.G. and Murphy J.M.D., Development of smooth torque in switched reluctance motors using self-learning techniques, *Proceedings of EPE '93, 5th European Conference on Power Electronics and Applications, IEE Conference Publication No. 377*, Brighton, UK, Vol. 6, pp. 14-19, 13 - 16 September, 1993.

(Roux 2000) Roux C. and Morcos M.M., A simple model for switched reluctance motors, *IEE Power Engineering Review*, pp. 49-52, October, 2000.

(Roux 2002) Roux C. and Morcos M.M., On the use of a simplified model for switched reluctance motors, *IEEE Transactions on Energy Conversion*, Vol. 17, No. 3, pp. 400-405, 2002.

(Russa 1998) Russa K., Husain I. and Elbuluk M.E., Torque-ripple minimisation in switched reluctance machines over a wide speed range, *IEEE Transactions on Industry Applications*, Vol. 34, No. 5, pp. 1105-1112, 1998.

(Russa 2000) Russa K., Husain I. and Elbuluk M.E., A self-tuning controller for switched reluctance motors, *IEEE Transactions on Power Electronics*, Vol. 15, No. 3, pp. 545-552, 2000.

(Schramm 1992) Schramm D.S., Williams B.W. and Green T.C.T., Torque-ripple reduction of switched reluctance motors by phase current optimal profiling, *PESC '92 Record, 23rd Annual IEEE Power Electronics Specialists Conference*, Toledo, Spain, Vol. 2, pp. 857-860, 29 June - 3 July, 1992.

(Sozer 2003) Sozer Y. and Torrey D.A., Closed loop control of excitation parameters for high speed switched-reluctance generators, *Proceedings of APEC 2003, IEEE 18th Annual IEEE Applied Power Electronics Conference and Exposition*, Miami, FL, USA, Vol. 1, pp. 75-82, 9 - 13 February, 2003.

(Sozer 2003a) Sozer Y., Torrey D.A. and Mese E., Automatic control of excitation parameters for switched-reluctance motor drives, *IEEE Transactions on Power Electronics*, Vol. 18, No. 2, pp. 594-603, 2003.

(Stephenson 1989) Stephenson M. and El-Khazendar M.A., Saturation in doubly salient reluctance motors, *IEE Proceedings, Part B, Electric Power Applications*, Vol. 136, No. 1, pp. 50-58, January, 1989.

(Sturgeon 1825) Sturgeon W., Improved electro magnetic apparatus, *Trans. Soc. Arts, Manufactures & Commerce*, Vol. XLIII, pp. 37-52, plates 3 & 4, 1825.
(Sugeno 1985) Sugeno M., Industrial applications of fuzzy control, *Book*, New York: Elsevier Science Publications Co., 1985.

(Taylor 1840) 'Taylor's Electro-Magnetic Engine': *Mechanic's Magazine*, No. 874, Saturday 9 May, 1840.

(Tormey 1991) Tormey D.P. and Torrey D.A., A comprehensive design procedure for low torque-ripple variable-reluctance motor drives, *Conference Record of IAS '91, the 1991 IEEE Industry Applications Society 26th Annual Meeting,* Dearborn, Michigan, USA, Vol. 1, pp. 244-251, 30 September - 4 October, 1991.

(Torrey 1993) Torrey D.A., Variable-reluctance generators in wind energy systems, *PESC '93 Record, 24th Annual IEEE Power Electronics Specialists Conference*, Seattle, WA, USA, pp. 561-567, 20 - 24 June, 1993.

(Torrey 2002) Torrey D.A., Switched reluctance generators and their control, *IEEE Transactions on Industrial Electronics*, Vol. 49, No. 1, pp. 3-14, 2002.

(Unnewher 1974) Unnewehr L.E. and Koch W.H., An axial air-gap reluctance motor for variable speed applications, *IEEE Transactions on Power Apparatus Systems*, Vol. PAS-93, No. 2, pp. 367-376, 1974.

(Using MATLAB 1999) Using MATLAB, Version 5, January, 1999.

(Using Simulink 1999) Using Simulink, Version 3, January, 1999.

(Vas 1999) Vas P., Artificial-intelligence-based electrical machines and drives, *Book*, Oxford Science Publications, Oxford University Press, ISBN: 019859397, 1999.

(Vukosavic 1990) Vukosavic S.N. and Stefanovic V.R., SRM inverter topologies: a comparative evaluation, *Conference Record of IAS '90, the 1990 IEEE Industry Applications Society 25th Annual Meeting*, Seattle, Washington, USA, Part II, pp. 946-958, 7 - 12 October, 1990.

(Zadeh 1965) Zadeh L.A., Fuzzy sets, *Information and Control*, Vol. 8, pp. 338-353, 1965.

Appendix A - Experimental system

A1: Schematics

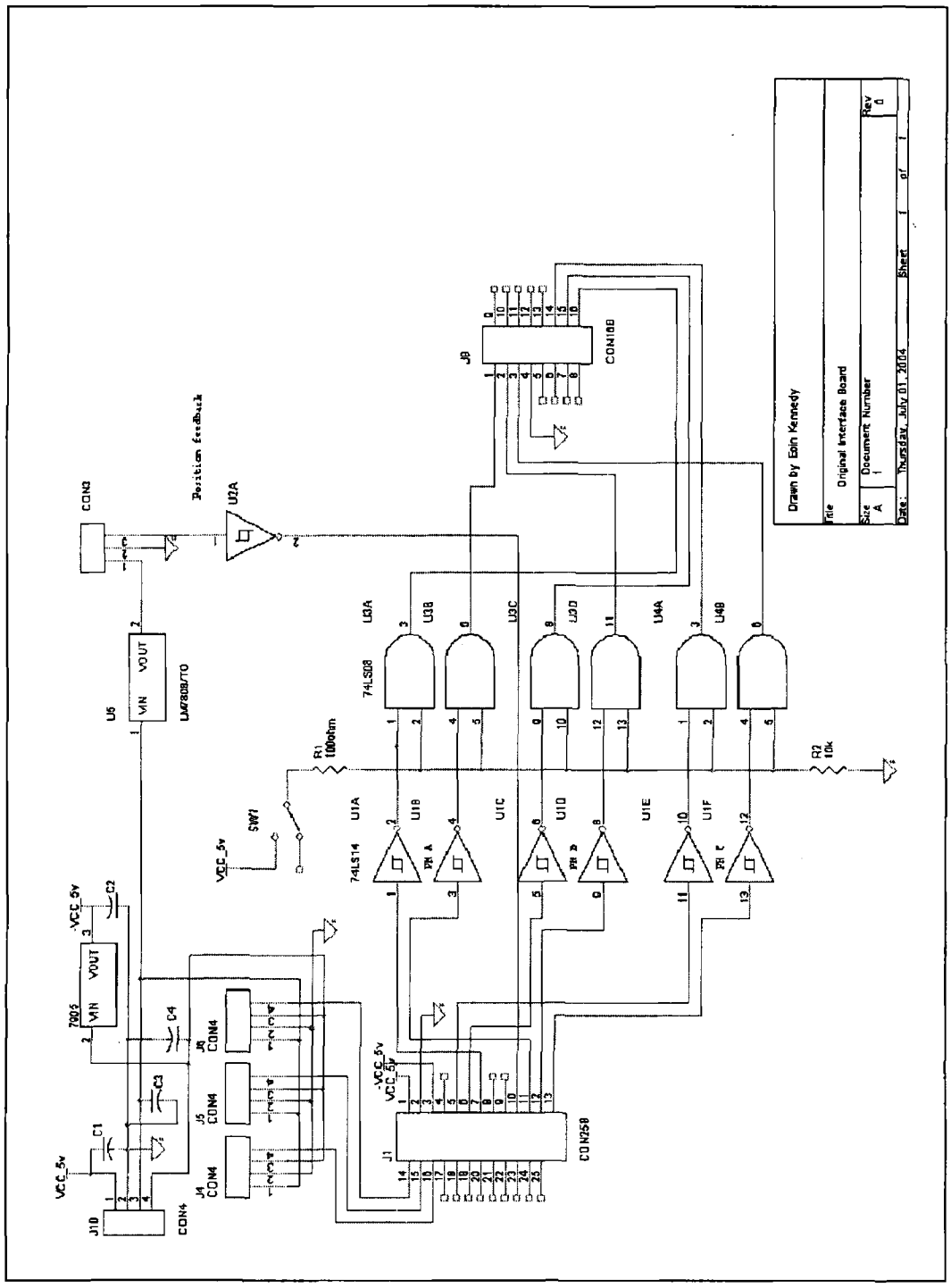

Figure A.1: Schematic of the original interface board.

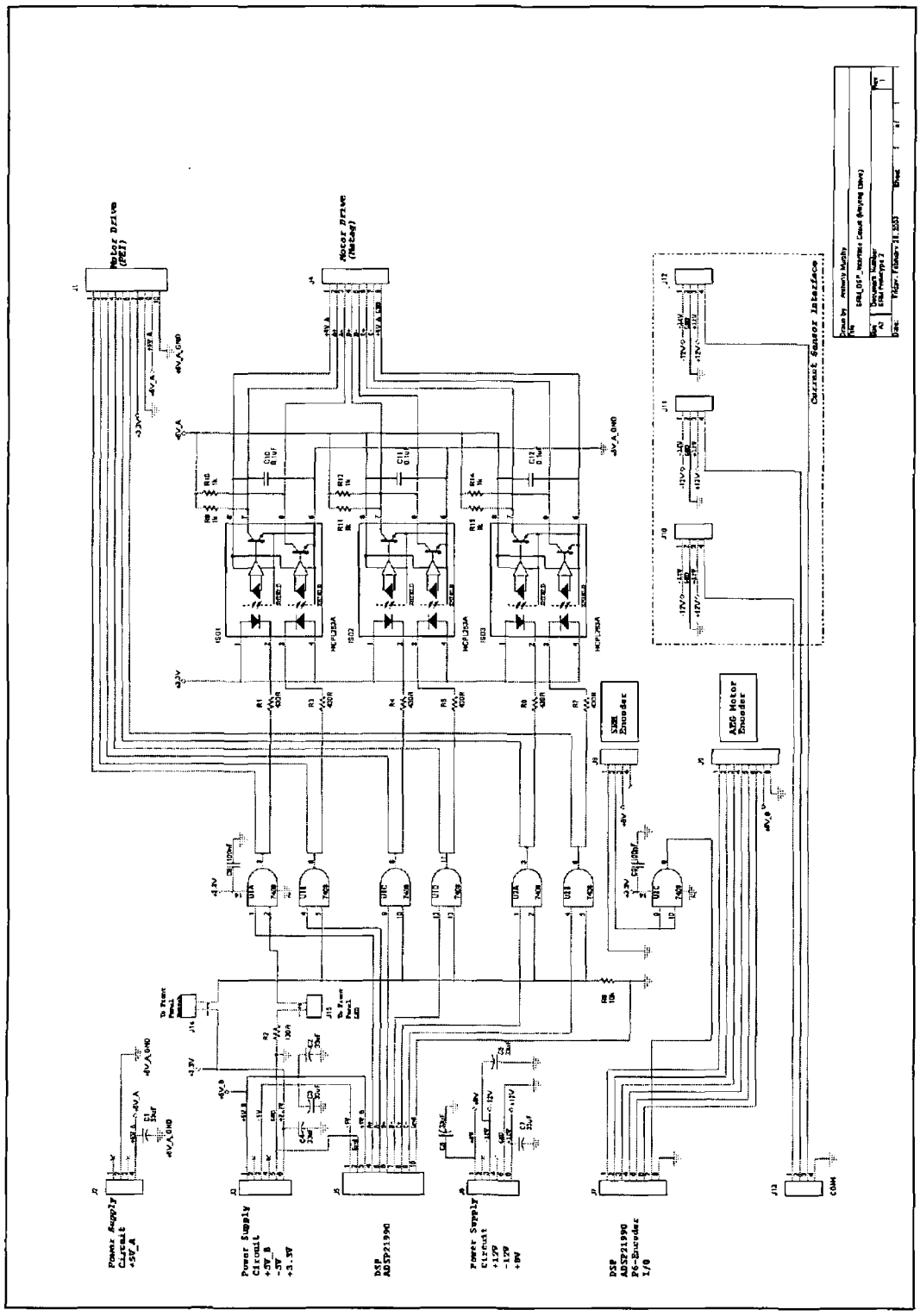

Figure A.2: Schematic of the redesigned interface board (Murphy 2002).

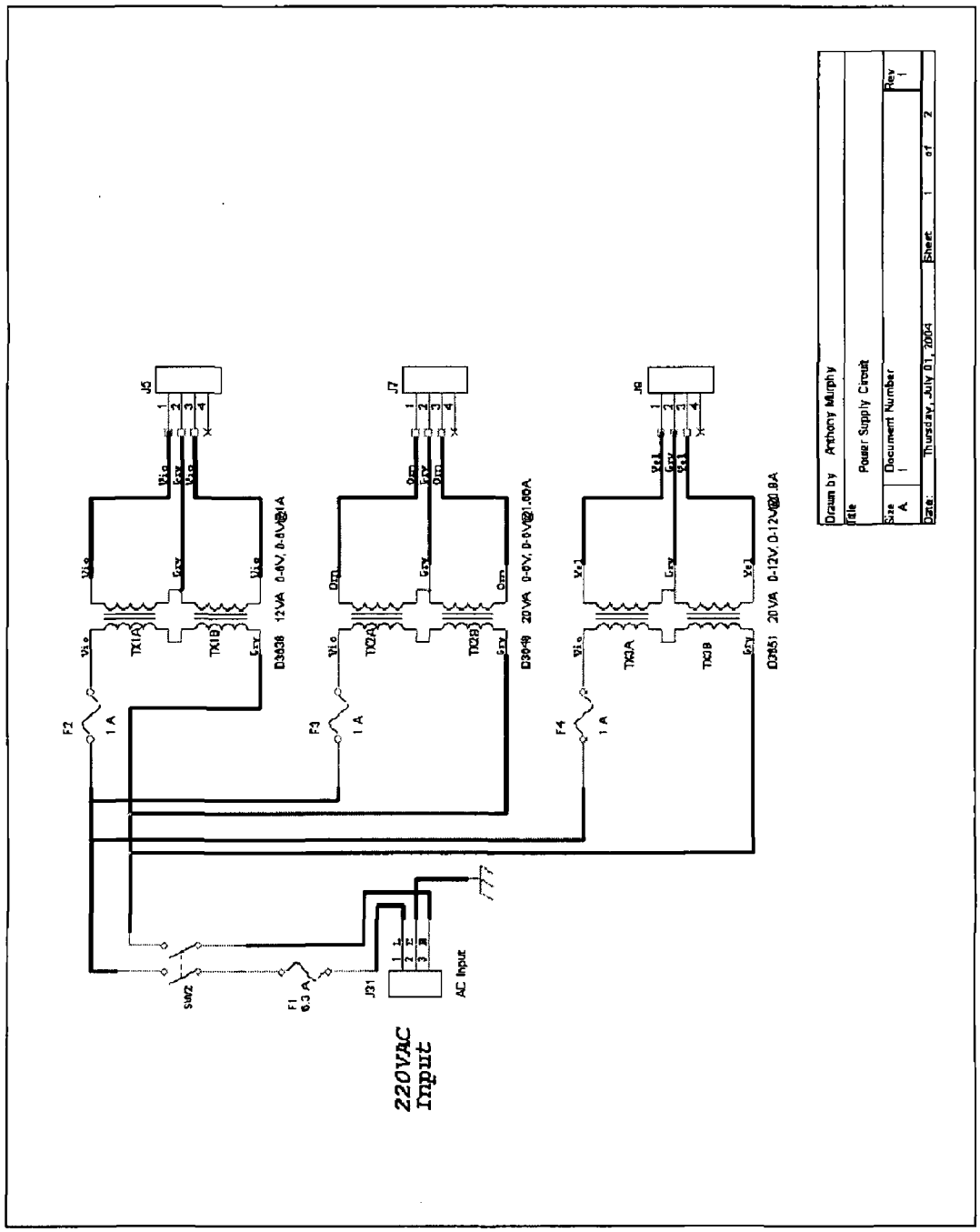

Figure A.3: Schematic of the power supply circuit (sheet 1 of 2) (Murphy 2002).

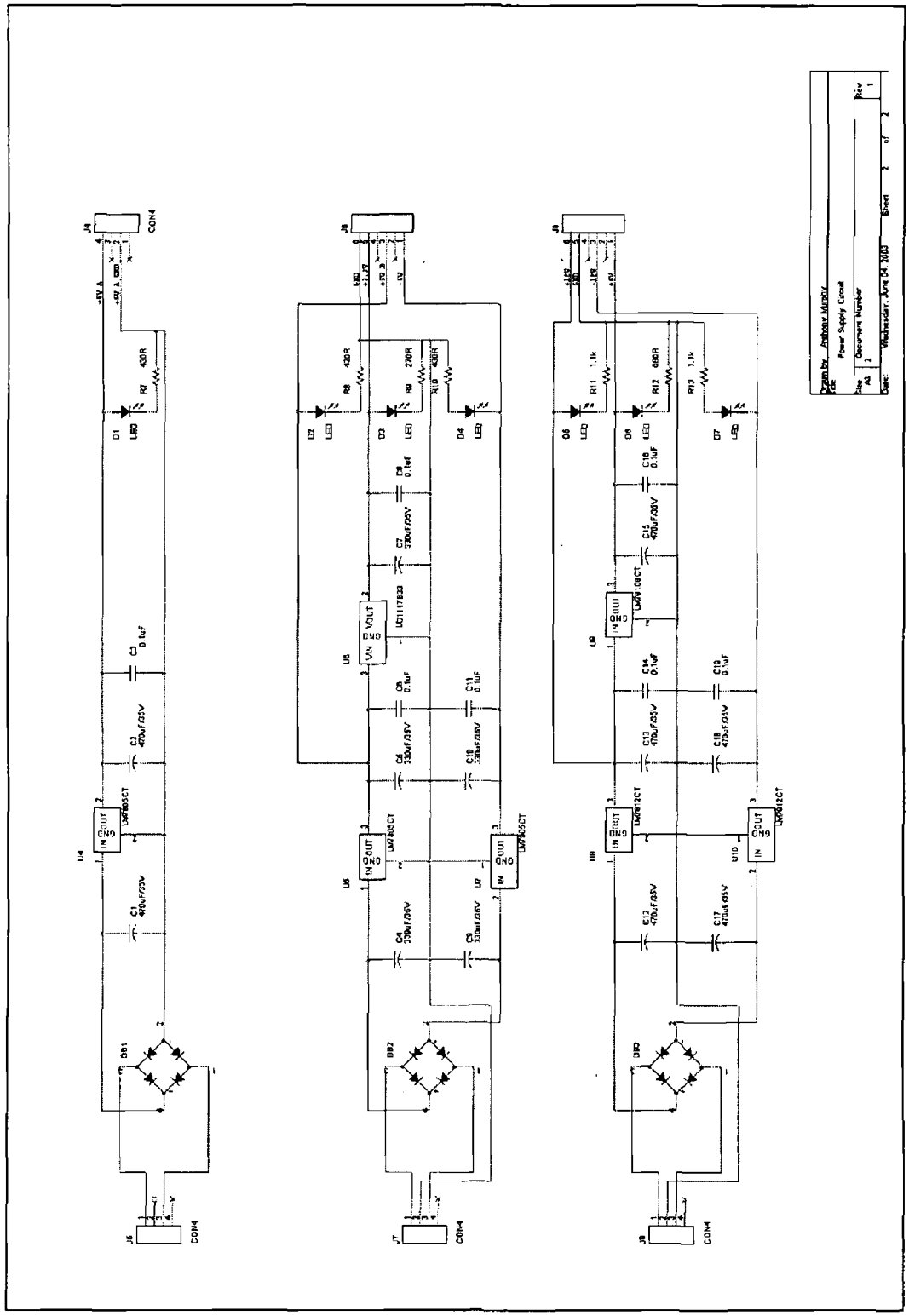

Figure A.4: Schematic of the power supply circuit (sheet 2 of 2) (Murphy 2002).

A2: Photos of the experimental system

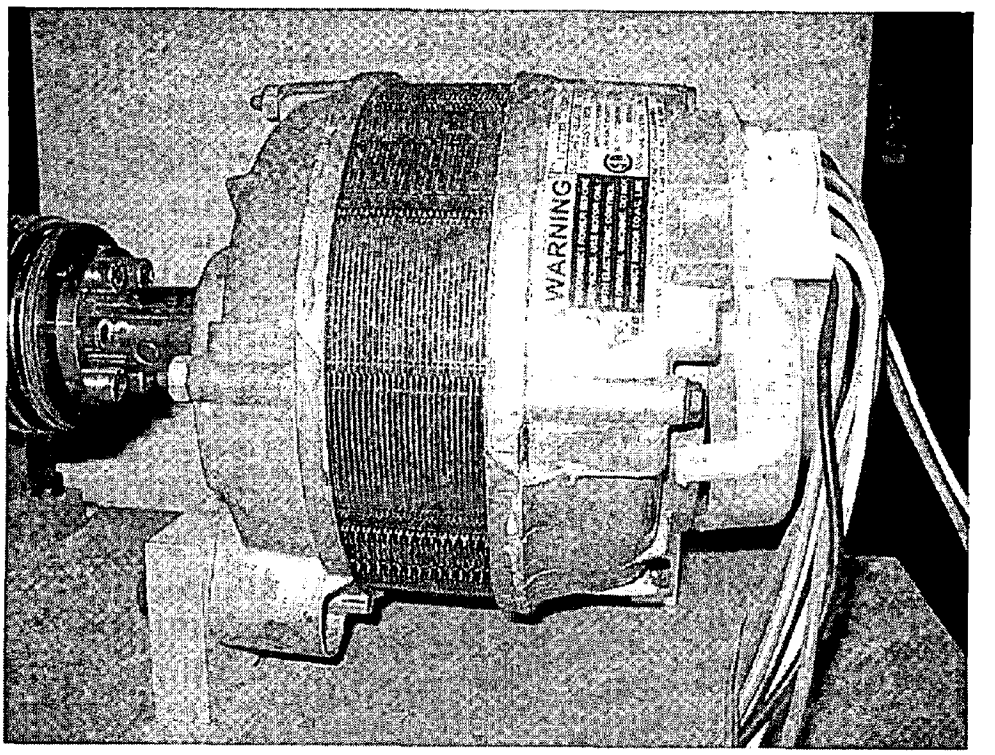

Figure A.5: 12/8 three-phase experimental SRM.

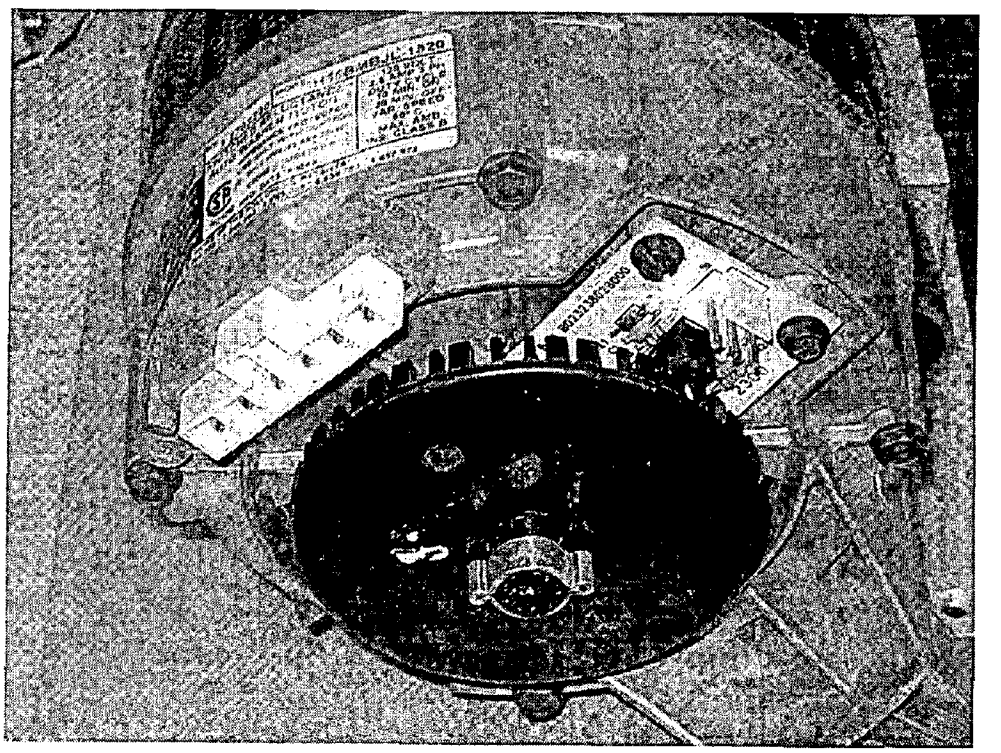

Figure A.6: Slotted optical disk encoder and phase terminal connections.

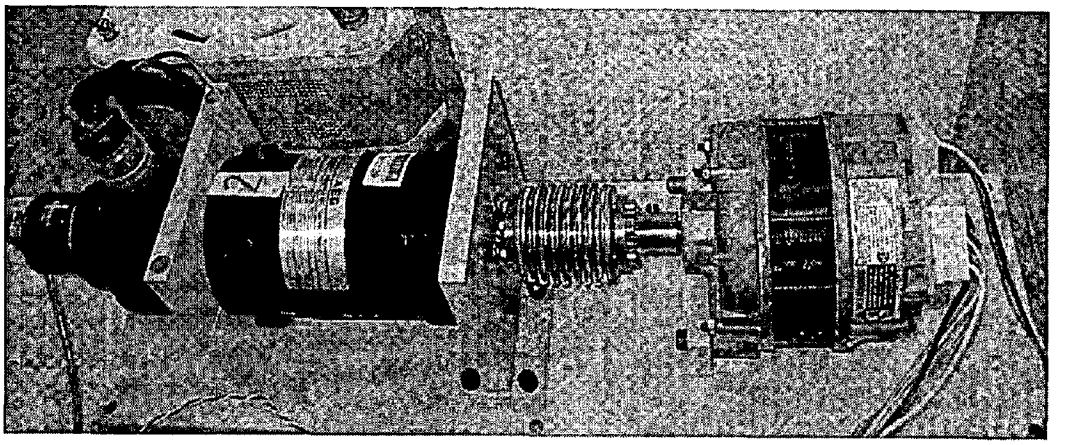

Figure A.7: Motor rig – dc motor and SRM coupled via their rotors.

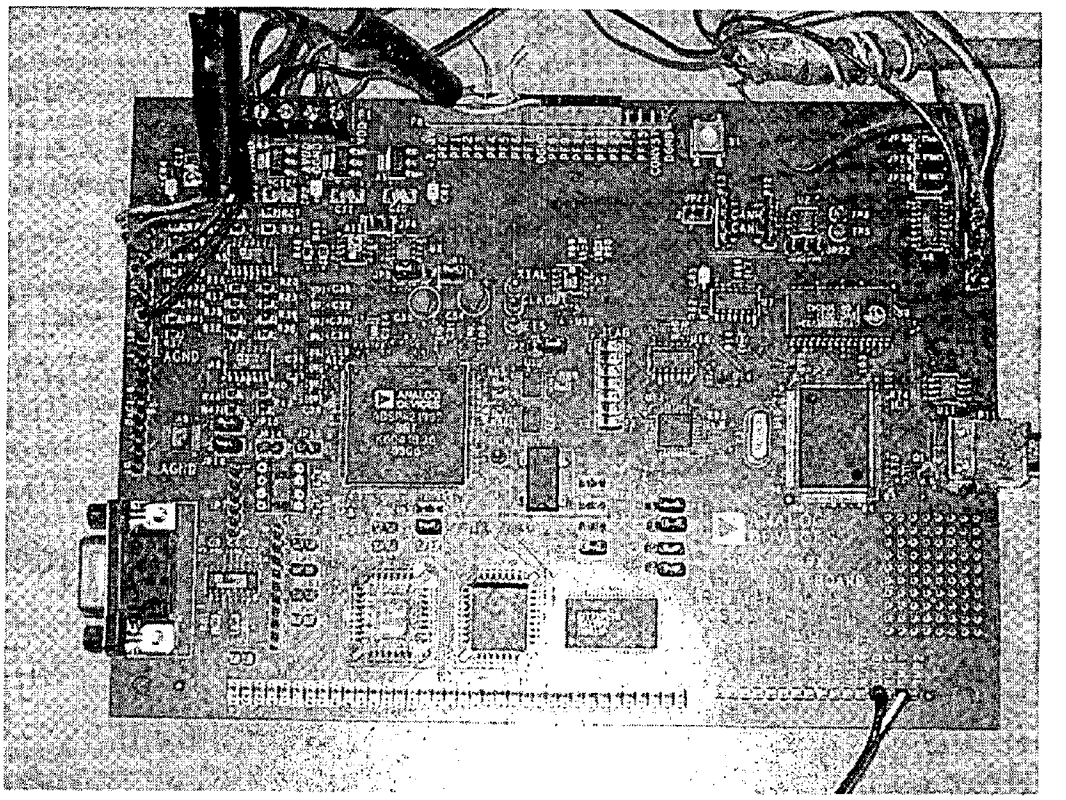

Figure A.8: ADSP-21992 EZ-KIT Lite board.

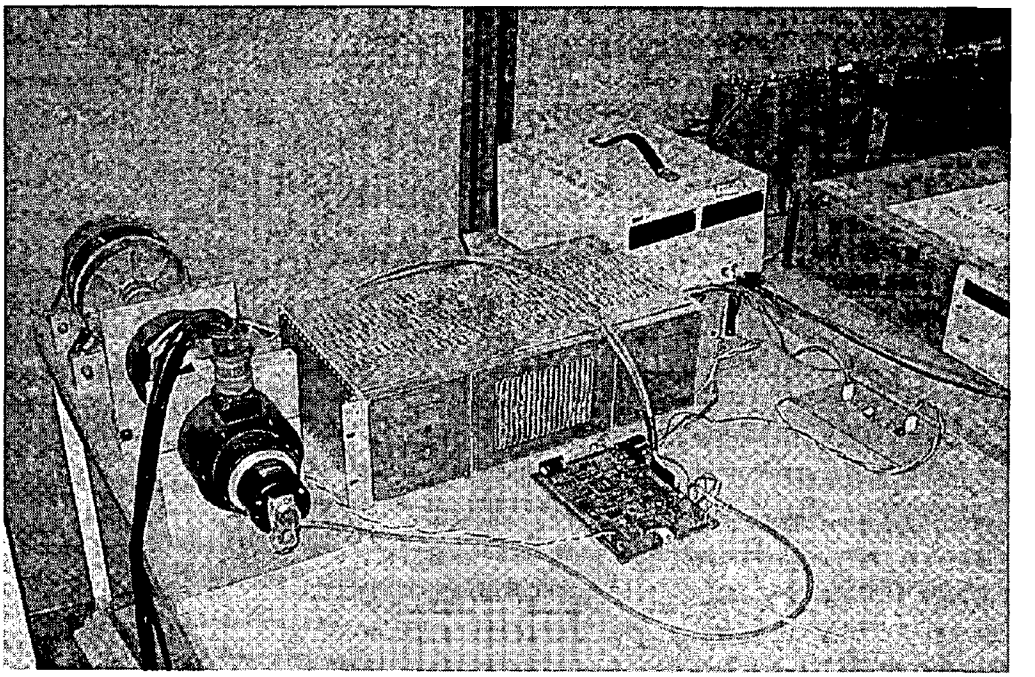

Figure A.9: Experimental system.

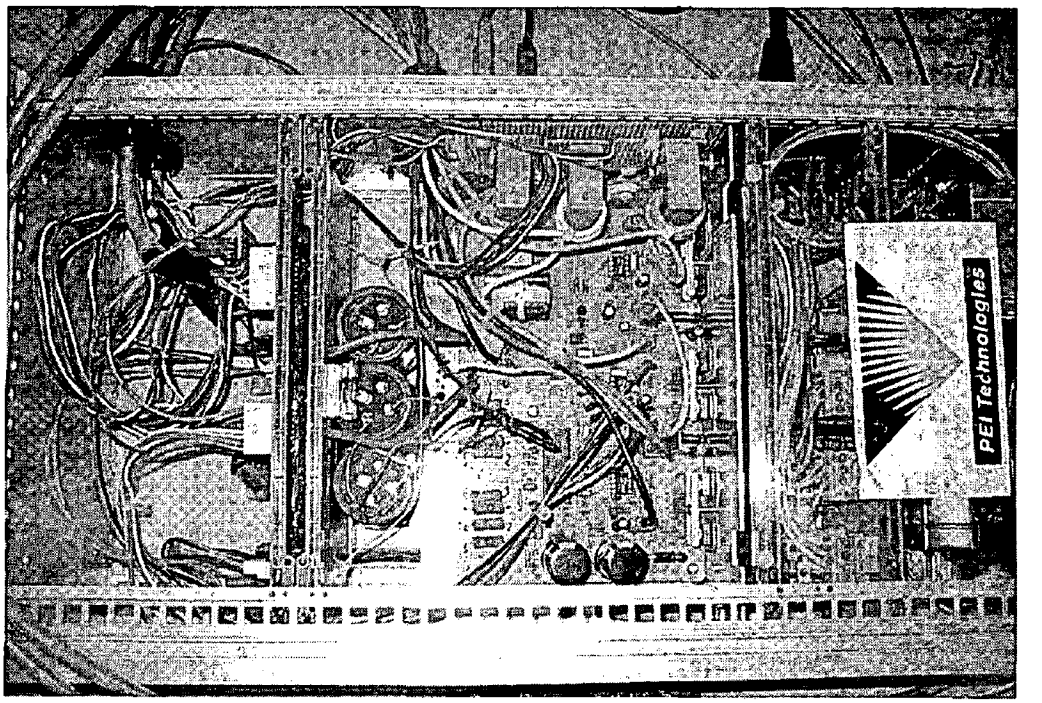

Figure A.10: Power converter, current measurement electronics, power supply circuitry and interface electronics.

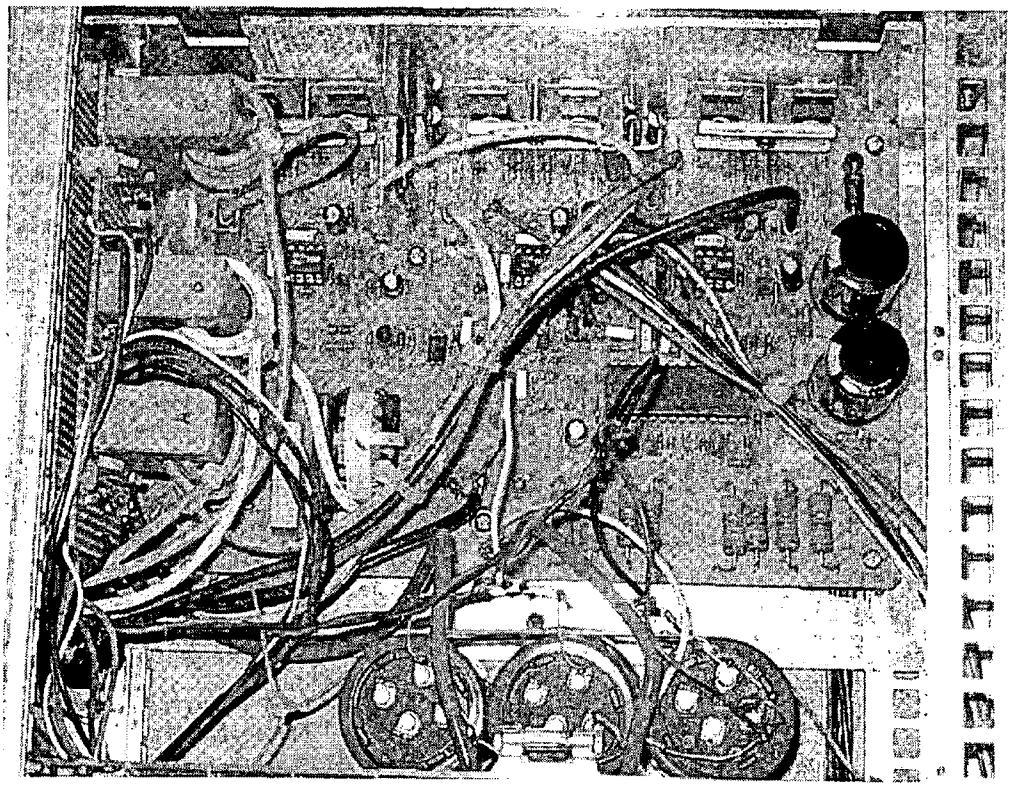

Figure A.11: Power converter and current measurement electronics.

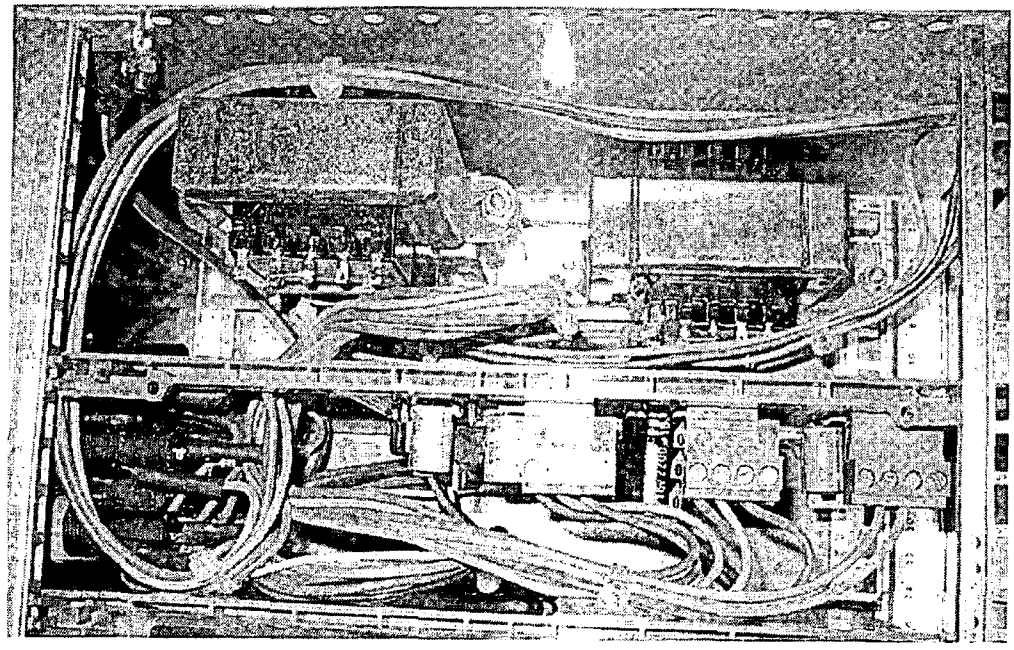

Figure A.12: Power supply circuitry.

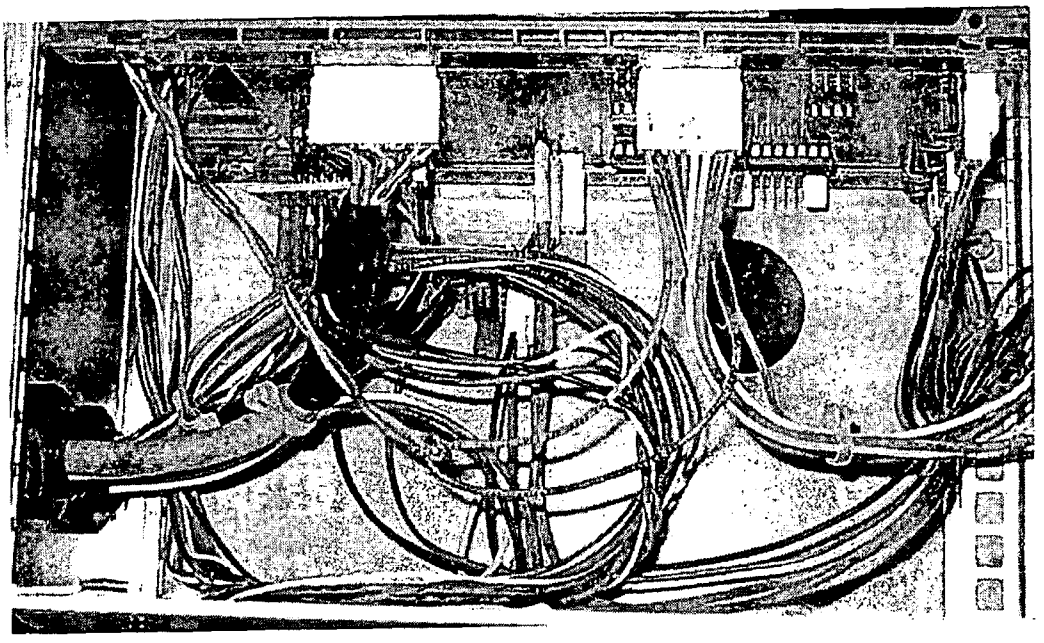

Figure A.13: Interface electronics board.

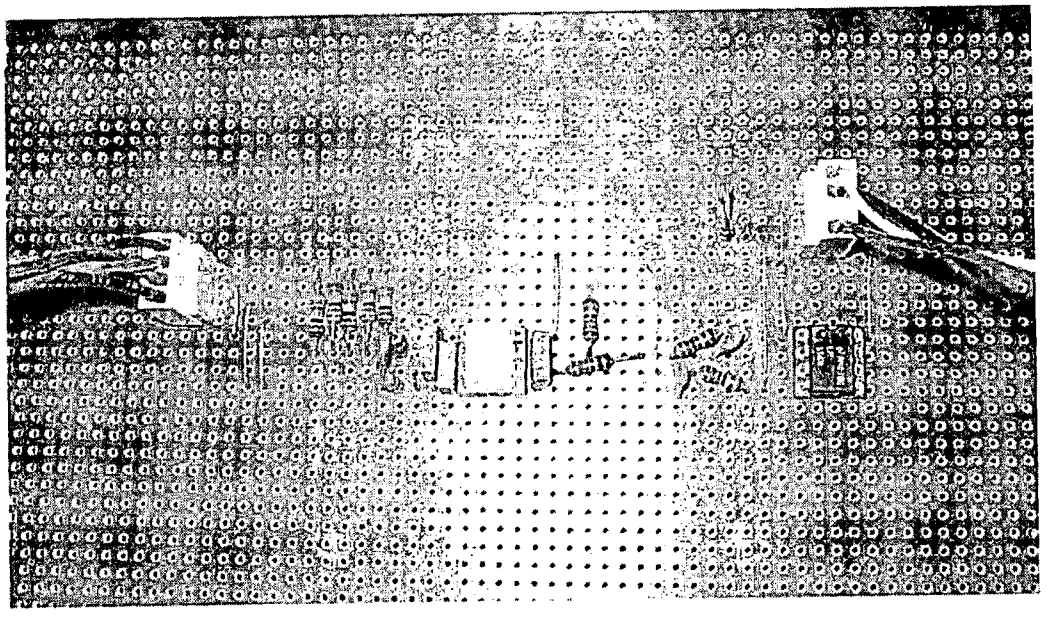

Figure A.14: Dc link voltage measurement electronics board.

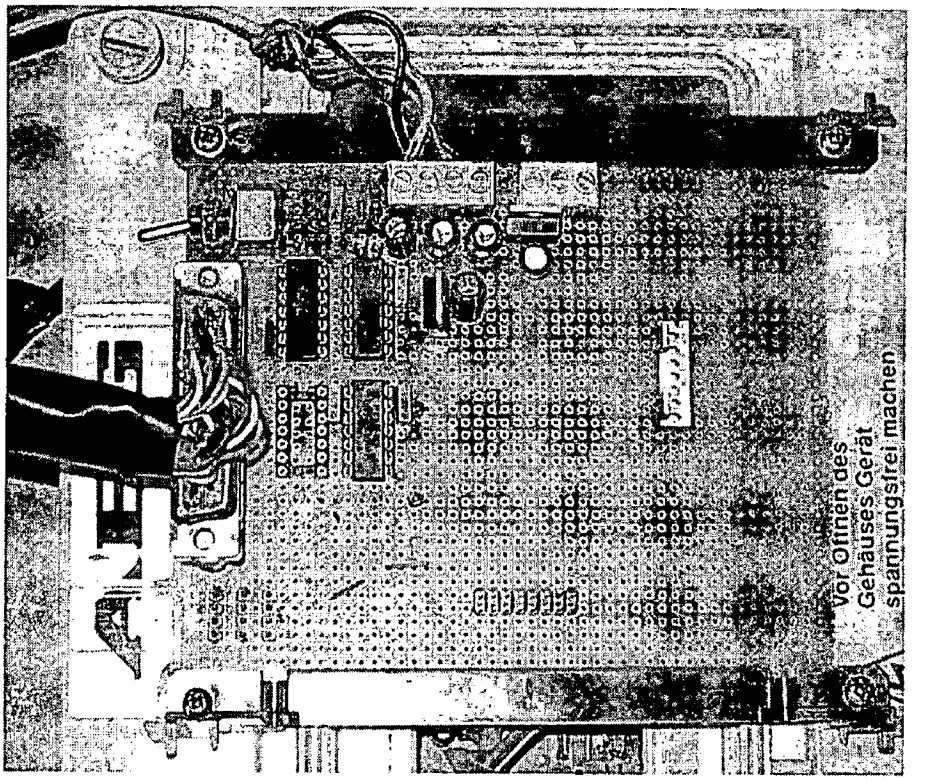

Figure A.15: Original interface electronics board.

Appendix B – ADSP-21992 EZ-KIT Lite evaluation board

For fast and efficient system development, Analog Devices developed an evaluation board called the ADSP-21992 EZ-KIT Lite. This board was employed in the experimental set-up for development and testing of the SRM control strategies. The EZ-KIT Lite development board provides access to all the capabilities of the ADSP-21992 processor. The board's features include (EZ-KIT manual 2003):

- Analog Devices ADSP-21992 160 MHz, mixed-signal DSP
- USB debugging interface
- Analog input circuitry
- 8-channel 12-bit DAC (AD5328BRU) on SPI interface
- PWM outputs interface
- External memory interface
- Encoder interface circuitry
- General-purpose I/O interface
- UART interface (RS-232)
- CAN interface circuitry
- Flash memory (512K x 8)
- External SRAM (64K x 16)
- Interface connectors
- 14-pin emulator connector for JTAG interface
- Analog inputs connector
- DAC outputs connector
- PWM outputs connector
- Encoder interface connector
- SPORT connector
- RS-232 connector
- External memory interface connector

The EZ-KIT Lite development board was designed for use in conjunction with the VisualDSP++ development environment. VisualDSP++, which runs on a Personal Computer (PC), enables advanced code development and debugging tasks to be performed. Access to the ADSP-21992 processor on the EZ-KIT Lite board from the PC is achieved through a USB port or an optional JTAG emulator. A block diagram of the ADSP-21992 EZ-KIT Lite development board is shown in Figure B.1 (EZ-KIT manual 2003).

It is clear that the ADSP-21992 is ideal for SRM control applications because of the number of integrated special purpose and motor control peripherals. In the work

described in this thesis, a number of these special purpose units were employed in the control of the SRM including the Analog-to-Digital Converter (ADC), the Encoder Interface Unit (EIU), the Flag I/O peripheral unit and the general-purpose timers. A brief description of each of these units is included below along with an explanation of how the programmable clock generation circuit works.

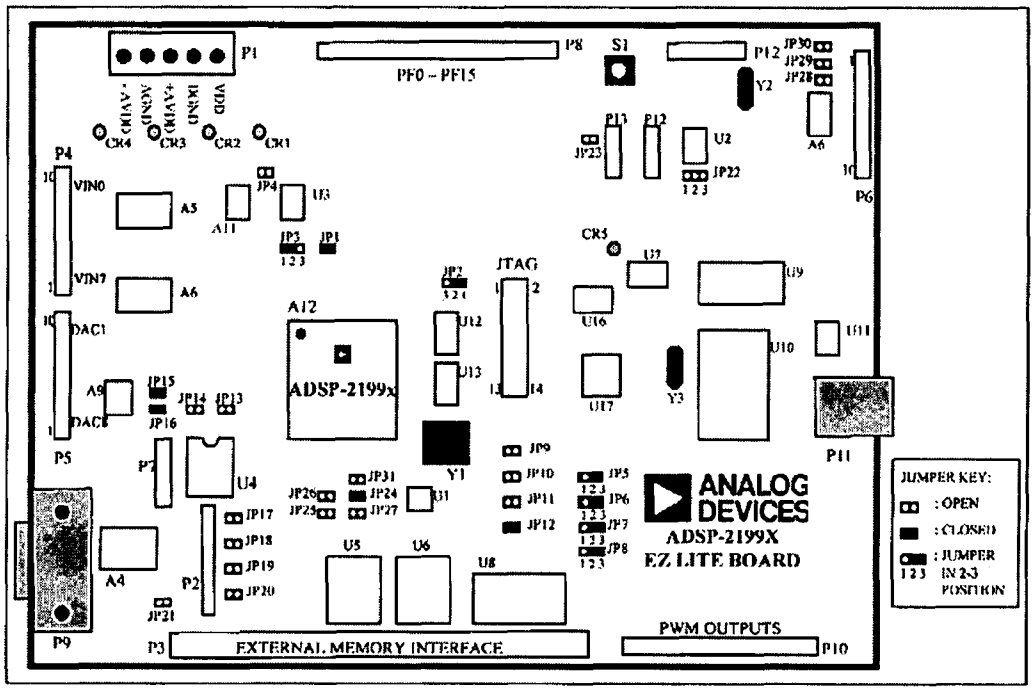

Figure B.1: Block diagram of the ADSP-21992 EZ-KIT Lite development board.

B1: Overview of the Analog-to-Digital Conversion unit

The ADC unit on the ADSP-21992 accurately converts up to eight independent analog signals, such as the current and voltage signals required for high performance SRM control, into digital signals through a 12-bit pipeline flash ADC. The ADC clock rate is programmable with a maximum ADC clock rate of 20MHz. The full conversion of a single channel takes six ADC clock cycles.

All eight analog inputs applied to the analog input connector on the EZ-KIT Lite board (Connector P4 in Figure B.1) must be in the range from –1V to +1V. The analog interface circuitry then converts the ±1V signals on the input connector to signals centred on the ADSP-21992 reference voltage level (either the internally derived 1V level or the externally provided 1.024V level). Effectively, the analog interface circuits offset the analog connector inputs by the reference voltage level.

A functional block diagram of the ADC unit of the ADSP-21992 is shown in Figure B.2 (ADMC501 Specification 1.0 2001). As can be seen, the eight input signals are divided into two banks of four signals. VIN0-VIN3 makes up one bank while the other is comprised of the signals on VIN4-VIN7. The internal multiplexors are used to connect the various analog inputs to the ADC.

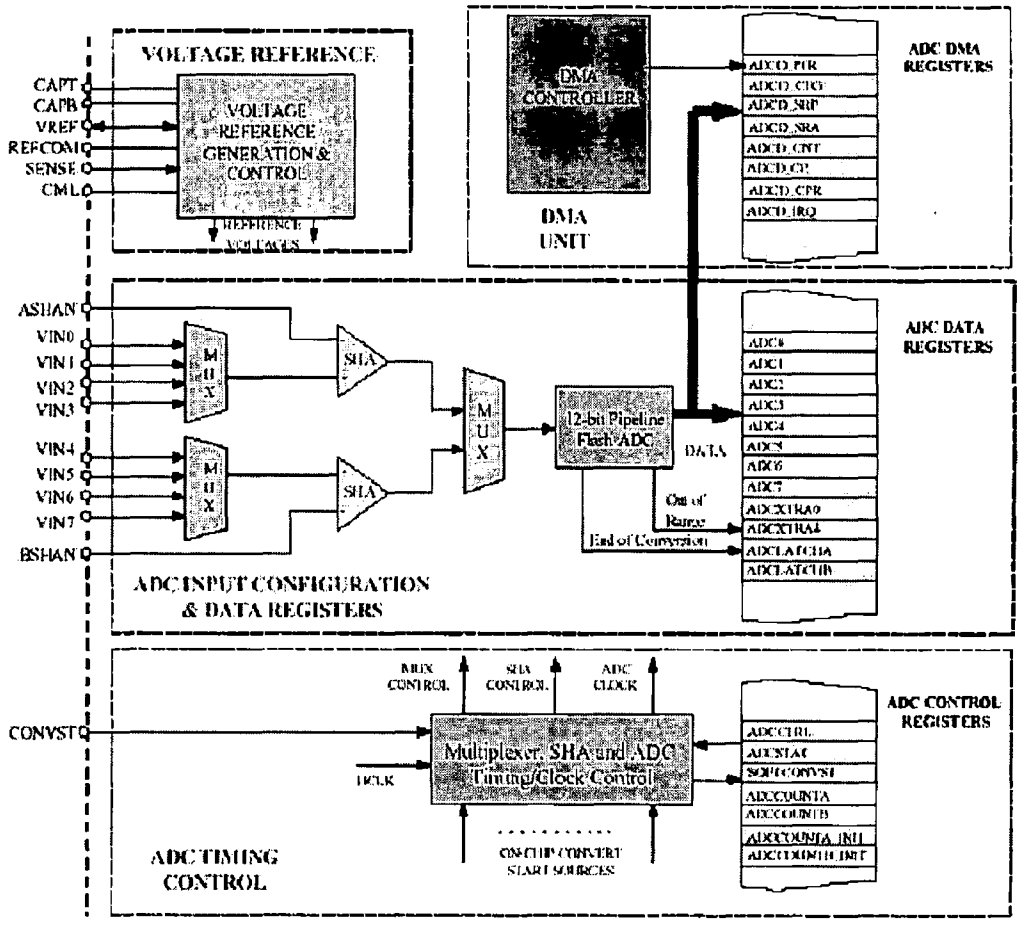

Figure B.2: Functional block diagram of the ADC unit of the ADSP-21992.

There are a number of different conversion modes that can be selected using bits 4-6 in the ADCCTRL register. However, during the course of this project only one mode of operation was employed: simultaneous sampling mode (selected by clearing bits 4-6). In this mode, two analog inputs (one from each four-signal bank) are sampled simultaneously. VIN0 and VIN4 are sampled first followed by the pairs VIN1/VIN5, VIN2/VIN6 and VIN3/VIN7 with two cycles of the ADC clock between the sampling of one pair of analog signals and the next. After each pair of inputs are converted, the

12-bit digital numbers are written to a dedicated 16-bit, 2's complement, left-aligned register i.e. the ADC register ADC0 stores the converted result for the signal on VIN0 etc. In addition, a dedicated bit is set in the ADCSTAT register. After the ADC has finished with all of the channels, an interrupt may be generated. Alternatively, the ADCSTAT can be polled to detect successful conversion of a given pair of inputs. There are a number of ways in which the conversion process can be started, determined by bits 0-2 in the ADCCTRL register. For the work described in this thesis, the conversion process was started by setting bit 1 of the SOFTCONVST register (a mode selected by setting bits 0-2 of the ADCCTRL register).

B2: Overview of the Encoder Interface Unit

The ADSP-21992 incorporates an encoder interface block that enables position and speed information to be derived from shaft encoder feedback signals. A functional block diagram of the EIU is shown in Figure B.3 (ADMC501 Specification 1.0 2001). The EIU has four dedicated chip pins. Quadrature encoder signals from an incremental encoder can be applied to the EIA and EIB pins. Alternatively, a frequency and direction set of inputs may be applied. The other two pins, EIZ and EIS, are zero marker and strobe inputs. The EIU incorporates programmable noise filtering on the four encoder inputs to ensure that EIU operation isn't adversely affected by spurious noise pulses.

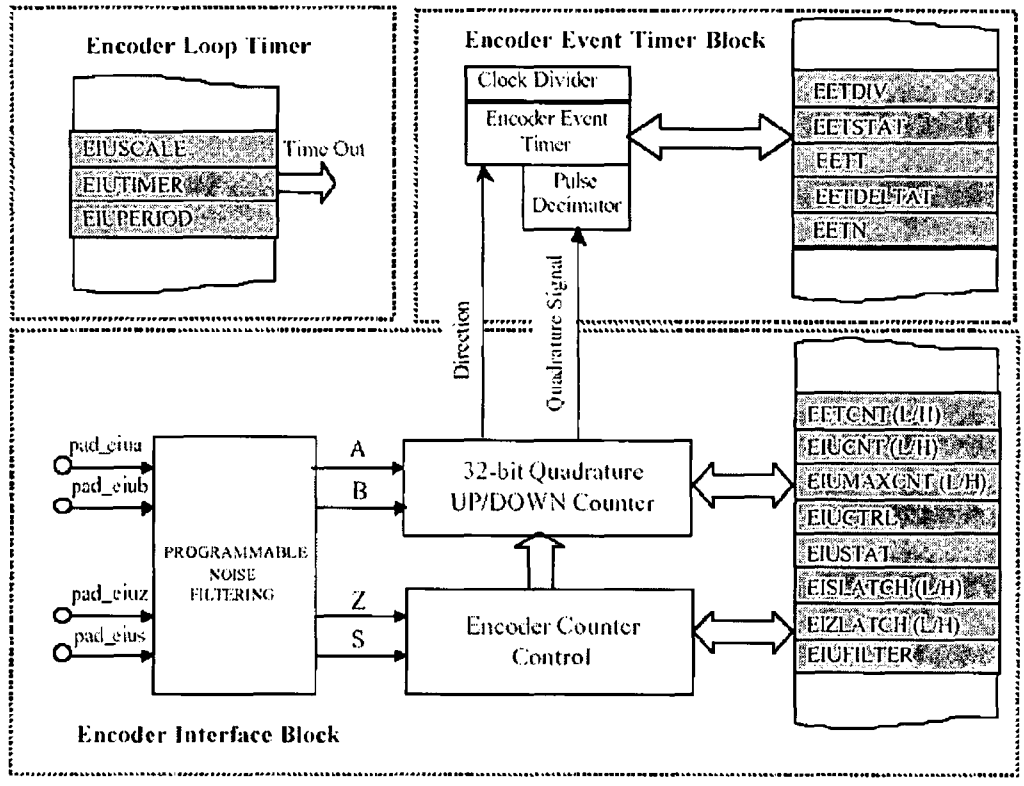

Figure B.3: Functional block diagram of the EIU.

The EIU includes a quadrature up/down counter whose value can be determined by reading the 32-bit EIUCNT register. This counter can be reset by a zero marker signal on the EIZ pin or alternatively, according to the contents of a maximum count register EIUMAXCNT. The desired mode of operation can be selected using the dedicated control bits in the EIU control register EIUCTRL. In order to initilise the EIU, in all modes of operation, the EIUMAXCNT register must be written to.

As can be seen in Figure B.3, the EIU also incorporates a 16-bit Encoder Loop Timer that can be programmed to time-out and reload at regular intervals. When the loop timer times out, an EIU loop timer timeout interrupt is generated which can be used to control the timing of particular control loops.

Another important module within the EIU is the Encoder Event Timer (EET), which enables the accurate timing of successive events on the encoder inputs. The EET can be programmed to time the interval between two or more encoder pulses up to a

maximum of 255 encoder pulses. The number of pulses is set by writing to the 8-bit EETN register and is useful for rotational speed estimation.

B3: Overview of the general-purpose timer unit

The ADSP-21992 has a built–in general-purpose timer unit that contains three identical 32-bit timers (Timer0, Timer1 and Timer2) with each timer capable of operating independently in one of the three following modes:

- Pulse Waveform Generation (PWM_OUT) mode
- Pulse Width Count/Capture (WDTH_CAP) mode
- External Event Watchdog (EXT_CLK) mode

Each timer has one bi-directional chip pin, TMR0 – TMR2. Each timer pin is configured as an output pin in PWM_OUT mode and as an input pin in the WDTH_CAP and EXT_CLK modes.

Each timer has seven 16-bit memory-mapped registers with six of these registers paired to achieve 32-bit precision. Thus each timer has a 16-bit configuration register, a 32-bit count register, a 32-bit period register and a 32-bit pulse-width register. The timer configuration register, CFGRx (x=0,1,2), enables selection of the operating mode of the individual timer (i.e. PWM_OUT etc.).

In addition, there is a single Global Timer Status and Control Register, GSR, which provides status and control functions for all three timers. The GSR is mapped to three separate addresses and at the different addresses the GSR register is referred to as GSR0, GSR1 and GSR2. The GSR register indicates the occurrence of an interrupt or timer overflow and permits the timer to be enabled or disabled.

The PWM_OUT mode of operation enables variable-period, variable-width pulses to be produced on the TMRx (x=0,1,2) pin of the associated timer. In the WDTH_CAP mode, the TMRx (x=0,1,2) pin becomes an input and the timer unit is used to capture the width and period of the signal applied to the input pin. Meanwhile, in the EXT_CLK mode, the 32-bit counter is clocked from an external clock source supplied at the TMRx (x=0,1,2) pin.

B4: Overview of the Flag I/O peripheral unit

The Flag I/O (FIO) unit is a parallel I/O interface that supports 16 bi-directional general purpose I/O signals (PF0-PF15). Each flag bit can be individually configured as an input or output depending on the contents of the direction (DIR) register. They can also be used as a source for an interrupt.

When a flag is configured as an input, the FIO can be programmed to invert the input value, latch a level or detect a signal edge (rising, falling or both) depending on the contents of the POLAR, EDGE and BOTH registers. When a flag is configured as an output, the output value is driven from the FLAG register. The 16-bit FLAG register exhibits 'sticky' behaviour; only writing a '1' to a bit can modify that bit. Writing a '1' to a bit of the FLAG register at the even address 0x0002 (FLAGC) clears the FLAG bit while writing a '1' to a bit of the FLAG register at the odd address 0x0003 (FLAGS) sets the FLAG bit. Writing a '0' to any bit in either FLAGC or FLAGS has no effect. On the EZ-KIT Lite board shown in Figure B.1, access to the 16 FIO programmable flag pins on the ADSP-21992 chip is via connector P8.

B5: Writing C-callable assembly functions and creating libraries

Successful implementation of the SRM control strategies on the DSP requires extensive employment of the peripheral units of the ADSP-21992 for (1) sampling of phase currents, dc link voltage etc., (2) deriving rotor position information from the encoder feedback signals and (3) outputting gate drive signals. As a result, the various peripheral unit registers are continuously being written to and read from. Access to registers on the DSP can only be achieved through assembly language instructions. These instructions can be embedded in the C programs implementing the SRM control using the 'asm' directive as follows:

```
asm("assembly instruction here");
```

However, the huge number of assembly instructions required to perform all the desired tasks associated with the various peripheral units would result in impenetrable code and consequent development and debugging difficulties. For this reason, it was decided to write C-callable assembly functions for many of the common tasks

performed by the peripherals. The manner in which this was done is illustrated with a detailed example that is included in Appendix C1.

Several functions similar to that outlined in Appendix C1 were written for each of the peripherals employed in the SRM control. For each peripheral unit, the associated functions were combined into a library file.

B6: DSP clock frequency

The ADSP-21992 contains a Clock Generation (CKGEN) module that enables the selection and the changing of the ADSP-21992 core clock (CCLK) and peripheral clock (HCLK) frequencies. The operation of the clock generation circuitry is controlled by the I/O mapped PLL Control Register (PLLCTL).

The ADSP-21992 on the EZ-KIT Lite board is supplied with a 32MHz input clock. To ensure a high control bandwidth for the implementation of the complex SRM control strategies, it was desirable to increase the DSP core clock frequency to its maximum of 160MHz. The code written to increase CCLK to 160MHZ and HCLK to its maximum of 80MHz is included in Appendix C2.

Appendix C – DSP C and assembly code

C1: Writing C-callable assembly language functions

As explained in Appendix B1, after each pair of ADC inputs are converted, each resulting 12-bit digital number is written to a dedicated 16-bit, 2's complement, left-aligned register. In the case of the signal on the VIN0 pin, the converted result is written to the register ADC0. An assembly language function was written to read the value in the ADC0 register and the code is shown in Figure C.1.

```
.section/code program;
.Global _read_data_0; //Function declared as global.

_read_data_0:
IOPG=0x0D;              //Access the correct page in memory.
AX1=IO(0x004);          //Value in ADC0 stored in AX1.
RTS;                    //Return command.
.read_data_0.end:
```

Figure C.1: C-callable assembly language function that reads the contents of ADC0.

An assembly source file must describe how code and data are mapped into the memory on the ADSP-21992. Such mapping is accomplished using the `.section` directive. Each `.section` name corresponds to an input section in the linker description file. In this case, the `.section` directive is used to put the function in a code section called 'program'. The function must be declared as 'global' or else the function could only be used within its own file. The name of the function is '`_read_data_0`'. In a C program this assembly function can be called using '`read_data_0()`' i.e. the leading underscore is removed when calling the function in the C program.

The DSP memory is divided into several pages and it is important to switch to the correct page before reading or writing to an address. This is accomplished using the '`IOPG`' command. The command '`AX1 = IO(0x004);`' writes the 16-bit value contained in the register at the address 0x004 to a register called AX1. To return a 16-bit value the AX1 register must be used. Hence, when the return command '`RTS;`' is

used, the program jumps back to the part of the program where the function example was called and the value in the AX1 register is returned.

C2: Increasing the DSP core clock frequency

```
/*This file is used to increase the DSP core clock
frequency from 32MHz to the maximum frequency of 160Mhz
and to increase the peripheral clock frequency to its
maximum of 80MHz*/

#include <signal.h>
#include<sysreg.h>

main()
{

//Bypass mode enable and PLL shutoff.
asm("iopg = 0x00;");
asm("ax1 = 0x0120;");
asm("io(0x200) = ax1;");
asm("nop;");


//Bypass mode enable and write the correct multiplier
value.
asm("iopg = 0x00;");
asm("ax1 = 0x0b50;"); //Multiple of 5 => 160MHz
asm("io(0x200) = ax1;");
asm("nop;");


//Bypass mode disable and maintain the same mulitplier
value. //as before
asm("iopg = 0x00;");
asm("ax1 = 0x0a50;"); //Multiple of 5 => 160MHz
asm("io(0x200) = ax1;");
asm("nop;");

}
```

Figure C.2: C code written to generate a DSP core clock frequency of 160MHz and a peripheral clock frequency of 80MHz from a 32MHz input clock.

C3: C functions employed in current and voltage measurement

```
void meas_cur_a()       //Function used to sample
                        //phase current A.
{
cur_a=read_data_0();    //Read ADC0 register.
cur_a=cur_a>>4;         //Shift the 12-bit number.
temp=(float)cur_a;
Ia=10*temp/0x7FF;       //Convert the sampled voltage
}                       //to the actual current value.
                        //5 turns on the sensor => 50/5=10
```

Figure C.3: C code function that converts the ADC sampled voltage from the phase current measurement circuit and returns the phase A current value.

```
cur_gen=read_data_4();  //Read ADC4 register.
cur_gen=cur_gen>>4;     //Shift the 12-bit number.
temp=cur_gen;
Igen=3.33*temp/0x7FF;   //Convert the sampled voltage
                        //to the actual current value.
                        //15 turns on the sensor => 50/15 = 3.33
```

Figure C.4: C code that converts the ADC sampled voltage from the dc link current measurement circuit and returns the corresponding measured current value.

```
start_adc();                          //Begin ADC conversion.
while(!(read_adc_status()&0x0002)); //Wait until converted.
volt_meas=read_data_3();              //Read ADC3 register.
volt_meas=volt_meas>>4;               //Shift 12-bit number.
temp=volt_meas;
voltage=94*temp/0x7FF;  //voltage is 94 times sampled value.
```

Figure C.5: C code that converts the ADC sampled voltage output from the dc link voltage measurement circuit and returns the actual measured dc link voltage value.

C4: Flux-linkage estimation

```
dt=(float)read_timer_1_CNTR()*(0.00000001667); //Convert to time.
set_timer_1_GSSR(0x0800);      //Disable timer1.
set_timer_1_GSSR(0x0400);      //Enable timer1.
fluxa += (Va - Rph*Ia)*dt;     //Va includes losses in
                               //diodes and switches.
if (fluxa < 0) fluxa=0;
```

Figure C.6: C code that estimates phase A flux-linkage using the measured phase current and the estimated phase voltage.

C5: Position derivation information

```
float eposition(void)
{
float out;
out = (read_eiucntlo()/45.51111)-29.5;
//(readcounter/2048)*45 degrees - 29.5 degrees
//29.5 is the required adjustment for Amax = 0 degrees

if(out<0) return(out+45);

return (out);
}
```

Figure C.7: Function employed to return a position value between 0 and 45 degrees using feedback from the incremental encoder.

Since the incremental encoder was attached to the dc machine (which was only subsequently coupled to the SRM via the two rotors), the zero marker wasn't aligned with the aligned position of phase A. This position had been designated as the 0 degree point. Hence, it was necessary to determine an appropriate offset to add to the output of the incremental encoder such that it produced the same positional value (between 0 and 45 degrees) as the SRM slotted disk rotary encoder.

Figure C.8 shows the position returned by the SRM slotted disk encoder (the correct position) and the position initially returned by the incremental encoder (which isn't aligned correctly). From the graph it is possible to determine that if 29.5 degrees is subtracted from the incremental encoder result (or alternatively 15.5 degrees is added to it) then the incremental encoder will produce the correct position. Figure C.9 shows the result of putting in this position offset. As can be seen, the position now returned

by both encoders matches very well. In fact, Figure C.10 shows that there is only a minute difference between the two positions returned (in the region of 0.05 degrees). This offset of 29.5 degrees was included in the '`eposition()`' function code of Figure C.7.

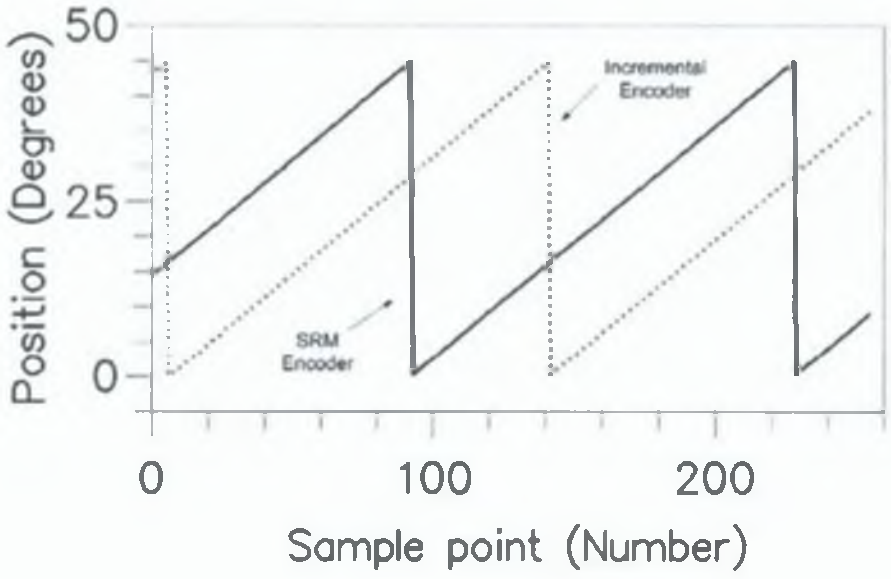

Figure C.8: The position returned by the SRM slotted disk encoder (correct position) and the position returned using the incremental encoder before the offset is added.

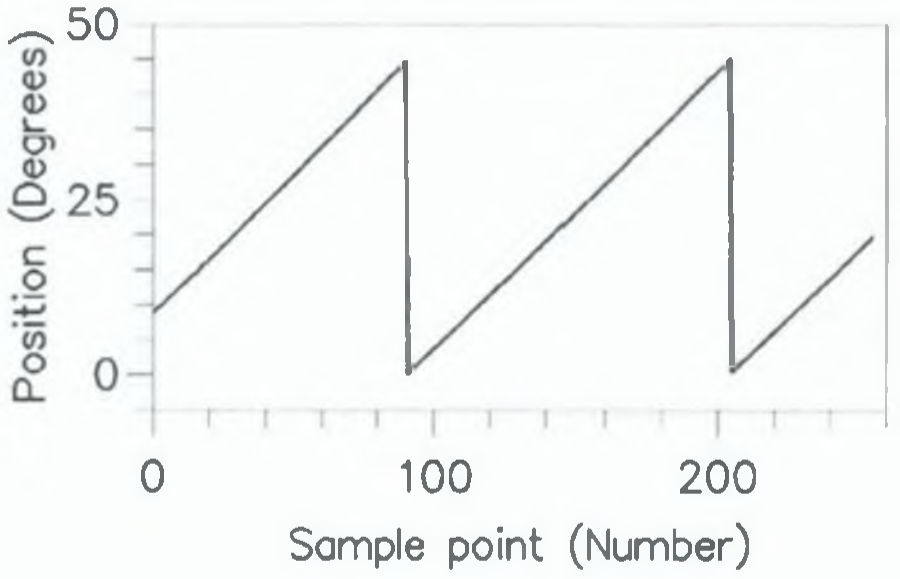

Figure C.9: The position returned using both the slotted disk encoder and the incremental encoder when the offset of 29.5 degrees is added. The two lines overlap and it is hard to distinguish between the values returned by both encoders.

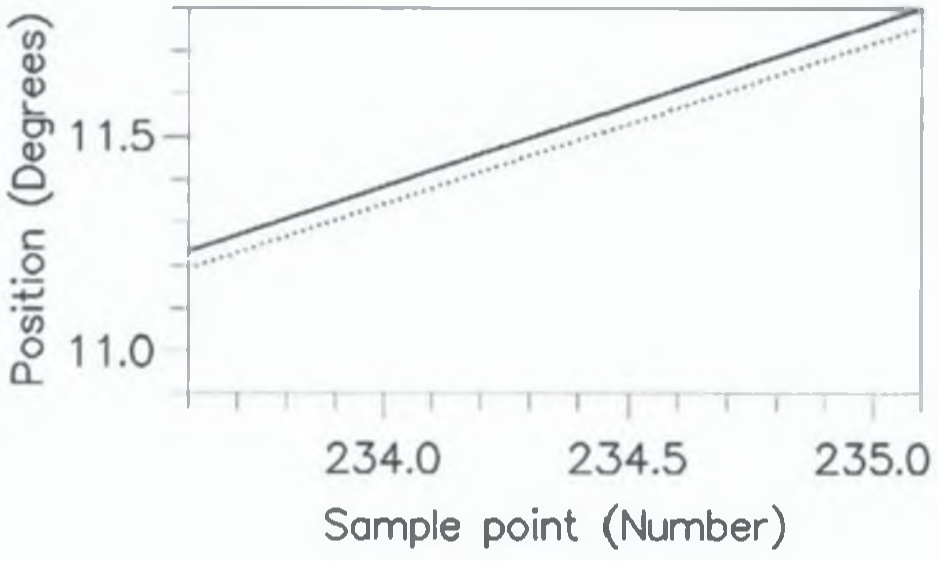

Figure C.10: The position returned using both the slotted disk encoder and the incremental encoder when the offset of 29.5 degrees is added. This is the same as Figure C.9 except the graph has been zoomed in on.

Appendix D - Publications

Refereed Journal Papers

Kennedy E., Murphy A.J., Condon M. and Dowling J., Closed-loop control of switched reluctance generators, *COMPEL: The International Journal for Computation and Mathematics in Electrical and Electronic Engineering*, Vol. 24, No. 2, pp. 662-681, 2005.

Abstract

Purpose of this paper	This paper deals with the closed-loop control of a switched reluctance generator (SRG).
Design/methodology/approach	The control objective when generating is to maintain the dc link voltage at the required value while achieving maximum efficiency. Three possible control schemes are presented and their performance is examined by testing on an experimental 12/8 3-phase SRG.
Findings	A very simple control scheme that requires no prior characterisation of the SRG, an approach based on the use of an inverse machine model and finally, a control scheme that is aimed at achieving optimal efficiency are described and experimental results for all three are presented.
Research limitations/implications (if applicable)	The inverse machine model control scheme and the optimal efficiency control scheme require operation at a constant voltage reference for accurate operation (although this is the case for many generator applications). Possible future research might include the expansion of these control schemes to operation with a variable voltage reference.
Practical implications (if applicable)	The importance of maximising efficiency is emphasised with a clear method of deriving the optimal efficiency firing angles described.
What is original/value of paper	This paper provides a good overview of SRG operation through the experimental implementation of three separate closed-loop voltage control schemes, each of which is described in detail.

Refereed Conference Proceedings:

Kennedy E., Condon M. and Dowling J., Torque-ripple minimisation in switched reluctance motors using a neuro-fuzzy control strategy, *EPE 2003, Proceedings of the European Conference on Power Electronics and Applications*, Toulouse, France, 2 – 4 September, 2003.

Abstract

This paper presents a neuro-fuzzy control strategy for torque-ripple minimisation in SRMs. The proposed technique adds a compensating signal to the output of a PI controller in a current-regulated speed control loop. The compensating signal is produced by a neuro-fuzzy compensator that is trained off-line prior to normal operation. The neuro-fuzzy compensator is based on the ANFIS system. A torque observer is employed in both the neuro-fuzzy compensator training process and during subsequent operation of the SR drive with the trained compensator included. Simulation results for both a 6/4 three-phase SRM and a 6/4 three-phase SRM confirm a very significant reduction in the torque-ripple.

Kennedy E., Condon M. and Dowling J., A neuro-fuzzy control strategy for torque-ripple reduction in switched reluctance motors, *ISSC 2003, Proceedings of the Irish Signals and Systems Conference*, Limerick, Ireland, 30 June – 2 July, 2003.

Abstract

A novel neuro-fuzzy control strategy for torque-ripple minimisation in switched reluctance motors is presented. A compensating signal is added to the output of a PI controller in a current-regulated speed control loop. The neuro-fuzzy compensator is trained off-line. Simulation results for a 12/8 three-phase SRM confirm a very significant reduction in the torque ripple.

Kennedy E., Condon M. and Dowling J., Torque-ripple minimisation in switched reluctance motors using a neuro-fuzzy control strategy, *MS2003, Proceedings of the IASTED International Conference on Modelling and Simulation*, Palm Springs, USA, 24 – 26 February, 2003.

Abstract

A novel neuro-fuzzy control strategy for torque-ripple minimisation in switched reluctance motors is presented. A compensating signal is added to the output of a PI controller in a current-regulated speed control loop. The neuro-fuzzy compensator is trained off-line. Simulation results for a 6/4 three-phase SRM confirm a very significant reduction in the torque ripple.

Kennedy E., Condon M. and Dowling J., Control of switched reluctance starter-generators, *MIC2002, Proceedings of the IASTED International Conference on Modelling, Identification and Control*, Innsbruck, Austria, 18 – 21 February, 2002.

Abstract

The paper proposes a strategy for controlling an integrated starter-generator system. The starter-generator system is based on the Switched Reluctance Machine (SRM) and is intended for automotive applications. The main focus of the paper is the development of a controller for the SRM when it is acting as a generator. The adaptive control strategy proposed by Russa et al. [1] is chosen for the starting phase when the SRM is acting as a motor. Once the engine reaches idle speed, the SRM becomes a generator and a control strategy based on that proposed by Kjaer et al. in [2] is suggested. Kjaer et al. [2] derive a mathematical relationship between the firing angles and the average generated current for a linear model of an SRM where saturation and fringing effects are neglected. The present paper examines the relationship between the turn-on angle and the average net generated current for a more general SRM model that includes non-linearities and saturation effects. The resultant relationship is subsequently used to develop a closed-loop controller for the Switched Reluctance Generator (SRG).